

**CORROSION FATIGUE  
OF A  
SUPERDUPLEX STAINLESS STEEL  
WELDMENT**

Thesis submitted to Dublin City University for the degree of  
**Doctor of Philosophy.**

**Author:** Anthony John Comer, B.E. (Mechanical Engineering).  
(50161547)

School of Mechanical and Manufacturing Engineering,  
Faculty of Engineering and Computing,  
Dublin City University.

**Supervisor:** Dr. Lisa Looney

**Date:** 02 / 12 / 2003

**E-mail:** *anthony.comer@dcu.ie*

## DECLARATION

I hereby certify that this material, which I now submit for assessment on the programme of study leading to the award of Doctor of Philosophy is entirely my own work and has not been taken from the work of others save to the extent that such work has been cited and acknowledged within the text of my work.

Signed:  ID No.: 50161547.

Anthony John Comer

Date: December 2, 2003.

## PUBLICATIONS ARISING FROM THIS RESEARCH

Comer A, Looney L, Corrosion fatigue of a welded superduplex stainless steel, Proc. International Conference on Advances in Materials and Processing Technologies, (AMPT), Dublin, Republic of Ireland, (July 2003). \* **Best Student Paper**

Comer A, Looney L, Corrosion fatigue of a superduplex stainless steel weldment, Proc. 2nd International Youth Symposium on Experimental Solid Mechanics (YSESM), Ravenna, Italy (May 2003).

Comer A, Looney L, Fatigue and corrosion properties of a welded superduplex stainless steel, Proc. International Manufacturing Conference (IMC-19), Belfast, Northern Ireland, (August 2002).

Comer A, Looney L, Corrosion fatigue crack propagation of a welded superduplex stainless steel, Poster presented at the 5<sup>th</sup> Sir Bernard Crossland Symposium, University of Ulster Jordanstown, Northern Ireland, (March 2002).

## ACKNOWLEDGEMENT

I would like to acknowledge Dr. Lisa Looney for her exceptional supervision of this research. Her approach was at all times conscientious, encouraging, helpful and constructive.

I would also like to acknowledge Weir Materials and Foundries, Manchester, UK, for sponsoring their material for this research. A special thanks to Dr. Roger Francis for much enlightening communication with regard to Zeron 100. In addition, I would like to thank Mr. Tim Healiss for his time and assistance while carrying out tests in Manchester.

I would like to acknowledge the technical staff in DCU who were involved at various stages in this research particularly Mr. Liam Domican, Mr. Chris Crouch, Mr. Michael May, Mr. Martin Johnson and Mr. Keith Hickey.

Last but not least, my special thanks to my family, parents Pat and Seán, Debra, Stephen, Sarah, Chloe and Martin for their continuous support and encouragement.

## **DEDICATION**

This research is dedicated to Laura, who encouraged, advised and listened to me throughout the years of my research. Thank You for your patience and I hope You enjoy the read !!

## TABLE OF CONTENTS

DECLARATION.....	ii
PUBLICATIONS.....	iii
ACKNOWLEDGEMENT.....	iv
DEDICATION.....	v
TABLE OF CONTENTS.....	1
ABSTRACT.....	3
LIST OF TABLES.....	4
LIST OF FIGURES.....	6
<b>1. INTRODUCTION.....</b>	<b>11</b>
1.1 PROJECT BACKGROUND.....	11
1.2 THE CURRENT STUDY.....	14
1.3 NOVELTY.....	20
1.4 THESIS OUTLINE.....	22
1.5 ACKNOWLEDGEMENT.....	23
<b>2. LITERATURE REVIEW.....</b>	<b>24</b>
2.1 STAINLESS STEELS.....	26
2.2 DUPLEX STAINLESS STEELS.....	34
2.2.1 Metallurgy.....	35
2.2.2 Base metal v weld metal.....	37
2.2.3 Welding procedure.....	39
2.3 TOUGHNESS OF DUPLEX STAINLESS STEEL WELDS.....	45
2.3.1 Review of test data.....	47
2.4 CORROSION RESISTANCE OF DUPLEX STAINLESS STEELS.....	52
2.4.1 Localised corrosion.....	53
2.4.2 Review of test data.....	59
2.5 HYDROGEN EMBRITTLEMENT (HE).....	63
2.5.1 Mechanistic models for hydrogen embrittlement.....	67
2.5.2 Review of test data.....	69
2.6 CORROSION FATIGUE BEHAVIOUR.....	73
2.6.1 Crack initiation resistance.....	76
2.6.2 Crack propagation resistance.....	83
2.7 LIMITATIONS OF PUBLISHED DATA.....	88
<b>3. EXPERIMENTAL WORK.....</b>	<b>89</b>
3.1 WELDMENT FABRICATION & BASIC INTEGRITY ASSESSMENT.....	90
3.1.1 Weldment fabrication.....	90
3.1.2 Tensile strength.....	93
3.1.3 Toughness.....	94
3.1.4 Hardness.....	96
3.1.5 Non destructive tests (NDT).....	98
3.2. MICROSTRUCTURAL AND CORROSION ASSESSMENT OF WELD METAL.....	100
3.2.1 Microstructural examination.....	100

3.2.2 SEM & image analysis .....	104
3.2.3 Calculation of percentage ferrite .....	106
3.2.4 Energy dispersive X-ray (EDX).....	109
3.2.5 Localised corrosion .....	110
3.2.6 Residual stress determination.....	116
3.3 CRACK PROPAGATION .....	117
3.3.1 Sample type selection.....	117
3.3.2 Crack propagation set-up.....	125
3.3.3 FEA analysis of angular misalignment .....	134
3.3.4 Test procedures.....	140
3.3.5 Fracture surface analysis .....	149
<b>4. RESULTS &amp; DISCUSSION .....</b>	<b>150</b>
4.1 WELDMENT FABRICATION AND BASIC INTEGRITY ASSESSMENT .....	150
4.1.1 Weldment fabrication .....	151
4.1.2 Tensile strength.....	153
4.1.3 Toughness .....	156
4.1.4 Hardness.....	158
4.1.5 Non destructive tests (NDT) .....	162
4.2 MICROSTRUCTURAL AND CORROSION ASSESSMENT OF WELD METAL .....	164
4.2.1 Microstructural examination.....	165
4.2.2 SEM and image analysis.....	169
4.2.3 Intermetallic and inclusion content .....	173
4.2.4 Calculation of percentage ferrite .....	176
4.2.5 Energy dispersive X-ray .....	180
4.2.6 Localised corrosion .....	183
4.2.7 Residual stress measurement.....	186
4.3. CRACK PROPAGATION .....	189
4.3.1 FEA analysis of angular misalignment .....	189
4.3.2 Fatigue precracking and crack growth thresholds.....	193
4.3.3 Stage II crack propagation and effect of residual stress fields .....	197
4.4 MODELLING.....	235
4.4.1 Fatigue life modelling.....	235
4.4.2 Mechanistic model of hydrogen assisted fatigue crack propagation .....	245
<b>5. CONCLUSIONS AND FUTURE WORK.....</b>	<b>256</b>
5.1 CONCLUSIONS .....	256
5.2 FUTURE WORK .....	258
<b>REFERENCES .....</b>	<b>259</b>
<b>APPENDIX A.....</b>	<b>278</b>
INTRODUCTION TO CORROSION AND ELECTROCHEMISTRY .....	278
<b>APPENDIX B.....</b>	<b>291</b>
INTRODUCTION TO FRACTURE MECHANICS .....	291
<b>APPENDIX C.....</b>	<b>304</b>
ZERON 100 WELDING GUIDELINES .....	304

## ABSTRACT

### Corrosion-Fatigue of a Superduplex Stainless Steel Weldment

Anthony John Comer

Superduplex stainless steels have superior mechanical and corrosion properties compared to austenitic stainless steels such as the grade 300 series. This is a result of a microstructure consisting of roughly equal percentages of austenite ( $\gamma$ ) and ferrite ( $\alpha$ ) and negligible inclusion content.

As a result, super duplex stainless steels are increasingly being used in the offshore oil and gas industries. It is also envisaged that they will find application in the emergent renewable energy sector in areas such as offshore wind, wave and tidal electricity / hydrogen generation. Corrosion fatigue (CF) conditions are expected in such applications. Of critical concern are weld joints where inherent sub critical surface/embedded flaws diminish crack initiation resistance enhancing the probability of subsequent crack propagation.

The current research investigates the CF crack propagation performance of weld metals produced by two welding techniques. Since sub sea components are always cathodically protected, this condition was simulated in the CF tests. In addition, high positive potentials were simulated, as this condition is possible in the absence of cathodic protection. One weldment was completed using the expensive and relatively slow gas tungsten arc (GTA) welding method. The other weldment was achieved using the GTA method for the root pass and subsequently filled using the cheap and relatively quick shielded metal arc (SMA) welding method.

The resultant crack propagation life was derived from the crack propagation tests by means of a numerical model. Fatigue life of the weld metals (assuming negligible residual stress influence) is similar to standard design curves for class D, carbon and carbon-manganese structural steel butt welds. Thresholds for the onset of crack growth in Zeron 100 base and weld metals are similar and were shown by means of the numerical model to correspond with the endurance limit specified in the standard design curve. Cathodic over protection is much more deleterious than high positive potentials above a critical stress level for Zeron 100 base and weld metals leading to an increase in crack propagation rates on average by a factor of 4.3 over rates in air. The GTA root/SMA fill weld metal performs equally well as the GTA root/GTA fill weld. Therefore, a potential economic saving is evident.

Finally, a new model for hydrogen assisted subcritical brittle crack propagation in ferrite is proposed.



## LIST OF TABLES

Table 2.1 Mechanical property ranges for various stainless steel classes. ....	33
Table 2.2 Unified numbering system (UNS) designation for selected duplex & superduplex stainless steels. ....	35
Table 2.3 Norsok acceptance criteria for wrought plate [cited in 12]. ....	38
Table 2.4 Diffusion coefficients for various stainless steels. ....	65
Table 2.5 Parameters and result format associated with S-N and da/dN type fatigue tests. ....	75
Table 2.6 Effect of saturation level, solution temperature and pH on fatigue limit in S-N type fatigue test [99]. ....	80
Table 3.1 Average welding parameters for GTA and GTA root/ SMA fill welds. ....	92
Table 3.2 Base metal & welding consumable composition (Wt %). Remainder Fe [112]. ....	92
Table 3.3 Grinding and polishing procedure. ....	101
Table 3.4 Synthetic seawater composition [16]. ....	112
Table 3.5 Material properties used in FE analysis [112]. ....	135
Table 3.6 Summary of crack propagation tests carried out in the current research. ....	147
Table 4.1 Angular misalignment in weldments. ....	151
Table 4.2. Tensile test results including percentage scatter. ....	154
Table 4.3 Charpy V Notch experimental values, average values in bold. ....	156
Table 4.4 Summary of base and weld metal mechanical properties. ....	163
Table 4.5 Number of passes required to complete weldments. ....	165
Table 4.6 Grain size in base and weld metals. ....	167
Table 4.7 Intermetallic contents in weld metals. ....	173
Table 4.8 Inclusion content in SMA weld metal. ....	174
Table 4.9 Wt % of heavy elements in three inclusions. ....	175
Table 4.10 Average % ferrite determined by image analysis. ....	176
Table 4.11 Element content of GTA weld metal determined by EDX analysis. ....	181
Table 4.12 Element content of SMA weld metal determined by EDX analysis. ....	181
Table 4.13 Selection of elements present in base metal & weld metal consumables [16, 112]. ....	181
Table 4.14 Summary of Microstructural investigation of weld metals. ....	188
Table 4.15 Threshold values obtained by $\Delta K$ increasing and $\Delta K$ decreasing tests, R-ratio =0.5. ....	194
Table 4.16 Fast fracture average values for base and weld metal samples. ....	200
Table 4.17 Paris equation coefficients and the coefficient of determination for data obtained in laboratory air. ....	202
Table 4.18 Paris equation coefficients, coefficients of determination and corrosion cell data for tests in synthetic seawater (+600mV SCE). R-ratio =0.5. Oxygen bubbled into seawater. ....	215
Table 4.19 Thresholds obtained in synthetic seawater (-1040mV SCE). ....	222
Table 4.20 Paris equation coefficients, coefficients of determination and corrosion cell data for tests in synthetic seawater (-1040 mV SCE), R-ratio =0.5. ....	223
Table 4.21 Experimental data from current research. ....	237

**Table 4.22 Coefficients for exponential function.....240**  
**Table 4.23 Additional experimental data calculated using simple beam theory considering  
    SEN4 samples employed in the current work.....241**

## LIST OF FIGURES

Figure 1.1. Crack initiation from poor root pass of single V butt weld. ....	17
Figure 2.1 Schematic of passive film prevalent in austenitic stainless steels [36].....	27
Figure 2.2 Schematic diagram showing compositional and property linkages in the stainless steel family of alloys [cited in 42]. ....	29
Figure 2.3 Schematic of general corrosion resistance for various stainless steel classes. ....	33
Figure 2.4 Vertical Section of an Fe-Cr-Ni phase diagram at 60% Fe. C <sub>0</sub> composition line represents commercial duplex stainless steel. $\delta = \alpha$ = ferrite, $\gamma$ = austenite, $\sigma$ = intermetallic [cited in 12]. ....	36
Figure 2.5 Schematic of epitaxial grain growth from fusion boundary. ....	39
Figure 2.6 Average mechanical properties for two superduplex stainless steels (Zeron 100 and SAF 2507) base and weld metals. ....	41
Figure 2.7 Welded plates exhibiting longitudinal contraction. ....	43
Figure 2.8 Schematic of toughness determined by charpy impact tests as a function of temperature for steels. ....	46
Figure 2.9 Typical impact values for Zeron 100 base and weld metal (100X consumables) [45]. .	51
Figure 2.10 ECPs of high alloy stainless steels as a function of seawater condition [71]. ....	55
Figure 2.11 Schematic of ECP as a function of current density for a stainless steel. ....	56
Figure 2.12 Passive film thickness (nm) versus ECP (Volts SCE) [cited in 36]. ....	57
Figure 2.13 Schematic of S-N curve showing initiation life, propagation life and total life. ....	74
Figure 3.1 Zeron 100 wrought plate. ....	90
Figure 3.2 Single V-butt preparation geometry - dimensions in mm. ....	91
Figure 3.3 Orientation of cross weld tensile sample with respect to rolling direction. ....	93
Figure 3.4 Standard charpy V notch impact sample for base metal – dimensions in mm [59]. ....	94
Figure 3.5 Impact sample orientation with respect to rolling direction. ....	95
Figure 3.6 Approximate positions of the 9 microhardness test regions. ....	97
Figure 3.7 Transverse weldment sample ....	100
Figure 3.8 Electrolytic etching cell. ....	102
Figure 3.9 Approximate location of field arrays used for point counting of ferrite content. ....	107
Figure 3.10 Determination of ECP as a function of corrosion rate - experimental setup. ....	111
Figure 3.11 Schematic of potentiostat electrical circuit [16]. ....	114
Figure 3.12 Weldment sample, x-ray source and detector - residual stress determination test. ....	116
Figure 3.13 Effect of loading mode on samples with angular misalignment. ....	118
Figure 3.14 Single edge notched four point bend (SENB4) sample. ....	120
Figure 3.15 Base metal sample. ....	121
Figure 3.16 Schematic of residual stress system induced transverse to weld bead in a weldment. Residual stresses are caused by weld bead contraction. ....	121
Figure 3.17 Centre cracked tension (CCT) sample – dimensions in mm. ....	123
Figure 3.18 CCT notch detail – dimensions in mm. ....	125
Figure 3.19 SENB4 sample set-up in laboratory air. ....	127

Figure 3.20 CCT sample set up on ESH fatigue machine. ....	128
Figure 3.21 SENB4 sample with environmental chamber attached. ....	129
Figure 3.22 Schematic of synthetic seawater circulation system. ....	130
Figure 3.23 Corrosion fatigue set up showing reference, auxiliary, noise reduction electrodes, remote reservoir and salt bridge. ....	131
Figure 3.24 Close up of luggin capillary, the tip of which is located 10 mm from the weld metal. .....	131
Figure 3.25 Experimental set up for corrosion fatigue. ....	132
Figure 3.26 Triangular quarter point elements and nodes used for calculating K. ....	134
Figure 3.27 Plane 2, 6 node triangular element. ....	136
Figure 3.28 Half model of SENB4 sample. ....	136
Figure 3.29 Close up of crack tip showing 8 singular elements (isosceles triangles) with 1 mm radius. Midside nodes are not shown. ....	137
Figure 3.30 Geometry, mesh and crack in misaligned SENB4 finite element model. ....	139
Figure 3.31 Development of residual tensile stresses ahead of a crack tip due to the application of fluctuating compressive loading [86]. ....	141
Figure 3.32 Development of a monotonic and cyclic plastic zone ahead of a crack tip [86]. ....	144
Figure 4.1 Angular misalignment in weldments. ....	151
Figure 4.2 Worst case strength for cross weld tensile samples ....	153
Figure 4.3 Worst-case ductility for cross weld tensile samples. ....	153
Figure 4.4 WMF Charpy impact toughness design values [112]. ....	157
Figure 4.5 GTA microhardness and 95% confidence interval. ....	158
Figure 4.6 SMA microhardness and 95% confidence interval. ....	159
Figure 4.7 Interaction of propagating crack with phases of different hardness. ....	160
Figure 4.8 S-N quality curves for steel weldments [19]. To qualify in a category, the type and severity of weld flaw must be assessed. Q1 is the highest quality category. ....	162
Figure 4.9 Macrograph of SMA weld metal etched using 20% NaOH. Attachment length 'L' also shown. ....	165
Figure 4.10 Micrographs of base, GTA and SMA weld metals. ....	166
Figure 4.11 Top left is the superstructure of weld metal [12] and schematic of primary ferrite grain growth (top right). Lower figure shows direction of welding and embrittled primary ferrite grains. ....	168
Figure 4.12 GTA fracture surface. ....	169
Figure 4.13 SMA fracture surface. ....	170
Figure 4.14 Fractured brittle inclusion. ....	170
Figure 4.15 Lack of fusion between GTA root pass and SMA weld metal ....	171
Figure 4.16 Schematic of flaw on fracture surface of CCT GTA weld metal sample. ....	172
Figure 4.17 Intermetallic at ferrite/austenite grain boundary in SMA weld metal. ....	173
Figure 4.18 Inclusions on SMA weld metal fracture surface. ....	174
Figure 4.19 Spectral analysis of inclusion found on SMA fracture surface. ....	175

Figure 4.20 % ferrite content of weldment regions - point count method & image analysis method. ....	177
Figure 4.21 EDX spectrum of ferrite (red) with austenite spectrum superimposed (green). Evident is higher Cr/Ni ratio of ferritic phase. ....	180
Figure 4.22 Average ECP v current density curves for base and weld metals at 20 <sup>0</sup> C.....	183
Figure 4.23 ECP as a function of current density for base metal in seawater at 20 <sup>0</sup> C and 80 <sup>0</sup> C.	184
Figure 4.24 Pitting on base metal sample at 20 <sup>0</sup> C, +1100mV SCE.....	185
Figure 4.25 Snapshot of rocking curve scan and Z scan from X-ray diffractometer software....	186
Figure 4.26 Snapshot of locked couple scan showing peaks for Fe, Cr and Mo.....	187
Pitting ECP (mV SCE) @20 <sup>0</sup> C.....	188
Figure 4.27 $\Delta K$ versus crack length for SENB4 sample. ....	190
Figure 4.28 FRANC 3D model of misaligned SENB4 sample (undeformed & deformed) at $\Delta K = 38\text{MPa}\sqrt{\text{m}}$ . ....	191
Figure 4.29 Crack front curvature prevalent on misaligned model & actual SENB4 sample. ....	192
Figure 4.30 Pre-crack data points for base, GTA and SMA SENB4 samples using cyclic compression technique. Total crack length = notch length (3.5mm) + crack length. ....	193
Figure 4.31 Schematic of threshold behaviour which depends on test type. ....	194
Figure 4.32 Three tests on the base metal in laboratory air.....	198
Figure 4.33 Three tests on the SMA weld metal in laboratory air. ....	198
Figure 4.34 Four tests on the GTA weld metal in laboratory air. ....	199
Figure 4.35 Results from nine tests carried out in laboratory air. ....	199
Figure 4.36 Test results in laboratory air from nine tests using SENB4 type samples and two tests using CCT type samples. ....	202
Figure 4.37 Current test data in laboratory air and data available in literature.....	203
Figure 4.38 Ductile striation spacing compared to macrocrack growth rates in laboratory air.	205
Figure 4.39 Ductile striations at $45\text{MPa}\sqrt{\text{m}}$ . ....	205
Figure 4.40 Crack path in base metal showing deflection at ferrite/austenite grain boundaries. Propagation direction, left to right. Etch 20% NaOH.....	207
Figure 4.41 Macrocrack propagation around columnar weld grains at $\Delta K < 10\text{MPa}\sqrt{\text{m}}$ .....	210
Figure 4.42 Base metal tested in synthetic seawater (+1040mV SCE). ....	213
Figure 4.43 SMA weld metal tested in synthetic seawater (+600mV SCE).....	214
Figure 4.44 Base and weld metal at high potential in seawater and in laboratory air. ....	214
Figure 4.45 Dissolution of grain boundaries evident on base metal fracture surface tested in synthetic seawater (+1034mV SCE). ....	216
Figure 4.46 Base metal in seawater at positive and negative potentials.....	218
Figure 4.47 Riverlines and brittle striations evident on base metal fracture surface tested in synthetic seawater (-1040 mV SCE). Propagation direction, left to right.....	219
Figure 4.48 Brittle cleavage facets fanning out in the direction of crack propagation (left to right) on the fracture surface of SMA weld metal tested in synthetic seawater (-1040mV SCE)...	219
Figure 4.49 Three tests on base metal cathodically overprotected in synthetic seawater. ....	220

Figure 4.50 Two tests on GTA weld metal cathodically overprotected in synthetic seawater. ....	221
Figure 4.51 SMA weld metal cathodically overprotected in synthetic seawater. ....	221
Figure 4.52 Test results in synthetic seawater at -1040mV SCE. ....	222
Figure 4.53 Current data and other researchers corrosion fatigue data. ....	224
Figure 4.54 Schematic of the effect of loading frequency on corrosion fatigue crack propagation on a time basis. ....	226
Figure 4.55 Crack propagation data for base metal cathodically overprotected expressed on a time basis. ....	227
Figure 4.56 Calcareous deposit formation and rust staining on SENB4 samples subsequent to testing. ....	228
Figure 4.57 GTA weld metal fractograph showing precrack grown in laboratory air and brittle facets, which occurred in synthetic seawater (-1040mV SCE). Crack propagation direction, left to right. ....	229
Figure 4.58 Base metal fractograph showing distribution of brittle cleavage facets, which occurred in synthetic seawater (-1040mV SCE). ....	229
Figure 4.59 Environment enhancement ratio v area fraction cleaved. ....	231
Figure 4.60 Ductile and brittle striations relative to macrocrack growth rates. ....	232
Figure 4.61 Standard S-N design curves (50% probability of failure) for steel weldments [19].	236
Figure 4.62 Correlation between $\Delta K$ and crack length for $\Delta P = 11\text{kN}$ using an exponential function. ....	239
Figure 4.63 Crack propagation life of weld metals in laboratory air and class D design line. ....	242
Figure 4.64 Crack propagation life of weld metals in synthetic seawater cathodically overprotected. R-ratio=0.5. ....	244
Figure 4.65 Bulk embrittlement model featuring semi-cohesive zone [26]. ....	246
Figure 4.66 Schematic of hydrogen concentration profile ahead of brittle crack tip. Ductile crack tip is up to three load cycles behind brittle crack tip. ....	249
Figure 4.67 Twins formed along 112 type planes ahead of brittle crack tip. Cleavage occurs on the 001 plane. Bursts of brittle crack growth initiate and arrest at twin boundary. ....	250
Figure 4.68 Brittle striations 2-3 micron in width on base metal fracture surface at high $\Delta K$ . ....	251
Figure 4.69 Twin boundaries and {001} & {112} type planes evident on fracture surface of GTA weld metal. ....	252
Figure 4.70 Twin boundaries on 112 type planes prevalent on fracture surface of GTA weld metal. ....	253
Figure 4.71 112 and 001 type planes formed during fatigue loading in the presence of a critical concentration of hydrogen. ....	254
Figure A1 Simple electrochemical cell/corroding system. ....	278
Figure A2 Potentiostat controlled electrochemical cell. ....	280
Figure A3 ECP of working electrode referenced to reference electrode. ....	280
Figure A4 Polarisation scan for a stainless steel. ....	282

<b>Figure A5 Potentials of high alloy stainless steels in seawater under a variety of conditions [71].</b>	
.....	<b>283</b>
<b>Figure A6 Fontana-Greene mechanism of crevice corrosion [161].</b>	<b>286</b>
<b>Figure A7 Schematic diagram of metallurgical variables which may initiate pitting in stainless steels [165].</b>	<b>288</b>
<b>Figure A8 Schematic of pit formation as proposed by Evans [164].</b>	<b>289</b>
<b>Figure B1 Schematic of short and long crack growth behaviour.</b>	<b>292</b>
<b>Figure B2 Schematic of crack tip showing process zone and region of K dominance.</b>	<b>295</b>
<b>Figure B3 Schematic of three basic modes of fracture.</b>	<b>296</b>
<b>Figure B4 Distribution of stresses in vicinity of a crack tip, r and <math>\theta</math> are polar coordinates [86].</b>	<b>296</b>
<b>Figure B5 Schematic of variation of <math>K_C</math> with sample thickness.</b>	<b>298</b>
<b>Figure B6 Schematic of the various fatigue regions and sigmoidal nature of fatigue crack extension in steels.</b>	<b>300</b>
<b>Figure B7 Metallic fatigue; crack initiation, stage I and II crack propagation.</b>	<b>301</b>
<b>Figure B8 Schematic of stage I type crack growth.</b>	<b>302</b>
<b>Figure B9 Schematic of stage II type crack growth.</b>	<b>303</b>

# 1. INTRODUCTION

## 1.1 Project Background

The EU White Paper on energy for the future defines a strategy and action plan to promote the market penetration of renewable energy sources in Europe [1]. The target is to double the use of renewable energy systems by 2010 (from 6% of total consumption in 1996 to 12% in 2010) [1].

By adhering to the national energy policy [2], Ireland will have 500MW of electricity generating capacity from renewable sources by 2005 – most of this capacity will come from wind energy\*. From an environmental viewpoint, the payback time of wind farms in energy terms is excellent. A lifecycle analysis of an offshore wind turbine farm was carried out where the energy required to produce, manufacture, transport and dispose/recycle the raw materials was compared to the energy produced by the farm. The analysis showed that the payback time in terms of energy for a 5MW wind farm consisting of ten 500kW wind turbines was only 0.39 years [3]. In line with international trends, wave and tidal projects also have a major role to play in the development of renewable energy resources.

Renewable energy systems are rapidly increasing in size. Currently, wind turbines have an average individual rating of 5MW. Future increases in renewable energy production targets will lead to much larger wind wave/tidal systems [4]. In addition, combined configurations, e.g. wind turbines and wave/tidal devices operating on the same structure may become a viable option [5]. This has implications with regard to structural costs. It has been observed in the offshore oil industry that total structural costs increase exponentially with the weight of structures which are fixed rigidly to the seabed [6]. Therefore, future larger offshore renewable energy systems may have to employ high strength corrosion resistant alloys such as superduplex stainless steels as construction materials. Longer structural lifetimes, weight and subsequent total cost reduction would result. In addition, the competitiveness of renewable energies with fossil fuel generating sources would be increased.

---

\* Construction started in mid 2003 on a 520MW offshore windfarm at Arklow bank, off County Wicklow, Ireland. The farm will consist of approximately 200 turbines at a capital cost of 630 million Euros. The wind farm developers 'Airtricity' expect the completion date to be in 2007.



Gooch [7] identified corrosion-fatigue as one of the main structural material issues with regard to offshore renewable energy equipment. In particular, corrosion fatigue of weldments is a major problem. It has been stated that “Paris’s materials constants need to be determined experimentally to evaluate corrosion fatigue life. The values from standard design codes can be used as a broad guideline, but for critical design, corrosion fatigue experiments are required to collect reasonably accurate data” [8].

### ***Fatigue loading***

In general, the purpose of designing against fatigue is to avoid failure problems for reasons of safety, economy, durability and liability.

With reference to a comprehensive review on the state of the art of fatigue in the 20<sup>th</sup> Century [9], it is plausible to state that understanding of fatigue to date is primarily qualitative. Currently, “a quantitative prediction of fatigue properties of a structure cannot be given because of the qualitative understanding of the complexity of fatigue damage accumulation” [9].

Consequently, safety factors on fatigue life predictions are a necessity. These factors must be judiciously chosen, based on experience, information on loading data, knowledge of the governing conditions, statistical variations and consequences of fatigue failure. Unfortunately, over conservative safety factors lead to uneconomical structures with regard to material usage and load carrying capability. The excellent mechanical and corrosion properties of high performance alloys such as *Zeron 100* are often under exploited as a result.

Offshore fatigue loading is typically a result of low frequency wind / wave interaction with a structure. This loading takes place in the presence of an aggressive medium - seawater.

Corrosion fatigue describes the subcritical growth of cracks induced by the simultaneous interaction of mechanical, metallurgical and electrochemical factors. The synergistic corrosion fatigue mechanism is considered a very dangerous and unpredictable phenomenon. This is particularly true when flaws/cracks are present. It is well known that offshore structural engineers must *‘live with cracks’*.

Fatigue loading serves to periodically expose fresh metal at the tip of a crack to an aggressive medium. If the frequency of loading is relatively low  $< 1$  Hz, the medium can influence the rate of crack growth, leading to catastrophic failure long before it would occur under the same loading conditions in a benign environment such as laboratory air.

Non-destructive crack detection techniques are typically used to assess such flaws and aid the establishment of repair schedules. However, fundamental crack propagation data is also required to carry out this task. In this way, it is of great concern to collect such data by assessing the crack propagation resistance of weld metal in a seawater environment.

## 1.2 The Current Study

### *The material – superduplex stainless steel - Zeron 100*

Duplex stainless steels (DSS) are no longer considered as exotic alloys but 'industrial steels' [10]. Situated mid-way between the austenitic and ferritic grades, DSS are a family combining the best aspects of both [11]. Critically, the yield stress is double that of austenitic steels, therefore regarding strength to weight ratios, potential exists for economic saving [11]. Similar thermal expansion and conductivity make them compatible with low alloy or plain carbon ferritic steels.

However, the use of higher alloyed superduplex alloys such as Zeron 100 requires extensive knowledge of the properties and capabilities of the alloy [10]. Further, the production of superduplex alloys remains confidential and project orientated. These alloys are appropriate structural materials for service in aggressive environments as evidenced by their increasing use in sub sea oil and gas developments [12]. This is mainly due to the long life cycles and weight savings achievable by using high strength corrosion resistant alloys (CRA's). Presently, superduplex alloys are used in thickness up to 100 mm, and with design temperatures as low as  $-50^{\circ}\text{C}$  [13, 14]. They are always cathodically protected when utilised offshore.

The most common and efficient method for joining superduplex stainless steels, and indeed most other alloys is by welding. However, it is widely known that welding of superduplex steels is more demanding than for standard austenitic stainless steel grades. Microstructural changes can occur due to bad welding practise and may diminish toughness and corrosion resistance of superduplex welded joints.

A considerable amount of research has been carried out on all aspects of superduplex stainless steel base metal, but it is accepted that the effect of low frequency corrosion fatigue conditions on weldments formed by different welding methods requires attention [12, 15, 16] as little of this type of data exists.

### *Weld processes*

The present research assesses the performance of the superduplex stainless steel Zeron 100 weld metal formed by two different welding processes - gas tungsten arc

(GTA) and shielded metal arc (SMA) methods. The GTA method performed by an experienced welder following superduplex stainless steel welding guidelines, typically results in a high quality weld in terms of basic mechanical properties, weld profile and inclusion content. However, the GTA process is relatively expensive, exhibits low deposition rates and is difficult to perform in the field. Alternatively, the SMA method is quicker, cheaper and portable. Therefore, it is easier to perform in the field, but the method compromises weld profile and inclusion content.

It is obvious that a GTA weldment should have better resistance to crack initiation than an SMA weld due to the better weld profile and absence of embedded flaws. However, the difference in resultant corrosion fatigue crack propagation behaviour is unknown.

#### ***Why crack propagation as opposed to initiation?***

A survey carried out by Komai [17] showed that in over half of the corrosion fatigue failure cases studied, stress sources were mechanically induced with about 45% attributed to resonance/vibration and cyclic thermal stresses. The recommended solution to the problem was structural modification to lower design stress and stress concentration in order to reduce the probability of crack initiation and subsequent propagation to failure.

As a result of such studies, weldments were most often fatigue and corrosion fatigue tested in the past using S-N type tests where the main objective was to find the fluctuating stress level which would guarantee a certain lifetime usually  $1 \times 10^7$  load cycles. At this stress level, up to 90% of the fatigue life was spent initiating a dominant crack. These tests were essentially initiation tests and didn't give an insight into crack propagation resistance. In addition, in the majority of cases, corrosion fatigue tests were carried out at unrepresentative high frequencies, which minimised environmental effects.

The current project recognises the fact that the crack initiation stage is often complete even before the commissioning of a welded component. This assumption is particularly valid for weld metals where embedded weld metal flaws such as porosity, slag inclusion etc are typically present even in the absence of external surface flaws. Therefore, the *damage tolerant approach* derived from the pioneering fracture

mechanics work of Griffith [18] is more appropriate for the analysis of weldments than traditional total life approaches, which fail to separate crack initiation and propagation. In the damage tolerant approach, it is assumed that flaws are inherent in the structure/component and as such, crack initiation has occurred. Therefore, the approach concentrates on crack propagation resistance.

State of the art non-destructive crack detection equipment, which is widely employed in the offshore industry, can only detect cracks greater than a fraction of a millimetre deep. Inspection intervals are defined based on relevant crack propagation data. Therefore, data on the relative corrosion fatigue crack propagation resistance of weld metal created using GTA/SMA techniques is paramount.

With regard to weldments, additional factors such as residual stresses and misalignment must be addressed. The current work aims to minimise and in some cases take account of the effect of weldment variables enabling a meaningful comparison between weld metal and base metal in an aggressive environment through a fracture mechanics approach.

#### ***Why not assess the HAZ ?***

The challenge in the current study is to assess the resistance of superduplex stainless steel (Zeron 100) weld metal formed by the GTA and SMA welding processes to corrosion fatigue crack propagation in a simulated offshore scenario. The justification for doing so is outlined below.

Firstly, a weldment consists of three regions, the base metal, heat affected zone (HAZ) and the weld metal. The base metal is unaffected by the welding process. Similarly, the heat affected zone, which occurs in between the base, and weld metal doesn't melt during welding. However, the HAZ experiences metallurgical changes due to the high temperature experienced during welding. The weld metal is formed on the cooling of molten auxiliary metal (consumables) deposited in long strips (beads) along the base metal plate interface. Undesirable features from a stress concentration point of view, occur on the surface of the weldment between the weld metal and base metal, i.e. at the weld toe.

Thus far, it appears most important to assess the crack propagation resistance of the HAZ region, as crack initiation is most likely to occur at the weld toe with subsequent propagation through the HAZ [19]. However, it is quite common for cracks to propagate through weld metal in offshore structures. This is particularly true where hollow structural members or circumferential butt welds in pipework are welded [19]. Here, it is difficult to achieve good root penetration and profile as access is limited to one side. Fatigue cracks will initiate at the edge of the root bead and propagate through the weld metal [19].

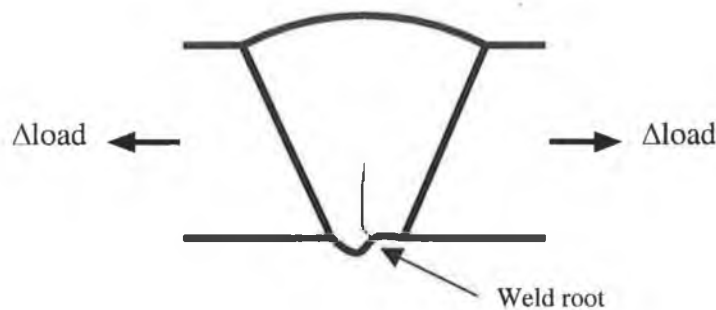


**Figure 1.1. Crack initiation from poor root pass of single V butt weld.**

Such a situation is common with regard to flowlines, which are parts of the process piping system on offshore oilrigs. Typically, they experience high pressures, high temperatures and sometimes severe vibrations. Fatigue failures in one such case were in connection with poor root bead geometry where a crack initiated from the inside of the pipe and propagated through the weld metal [13].

In addition, cracks will almost certainly initiate and propagate through weld metal when the weld profile (including the weld toe) is ground flush with the base metal. Here, weld metal inclusions and porosity act as stress raisers and provide internal stress concentrations for crack initiation [19].

It will also be seen that duplex weld metals usually show lower toughness values than HAZ regions. This point is particularly important with regard to crack propagation and fracture resistance.

Concern regarding ‘weldment susceptibility to environmental assisted cracking’ is also prevalent in the power generation industry where numerous studies have been carried out on the topic [20-23]. Here alloys under fluctuating loads are often in contact with corrosive aqueous environments. The following characteristics were cited in a study of environmentally assisted cracking (EAC) in weldments carried out by Bulloch [24].

- Cracks occurred in welds and heat affected zones (HAZ).
- The majority of cracks were found below the water level.
- Cracks were not limited to any particular design, fabricator or material specification.
- Residual stresses in non-stress relieved weldments were about equal to the material yield stress and, as such, influenced cracking.

It is widely acknowledged that residual stresses are inherent in weldments. Tensile residual stresses both transverse and parallel to the weld bead are maximum in the centre of the weld metal [19]. Often, these tensile stresses approach the yield point of the specific alloy and can increase stress locally decreasing initiation and propagation resistance.

Overall, it is clear that the current project which concentrates on characterising weld metal and assessing crack propagation through the weld metal is necessary.

### ***Cathodic protection***

In order to mitigate general corrosion of structures operating in seawater, it is typical to cathodically protect components. Superduplex components are either directly cathodically protected or bolted onto another component, which is cathodically protected.

Cathodic protection aims to control the electrochemical potential (ECP) of the component. Essentially, every alloy has a critical ECP, above which anodic dissolution or “rusting” occurs. By lowering the ECP of a component sufficiently this problem can be eliminated. This can be done simply in practice by attaching a sacrificial anode (zinc/aluminium alloy) to the component to be protected (Galvanic method). In the presence of an electrolyte, the sacrificial anode will be

attacked/dissolved in preference to the critical component. Alternatively, a particular potential (ECP) can be imposed on a component, which ensures it is protected (Potentiostatic method).

Unfortunately, another damaging mechanism can occur especially in medium to high strength steels at very low ECP's. It is commonly referred to as hydrogen embrittlement (HE) and can have catastrophic consequences, namely rapid crack propagation and fast brittle fracture.

In order to achieve a high degree of equivalence between the 'real life scenario' and the current research, corrosion fatigue tests are carried out on cathodically protected samples at low frequency. The ECP of the samples is fixed to simulate sub sea components with cathodic overprotection, which is a worst-case scenario. If superduplex stainless steels are not protected in seawater, a high positive potential can be assumed. This situation is also investigated by applying a high potential to the samples.



### 1.3 Novelty

The data resulting from this project constitutes a significant advancement to knowledge in the field in two ways.

First, the relative corrosion fatigue crack propagation resistance of superduplex stainless steel weld metal formed by state of the art GTA and SMA welding techniques was unknown for the particular superduplex alloy in question. No such data has been published\*. Further, data relating to the effect of residual stresses arising from the welding process on crack propagation rates has not been published for the alloy in question. Only limited corrosion fatigue crack propagation data exists for the superduplex base metal, and the majority of this data does not represent field conditions, i.e. low frequency loading, cathodic overprotection.

Secondly, there is no threshold and crack propagation data (at low stress levels) available for the weldmetals in laboratory air. The current research is comprehensive in that the total life of weld and base metal from the occurrence of crack propagation from an initial flaw to final fracture is accessed.

A small portion of Mayaki's Ph.D. thesis [25] concerns the corrosion fatigue resistance of a Zeron 100 weld metal in 3.5% NaCl solution. However, the value of these results is limited. Unfortunately, the welding process was not stated. In addition, the lowest loading frequency examined was 1 cycle per second, which is now considered high for investigating environmental effects on crack propagation. A low mean stress was used, where currently researchers typically use a relatively high mean stress to negate closure effects, which produce non-conservative crack propagation data.

Marrow [26] also investigated Zeron 100 base metal; more specifically the interaction of embrittlement (caused by ageing or hydrogen ingress) with fatigue mechanisms. Tests were performed on the base metal in brine, high purity water and hydrogen gas at an appropriately low loading frequency (1 cycle per 10 seconds) and with a relatively high mean stress. However, highly important crack propagation data in air

---

\* Abstract search carried out on EI engineering villages compendex database, last accessed 22 October 2003.

at low stress levels was not obtained. Further, weld metals were not considered. Marrow developed a mechanistic bulk embrittlement model to explain the cyclic cleavage mechanism responsible for increased crack growth rates in aqueous solutions.

Since these projects were completed, much research has been carried out on the corrosion and mechanical properties of duplex weld metal formed by various techniques in order to establish best practices that yield microstructures with properties comparable to the base metal [27-33]. However, there is now great concern and speculation regarding the corrosion fatigue performance of such joints. For example, no data exists concerning the corrosion fatigue crack propagation resistance of Zeron 100 weldments, even though they are used in many critical applications. Up to now, fitness for purpose has been based on basic mechanical and corrosion tests.

As such, assessment of the corrosion fatigue performance of these weld metals, fabricated to offshore industry standards, constitutes a significant advancement in the field, building on the mechanistic and experimental basis provided by Mayaki and Marrow. In addition to gaining an increased knowledge of corrosion fatigue damage mechanisms, the current project also addresses issues of commercial concern.

1. Are superduplex weldmetals more susceptible than superduplex base metal in a corrosion fatigue scenario ?
2. Is the performance of the cheaper SMA welding method comparable to the performance of the more expensive GTA method under corrosion fatigue crack propagation conditions ?
3. Is the fracture toughness of weldmetals in a corrosion fatigue scenario reduced and, if so, by how much ?
4. Is cathodic protection effective ?

Economic pressures necessitate more cost-effective offshore components with regard to lifetime and maintenance intervals. Data and mechanistic information from the current research will aid the realisation of such components. Therefore, the results are of significant interest to the offshore technology community.

## **1.4 Thesis outline**

First, the literature review contains an extensive overview of stainless steels. This section is supplemented by an in depth discussion on duplex stainless steels including welding methods employed and weld metal metallurgy.

Secondly, data concerning base and weld metal properties most applicable to the current work is presented. Topics discussed include corrosion resistance, toughness, hydrogen embrittlement and most importantly corrosion fatigue resistance. In addition, relevant concepts, models and mechanisms are introduced. The key points from each section are then summarised.

Experimental work comprises of initial characterisation of the base and weld metals. Tests include basic mechanical and corrosion characterisation along with non-destructive testing. The design and set-up of a corrosion fatigue test-bed is then detailed along with the experimental procedures carried out.

The results of the characterisation and the corrosion fatigue tests are then presented and discussed. The results are subsequently modelled to enable design engineers to interpret the results more easily. In addition, a mechanistic model backed up by evidence available from fracture surfaces is proposed. Finally, the conclusions arising from the work are stated and future work suggested.

## **1.5 Acknowledgement**

I would like to acknowledge Weir Materials and foundries, Manchester, UK. for their contribution to this project. Firstly, Weir provided the superduplex stainless steel 'Zeron 100' plate and welding consumables.

Weir were anxious to gain knowledge of the fatigue performance of superduplex weldmetals formed by different welding techniques. Current applications areas such as desalination systems and seawater cooling systems necessitate such research.

Secondly, some experimental work was carried out using Weirs facilities. This included electrochemical etching and non-destructive testing. Finally, Weir were always helpful in answering queries regarding their material and welding techniques and permitted access to their comprehensive collection of conference proceedings.

## 2. LITERATURE REVIEW

As mentioned previously, the production of superduplex stainless steels is confidential and project orientated. Consequently, most research is carried out by the producers in-house and results of commercial relevance relating to superduplex stainless steels and corrosion are presented at international conferences. The majority of the data presented in the current literature review was sourced from the conferences listed below.

Duplex stainless steel conference:

- The Hague, Netherlands, 1986
- Beaune, France, 1991
- Glasgow, Scotland, 1994
- Maastricht, Holland, 1997
- Venice, Italy, 2000

Stainless steel conference:

- York, UK, 1987

Stainless steel world conference:

- The Hague, Netherlands, 1999

Duplex conference:

- Houston, Texas, USA, 2000

National association of corrosion engineers (NACE) corrosion conference:

- Houston, Texas, USA, 1994
- Houston, Texas, USA, 2001

However, effort was made to source studies relating to the current research from international journals. These journals were mainly accessed through the online database 'Science Direct'. Journals not available on the science direct database or journals sourced on the EI Engineering Village 'compendex' abstract database were obtained in either of two ways. First, journals were obtained from other libraries in Dublin by means of the 'academic libraries co-operating in Ireland' agreement. Secondly, journals not available in libraries in Dublin were sourced by means of interlibrary loans from 'The British Library'. Some of the journals referenced are listed below:

- International journal of fatigue
- Fatigue and fracture of engineering materials and structures
- Materials science and engineering
- Corrosion engineering
- Corrosion science
- International journal of pressure vessel and piping

Relevant books, which were not available in the library in Dublin City University, were either accessed by one of the methods mentioned above or through the Institution of Mechanical Engineers (IMECHE) on line library where access to core engineering reference books is available to members.

With regard to theses consulted, twenty-nine PhD theses have been submitted in the UK and Ireland since 1970 concerning duplex stainless steels [34]. Two theses carried out in the early 1990's in the University of Nottingham and Cambridge University concerned the fatigue of duplex stainless steels. These two theses are referenced in the current research.

Finally, international material testing standards have been referenced where appropriate throughout this thesis. Both relevant American standards (ASTM, American society for the testing of materials) and handbooks have been consulted along with British standards (BS).

## 2.1 Stainless Steels

Steels, which contain at least 10% chromium, are usually referred to as “stainless steels” because of their resistance to the formation of visible corrosion products when left exposed to the atmosphere. The addition of strong oxide-forming element such as chromium replaces the oxide on the surface of alloys by a tenacious film, which confers corrosion resistance to the alloy [35]. Needless to say that if the passive film is destroyed, corrosion resistance approaches that of low alloy steels.

Olsson recently reviewed results obtained over the last two decades regarding the investigation of ‘passive’ films on stainless steels [36]. Firstly, it must be noted that it is not necessary to chemically treat stainless steels to achieve passivity. The passive film forms spontaneously in the presence of oxygen [37]. The passive film is typically 1-3nm thick [37]. Once a film is formed, the reaction rate between the metal and the environment is reduced by several orders of magnitude [36]. However, the passive film can change with the environment. It can grow or dissolve, and may adsorb or incorporate anions such as the chloride anion,  $\text{Cl}^-$  [36].

With regard to the actual composition of the passive film, a model has been suggested for passive films formed on austenitic stainless steels [36]. The outer part of the film consists of a hydroxide (compound containing  $\text{OH}^-$ ) film. Indeed an analytical study on the austenitic stainless steel 316L has shown that during immersion in artificial seawater the passive film formed is enriched in chromium hydroxides ( $\text{CrOH}_2$ ) [38]. Chromium is the most abundant cation in the passive film as iron is selectively dissolved in the production of  $\text{OH}^-$  anions. The hydroxide film forms on top of an oxide layer. The oxy-hydroxide film is formed on top of a nickel-enriched layer, which is next to the bulk metal.

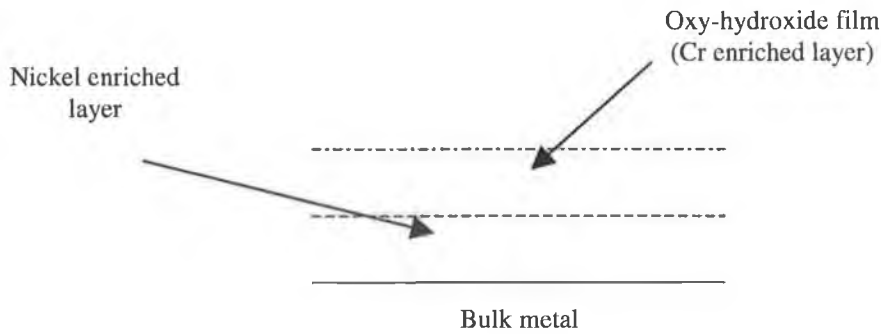


**Figure 2.1 Schematic of passive film prevalent in austenitic stainless steels [36].**

Evident from the model depicted in figure 2.1 is the fact that the composition and properties of the passive film depend on the alloy composition. In addition, factors such as the ECP, the presence of anions such as  $\text{Cl}^-$ , pH and temperature influence the passive film [36].

A wide range of stainless steels have been developed during the last 80 years to meet the demands of service in highly corrosive media, and these alloys also offer attractive mechanical properties at temperatures from absolute zero to above  $800^\circ\text{C}$ . Consequently, the term “stainless steel” now applies to several different classes of material with entirely different metallurgical characteristics and chemical compositions, which are used in diverse applications. For example, stainless steels are used in the offshore industry for their corrosion resistance and low maintenance needs [39]. On the negative side are the higher investment costs. However, the initial cost may be offset by the longer lifetimes attainable. It is interesting to note that the cleanability and corrosion resistance of stainless steels makes them ideal for use where stringent sanitary and health conditions are of utmost importance.

Stainless steels have been developed using alloying additions and processing routes designed to impart specific chemical, physical and mechanical properties; effectively through microstructural control [40].



### *The Stainless Steel Family*

The information in the following review is drawn from standard mechanical engineering reference books [35, 41].

There are more than 200 different grades of stainless steel. Stainless steels may be divided into five families (figure 2.2): (1) austenitic, (2) ferritic, (3) martensitic, (4) precipitation hardened and (5) duplex. Each family has some unique physical and mechanical properties; however, there is within each family a range of corrosion resistance that is achieved by varying the alloying elements. This allows for the substitution of an alloy from one family for that of another and thus advantage can be taken of particular physical/mechanical properties. Some general characteristics are noted in figure 2.2.

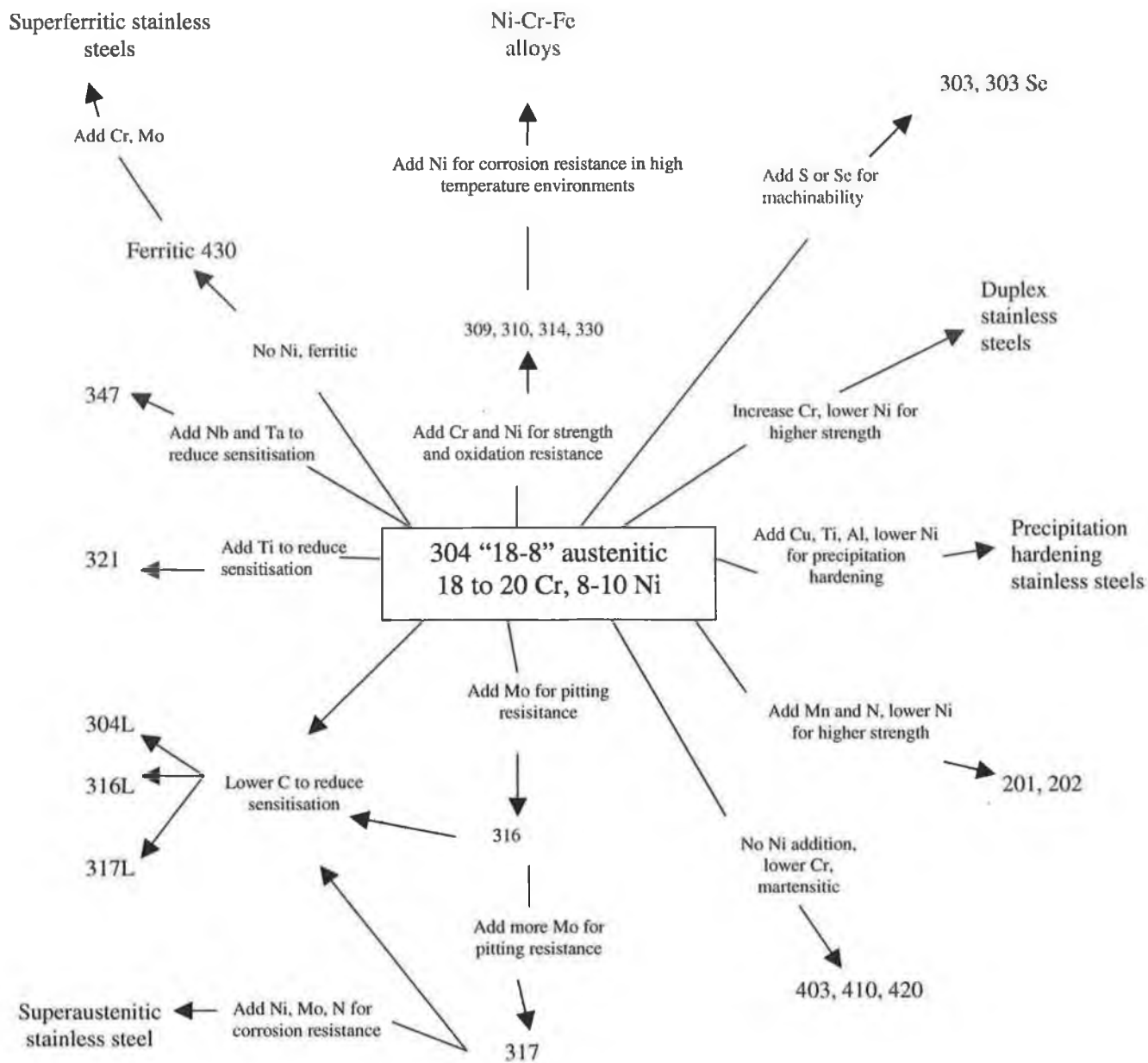


**Figure 2.2 Schematic diagram showing compositional and property linkages in the stainless steel family of alloys [cited in 42].**

***Austenitics ( $\gamma$ )***

Referred to by its unified numbering system designation, UNS S30400 (type 304), or “18-8” (18Cr, 8Ni) of the 300 series alloys, is probably the most widely used stainless

steel. When improved corrosion resistance is required, alloys with higher chromium, nickel or molybdenum content, or both, such as UNS S31600 and S31700 are used.

Compositions lie typically in the range of 18-25% Cr, 8-20% Ni, with low C and some Mo, Nb or Ti. Yield strengths range between 170MPa and 260 MPa.

Austenitic stainless steels are chosen because of their resistance to general corrosion, which is superior to that of a ferritic steel of similar chromium content. In addition, the face-centered cubic (FCC) structure implies good ductility.

Austenitic grades can be hardened by cold work but not by heat treatment; cold work increases strength with an accompanying decrease in ductility. They are relatively easy to form and are readily welded. Austenitic stainless steels may contain some ferrite, generally in castings and welds. Two significant advantages are conferred by the presence of a proportion of ferrite; the prevention of fissuring on solidification and resistance to intergranular corrosion. Compared to carbon steel, austenitics have higher coefficients of thermal expansion and lower thermal conductivities.

Applications range from domestic to architectural to the petrochemical and chemical processing industries. As a result, they are the most commonly used of all stainless steels. At the high end of the spectrum are the relatively high alloy 6% Mo superaustenitic stainless steels, which have accumulated many years of service experience in piping systems on offshore oil and gas platforms.

### ***Ferritics ( $\alpha$ )***

Ferritic stainless steels are iron-chromium alloys with 11 to 30 percent chromium. The largest quantity produced is Type 409 (11 Cr), which is used extensively for automobile catalytic converters, mufflers, and exhaust system components.

The ferritic alloys have a body centered cubic structure (BCC). Grain growth is rapid due to the high atomic mobility in the BCC lattice, resulting in a coarse-grained microstructure and consequently poor toughness. As a result, ferritic stainless steels

are not readily weldable. The coefficient of thermal expansion is similar to that of carbon steel. Yield strengths range between 170MPa and 275 MPa.

Ferritic stainless steels can be strengthened slightly by cold working but have poor formability compared to austenitics. They are difficult to produce in plate thicknesses, but are readily available in sheet and bar form.

Some contain molybdenum for improved corrosion resistance in chloride environments. In contrast to austenitic stainless steels, they exhibit excellent resistance to chloride stress corrosion cracking due to an absence of nickel. Resistance to pitting and crevice corrosion is a function of the total chromium and molybdenum content. Superferritics contain 28% Cr and 4% or more Mo and have exceptional resistance to general, stress and pitting corrosion.

In general, ferritic stainless steels are significantly cheaper than austenitic steels due to the absence of nickel and are used for chemical plant components, domestic and catering equipment, automobile trim, domestic and industrial heater parts, exhaust systems and fasteners. The most highly alloyed ferritic stainless steels have a long service history in seawater-cooled utility condensers.

### ***Martensitics***

The alloys in this family have a body centered tetragonal structure. Martensitic stainless steels are alloyed with chromium and relatively high levels of carbon. The most common martensitic alloy is type 410 (UNS S41000) and contains about 11.5% Cr. The high carbon contents help to produce and strengthen the martensitic structure.

Martensitics are typically difficult to form and weld. However, high strength (yield strength range 205–275MPa) and hardness are prevalent. In addition, they have excellent wear/abrasion resistance but limited corrosion resistance. In most environments, the martensitic grades have less corrosion resistance than austenitic and ferritic grades.

The martensitic grades can be strengthened by heat treatment. Hardness levels up to 60HRC can be achieved in those grades with high carbon contents. The steels are

hardened by quenching from above 950°C to form a hard and brittle structure, which must be tempered. To achieve the best combination of strength, corrosion resistance, ductility, and impact toughness, they are tempered in the range of 150 to 370°C.

Martensitics are particularly suited to operations requiring a cutting edge and their applications include valves, tools, cutlery, scissors, turbine blades, coalmining equipment and surgical instruments.

### ***Precipitation Hardening***

Alloys in this group such as UNS S17700 are used in applications requiring high strength and a moderate degree of corrosion resistance. While some precipitation-hardening stainless steels have a 600-series designation, they are most frequently known by names, which suggest their chemical composition, for example, 17-4PH (17Cr, 4Ni).

Precipitation-hardening stainless steels can be strengthened by a relatively low-temperature heat treatment. The low-temperature heat treatment minimizes distortion and oxidation associated with higher-temperature heat treatments. They can be heat-treated to strengths greater than heat-treated martensitic grades.

The range of corrosion resistance achievable is not as comprehensive as either the austenitics or ferritics. However, most exhibit corrosion resistance superior to the martensitics and approach that of the austenitic grade 304.

Their excellent mechanical properties and corrosion resistance has caused precipitation-hardened stainless steels to be used for gears, fasteners, cutlery and aircraft and steam turbine parts. Extremely practical is the fact that they can be machined to finished size in the soft condition and precipitation hardened later. Their most significant drawback is the complex heat treatment required which, if not properly carried out, may result in extreme brittleness.

The basic mechanical properties and general corrosion resistance of the stainless steel family are summarized in table 2.1 and figure 2.3 respectively.

Alloy type	UTS	Yield strength	Elongation	Hardness
	MPa	MPa	%	HRB
Austenitic 200-300 series	485-655	170-260	40	88-96
Ferritic 400 series	380-515	170-275	21	88-96
Martensitic	415-485	205-275	21	89-96
Precipitation Hardening	895-1620	655-1520	6-16	105-116
Austenitic/ferritic (duplex/Superduplex)	600-750	450-550	15-25	105

**Table 2.1 Mechanical property ranges for various stainless steel classes.**

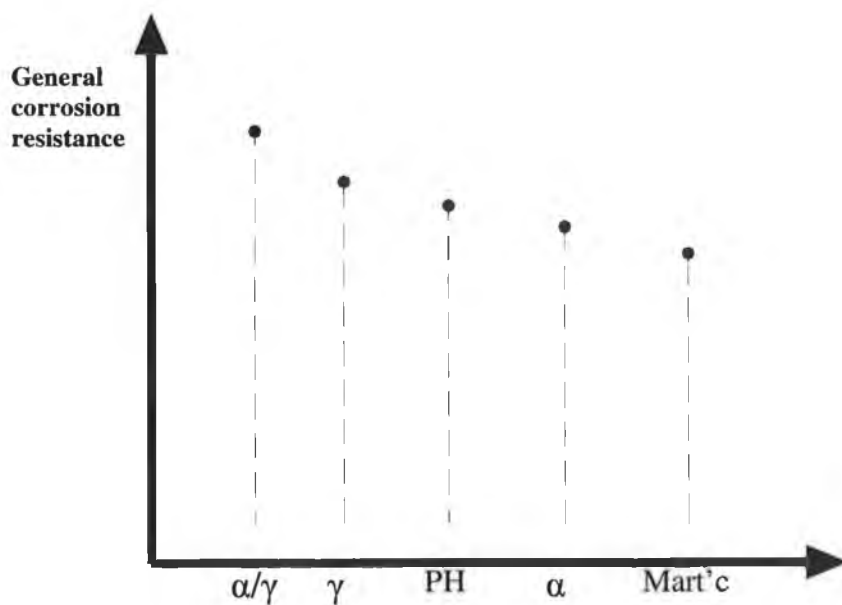


**Figure 2.3 Schematic of general corrosion resistance for various stainless steel classes.**

## 2.2 Duplex Stainless Steels

Presently, most applications of duplex stainless steels (DSS's) concern medium to severe corrosion resistant applications, i.e. chemical, petrochemical, on/offshore, pulp and paper, chemical tankers [14]. In the future, due to their cost saving and maintenance free products, they are likely to be considered as materials for buildings, bridges etc even in hot, wet and coastal locations [14].

Modern DSS's are characterised by a two-phase structure, generally consisting of a mixture of about 50% by volume FCC austenite and 50% by volume BCC ferrite. The two-phase structure consists of austenite colonies (or islands) in a ferritic matrix. Wrought forms contain a rolling texture obtained by hotworking (figure 4.10). One researcher has described the microstructure as a laminated structure composed of alternating ferrite and austenite bands [43]. Both wrought and cast forms are treated with a solution anneal and quench.

The more highly alloyed superduplex stainless steels developed to withstand environments that are extremely aggressive only emerged in the 1980's. The main difference between the superduplex and duplex grades listed in table 2.2 is that the superduplex grades have higher chromium, nickel, molybdenum and nitrogen contents. The superduplex grades also contain small amounts of other alloying elements typically not present in duplex grades such as tungsten and copper.

UNS	Trade Name	Superduplex	Manufacturer
S32520	Uranus 52N+	*	Creusot-Loire Industrie
S32750	SAF 2507	*	Avesta Sheffield Ltd.
S32760	Zeron 100	*	Weir Materials Ltd.
S39274	DP3W	*	Sumitoto Metal Industries
S31260	DP3		Sumitoto Metal Industries
S32550	Ferralium		Haynes International
S32900	329		Various
S32404	Uranus 50		Creusot-Loire Industrie
S31803	SAF 2205		Avesta Sheffield Ltd.

**Table 2.2 Unified numbering system (UNS) designation for selected duplex & superduplex stainless steels.**

Chromium is the main element that provides all stainless steels with their corrosion resistance. Chromium has a body centered cubic (BCC) structure, like iron, and so Fe-Cr alloys possess a BCC or ferritic structure. Alloying with nickel, which has a face centered cubic (FCC) structure can produce Fe-Cr-Ni alloys with an FCC or austenitic structure. If the Fe-Cr-Ni alloy is properly heat treated and nitrogen introduced, duplex microstructures containing both ferrite and austenite are obtainable. Elements such as Aluminium (Al), Niobium (Nb), Copper (Cu), Manganese (Mn), Molybdenum (Mo), Silicon (Si) and Titanium (Ti) can be added to enhance passivity and stability of the protective film under various conditions [40].

### **2.2.1 Metallurgy**

Obtaining an effective duplex microstructure depends on having good control over both alloy composition and temperature. This is more easily achievable for the base alloy, which is produced under controlled factory conditions. The evolution of the ferritic/austenitic microstructure for the base and weld metals are similar and are discussed below with the aid of a pseudo binary diagram. However, resulting grain structures are quite different and this is discussed later.



Attempts have been made to demonstrate the effect of different elements on the ratio of austenite and ferrite present in a duplex stainless steel [cited in 12]. A chromium equivalent,  $Cr_{eq}$ , is often used to account for elements, which stabilise the ferrite. Similarly, a nickel equivalent accounts for elements, which stabilise the austenite.

$$Cr_{eq} = \%Cr + \%Mo + 0.7 \times \%Nb \quad 2.1$$

$$Ni_{eq} = \%Ni + 35 \times \%C + 20 \times \%N + 0.25 \times \%Cu. \quad 2.2$$

The influence of alloy composition can be demonstrated with a Fe-Cr-Ni phase diagram (figure 2.4) at the 60% iron level, which is typical for duplex stainless steels [cited in 12].

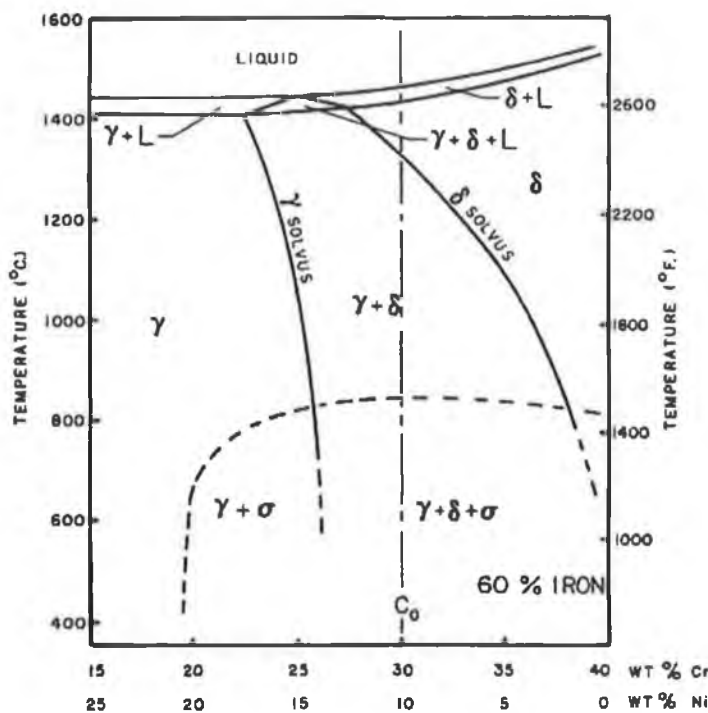
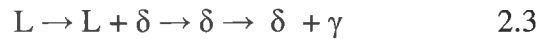


**Figure 2.4 Vertical Section of an Fe-Cr-Ni phase diagram at 60% Fe.  $C_0$  composition line represents commercial duplex stainless steel.  $\delta = \alpha =$  ferrite,  $\gamma =$  austenite,  $\sigma =$  intermetallic [cited in 12].**

The diagram predicts that the primary solidification of duplex stainless steels occurs as delta ferrite ( $\delta$ ) and that the structure is fully ferritic at the completion of solidification. The structure remains ferritic until cooling below the ferrite solvus, at

which point a partial solid-state transformation from ferrite to austenite occurs. The extent of this transformation is a function of composition and the cooling rate through the ferrite plus austenite phase field. The solidification and transformation sequence can be summarised as follows:



Where: L = liquid,  $\delta$  = ferrite,  $\gamma$  = austenite

### ***2.2.2 Base metal v weld metal***

Fusion welds can be made in duplex stainless steels with corrosion resistance close to that of the parent material [44]. Many different welding processes can be chosen for welding duplex and super duplex stainless steels, but GTA and SMA are regarded to be the most practical in a large number of applications. GTA is usually chosen for root passes due to its clean spatter and inclusion free beads. Weld profile is also good. However, welding with GTA requires good skill and a sheltered environment. Deposition rates are relatively low. SMA is the easiest all-weather method. Relative to GTA type welding, higher deposition rates are possible, but toughness properties and weld profile are often poor. In addition, slag on the weld surface must be removed during each weld pass.

Subsequent to a welding operation, weld metal with a 50/50 phase balance similar to the surrounding base alloy is desirable. This must be achieved without deleteriously affecting the microstructure of the surrounding alloy (heat affected zone, HAZ) by prolonged times at high temperatures.

With regard to the base metal, plate, pipes fittings, flanges etc are supplied in a solution annealed and quenched condition to give an optimum duplex microstructure with correspondingly high corrosion resistance and good mechanical properties (strength & toughness) [45]. Welds are put into service 'as deposited'; it is usually impractical to solution anneal completed weldments [45]. Therefore, welding consumables and procedures have to combine to give the necessary microstructure, properties and performance in the as-welded condition. Obviously, these requirements

are similar to the base metal requirements. A qualification test for a superduplex steel to be used offshore typically includes strength, ductility and corrosion requirements [cited in 12]. The Norwegian offshore (Norsok) acceptance criteria for plate includes the following:

Yield stress (MPa)	550
UTS (MPa)	750
% elongation	15
Hardness (HRC)	28
Impact toughness at $-46^{\circ}\text{C}$ (J)	45
Ferric chloride test at $50^{\circ}\text{C}/24\text{hours}$	No Pit
Ferrite (%)	35-55

**Table 2.3 NORSOK acceptance criteria for wrought plate [cited in 12].**

As mentioned previously, wrought forms of DSS's contain a rolling texture obtained by hot working, followed by solution anneal and quench. Increasing rolling reduction decreases the thickness of the individual lamellae [45]. Both phases are comprised of recrystallised grains. In almost all cases, the ferrite and austenite lamellae are essentially one grain thick, so the lamella spacing may be considered to a good approximation as the grain size. Mutual interactions take place between the phases, which results in the aggregate having a greater strength than either of the constituents.

The weld metal structure differs from the parent material, because of variations in chemical composition and its total thermal history. Duplex stainless steel weld metal solidification involves epitaxial growth of primary ferrite grains from the parent material at the fusion boundary [46]. This is shown in figure 2.5. Initial growth is orientated in relation to the thermal gradient [47] and produces a columnar ferritic structure. This provides the starting conditions for further solid-state transformations upon cooling, and dominates the final weld metal structure. The ferrite content, grain size and orientation, influence weld metal properties.

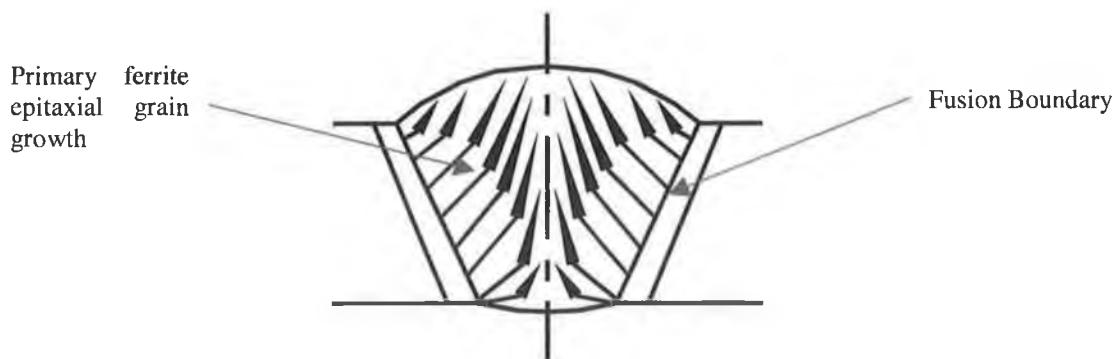


**Figure 2.5 Schematic of epitaxial grain growth from fusion boundary.**

### **2.2.3 Welding procedure**

Early welding of duplex stainless yielded weld metal with high ferrite contents and very coarse grain structures [48]. High temperatures and rapid cooling rates experienced by the weld metal promoted dissolution of austenite on heating and retardation of austenite reformation on cooling [48]. Highly ferritic microstructures promoted extensive precipitation of Cr rich nitrides such as  $\text{Cr}_2\text{N}$ . These factors produced weld metal with reduced fracture toughness, localised corrosion resistance and hydrogen embrittlement resistance [48].

However, advances have been made. The relatively sophisticated metallurgy of super duplex stainless steel welds has demanded a degree of refinement of standard stainless steel welding procedures [45]. The key to successful achievement of corrosion resistant welds in duplex stainless steels is via control of the ferrite austenite phase balance, and of nitrogen level [44]. Weld surface cleaning also benefits corrosion resistance. As a rule, arc energy must be high enough to ensure adequate austenite reformation. However, too high arc energy will cause intermetallic precipitation. Arc energies of 1-2kJ/mm for 10 mm thick butt welds, given a maximum interpass temperature of  $150^\circ\text{C}$ , are recommended [44].

Tests have been carried out on Zeron 100 weld metals formed with Zeron 100X consumables [45]. This consumable is an overmatching parent alloy composition for fabrications subject to service in the as-welded condition. Additional nickel content promotes austenite phase formation essential to weld metal corrosion resistance and fracture toughness. In addition, consumable nitrogen levels inhibit nitrogen migration from other regions e.g. high temperature HAZ. Satisfactory basic mechanical and corrosion resistance similar to the base metal were found.

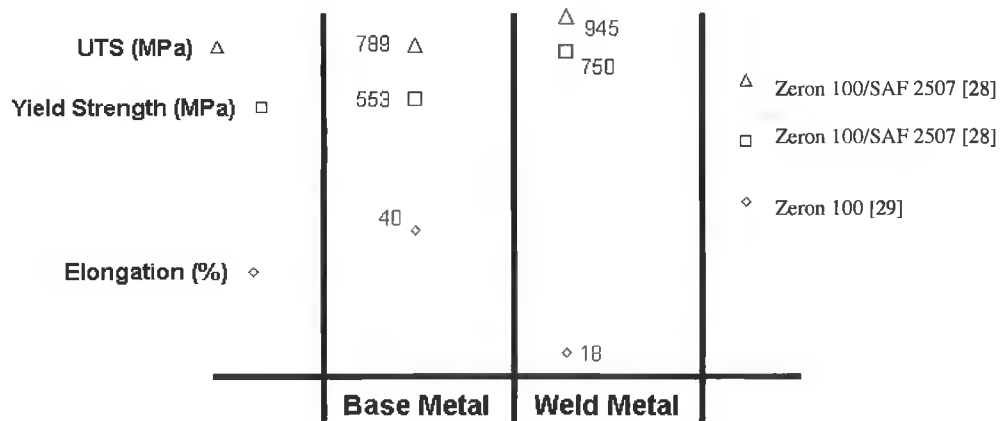
Further research was carried out to find the most important factors, which must be controlled in order to achieve satisfactory mechanical and corrosion properties for duplex and superduplex weld metals [49]. A sufficient level of nitrogen in weld metal was found to be fundamental for adequate corrosion resistance: minimum contents of 0.14% and 0.22% are recommended for duplex and superduplex stainless steels respectively. Nickel content must be controlled for an adequate ferrite/austenite phase ratio to be achieved. This guarantees toughness at  $-50^{\circ}\text{C}$  [49]. Nickel content may be adjusted in a range of 7 ~ 8% for low oxygen weld materials (GTA) but its content must increase (8.5-9.5%) for higher oxygen contents (SMA) with rutile type consumables. Rutile type coated electrodes are popular as they can be used in all conventional welding positions. In addition, they can tolerate a limited amount of moisture. However, they don't offer the best low temperature impact toughness. Basic type electrodes produce higher impact toughness but are less appealing to welders due to the need for frequent inter run de-slagging. Secondly, electrodes must be vacuum packed or else stored at temperatures above  $100^{\circ}\text{C}$  to prevent them from absorbing moisture.

If the chemistry is mainly controlled by the consumables, the second fundamental parameter for achieving good weld metal properties is the cooling time since it governs the occurrence of deleterious precipitation such as intermetallics and nitrides [49]. For example, brittle intermetallic precipitates can either fracture or disbond from surrounding austenite and ferrite, act as local stress raisers and encourage cleavage through the ferrite phase [50].

In a study on welded joints of 25%Cr (UNS S31260, 32550) and superduplex stainless steels (UNS S32750 and 60) using GTA root and SMA fill welding

processes [33], corrosion resistance decreased at high arc energies. A limit of 1.2 kJ/mm (15-20mm thick) was suggested. Weld metal consumables with a composition at least equal to and preferably above the base steel were recommended to maximise corrosion properties. However, it was noted that increased alloy contents promote intermetallic formation. In a study on SAF 2205 weld metal formed by GTA and GTA/SMA weld processes [51], tensile and yield strengths were not affected by arc energies over the range 1-6 kJ/mm.

Dilution of the weld metal with parent metal was found to be directly related to the amount of precipitate formed in weld metal [52]. Precipitates compromise weld metal toughness through a decrease in ductility. Joint geometry also has an effect on dilution. For example, X joints have lower toughness than V joints at weld centre. In addition, avoiding excessive heat inputs is essential in achieving good toughness and ductility. Limiting the interpass temperature (from 150 to 100<sup>0</sup>C) while welding thicknesses over 25 mm allows one to reduce the time spent at temperatures where embrittling phases can precipitate [53].



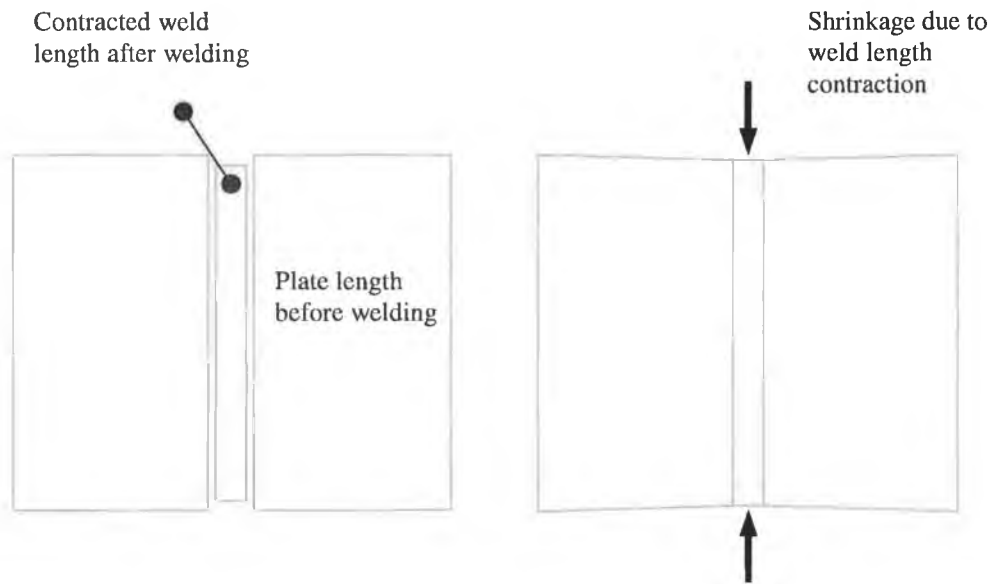
**Figure 2.6 Average mechanical properties for two superduplex stainless steels (Zeron 100 and SAF 2507) base and weld metals.**

Figure 2.6 shows some basic mechanical properties for superduplex stainless steel base and weld metal. Other fundamental properties such as toughness and corrosion resistance are discussed later.

During the fabrication of a multipass weld an initially steep temperature gradient exists between the weld beads and the cooler surrounding material. Consequently, as the weld beads cool and contract the restraining action of the surrounding material leaves a portion of the weld metal in tension. The tensile stresses are balanced by compressive stresses in other portions of the weld metal. These stresses, which are generally considered of yield magnitude lead to distortion in weldments. For example, the contraction associated with the cooling of individual weld beads can result in angular distortion. In addition, tensile/compressive residual stress fields influence mean stress levels locally, for example at the tip of a propagating crack. This point will be discussed later.

A study was carried out on Zeron 100 weldments to assess the effect of the stresses due to welding on the weldmetal [54]. Weld zone hardening was attributed to strain hardening caused by high local (residual) stresses. The extent of strain hardening is related to the thickness of the joint. The thicker the weld joint, the higher the hardness of the weld metal relative to the base metal. Metallurgical factors were found not to contribute. It was deemed important to minimise weldment distortion. This results in lower local stresses and consequently minimal strain hardening in the weld metal.

Therefore, in order to minimise the variation in hardness/strength across a weldment, an effort must be made to minimise distortion. Lateral distortion (contraction parallel to the weld bead) as shown in figure 2.7 occurs on all joints and is practically impossible to alleviate.



**Figure 2.7 Welded plates exhibiting longitudinal contraction.**

However, steps can be taken to minimise angular distortion. For single V butt joints, one method is to offset the plates before welding so that as the joint is filled, the plates continually *pull up* until perfectly aligned on joint completion. However, even experienced welders can have trouble obtaining perfect alignment.

### ***Effect of Nitrogen on duplex stainless steels***

The importance of nitrogen content in superduplex base and weld metals cannot be underestimated. Nitrogen (N) is well known to have beneficial and detrimental effects on the properties of duplex stainless steels. Nitrogen is an interstitial solution-strengthening element and mainly becomes solved, in the austenitic phase [55, 56]. Consequently, in DSS's nitrogen preferentially hardens and strengthens the austenitic phase, but simultaneously decreases its ductility.

An investigation has been carried out on the duplex stainless steels UNS S31803 with variation in nitrogen [57]. High nitrogen gave good ductility and toughness in the weld metal and heat affected zone in the as welded condition. Nitrogen was found to govern the reformation of austenite during welding. It is also beneficial with regard to



the pitting resistance of the base metal, probably because it increases the pitting index of austenite. Problems with chromium nitride precipitation are not pronounced for superduplex steels alloyed with high nitrogen levels, because the austenite reformation is extremely good [58].

An investigation was carried out into the microstructural changes in weld metal and HAZ of nitrogen alloyed duplex stainless steel SAF 2205 [55]. It was found that excess nitrogen in ferrite precipitated as CrN in weld metal/HAZ during cooling in SAF 2205. The degree of CrN precipitation depended on the amount and distribution of austenite formed under cooling from the ferritised state.

In summary, the following can be said of welding of superduplex stainless steels:

- Obtaining an effective duplex microstructure depends on having good control over both alloy composition and temperature.
- Fusion welds have a coarse columnar macrostructure, which is not present in the base metal.
- Nitrogen is an interstitial element, which governs austenite reformation and can strengthen the austenitic phase.
- For adequate corrosion resistance, a nitrogen level of 0.22% is required for superduplex welds.
- Nickel contents must be at least greater than 7% to guarantee adequate toughness.
- Arc energies of 1-2 kJ/mm for 10 mm thick butt welds given a maximum interpass temperature of 150°C are recommended.
- When welding superduplex stainless steels to approved guidelines, the only degree of freedom available to the welder is the arc energy/welding speed.
- Duplex and superduplex weld metals have UTS and yield strengths greater than their respective base metals. However, ductility is reduced probably due to strain hardening of the weld metal caused by the welding process.

## 2.3 Toughness of Duplex Stainless Steel Welds

### *Introduction*

It is now well known that alloys become stronger but also brittle at low temperatures. Reduced ductility at stress concentrations inhibits blunting by plastic deformation. In other words, the material loses its ability to accommodate cracks. Rapid unstable crack propagation from a stress concentration may result on loading leading to catastrophic brittle fracture. A materials resistance to crack advance is commonly referred to as toughness. As such, toughness is of critical importance in the current crack propagation study. In general, toughness decreases with increasing strain rate and decreasing temperature.

Alloy toughness is generally quantified in two ways. Impact tests on Charpy V notch (CVN) samples such as those described in BS 131-6:1998 [59] are simple and quick and give a useful ranking order of toughness in terms of impact energy. This type of test is typically carried out at  $-40^{\circ}\text{C}$ .

The ductile brittle transition temperature (DBTT) is sometimes reported as at this temperature, the behaviour of the alloy changes from ductile to brittle (figure 2.8). A significant reduction in the impact energy required to fracture the alloy occurs at this temperature. The DBTT can be found by performing impact tests over a range of temperatures, e.g. room temperature down to  $-100^{\circ}\text{C}$ . Alternatively, only the temperature at which the impact energy reaches a critical level (usually 40J) is reported.

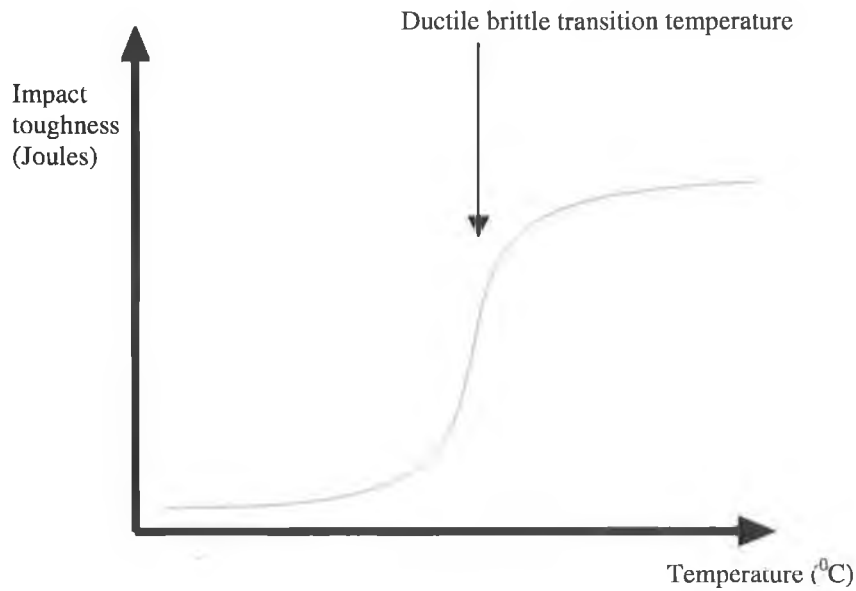


**Figure 2.8 Schematic of toughness determined by charpy impact tests as a function of temperature for steels.**

Toughness can also be assessed using fracture mechanics techniques as described in BS 7448-1:1991 [60]. The basis of fracture mechanics is reviewed in appendix B. Although more complex, plane strain fracture toughness values ( $K_{IC}$ ) can be related quantitatively to the behaviour of an engineering component by comparing stress intensities inherent in a component with the limiting  $K_{IC}$  of the material. However, for extremely tough materials such as Zeron 100 an excessively large sample is required to determine a valid  $K_{IC}$ . According to BS 7448-1:1991 [60], crack length ( $a$ ), specimen thickness ( $B$ ) and the uncracked ligament ( $W-a$ ) must be greater than:

$$2.5 \left( \frac{K_{IC}}{\sigma_y} \right)^2 \quad 2.4$$

where:

$W$  = sample width

$\sigma_y$  = yield stress of material.

Therefore a sample with a thickness ( $B$ ) greater than 100mm and a width ( $W$ ) greater than 200mm would be required in the case of Zeron 100.

In order to reduce the cost of fracture toughness tests, elastic-plastic fracture toughness parameters such as crack tip opening displacement (CTOD) values are determined instead of  $K_{IC}$  values. Here constraints on sample size are more relaxed. CTOD tests are typically carried out at  $-40^{\circ}\text{C}$ . Higher CTOD values imply better toughness.

With regard to weldments, low toughness at the centre of weldments has been attributed to the highly restrained conditions under which solidification and cooling take place [61]. In multipass welds, a through thickness notch coincides with both the weakest planes of the coarse columnar solidification structure and the greatest concentration of weak grain boundary segregates. In addition, the welding process can have a major bearing on weld metal toughness.

#### *GTA method*

Through a combination of exceptionally low filler wire oxygen content and fully inert gas shielding, acceptable weld metal toughness down to  $-70^{\circ}\text{C}$  is possible with the GTA method [27]. As such, the method is invariably used for initial root passes; higher deposition methods are generally preferred for the fill, in all but the most critical applications.

#### *SMA method*

SMA electrode types predominantly have a basic flux coating for two reasons; maximum toughness potential and positional operability. Deposition rates are relatively high but protection of the molten metal is inferior to the GTA method. Electrodes with rutile type coatings are confined to applications where sub zero toughness is not a critical factor.

### **2.3.1 Review of test data**

The following is a review of toughness data from tests carried out on a range of duplex and superduplex base and weld metals. Only weld metals formed using the GTA and SMA method are considered, as these are of main concern in the current research.

Excellent CTOD values have been recorded for the duplex UNS S31803 (1.81mm) and superduplex UNS S32760 (1.87mm) base metals at  $-40^{\circ}\text{C}$  [29]. CTOD values were only reported for the duplex SMA weld. The lowest CTOD value obtained was 0.12mm at  $-40^{\circ}\text{C}$  for the weld metal centre. Using tensile tests on deliberately cracked weldments 40 mm in thickness, it was shown that surface breaking defects 3mm in depth and 15 mm in width can be tolerated in the weld metal at  $-40^{\circ}\text{C}$  (where a maximum design stress of 512 MPa was used). A defect this size is easily detectable by NDT.

CVN type tests were also carried out as part of this study. Toughness values exceeding 50J were found down to  $-100^{\circ}\text{C}$  for the base metal. With regard to weld metal, 40 J transition temperature values were only reported for the duplex metal. The worst case was found for the weld metal ( $-15^{\circ}\text{C}$ ) as opposed to the HAZ ( $-20^{\circ}\text{C}$ ).

Charpy and CTOD tests have been carried out on the superduplex grades SAF 2507 and Zeron 100 [28]. Values for the base metal range between 150 and 250 Joules at  $-40^{\circ}\text{C}$ . Lower values were obtained when the V notch was orientated parallel to the rolling direction. The V notch was perpendicular to the rolling direction when higher values were obtained. The 40 J Charpy energy transition temperature was lower than  $-60^{\circ}\text{C}$  for the parent steels and GTA root and fill weld metal. However, the GTA root SMA fill welds were equal to or lower than  $-20^{\circ}\text{C}$ .

Worst-case CTOD values at  $-40^{\circ}\text{C}$  were 0.12 mm for the GTA root SMA fill and 0.33 mm for the GTA root and fill welds. None of the materials investigated exhibited brittle fracture events during fracture toughness testing carried out between  $-20$  and  $-100^{\circ}\text{C}$ .

Further research has been carried out on the duplex UNS S31803 and superduplex UNS S32760 stainless steels [30]. 40 J impact transition temperatures were reported. Again, the worst case was found for the centre of the SMA weld metal as opposed to the HAZ. The worst case values  $-15^{\circ}\text{C}$  duplex and  $-22^{\circ}\text{C}$  superduplex were reportedly a result of using heat inputs beyond 3 kJ/mm.

CTOD at  $-40^{\circ}\text{C}$  values for the SMA weld method were lower for the weld metal than in the HAZ, 0.12mm for the duplex and 0.20mm for the superduplex. It was proposed from a review of substantial amounts of data that adequate charpy and CTOD requirements are 27 J and 0.15mm respectively determined at the minimum service temperature of at least  $-40^{\circ}\text{C}$ . This appears to be easily achievable with superduplex base and weld metals formed by the GTA and SMA methods.

Some large-scale tensile tests were carried out on wide plates (300mm wide x 40mm thick) of SMA weldments at  $-40^{\circ}\text{C}$ . Defects with depths and lengths, 3mm x 55mm and 6 mm x 30mm were shown not to endanger the integrity of duplex and superduplex welds. Again, a maximum design stress of 512 MPa was invoked.

Charpy impact values for Zeron 100 weld metals at  $-40^{\circ}\text{C}$  have been reported [27]. Toughness was noted to increase with austenite content, and decrease with oxygen content. The high oxygen SMA process was characterised by lower toughness values. Fully GTA weld toughness values averaged at 100 J, whereas basic SMA weld metal averaged at 40 J. SMA weld metal formed with rutile flux coatings exhibited lower values of 25 J. The extent of oxygen pick up was the decisive factor.

CVN values have been reported for the superduplex weld metal of UNS S32750 [31]. GTA root and SMA fill weld metal tested at  $-40^{\circ}\text{C}$  yielded a value of 49 J. Fully GTA weld metal yielded values around 85 J. Oxygen levels were cited as the reason for the different values. In addition, high nickel contents promoted high impact strength at low temperatures in the as-welded condition. In the heat-treated condition, nitrogen improves impact values.

Notch impact toughness values were reported for the weldmetal of the superduplex grade UR 52N+ at  $-50^{\circ}\text{C}$  [32]. SMA values averaged at 36 J while GTA values averaged at 69 J. It was also noted that toughness values depended primarily on the oxygen content and secondarily on the ferrite level.

In a study on welded joints of superduplex stainless steels (UNS S32750 and 60) using GTA root and SMA fill welding processes [33], the base steels showed ductile/brittle transition toughness behaviour, but with transition temperatures well

below  $-50^{\circ}\text{C}$  approaching  $-100^{\circ}\text{C}$ . Impact toughness of weld metal was significantly below that of parent material, this was reflected by the shift of the DBTT to higher temperatures ( $-30^{\circ}\text{C}$ ). Ferrite contents below 50% were necessary to obtain DBT temperatures below  $-40^{\circ}\text{C}$ .

The presence of nitride precipitates in UNS S32760 reduces Charpy impact performance [62]. Differences in performance between material with precipitates and those without became enhanced at low temperatures.

In a study on SAF 2205 weld metal formed by GTA and SMA weld processes, it was noticed that higher toughness was obtained for higher arc energies [55]. This effect was attributed to reduced ferrite content.

Overall, the toughness of a given welded joint is always less than base metal toughness at a given temperature. However, the actual reduction in toughness depends largely on the welding process (e.g. figure 2.9). If high deposition rates are required such as those achievable by SMA welding, a sacrifice in toughness is inherently involved.

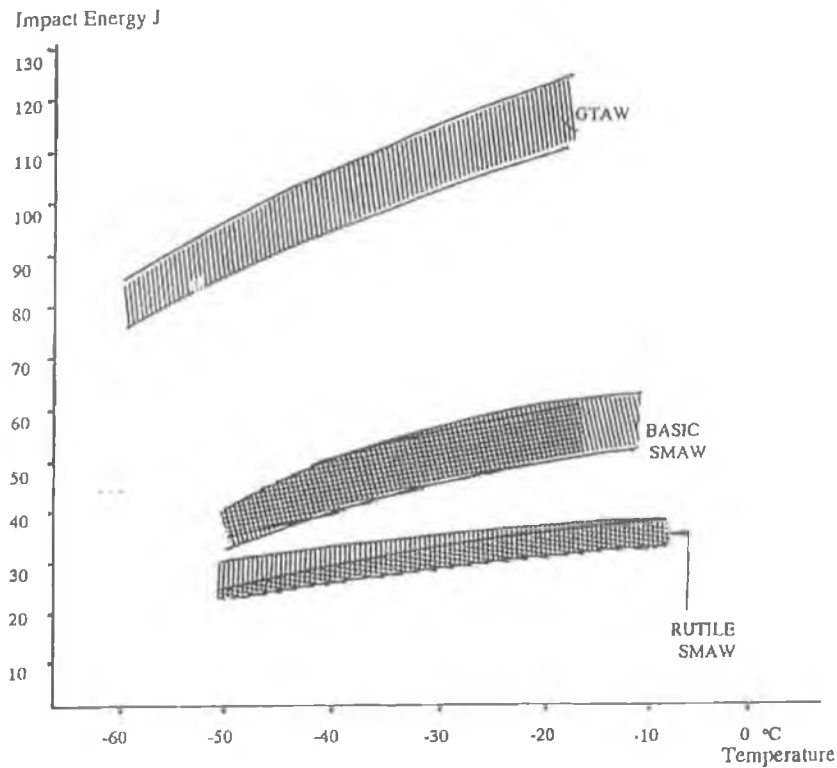


**Figure 2.9 Typical impact values for Zeron 100 base and weld metal (100X consumables) [45].**

In summary, the main points of the above review are:

- Lowest toughness values are usually found in the centre of the weld metal.
- GTA root and fill welds are used when toughness levels approaching toughness levels of the base metal are required at very low service temperatures.
- GTA root - SMA fill welds have lower toughness levels than fully GTA welds due to high oxygen contents.
- High oxygen contents, low austenite contents and the presence of nitrides reduce toughness levels.
- Basic coated electrodes improve the toughness of SMA type welds over acid rutile coated electrodes.



## 2.4 Corrosion Resistance of Duplex Stainless Steels

It has been reported that in general, the resistance of duplex stainless steels to various types of corrosion is excellent [63]. This can be considered as resistance to either general (corrosion of bulk material in acids and caustics) or localised corrosion (pitting and crevice corrosion, stress corrosion cracking (SCC) in chloride environments and intergranular corrosion).

The exceptional resistance to corrosion is partly due to the very low inclusion content, which is a characteristic of the argon oxygen decarburisation melting route employed for duplex stainless steels [32]. Laboratory investigations and field tests have shown that superduplex stainless steels perform better than austenitic stainless steels in many fields: polluted inorganic acids (sulphuric, phosphoric), hot organic acids, chloride containing media and abrasion corrosion [64]. For these reasons many industrial applications have been developed in most of the chemical industries including: pulp and paper, hydrometallurgy, fertiliser, petrochemistry, organic products and pollution control equipment.

### *Seawater*

Offshore installations are another major application area for duplex stainless steels. With regard to seawater, it may be looked upon as a neutral chloride containing solution. Chloride ions ( $\text{Cl}^-$ ) are well known for their ability to destabilise the protective passive film inherent on stainless steels [36]. Seawater has a surprisingly homogenous composition around the world. The salinity is about 3.5% by weight (wt.). The pH ranges between 7.9-8.1 [65]. Synthetic seawater containing manganese chloride, calcium chloride and sodium chloride can be used to simulate natural seawater. However, since the concentration of sodium chloride is relatively high compared to the other salts, 3.5% wt sodium chloride ( $\text{NaCl}$ ) is used in the majority of cases.

Ferric chloride is often used to simulate environments more severe than seawater. In contrast to seawater, ferric chloride ( $\text{FeCl}_3$ ) is a much more aggressive solution. For example, general corrosion rates on a 316L austenitic stainless steel have been found

to be greater than fifty millimetres per year in 5-15% wt ferric chloride at 25<sup>0</sup>C [66]. The corrosion rate in 5-35% wt sodium chloride is less than twenty millimetres per year under the same testing conditions [66]. Ferric chloride concentrations up to 50% wt. are often used in corrosion tests (ASTM G48 [67]) to evaluate a materials resistance to localised corrosion.

#### ***2.4.1 Localised corrosion***

General corrosion implies corrosion occurs uniformly over the whole surface area of an alloy producing a uniform passive layer through oxidation. The rate of general corrosion over the whole alloy surface decreases, as the passive layer gets thicker eventually reducing the corrosion rate to an extremely low level. This is in contrast to low alloy steels where the corrosion product is stable but fails to adhere tightly to the surface and as such doesn't protect the alloy.

In contrast to general corrosion, localised corrosion phenomena such as pitting and crevice corrosion are acknowledged to be the most deleterious corrosion mechanisms with regard to stainless steels [68]. Crevice corrosion begins when discrete areas on a passive surface are physically isolated or occluded such as in a crack. The occurrence and extent of crevice corrosion damage is highly dependent on a number of interrelated factors. Alloy composition, material surface finish, crevice geometry, bulk environment chemistry and temperature may all influence resistance to crevice corrosion [68].

In contrast to crevice corrosion, pitting is a plane surface phenomenon. Pitting corrosion occurs when discrete areas of a material undergo rapid attack while the vast majority of the surface remains virtually unaffected. It is generally agreed that for stainless steels in seawater, crevice corrosion is more potent than pitting. Refer to appendix A for an introduction to electrochemistry, crevice and pitting corrosion.

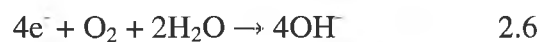
Before looking at the reasons for the occurrence of localised corrosion, a brief review of the electrochemistry underlying the corrosion mechanism is required.

Corrosion occurs when two dissimilar alloys are in electrical contact in an aqueous solution. A galvanic cell is created because different alloys have different characteristic or 'free' electrochemical potentials (ECP's). The alloy with the lower ECP is dissolved while the other alloy remains unaffected\*.

The electrochemical reaction is controlled by the transfer of charge (electrons,  $e^-$ ) across a metal solution interface [69]. Therefore, an electrochemical cell consists of two half-cells. One half-cell consists of an anodic reaction (oxidation), typically the **dissolution** of iron. This may be represented as



The generation of iron cations ( $\text{Fe}^{2+}$ ) is counterbalanced electrostatically by the creation of negative hydroxyl ions ( $\text{OH}^-$ ). Typically, this cathodic reaction consists of the reduction of oxygen and takes place away from the anodic site.



As such, dissolution processes are oxygen supported and are most efficient when oxygen supply to the cathode is maximised. Since the corrosion mechanism is under charge transfer control, the corrosion rate can be quantified by measuring the flow of electrons (monitoring the current) between the anodic and cathodic areas [70].

Alloys such as stainless steels are protected from corrosion in aqueous solution by, for example, electrically connecting an alloy with a relatively lower ECP (e.g. zinc) to the stainless steel [37]. The zinc corrodes in preference to the stainless steel. However, even if stainless steels are cathodically protected in seawater, local regions can assume different ECPs than the bulk material. Therefore, dissolution can occur. Local variations in ECP can arise due to a number of reasons including local metallurgy (in the case of pitting) and geometry (in the case of crevice corrosion) [37]. In addition, local ECP depends on the condition of the seawater (oxygen content, chlorine level) [71]. This is shown in figure 2.10.

---

\* This is not strictly true as will be seen in the section on hydrogen embrittlement.

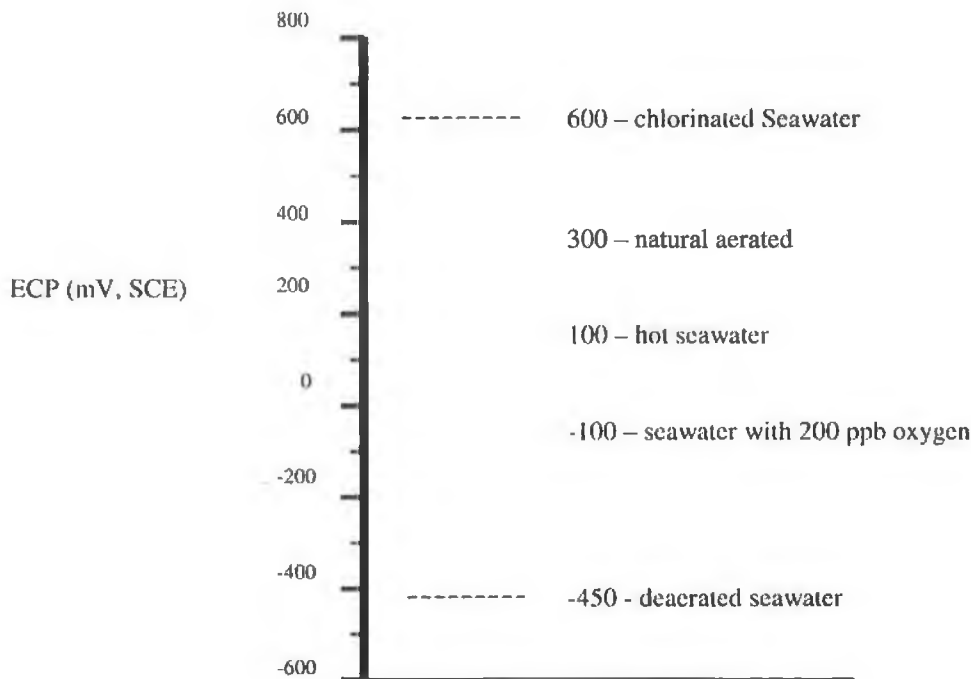


**Figure 2.10 ECPs of high alloy stainless steels as a function of seawater condition [71].**

Since local regions of stainless steels may actively corrode, it is necessary to assess the corrosion rate of stainless steels over a range of possible ECPs. A potentiostat can be used for this purpose. This is an electronic circuit, which can be used to set the ECP of an alloy in a solution such as saltwater. The corrosion rate is then assessed in terms of current density (amps/surface area of sample). A schematic of a polarisation plot for a stainless steel is shown in figure 2.11.

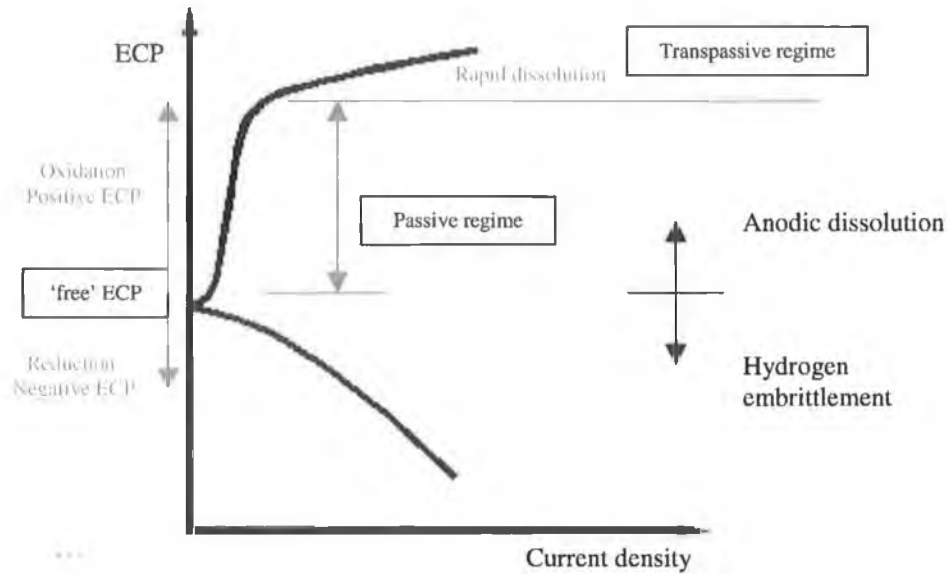


**Figure 2.11 Schematic of ECP as a function of current density for a stainless steel.**

In order to determine the ECP of an alloy, it is necessary to compare its potential in seawater against a reference electrode [69]. Two reference electrodes commonly used in seawater are the silver chloride (AgCl) and saturated calomel electrodes (SCE).

The following section explains how localised corrosion can occur on stainless steel immersed in seawater. After initial immersion of a stainless steel in seawater the ECP attains a value of about  $-200\text{mV SCE}$  [71]. Here, the alloy could be described as being in a pseudo-equilibrium condition [69]. Under these circumstances, the net measurable current density is zero. Therefore, the rate of corrosion is extremely low. This is the free ECP value of the alloy. As can be seen in figure 2.12 the passive film is not very thick (1.2nm) at free ECP. The solution in figure 2.12 is not seawater but sulphuric acid. However, the behaviour of the passive film in seawater is thought to be similar.

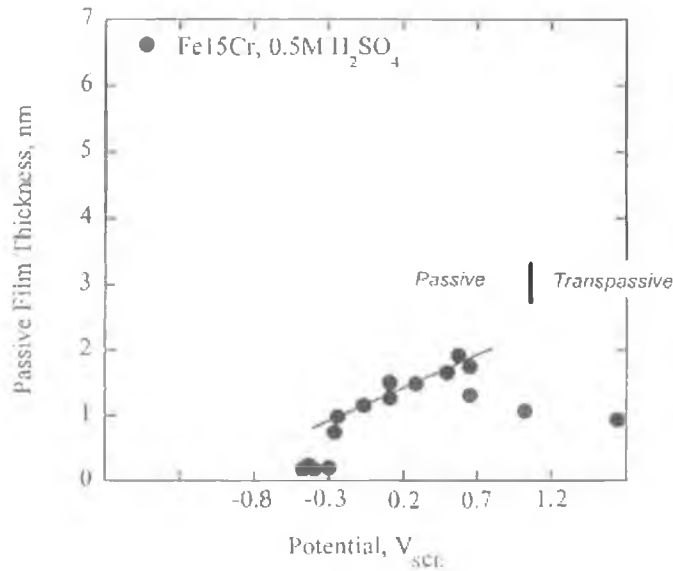


**Figure 2.12** Passive film thickness (nm) versus ECP (Volts SCE) [cited in 36].

A bio film forms over a period of a few days to weeks after the immersion of a stainless steel in seawater [37]. The biofilm is organic consisting of microbial cells (algal, fungal, or bacterial) [37]. However, the thickness of the biofilm is seldom uniform, and patches of exposed metal may even be found on components with significant biofilm present [37]. As a result, preferential sites are formed for fast oxygen reduction. As mentioned earlier, this must be balanced by dissolution of iron.

Therefore, through creating preferential sites for oxygen reduction, the biofilm catalyses the occurrence of dissolution (equation 2.5) [37]. However, adequate oxygen levels must be present in the seawater. This is typically the case in the splash/spray zone.

The relatively high rate of local dissolution results in a thickening of the passive layer (figure 2.12). Local ECP rises in the range of +250 to +350mV SCE due to increased resistance to charge transfer. In the absence of a biofilm, single oxygen reduction kinetics apply to the whole metal surface and corrosion rates are lower [65].

With chlorination levels of 0.5-1.0mg/L, the ECP of the alloy increases further to +500mV to +700mV SCE [71]. In this ECP range, the passive film becomes unstable. Evident in figure 2.12 is that the passive film thickness is reduced. Severe dissolution occurs in the transpassive regime.

The above discussion is for fully aerated seawater, but if the dissolved oxygen content decreases, oxidation is reduced and the passive film becomes thinner. This occurs due to the decreased rate of equation 2.6 due to insufficient oxygen. The dissolution process is dependent on this reaction and as such the rate of dissolution is decreased. Thinning of the passive layer is evident in figure 2.12. Correspondingly, the ECP becomes more electronegative. In fully deaerated seawater the ECP decreases to about  $-450\text{mV SCE}$  and the cathodic reaction changes from the reduction of oxygen to the reduction of hydrogen or water [37]. Here, the generation of hydrogen becomes an issue. This will be discussed in the section on hydrogen embrittlement.

### *Effect of Composition & Microstructure*

As mentioned earlier and as explained in appendix A, the local corrosion resistance of stainless steel is largely dependent on metallurgy and thus composition [36]. The effect of alloying content is commonly calculated by an index termed the “pitting resistance equivalent” (PRE). PRE values essentially indicate the degree of alloying elements in a particular stainless steel and therefore indicate resistance to the initiation of localised corrosion [72].

Superduplex grades have a pitting resistance equivalent number ( $\text{PRE}_N$ ) greater than 40, which ensures relatively good resistance to pitting corrosion, where:

$$\text{PRE}_N = \%Cr + 3.3 \times (\%Mo) + 16 \times (\%N) \quad 2.7$$

However, a modified form of the PRE relationship is used for grades with both nitrogen and tungsten.

$$\text{PRE}_W = \%Cr + 3.3 \times (\%Mo + 0.5 \times 5\%W) + 16 \times (\%N) \quad 2.8$$

Critical pitting temperature (CPT) tests (discussed later) are employed to experimentally rank alloys with regard to pitting resistance and validate the theoretical PRE relationship.

As such, the pitting resistance of the base metal is controlled in the foundry through the alloying content. In neutral, chloride-containing environments, the corrosion resistance of duplex stainless steels is determined by the phase with the poorer corrosion resistance rather than by the corrosion resistance of the bulk [73, 74].

In contrast to the base metal, it is often difficult to control the corrosion resistance of weld metal due to the weld thermal cycle, which affects compositional makeup of the phases and phase proportions. Therefore, the corrosion resistance is largely dependent on the welder, his/her experience and technique. The weakest areas of a weld with regard to corrosion are the stop/start areas where the welder rested the arc while repositioning [70]. The welding thermal cycle here can be extended. Therefore, cooling rates are slow and the probability of intermetallic precipitation is high.

#### ***2.4.2 Review of test data***

There are a number of localised corrosion tests employed on stainless steels and their weld metals. Polarisation scans [75] give an informative picture of the corrosion resistance of an alloy over a range of ECP's in a solution of interest such as seawater.

Critical pitting/crevice temperature (CPT/CCT) tests in chloride containing solutions are also often employed [67, 76]. Crevices are often formed artificially by fitting tight nylon sleeves on a cylindrical sample. Critical pitting temperature tests are carried out on plane smooth samples. These tests are used to rank alloys by reporting the temperature at which localised corrosion proceeds in a certain solution. Visual inspection and mass loss measurements yield information on whether localised corrosion mechanisms have occurred. If no localised corrosion is observed at a particular temperature, the solution temperature is incrementally increased until localised corrosion is observed. The solution temperature at the onset of localised corrosion is defined as the critical temperature.

Alternatively, corrosion resistance of alloys can also be ranked according to their performance over time in a certain solution at a certain temperature. The NORSOK acceptance criteria for superduplex stainless steel plate prescribes no pitting should be evident after immersion in ferric chloride solution at 50<sup>0</sup>C for 24 hours [cited in 12].



Polarisation tests yield much more useful information in that they record the current density (corrosion rate) of the sample at different ECP's. Scans can be carried out in solution of various concentration at different temperatures in order to obtain an insight into the effect of concentration and solution temperature.

Immersion tests in natural seawater have shown that superduplex and superaustenitic 6Mo steels have about the same resistance to the initiation of crevice and pitting corrosion, and the same ability to repassivate a crevice [68]. Duplex and superduplex alloys welded and unwelded, have superior performance to austenitic grades [77].

Superduplex stainless steels UNS S32750, S32550, S32760 and S39724 were crevice corrosion tested in flowing seawater as tubular alloys with a moderately severe fitted sleeve acting as a crevice former [68]. No evidence of crevice corrosion was found in grades S32760 and S39724 after 60 days. These two alloys benefit from the addition of tungsten, 0.7 and 2.0 % respectively. The other alloys exhibited some measurable attack within the confines of the tight crevices.

Crevice corrosion testing was also carried out on UNS S 32750 and S39724 in mud zones [68]. Crevices were formed by extremely tightly fitted vinyl sleeves. Full resistance was found when samples were fully buried in sea bottom mud. However, partial exposure to seawater in the mud zone caused crevice corrosion at deep and shallow crevice locations. Therefore, oxygen supported cathodic areas influenced the crevice corrosion process. Anodic dissolution was the active mechanism.

Tests carried out on SAF 2507 base material in natural seawater for eight years revealed no corrosion attack even though biological species (similar to the biofilm introduced earlier), which aid the initiation of localised corrosion were present [65]. Welds were also tested for a minimum of 6 years. SAF 2507 weld metal formed by the GTA root and fill method showed some pitting attack in the root pass, 0.03mm in depth. SMA root and cap weld metals exhibited no attack.

CPT values were determined for type UNS S32750 weld metals using the ferric chloride test [31]. Joints completed by GTA root and fill and GTA root, SMA fill all

exhibited CPT's greater than 40<sup>0</sup>C. Consumables with high nickel enable CPT's between 40<sup>0</sup>C to 50<sup>0</sup>C. Nitrogen additions resulted in a better reliability of high CPT's by minimising nitrogen loss from the weld metal.

Corrosion tests were carried out on welded joints of 25%Cr (UNS S31260, 32550) and superduplex stainless steels (UNS S32750 and 60) using GTA root and SMA fill welding processes [33]. All the parent steels showed high pitting resistance, compared to 316L and 22% Cr steels. The relative behaviour depends on composition and relates to the PRE<sub>w</sub>. Weldment corrosion resistance was below that of the parent steel in all cases often as a result of use of underalloyed consumables. Other factors included alloy redistribution between ferrite and austenite at phase boundaries and from the precipitation of secondary phases.

Corrosion resistance of UNS S32760 in ferric chloride and in synthetic seawater by CPT tests, did not deteriorate until significant levels of nitride were present [62]. Similarly, in a study on SAF 2205 weld metal formed by GTA and SMA welding processes, the presence of Cr<sub>2</sub>N considerably decreased the resistance to pitting [51]. Increased arc energy improved the resistance to pitting owing to reformation of austenite at the expense of Cr<sub>2</sub>N.

In summary a review of relevant literature has shown that:

- Stainless steels derive their corrosion resistant properties from a stable, durable passive film.
- Corrosion behaviour depends mainly on composition. Composition influences the stability of the passive film.
- Localised corrosion resistance is critical for stainless steels.
- Localised corrosion mechanisms such as crevice corrosion are oxygen supported, indicating dissolution type mechanism
- Duplex and superduplex stainless steels and weld metals are highly resistant to pitting and crevice attack in seawater and are more resistant than austenitic alloys.

- Corrosion resistance is always lower for the weld metal when compared to the base metal.
- Welding method (GTA/SMA) appears to have little influence on localised corrosion resistance. In one study SMA weld metal out performed GTA weld metal.

## 2.5 Hydrogen Embrittlement (HE)

Hydrogen may be introduced into steels by cathodic protection [78], galvanic coupling to less noble materials, from hydrogen sulphide during handling of crude oil or during welding processes [79]. It is well known that once inside the metal, hydrogen can cause embrittlement leading to reduced crack propagation resistance and premature failure. There are no known favourable effects of hydrogen in steel.

There are three key stages in the premature failure of alloys as a result of hydrogen embrittlement, namely the:

- Generation of hydrogen
- Transport of hydrogen through the lattice
- Embrittlement and failure of the lattice

These are now discussed in sequence.

### *Generation of hydrogen*

Atomic hydrogen (H) is produced on the surface of an alloy due to the occurrence of a half-cell reaction at the metal/solution interface as discussed in the section on localised corrosion. Evident in equation 2.9 is that the other half-cell must only produce electrons for atomic hydrogen to be produced. A potentiostat can supply the electrons and as such simulate the other half-cell.

The electrochemical half-cell (equation 2.9) concerns the reduction of hydrogen. The  $H^+$  ion is available, as it is well known that the water molecule ( $H_2O$ ) dissociates (reversible separation) into  $H^+$  and  $OH^-$ .



Reduction of the water molecule is also possible.



Olive *et al* [80] observed that the quantity of adsorbed and absorbed atomic hydrogen is lower than gaseous hydrogen by an order of magnitude. Therefore, the reaction shown in 2.10 where hydrogen gas is produced is dominant. The hydrogen gas does not enter the alloy but bubbles out of the crack enclave [80]. Therefore, a limiting factor in the severity and extent of hydrogen embrittlement is the availability of adsorbed atomic hydrogen. Production of atomic hydrogen is maximised when hydrogen recombination poisons such as sulphide (perhaps in the form  $\text{H}_2\text{S}$ ) are present [16, 81]. These poisons minimise the occurrence of reaction 2.10 maximising reaction 2.9.

It is well known that adsorbed atomic hydrogen (H) can both diffuse through the lattice and be transported by the movement of dislocations. These transport processes are discussed further in the following sections.

### ***Transport Processes***

It was seen earlier that a limiting factor on the extent and severity of hydrogen embrittlement was the availability of atomic hydrogen. Transport processes are also crucial as they determine the quantity and speed of atomic hydrogen reaching a specific location. First, it is appropriate to discuss hydrogen traps as they play a key role in hydrogen transport and failure mechanisms.

Dislocations and grain boundaries are the main hydrogen trapping sites for duplex stainless steels in the as-rolled condition [82] - hydrogen will essentially concentrate along these at room temperatures. These trapping sites are characterised by a reversible behaviour, with a continuous releasing of hydrogen during degassing experiments. Irreversible traps release hydrogen once a critical temperature is reached.

For two duplex (Uranus B50, SAF 2205) and a superduplex (SAF 2705) alloy, a binding energy of 50 kJ/mol was estimated using a simplified diffusion trapping model where interfacial trapping dominated [83]. In comparison, a hydrogen bond

(H<sub>2</sub>) has a binding energy of 4.318kJ/mol. Therefore, the ability of a trap to hold hydrogen is clear.

### *Diffusion*

The diffusion coefficient  $D_H$  in a metal is known to depend on its crystalline system (BCC, FCC, HCC), on its microstructure (ferrite, martensite, bainite), on the presence of traps such as dislocations, dispersed phases, grain boundaries and finally on temperature.

BCC (ferrite) and FCC (austenite) structures have a completely different hydrogen diffusion behaviour, with differences in the diffusion coefficient values. At room temperature,  $D_{H\alpha}$  is approximately equal to 3-5 times  $D_{H\gamma}$  [82]. This is a key reason why ferrite as opposed to austenite is particularly susceptible to hydrogen embrittlement.

It has been found that duplex diffusion coefficients are intermediate between published data for ferritic and austenitic alloys [84]. Diffusion coefficients for various alloys are shown in table 2.4 below.

ALLOY	Diffusion Coefficient $D_H$ $m^2/s$ at 20°C	Reference
Various duplex	$2 \times 10^{-14}$	82
Uranus B50	$2 \times 10^{-14}$	83
SAF 2205	$3 \times 10^{-15}$	83
SAF 2507	$1 \times 10^{-15}$	83
Ferritic (27Cr)	$6.7 \times 10^{-12}$	85
Duplex (50/50)	$1.4 \times 10^{-14}$	85
Zeron 100	$4.31 \times 10^{-16}$	85

**Table 2.4 Diffusion coefficients for various stainless steels.**

The relationship between the hydrogen diffusion coefficient ( $D_H$ ) and the test temperature (T) in Kelvin is given by the well-known Arrhenius law:

$$D_H = D_0 \exp\left[-\frac{E_H}{RT}\right] \quad 2.11$$

where  $D_0$  is a constant and  $E_H$  is the activation energy of diffusion. R is the universal gas constant. It has been estimated that the time necessary to saturate the interstitial sites of a 1mm thick duplex stainless steel specimen is between 3.5 - 7 hours [82].

A further study showed that the time to achieve 65% steady state hydrogen concentration at a depth of 500 micron in a 2.5mm diameter SAF 2205 sample at 80°C was about 72 days [83]. At steady state, the effect of austenite on diffusion was considered to be the creation of a tortuous path [83]. However, in a different study austenite was considered to play a further role in acting as a hydrogen sink [81]. Austenite is known to have a higher hydrogen solubility level than ferrite.

It is important to note that Lynch (cited in 86) observed that brittle crack growth can occur at velocities that are too high to permit the diffusion of hydrogen directly ahead of the crack tip. Therefore, a mechanism other than diffusion must be available for hydrogen transport.

#### *Dislocation Motion*

Some HE models which will be discussed later incorporate dislocations to explain the transport of hydrogen. It is well known that the generation of dislocations is increased as applied stress increases and that the ability of dislocations to transport atomic hydrogen is strain rate dependent [86]. Since dislocations move at the speed of sound, they can carry hydrogen at least as fast as diffusion mechanisms and with less dependence on temperature. Dislocations can also annihilate each other and, as such, enrich the lattice with hydrogen [86]. Currently, it is still not clear whether diffusion or dislocation is the dominant transportation process or whether the two processes act together.

### ***2.5.1 Mechanistic models for hydrogen embrittlement***

Numerous mechanistic models have been proposed by different researchers to explain hydrogen damaging mechanisms. The more popular ones are the:

- Dislocation sweeping model
- Decohesion model
- Localised slip model
- Stress sorption model
- Hydride – formation model
- Trap theory

Jarvis [87] extensively reviewed these models in relation to environment enhanced cracking in low alloy steels operating in environments containing hydrogen sulphide. The following are the key points of that review.

#### *Dislocation sweeping model*

In the dislocation-sweeping model, hydrogen is carried by dislocations and may limit dislocation movement and/or provide localised hydrogen accumulation. Such effects may embrittle the lattice locally. For example, slip may be impeded inducing stress concentrations. Microcracks may form and propagate rapidly through the embrittled material. A local build up of pressure may aid this process.

#### *Decohesion model*

The decohesion model is concerned with the cohesive strength of the alloy matrix. This cohesive strength is reduced by dissolved hydrogen. The reduction of the cohesive strength is assumed proportional to the local concentration of hydrogen  $c_h$ ,



$$c_h = c_0 \exp\left(\frac{\sigma_H \bar{V}}{R_0 T}\right) \quad 2.12$$

where:

$c_0$  is the equilibrium concentration of hydrogen in the unstressed ferrous lattice,

$\bar{V}$  is the partial molar volume of hydrogen in iron,

$\sigma_H$  is the tensile hydrostatic stress,

$R_0$  is the universal gas constant,

$T$  is the absolute temperature.

Plastically deformed material allows the local hydrogen concentration to be higher than the equilibrium concentration due to the lower potential energy of the dissolved hydrogen. A high hydrogen concentration decreases the bond strength between the lattice atoms. Therefore, crack propagation is likely under an applied load.

#### *Localised slip model*

The localised slip model suggests that absorbed hydrogen allows dislocations either to move more readily or to be generated. Hydrogen is transported by diffusion into the lattice just ahead of the crack tip and aids whatever deformation processes the matrix will allow. Microvoid coalescence (MVC), quasicleavage (QC), or intergranular (IG) fracture can occur. MVC is the highest energy form of crack propagation whereas IG is the lowest energy form of crack propagation. The type of fracture that occurs depends on the concentration of hydrogen dissolved in the crack tip material and the stress intensity factor,  $K$ . The main difference between this model and the other models is that it suggests that hydrogen allows dislocations to move at lower stresses instead of locking them in place.

#### *Stress sorption model*

The stress sorption model is similar to the decohesion model. However, in this model, decohesion is thought to occur at the surface, rather than within the material. As a result, there is a reduction in the amount of surface energy required for crack formation and therefore a reduction in fracture stress.

### *Hydride formation model*

The hydride-formation model involves the formation of a brittle hydride phase such as the ionic compound NaH (sodium hydride), which has properties different from those of the matrix, i.e brittle versus ductile. Hydrides have been found at fracture surfaces, giving support to this mechanism.

### *Trap theory*

The trap theory of hydrogen embrittlement proposes that various sites in a particular steel can act as traps or sinks for hydrogen; some are reversible and some are not. Reversible traps can be either favourable or unfavourable to a steels cracking resistance depending on testing conditions. If the hydrogen source is external then some hydrogen being charged to a material will be collected at traps, both reversible and irreversible. A flaw in the material that requires a given combination of applied stress and hydrogen combination will therefore take longer to crack since some of the hydrogen being charged is 'lost' in traps. However, if the material has been precharged with hydrogen then there will be less hydrogen lost and cracking will start earlier.

### **2.5.2 Review of test data**

With these mechanistic models in mind, it is appropriate to review hydrogen embrittlement data for duplex stainless steels and their weld metals. The aim of the various tests is to assess the effect of hydrogen on fundamental mechanical properties. Stress at failure is reported most often. However, ductility is also a key property in embrittlement studies. In addition, the effect of metallurgical variables such as austenite/ferrite phase balance is assessed.

Data was compiled using a range of test methods including constant load, constant displacement and slow strain rate (SSRT) tests. However, displacement control has been found to be less severe for duplex stainless steels due to low temperature creep, which allows stress relaxation [88]. The most common method of charging the specimens with hydrogen is cathodic protection in aqueous solution. However, hydrogen gas environments were sometimes used.

Under constant load tests on UNS S31803 and UNS S32750, cracking only occurred after stresses corresponding to 90% of the tensile strength (UTS) of the alloy when cathodically protected by zinc in chloride containing solution [89, 90]. Precharging had no influence [90].

#### *Base metal*

In SSRT tests, yield and tensile strengths were not affected by hydrogen charging [89]. However, ductility was reduced [89, 90], showing that plastic straining during service should be avoided. Ferrite contents of 40-45% were recommended to keep the risk of hydrogen embrittlement low. This phase re-balance was found not to affect other material properties [89]. Overall, superduplex grades were found to be more resistant than duplex grades.

A stress of 545MPa was required before hydrogen assisted cracking occurred in a superduplex stainless alloy, UNS S32760 under cathodic protection [88]. This value was derived from an actual hub on a manifold, which failed in service due to hydrogen embrittlement. The value is slightly below the conventional 0.2% proof stress. The coarse aligned microstructure was the key factor in the relatively low stress level required for failure. Ferrite volume fraction and hardness were apparently of secondary importance.

Nitride precipitation was found to reduce the resistance of UNS S32760 to hydrogen embrittlement [62]. Constant load tests demonstrated the reduction in stress required for the onset of cracking from 750MPa (nitride free) to 580MPa (0.77 UTS with nitrides present). In slow strain rate tests, a 40% deterioration in performance was measured at a potential of -1040mV SCE.

#### *Weld metal*

SSRT testing of stainless steel base material ( duplex SAF 2205 and superduplex SAF 2507) and weld metal (2205 SMA, GTA and 2507 SMA) was performed under cathodic hydrogen charging conditions in 3.5% NaCl at -1000mV<sub>AG-AGCL</sub> [79]. SAF 2507 had the highest resistance to cracking (90% UTS) followed by SAF 2205 (75% UTS). Weld metals showed lower resistance and scatter was large. Values ranged from 47-77% of UTS. The importance of maintaining adequate austenite in the

weldmetal was highlighted by the poor resistance (30% UTS) of a weld metal, heat treated to give a high ferrite content of 67%. Highest hydrogen levels were observed in the SMA welds.

It has been found that the higher the ferrite volume fraction in Zeron 100 weldments, the lower the critical hydrogen level causing cracking [85]. Here, hydrogen was deliberately introduced into the weld metal through the shielding gas during welding. Crack propagation in the duplex stainless steel was blocked by the austenite phase. High stresses sufficient to plastically deform the austenite are needed to initiate and propagate cracks. Cracking occurs at areas of high stress concentration, high ferrite percentages and high hydrogen levels. Nitrides may act as initiation sites.

Finally, it has been argued that whilst hydrogen can enter duplex stainless steels under cathodic protection subsea, the chances of failure are extremely low because a very high nominal stress (close to UTS) is still required to initiate and propagate cracks in the unembrittled austenite [78, 91]. These deductions were made from constant load and SSRT type tests. Austenite essentially hinders crack propagation. As such, HE is reduced by a fine grain size and a phase balance with 50% or more austenite [78].

In summary, the following are the main points regarding hydrogen embrittlement of superduplex stainless steels and their weld metals:

- A limiting factor in the severity and extent of hydrogen embrittlement is the availability of adsorbed atomic hydrogen.
- Hydrogen transportation may be by diffusion and /or dislocation motion.
- Numerous mechanistic models have been proposed to explain hydrogen damaging mechanisms.
- The decohesion model proposes that hydrogen concentrates in plastically deformed material.
- Superduplex grades show better resistance to HE than duplex grades.
- Stresses for failure by hydrogen embrittlement approach 90% of UTS for superduplex base metals.

- Weld metals are much more susceptible to hydrogen embrittlement, stresses below 50% UTS can cause failure.
- Alloys with a high ferrite content and high hydrogen levels are most susceptible to embrittlement. Ferrite contents below 45% are recommended.
- Hydrogen decreases ductility, leading to brittle crack propagation.
- Austenite impedes hydrogen diffusion and hinders crack propagation from embrittled ferrite regions.

## 2.6 Corrosion Fatigue behaviour

In the 1970's much research into the corrosion fatigue behaviour of various alloys which were committed to U.S. Navy programs was carried out, with support from the U.S. Naval Material Command. Even then, serious concerns were expressed over the corrosion fatigue performance of certain alloys. A study was carried out on one such alloy (HY-130 high strength steel) regarding its crack propagation resistance in fresh natural seawater [92]. Crack propagation rates at a low frequency (0.167Hz) with cathodic protection (-665mV Ag/AgCl) were on average a factor of 2 greater than rates in air. Over protection (-1050mV Ag/AgCl) increased growth rates again by a factor of 4 over rates in air. Lowering the frequency to 0.0167 Hz increased growth rates by a factor of 4.66 over rates in air. In this way, corrosion fatigue performance was identified as a critical factor in the service lifetime of alloys employed offshore.

Corrosion fatigue has remained to the present day an area of much research since a vast range of applications necessitate alloys operating in harsh environments. Cyclic loads can arise from many sources including wind/wave action on offshore structures.

Early investigations [93], advised that experimental programs should be initiated to investigate the corrosion fatigue performance of all alloys intended for offshore use in critical applications. Key points for investigation were identified as

- Crack initiation resistance of as welded specimens at lives up to  $10^9$  cycles.
- Crack propagation resistance of pre-cracked specimens down to rates of  $2.5 \times 10^{-7}$  mm/cycle.
- Environment: seawater at 4-20°C, ~ 3.5% salinity and about 7.5 pH.
- Three levels of ECP: free ECP, adequate protection - 850mV Cu/CuSO<sub>4</sub> and overprotection -1000mV Cu/CuSO<sub>4</sub>.
- Constant amplitude loading at 0.2, 1 and 10Hz. Variable amplitude to be used in later studies.

Stress-life plots (S-N curves) are typically generated to investigate the initiation resistance of as welded specimens compared to smooth base metal samples. The resulting life (N) at a particular stress range ( $\Delta\sigma$ ) is comprised of both a period of crack initiation and propagation (figure 2.13). Iron based steels classically exhibit a plateau on the stress life plot beyond about  $10^6$  cycles (high cycle fatigue >  $10^5$  cycles). This stress range is known as the endurance limit and is usually 35 to 50% of

UTS for steels. Here, the initiation portion is typically up to 90% of the total life  $N$  and as such, the period of crack propagation is relatively insignificant. When a plateau is not observed which is typical if a test is performed in a corrosive environment, then, a 'fatigue limit' is usually defined at  $10^7$  cycles.

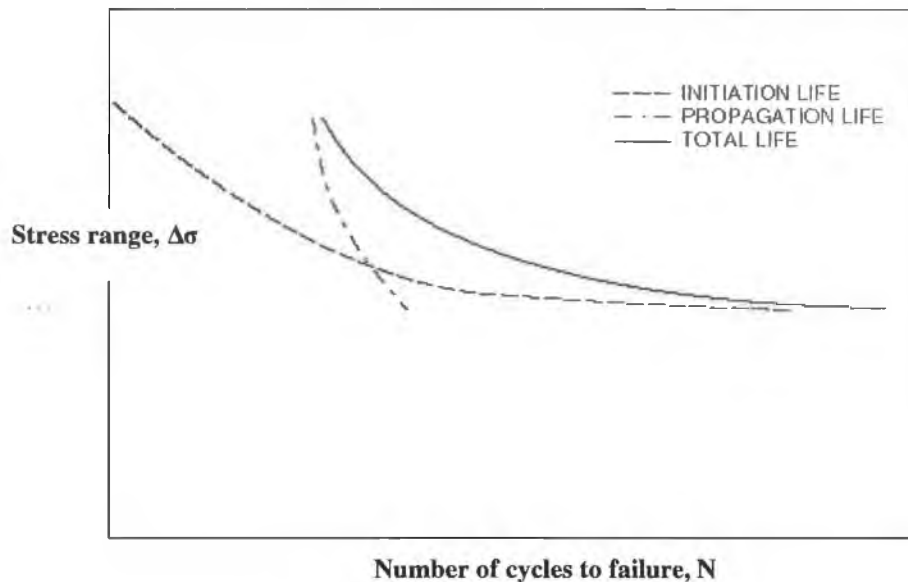


**Figure 2.13 Schematic of S-N curve showing initiation life, propagation life and total life.**

In recent years there has been a move away from initiation resistance type tests towards fracture mechanics crack propagation tests in simulated environments at representative loading frequencies. This is due to a number of reasons:

- Geometry/condition of welded engineering components often renders initiation stage obsolete.
- Recognition of the importance of crack propagation resistance.
- Steady state crack growth rate can be established from which NDT inspection interval can be defined.

Therefore, data from crack propagation tests can be applied to real life scenarios, if the degree of similitude is very high, i.e. the test system accurately simulates the real situation.

Although crack propagation tests are much more involved compared to S-N type tests, the resulting data is extremely informative as it solely concerns the crack propagation resistance as opposed to total life. The crack growth rate per load cycle ( $da/dN$ ) is plotted against the stress intensity factor range,  $\Delta K$ , which increases as crack length increases in a constant load amplitude fatigue test. On this basis, the crack propagation resistance of weld metal for example can be compared to base metal.

The table below shows the variables, namely mechanical, environmental and material, associated with initiation (S-N) and propagation ( $da/dN$ ) type tests reviewed in the current research. In addition, the form of the results reviewed is shown.

<b>Mechanical</b>	<b>Environmental</b>	<b>Metallurgical</b>	<b>Results</b>
	(aqueous)		
<b>S-N test</b>			
Stress range, $\Delta\sigma$	Concentration of aggressive species	Surface condition	Endurance limit, $\sigma_e$
R-ratio, $\sigma_{min}/\sigma_{max}$	pH	Microstructure	Fatigue limit at $10^7$ cycles
Frequency, $\nu$	Electrochemical potential, ECP	Alloy content	Endurance ratio, fatigue limit/ UTS
Waveshape	Temperature		Corrosion mechanism active, dissolution/embrittlement
			Ratio of fatigue limit in environment to fatigue limit in air
<b>da/dN test</b>			
Stress intensity factor range, $\Delta K$	Concentration of aggressive species	Microstructure	Crack growth rate, $da/dN$
R-ratio, $K_{min}/K_{max}$	pH	Alloy content	Paris law constants, C and m
Frequency, $\nu$	Electrochemical potential, ECP		Crack growth threshold, $\Delta K_{th}$
Waveshape	Temperature		Fracture toughness, $\Delta K_c$
			Ratio of $da/dN$ (environment) to $da/dN$ (air)
			Corrosion mechanism active, dissolution/embrittlement

**Table 2.5 Parameters and result format associated with S-N and  $da/dN$  type fatigue tests.**

With regard to the effects of the mechanical factors on corrosion fatigue rates in aqueous chloride environments, a number of key points are well established and referred to in current standards such as ASTM E 647-95a, BS ISO 11782-2:1998 and BS 6835-1: 1998 [94, 95, 96].



1. Increasing the R-ratio/mean stress increases the fatigue crack growth rates at a given value of  $\Delta K$  for base metals. (However, results for weld metals are independent of applied R due to residual stresses inherent in weld metal).
2. Lowering the cyclic frequency ( $<0.5\text{Hz}$ ) can dramatically increase crack propagation rates in aqueous environments.
3. Waveforms which induce low strain rates (shallow rise) such as sinusoidal are the most damaging to fatigue crack growth.

Refer to appendix B for an introduction to fracture mechanics and its application in fatigue analysis.

Therefore, the current review aims to assess the effect of both the environmental and metallurgical variables on fatigue performance. A comprehensive review of available corrosion fatigue data on duplex stainless steels was carried out in 1986 [72] and again in 1991 [97]. What follows is drawn from those sources and other more recent relevant corrosion fatigue data encompassing crack initiation and propagation resistance tests. The majority of the data relates to the performance of stainless steel base and weld metal in chloride containing solutions.

### ***2.6.1 Crack initiation resistance***

#### ***In laboratory air***

A main finding from a review of initiation tests carried out in air on duplex stainless steels is the fact that the fatigue limit (at  $10^7$  cycles,  $R=-1$ ) is related to the yield and UTS of the alloy [97]. Alloys having high UTS, have high initiation resistance often of the order of the material yield stress [97]. At the very minimum, a fatigue limit of 50% UTS has been proposed for all types of stainless steels initiation tested in air ( $R=-1$ ) [12].

With regard to the initiation resistance of stainless steel weld metals, the ratio of the fatigue limit to UTS was found to be the same for base and weld metal ( $R\text{-ratio}=0.1$ , submerged arc welding method, all specimens machined smooth). As such, a metallurgical effect on initiation resistance was not evident. The endurance ratios for

the alloys considered were 0.65 for a 316L austenitic and 0.68 for an SAF 2205 duplex alloy [98].

With regard to the initiation process, it has been observed from tests performed on a duplex stainless steel (X3 25Cr 6Mn 4Ni) in air at 20<sup>0</sup>C, that more than 90% of cracks initiate on the surface [99]. Ten percent of these were attributed to surface inclusions. Initiation mainly occurred at slip bands in the austenite, or near phase boundaries under high cycle fatigue (>10<sup>5</sup> cycles). Crack arrest was common at austenite/ferrite grain boundaries.

Under low cycle fatigue (<10<sup>5</sup> cycles), initiation and propagation was noted in both the austenite and the ferrite and was transgranular in nature. It was concluded that depending on the strain level and nitrogen content, crack initiation could occur in either the austenitic phase or the ferritic phase.

### *In seawater*

In this section, it is useful to report the ratio between the fatigue limit in seawater and the fatigue limit in air so that the contribution of the aggressive environment to initiation is evident.

It is widely appreciated that initiation resistance is reduced significantly in chloride containing solutions. This is due to the ability of the chloride ion (Cl<sup>-</sup>) to destabilise the passive film as seen in the section on corrosion resistance. Under fluctuating load, corrosion pits form due to local breaches of the passive film and act as stress raisers reducing initiation resistance. For example, corrosion pits were clearly evident at the crack initiation region on the fracture surface of a martensitic stainless steel initiation tested in NaCl solution [100]. Therefore, the stability of the passive film is a key point with regard to initiation resistance.

Loading frequency is also generally acknowledged as a key variable in fatigue tests performed in aggressive environments. Its role in initiation resistance is now discussed.

A low frequency (0.5Hz) initiation test (R=-1) was carried out in 3% NaCl on a duplex stainless steel, DP3 (25Cr, 6Ni, 3Mo, 0.3W), yield strength = 610MPa [97].

The number of cycles to failure was shorter than in air only in the low cycle regime ( $<10^5$  cycles). The fatigue limit at  $10^7$  cycles for the duplex stainless steel was the same as in air ( $\Delta\sigma = 340\text{MPa}$ ) [97]. Therefore, damage in the high cycle regime was by mechanical means only. As will be seen, much data exists regarding tests carried out at high frequencies in an aggressive environment where a decrease in the fatigue limit was noted.

Therefore, the role of loading frequency is not clear. It is reasonable to assume that at low frequencies, contact time between the corrosive solution and the fresh metal exposed during loading would be maximised. Thus, the environmental effect would be maximised and a low fatigue limit would be obtained. Conversely, a high fatigue limit would be expected at high frequencies, since exposure time would be minimised. In order to explain the reviewed data, it is necessary to look at the ECP of a sample throughout the duration of an initiation test.

ECP was monitored during an initiation test carried out at 50Hz on a duplex stainless steel [101]. ECP was seen to continuously decrease in the low cycle fatigue regime. Linder [102] observed a similar trend in crack propagation tests at 0.2Hz on a range of stainless steels. A steady decrease in ECP was noted with increase in crack length. Therefore, the rate of corrosion increases as the extent of fresh metal exposed increases independent of loading frequency.

Oscillations in the ECP were recorded at low loads (high cycle fatigue), which were attributed to cycles of depassivation and repassivation [101]. Therefore, it appears that the passive film was not progressively damaged but was able to maintain a quasi steady state resistance to corrosion throughout the cycles of depassivation and repassivation. However, this quasi steady state level is a function of the stability of the passive film.

Therefore, independent of frequency, weakly passivated stainless steels should show a decrease in fatigue limit when tested in an aggressive solution. Conversely, strongly passivated stainless steels tested in an aggressive solution may achieve their fatigue limit in air. Loading frequency may have a significant effect in the low cycle regime where crack propagation dominates. Contact time between solution and fresh metal exposed may be a key factor.

Since, loading frequency has little effect in the high cycle regime and thus on the determination of a fatigue limit, it is common for researchers to perform such tests at relatively high frequencies in order to reduce test duration.

Good correlation has been found for various stainless steels between the ratio of fatigue limits in seawater to air (R-ratio =-1) versus the pitting resistance equivalent (PREN, which depends on the alloy content) of the alloys [cited in 12]. A PREN of approximately 40 is required to ensure minimum risk of initiation resistance reduction in seawater. Superduplex grades such as Zeron 100 have a PREN around 40.

Dependence on PREN highlights the importance of a stable passive film as mentioned previously. However, the fatigue limit ratios just discussed resulted from tests on ferritic, austenitic and duplex stainless steels and therefore may be dependent on microstructure (BCC, FCC, BCC/FCC) as well as compositional makeup.

Initiation tests were performed on an austenitic AISI 316 (16 Cr, 11Ni, 2Mo) duplex (21Cr, 6Ni, 2.4Mo) and ferritic (26Cr, 1Mo) stainless steels in 3% NaCl [101]. R-ratio was -1 and loading frequency was 100Hz. Endurance ratios (fatigue limit / UTS) of 0.54, 0.61 and 0.62 were found in air respectively, while values of 0.41, 0.45 and 0.48 were found in the corrosive solution under free ECP. The higher Cr content of the ferritic phase was thought to result in a more stable or rapidly recovering passive film and as such was probably responsible for the good performance of the ferritic alloy. When the imposed potential was kept well below the pitting potential, ratios of 0.51 and 0.59 were obtained for the duplex and ferritic alloys respectively. The trend of the endurance ratios suggests that alloy composition (PREN) is the key factor with regard to the stability of the passive film as opposed to the microstructure.

Further tests showed the high initiation resistance of duplex alloys (329 and SAF 2205) in 3% NaCl at high frequency (70Hz) [97]. R-ratio was -1. Fatigue limits were almost equivalent to the alloy yield strengths in air (500MPa at  $10^8$  cycles) and decreased by 20% relative to the fatigue limit in air in the solution. As such high yield strength and corrosion resistance implied high initiation resistance.

### *Effect of pH*

Crack initiation tests were carried out on a duplex stainless steel (26Cr-3.5Ni-5.6Mn-2.2Mo-0.3N) in air, neutral chloride (pH =7) and in an acid chloride (pH=2) solution [97]. R-ratio was 0.1 and loading frequency was between 50 and 60 Hz. Minimal reduction in the fatigue limit was noted at 80°C in the neutral solution relative to tests in air. However, there was a significant reduction in the fatigue limit at pH =2. The reduced fatigue limit was attributed to decreased stability of the passive film.

A duplex stainless steel SAF 2205 and an austenitic 316L displayed similar behaviour in 3.5% NaCl (40°C) at 100Hz [97]. R-ratio was -1. The duplex alloy performed better in the salt solution (pH =7). Endurance ratios were 0.58 for the duplex and 0.42 for 316L. Both alloys performed practically the same with a ratio of 0.23 at pH=1 showing that the alloys have equivalent initiation resistance when their passive films are destroyed.

### *Effect of temperature, pH and salt concentration*

Initiation tests were performed on a duplex stainless steel (X3 25Cr 6Mn 4Ni) in saturated (22% NaCl) and dilute (0.5% NaCl) solutions at 80 and 150°C [99]. Max R-ratio examined was 0.4.

<b>Saturated/dilute solution</b>	<b>Solution temperature (degrees centigrade)</b>	<b>pH</b>	<b>Fatigue Limit (MPa)</b>
dilute	80	7	500
dilute	150	7	450
dilute	80	3	400
dilute	150	3	350
saturated	80	7	350
saturated	150	7	250
saturated	80	3	320
saturated	150	3	200

**Table 2.6 Effect of saturation level, solution temperature and pH on fatigue limit in S-N type fatigue test [99].**

Clearly, salt concentration had a greater effect on the initiation resistance than pH and solution temperature. The reduction in fatigue limit at the two temperature levels averaged at 175MPa at pH 7 and 115MPa at pH 3. Importantly, pits which can act as stress raisers were commonplace on the surface of samples tested in the saturated solution.

The effect of pH level was described as minimal. The reduction in pH caused the fatigue limit to be reduced on average by 40MPa in the saturated solution and by 100MPa in the dilute solution. These values appear appropriate, as pH is dependent on ionic concentration. Minimal reduction in the fatigue limit was observed in the saturated solution where ionic concentration was initially high, whereas a significant reduction was found in the dilute solution due to the significant increase in ionic concentration. Finally, the increase in solution temperature caused a reduction in the fatigue limit averaging at 75MPa at pH 7 and 85MPa at pH 3.

The fatigue limit of a duplex stainless steel SAF 2205 has been determined in a 3% NaCl solution at 45 and 80<sup>0</sup>C [97]. R-ratio was 0.1. The fatigue limit at  $2 \times 10^6$  cycles was 487MPa in air. The ratio of the fatigue limit in NaCl to the fatigue limit in air was 0.9 at 45<sup>0</sup>C and 0.87 at 80<sup>0</sup>C. Loading frequency in the NaCl solution was 5Hz. It was observed that some cracks initiated at corrosion pits at the higher temperature. However, the decrease in the fatigue limit was explained by the decrease in yield strength at the higher temperatures.

A superduplex stainless steel SAF 2507 was also tested in air at 20<sup>0</sup>C and in 3% NaCl solution at 80<sup>0</sup>C. The fatigue strength in air was found to be 528MPa while the ratio of fatigue limit in air to the fatigue limit in the solution was 0.93. Again, the slight decrease in the fatigue limit could be explained by a reduction in the yield strength at the higher temperature.

It appears that relatively dilute solutions (up to 3.5% NaCl) even at temperatures up to 150<sup>0</sup>C don't cause a major reduction in initiation resistance for adequately alloyed duplex and superduplex stainless steels, i.e. PREN approaching 40. Therefore, good resistance to pitting and therefore a stable passive film is a key factor as pits induce stress concentration. Mechanical and metallurgical factors such as a reduction in yield

strength with increasing temperature and inclusion content are responsible for minimal reductions in initiation resistance. However, high ionic concentrations appear capable of destabilising the passive film causing pits from where cracks initiate. As a result, initiation resistance is reduced considerably.

The other key factor governing initiation resistance is tensile strength. High tensile strength induces good crack initiation resistance in air. However, this must be coupled with a high PREN in aggressive solutions. Weld metals formed with overalloyed consumables perform similar to base metal in air/salt water when machined smooth. This indicates that a metallurgical effect is not an issue.

Finally, the effect of loading frequency with regard to initiation resistance in aggressive environments is not clear. It appears critical to carry out test at the actual loading frequency expected in service.

#### ***Mechanistic model for crack initiation***

From the data reviewed, it appears that a dissolution mechanism (pit formation) is commonly advocated as an aid to crack initiation in aggressive environments. One researcher concluded that for stainless steels the mechanism of corrosion fatigue (CF) and stress corrosion cracking (SCC) are similar [101]. (Stress corrosion cracking occurs under static load).

In CF, the passive film is destroyed locally by intrusions and extrusions or slip steps which slide in different directions under fluctuating load. In SCC slip bands penetrate the passive film. Any defect on the surface of the alloy e.g. inclusions or carbon-nitrides, promote these phenomena. The essential difference between the mechanisms of CF and SCC is the fact that intrusions and extrusions appear at lower stress levels than are necessary to produce slip bands, which induce SCC.

## 2.6.2 Crack propagation resistance

### *In laboratory air*

Fatigue crack growth rates of a Superduplex stainless steel (Zeron 100) tested in air at 5Hz with an R-ratio of 0.5 were determined [103]. The crack growth rate was found to decrease with increasing frequency of ferrite/austenite grain boundaries encountered by the crack tip. Crack propagation rates in air also depended on extrinsic effects such as roughness-induced closure at low R-ratio and  $\Delta K$ .

Further research was carried out on aged Zeron 100 [104]. Ageing increases the ferrite yield stress without altering the austenite flow stress, grain size or texture. Significant increases in crack propagation rates were noted and attributed to transgranular cleavage of the ferrite matrix associated with deformation twinning. The onset and extent of ferrite cleavage was found to be insensitive to R-ratio but characterised by  $\Delta K_{crit}$ . A proposed model predicted a very strong effect of ferrite volume fraction on crack propagation rates.

Much work has been carried out in Japan on the duplex stainless steel SUS329 [105-107]. At a low R-ratio (0.1) in air, crack closure due to residual stresses inherent in the weld metal ensured that crack growth rates there were lower than in the base metal. However, once the extrinsic stresses were taken into account by means of an effective  $\Delta K$  ( $\Delta K_{eff}$ ), the weld metal performed less well than the base metal due to the relatively high non-metallic inclusion content in the weld metal. Further tests showed that base metal samples with varying percentages of austenite (50, 28 & 12%) exhibited similar crack propagation resistance.

Crack propagation tests have been carried out in air on a superduplex alloy UR 52N+ base and weld metal (welding method not specified) [98]. An R-ratio of 0.5 was used while loading frequency was 2Hz in air. Crack propagation rates were found to be very similar, independent of the placement of the crack (base metal, heat affected zone or weld metal).



### *In seawater*

In contrast to crack initiation tests, the effect of loading frequency in crack propagation tests is clear. At frequencies below 1Hz environment contributions to crack growth are almost always evident. As just seen, tests in air are carried out at relatively high frequencies due to the negligible effect of benign environments on crack propagation.

Crack propagation tests were carried on a superduplex stainless steel (Zeron 100) in brine and high purity water [103]. Crack growth rates increased over rates in air. Cyclic transgranular cleavage of the ferrite was found to be responsible. This was encouraged by cathodic overprotection and resulted from hydrogen embrittlement. Cyclic cleavage was considered to arise from hydrogen trapping ahead of the crack tip. Embrittlement was controlled by the distribution and concentration of trapped hydrogen, and was sensitive to stress intensity, cyclic frequency, temperature and chemical environment at the crack tip.

Crack propagation tests were carried out on the duplex stainless steel SUS329 in synthetic seawater at 0.17Hz [105-107]. R-ratio = 0.1. For the base metal, it was concluded that cathodic protection is not effective in protecting the alloy in seawater, as crack propagation rates were appreciably higher due to embrittlement of ferrite caused by hydrogen ingress. Weld metal was also examined at 0.17Hz in synthetic seawater cathodically charged. Here the weld metal out performed the base metal due to the high ferrite content of the base metal, which ensured hydrogen embrittlement occurred on a greater scale in the base metal.

Crack growth rates were also carried out on the base metal with varying percentages of austenite (50, 28 & 12%) in seawater at 0.017Hz. The alloys with the lowest austenite content (28 and 12%)/high ferrite contents exhibited crack growth rates almost twice crack growth rates in air. This effect was attributed to embrittlement of the ferrite.

Crack propagation tests were also carried out on the superduplex alloy UR 52N+ base and weld metal in artificial seawater [98]. An R-ratio of 0.5 was used while loading

frequency was 0.2Hz in seawater. The influence of seawater with the sample at free corrosion potential was to increase crack propagation rates by a factor of three.

An example of the effect of loading frequency can be seen in crack propagation tests carried out on a duplex stainless steel (25Cr, 6Ni, 3Mo) in air and synthetic seawater [97]. R-ratio used was 0.6 at a frequency of 10Hz. Crack growth rates in seawater were almost identical ( $10^{-5}$  mm/cycle at 10 MPa $\sqrt{m}$ ) to rates in air. The high frequency employed probably didn't allow the corrosive solution sufficient time to influence the crack propagation mechanism. Therefore, solution contact time with fresh metal exposed during each load cycle is a key factor in crack propagation mechanisms.

#### *Effect of seawater temperature*

The corrosion fatigue crack propagation resistance of a duplex stainless steel X6CrNiMoCu (25Cr-6Ni) in air and artificial seawater at 70<sup>0</sup>C at 0.1Hz has been investigated [108]. Growth rates were 1.8 orders of magnitude greater in the seawater as opposed to in air. Brittle striations in the ferrite phase were shown to correspond with the macroscopic crack growth rate in seawater at 70<sup>0</sup>C as opposed to the good correspondence with ductile striations in austenite in air. Hydrogen embrittlement of the ferrite was found to be responsible for the dramatic increase in crack growth rates in the heated solution.

A study was performed on the crack propagation resistance of stainless steels in air at room temperature and in 3.5% NaCl at room temperature (RT) and at 80<sup>0</sup>C [102]. For the superduplex stainless steel SAF 2507 crack growth rates in 3.5% NaCl at RT were about 2 times greater than rates in air (f=0.2Hz) at free corrosion potential. The effect of temperature was minimal. A high threshold value was found for the superduplex alloy at 17.5 Mpa $\sqrt{m}$ , ( $10^{-6}$  mm/cycle). This was attributed to residual stress effects. The environmental effect was attributed to a dissolution-hydrogen embrittlement mechanism.

### ***Mechanistic model for crack propagation in seawater***

As just discussed in the review, the mechanisms deemed responsible for increased crack propagation rates under low frequency loading in seawater are largely hydrogen based. This is especially true when cathodic protection is employed.

The consensus appears to be that ferrite is embrittled by hydrogen. This causes subcritical cleavage of the ferrite during a load cycle. The macroscopic crack growth rate is then controlled by the remaining unembrittled ductile ligaments. However, higher solution temperatures may cause the macroscopic crack growth rate to be controlled by the cyclic cleavage of the ferrite. In both cases, environmental contribution is maximised above a critical  $\Delta K$ .

This mechanism is in stark contrast to the mechanism for crack initiation in seawater which is dissolution based. However, some researchers advocate a dissolution-embrittlement mechanism.

The main points of this review are as follows:

#### ***Crack initiation***

- High strength duplex/superduplex stainless steels have good crack initiation resistance in air, which can approach the yield stress of the alloy.
- Initiation resistance in chloride containing solution depends on a number of factors including alloy UTS, alloy PREN (composition), solution pH, chloride (ion) concentration and solution temperature.
- The effect of loading frequency is not clear, but low frequencies appear to be deleterious to fatigue limits if the passive film is only partially effective under fluctuating load in chloride containing solution.
- High solution temperature, low pH, high chloride concentration and low PREN reduce initiation resistance.
- Up to around 100<sup>0</sup>C, ion concentration appears to be the key environmental factor in crack initiation resistance.

- A passive film, which is stable in a particular solution, leads to a fatigue limit similar to the fatigue limit in air where a crack initiates by mechanical means from a surface defect.
- A passive film, which is unstable/quasi stable in a particular solution, leads to a fatigue limit significantly lower than the fatigue limit in air. Cracks initiate from corrosion pits formed on the sample surface.
- Dissolution is the dominant corrosion mechanism influencing crack initiation resistance in chloride containing solution.
- Smooth weld metal samples have the same initiation resistance as smooth base metals in air and in chloride containing solution.

### *Crack Propagation*

- Austenite/ferrite grain boundaries are effective in reducing crack propagation rates in laboratory air especially at low  $\Delta K$ .
- Propagating cracks are extremely efficient at destroying the passive film locally due to the extremely high stresses at the crack tip.
- Low loading frequencies allow time for chemical attack and thus significant environmental contribution to crack propagation when the passive film is destroyed locally.
- Duplex/superduplex alloys and weld metals with high ferrite contents are susceptible to hydrogen embrittlement and rapid crack propagation especially when cathodically protected.
- Hydrogen embrittlement is the dominant corrosion mechanism influencing crack propagation resistance in aqueous solution.

## 2.7 Limitations of published data

It can be seen from the above review that much research has been carried out on the corrosion fatigue behaviour of duplex and superduplex stainless steels.

However, it is clear that the effect of loading frequency on crack initiation resistance is not well understood. However, initiation resistance is not of primary concern with regard to welded structures as considered in the current research. This is due to the effect of flaws/defects inherent in weldments, which render the crack initiation stage practically insignificant.

Of more concern is the corrosion fatigue crack propagation behaviour at low loading frequencies. It is widely appreciated that weld joints are critical locations for structural integrity and most failures occur there. However, an in-depth study on corrosion fatigue crack propagation in commercial duplex or superduplex weld metal does not exist. Some studies include perhaps one weld metal for comparative purposes. The welding method is rarely stated. In any case, the influence of residual stresses on crack propagation rates in air and seawater has not been taken into account. Therefore, more specifically, the intrinsic crack propagation resistance of commercial superduplex weld metals formed by different welding methods is not known.

Further, it is not evident from the literature whether dissolution corrosion contributes to crack propagation. It is clear that hydrogen embrittlement is prevalent but the critical  $\Delta K$  ( $\Delta K_{crit}$ ) where embrittlement begins is not clear. In addition, very little data is available on threshold values for the onset of crack growth in air.

Therefore, the crack growth threshold, propagation resistance and relative fracture toughness of superduplex weld metal formed by different welding procedures needs to be investigated in both air and seawater. It is appropriate to present the data in a form readily understandable to the design engineers. In addition, a mechanistic model of the governing corrosion fatigue mechanism would aid further understanding and successful life prediction. Overall, “much more research is needed to predict corrosion fatigue with confidence [109]”.

### **3. EXPERIMENTAL WORK**

This chapter on experimental work comprises four sections. Firstly, the fabrication of weldments is described, together with all pertinent welding data. The basic integrity of the weldments is then addressed. Integrity tests include cross weld tensile tests, impact tests and hardness tests. Non-destructive tests comprising of radiographic and dye penetrant tests are also carried out to supplement the mechanical tests. Such tests are necessary, as weld procedure qualification should always be based on direct measurement of mechanical properties and corrosion resistance [110].

This preliminary work is followed by characterisation of the weldments in terms of metallurgy, corrosion resistance and residual stress levels prevalent. First, the microstructure and compositional makeup of the weld metals and the base metal is examined. These aspects are important since mechanical properties and corrosion resistance depend largely on microstructure and composition respectively. Further tests are carried out to ensure the weld metals have corrosion resistance at least comparable to that of the base metal. Finally, residual stresses, which are inherent in weld metals, are addressed. The determination of residual stresses is crucial as they may influence the rate of crack propagation.

The third section is the main focal point of the project, as it concerns corrosion fatigue crack propagation tests. Firstly, choice of test specimen including considerations such as loading configuration, effect of angular misalignment, specimen dimensions and residual stresses are addressed. Subsequently, the intrinsic crack propagation resistance of the base and two weld metals in laboratory air is assessed. This data is used as a reference for subsequent environmental tests. Tests are carried out in synthetic seawater at critical potentials often assumed by superduplex stainless steels operating offshore, i.e.  $-1040\text{mV SCE}$  and  $+600\text{mV SCE}$ . The data obtained not only yields crucial information on crack propagation rates, but also on threshold levels and fracture toughness.

Finally, in the fourth section the fracture surfaces of the samples used in the crack propagation tests are analysed. The observations and data obtained will be invaluable in determining the mechanisms responsible for environmental assisted crack growth

### 3.1 Weldment Fabrication & Basic Integrity Assessment

#### 3.1.1 Weldment fabrication

Weir Materials & Foundries (WMF) are the sole worldwide producers of Zeron 100. Fabrication involving Zeron 100 is carried out either by their own welders or by contractors working to guidelines devised by Weir from their own experience and researchers recommendations as discussed in the literature review.

Due to the small number of chemical and offshore industries in Ireland, it was obvious that fabrication shops would have little, if any, experience of welding superduplex stainless steels such as Zeron 100. However, it was decided to supply welding guidelines to such a fabrication shop and have them carry out the welding. Therefore, the weldments tested in the current project can be considered to constitute a worst-case scenario with regard to welders experience with the material.

Six wrought plates of the superduplex stainless steel Zeron 100, each measuring 500mm x 150 mm x 10mm were supplied by WMF.

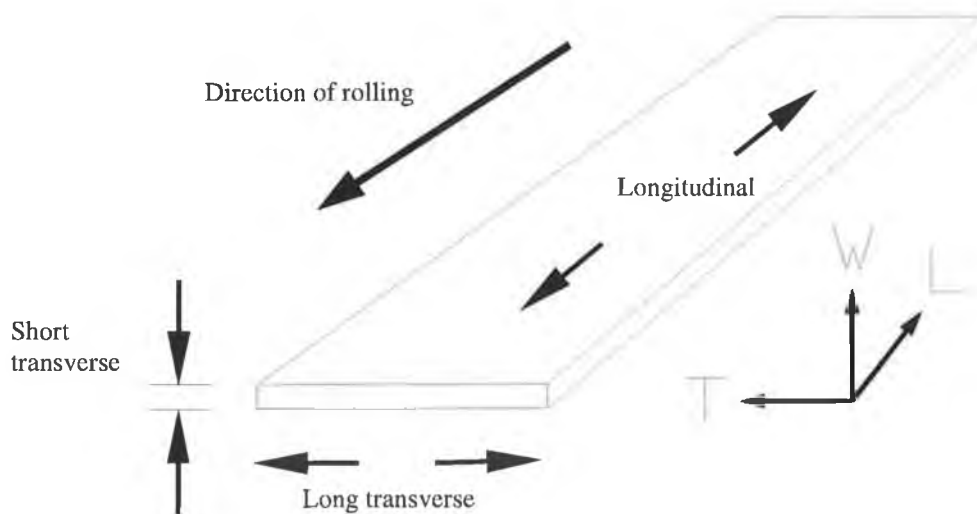


Figure 3.1 Zeron 100 wrought plate.

The plates, along with WMF's comprehensive welding guidelines [111] for Zeron 100, were sent to a pressure vessel fabrication shop 'Multitech' in Cootehill, Co. Cavan, Republic of Ireland. In the fabrication shop, the plates were prepared for butt-welding by machining a chamfer. The joint geometry recommended by WMF for 10mm thick plate and used in the current research is shown in figure 3.2.

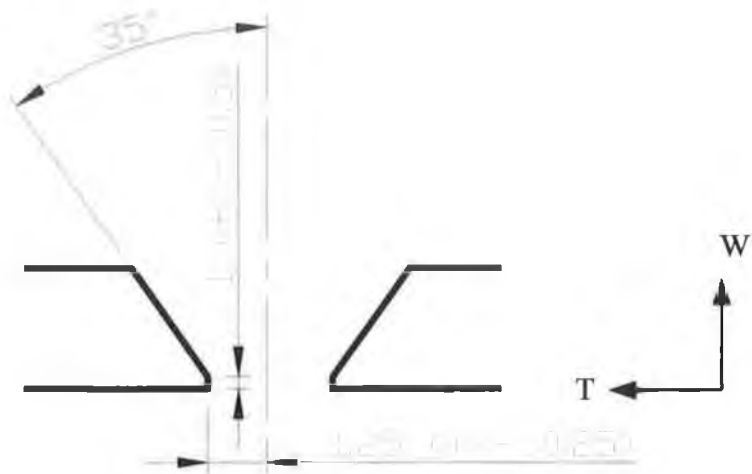


Figure 3.2 Single V-butt preparation geometry - dimensions in mm.

Weldments were fabricated by welding two plates together along the 500mm length of the plates. Three weldments were fabricated in total. Two weldments were completed using a combination of the gas tungsten arc (GTA) welding process for the root pass and the GTA process in order to fill the joint. One weldment was completed using the GTA method for the root pass and the shielded metal arc (SMA) method to fill the joint. Welding parameters are given in table 3.1.



Parameter	GTA	SMA
Gas Shielding (L/min)	Industrial Grade Argon (99.995%) 8-12 L/min	N.A.
Backing Gas (L/min)	Commercial Purity Argon (0.5 % Oxygen) 10 – 15 L/min	N.A.
Weld Sequence	Same direction stringer runs (no weave)	Same direction stringer runs (no weave)
Current (Amps)	140	93
Voltage (V)	22.2	16.8
Polarity	- ive	+ ive
Maximum Interpass Temperature	< 150 degrees	< 150 degrees

**Table 3.1 Average welding parameters for GTA and GTA root/ SMA fill welds.**

Filler metal composition is given in table 3.2 along with the maximum wt% composition of the base metal. The GTA welding consumable was a Zeron 100X (overalloyed) welding wire of 2.4mm diameter, obtained from the producer. WMF also supplied the 3.2mm diameter SMA “Jungo Zeron 100X” welding electrodes.

Element	Cr	Ni	Mo	Cu	Mn	W	Si	N	C	P	S
<b>Base</b>	26	8.0	4.0	1.0	1.0	1.0	1.0	0.3	0.03	0.03	0.01
<b>GTA</b>	24.8	9.35	3.8	0.61	0.69	0.6	0.39	0.225	0.018	0.03	0.001
<b>SMA</b>	25.0	9.5	3.6	0.8	0.7	0.7	0.5	0.2	0.03		

**Table 3.2 Base metal & welding consumable composition (Wt %). Remainder Fe [112].**

On completion of the three weldments, they were returned to the Mechanical Engineering workshop in DCU for preliminary assessment. This included measurement of angular misalignment by means of a bevel protractor.

### 3.1.2 Tensile strength

Before time consuming crack propagation tests were carried out, simple tensile tests were performed on cross weld tensile samples and on the base metal to ensure the weldments had sufficient integrity. Samples had constant rectangular cross-sectional dimensions of 4mm x 10mm and were laser cut transverse to the weld bead as shown in figure 3.3. The cap and the crown of the weld metal were ground off before testing commenced.

The tensile tests were carried out on an Instron 4202 electromechanical testing machine with a 50kN load cell. Cross head speed was 1.5mm/min for all tensile tests. Extensometer gauge length was 101.6mm. Percentage elongation and the stress on the samples were calculated from:

$$\text{Stress}(MPa) = \frac{\text{Force}(N)}{\text{Area}(mm^2)} \quad 3.1$$

$$\% \text{elongation} = \left( \frac{\text{displacement}(mm)}{\text{gauge length}(mm)} \right) \times 100 \quad 3.2$$

Two tests were carried out on the base metal. Five tests were carried out on each of the cross weld samples, i.e. a total of fifteen to ensure consistency of results.

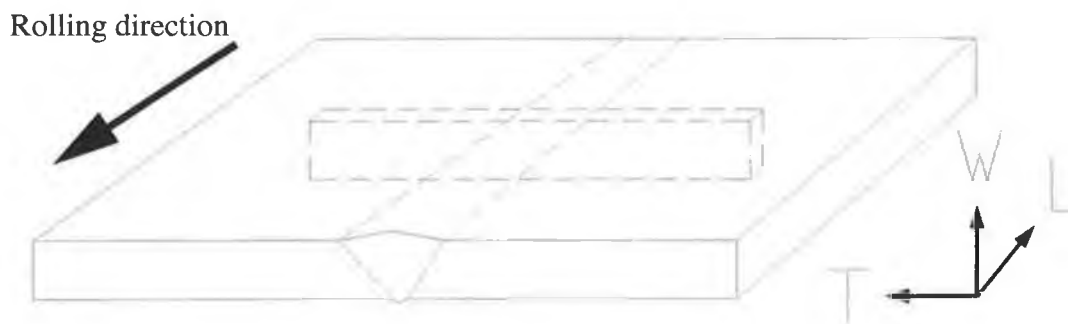
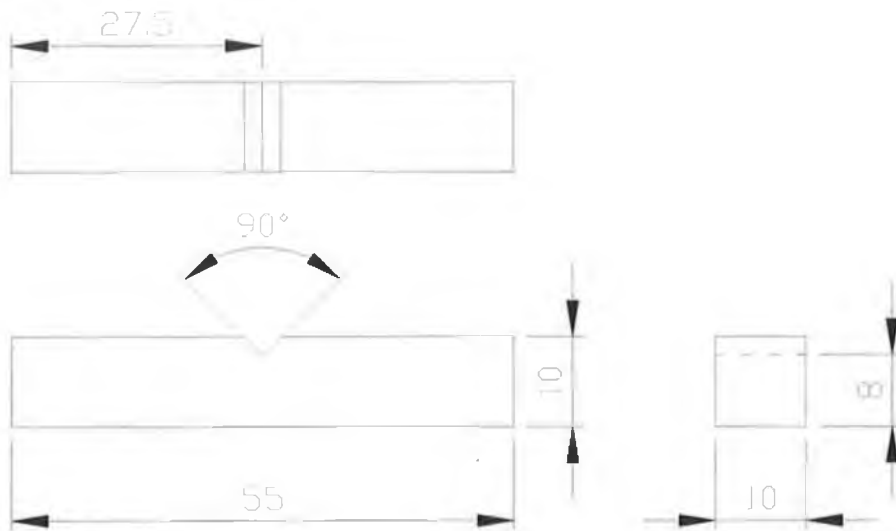


Figure 3.3 Orientation of cross weld tensile sample with respect to rolling direction.

### 3.1.3 Toughness

In order to quickly and easily evaluate the toughness of the weld metals, Charpy V notch (CVN) impact tests in accordance with BS 131-6:1998 [59] were carried out on a Denison Mayes Group 300J pneumatic impact tester with a C type hammer and an 8mm striker.

Standard Charpy impact samples were fabricated from the base metal; 10mm x 10mm x 48 mm with a 2mm deep notch (figure 3.4). For the weld metals, the notch was located in the centre of the weld metal and the weld cap and crown were not removed.



**Figure 3.4 Standard Charpy V notch impact sample for base metal – dimensions in mm [59].**

Seven tests were carried out on the base metal. Samples orientation was both TL and LT for the base metal (figure 3.5). Four and two tests were carried out on the SMA and GTA weld metals respectively. Weld metal samples were in the TL orientation. All tests were performed at  $-40^{\circ}\text{C}$ .

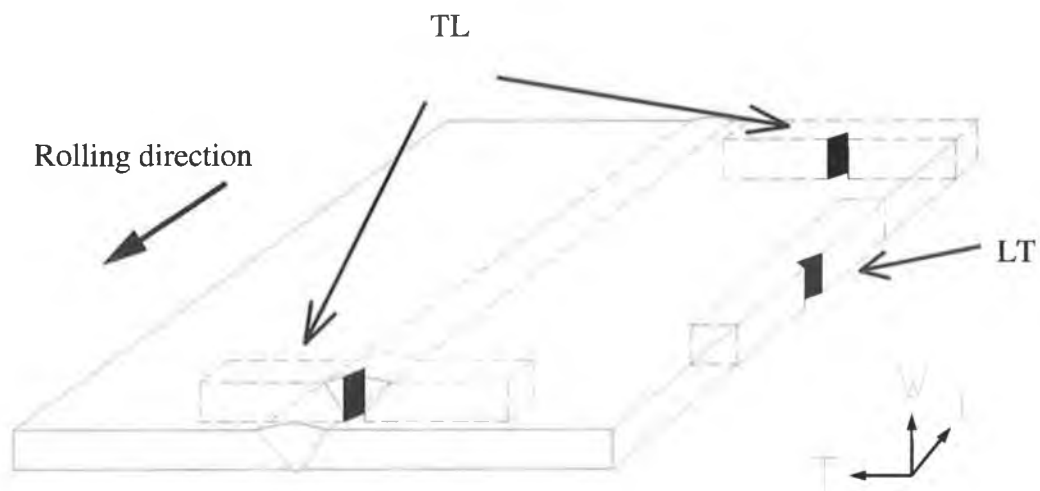


**Figure 3.5 Impact sample orientation with respect to rolling direction.**

### **3.1.4 Hardness**

It was also deemed necessary to characterise the weld metals in terms of hardness. Hardness is a good indicator of strength and it is well known that local regions of high hardness are susceptible to environmental assisted cracking. In addition, phases with different hardness levels prevalent in an alloy may influence the path of a propagating crack.

Macro hardness measurements were carried out using a rockwell hardness measurement system, C scale (HRC). Hardness is normally indicative of strength, and certain limits have been proposed for superduplex weldments in specific environments, e.g. 28-34 HRC in sour environments (NACE MR0175) [cited in 12].

Thirty readings were taken in the centre of the base metal on the TW plane. A conical indenter with a 120-degree angle and 150kg load were used. However, this system was too coarse for accurate measurement of discrete weldment regions, e.g. heat affected zone (HAZ) and individual phases. Therefore, microhardness tests were also carried out.

Tests were carried out in accordance with ASTM E 384 –89 [113]. Microhardness tests were carried out on the TW plane of samples selected from the middle of each weldment type. These samples were assumed representative of conditions along the full length of the weldment. The weldment region was prepared by polishing until a mirror finish was obtained and subsequently electrolytically etched so that individual phases could be distinguished. (This procedure is described in section 3.2.1) Microhardness tests were performed using a Leitz microhardness tester with a Vickers pyramidal diamond indenter and an objective lens with a magnification of 1000. All measurements were taken on the same sample in the same testing session and machine calibration was checked using standard samples before testing each weldment sample.

Tests were carried out on the base metal, HAZ's and weld metals. Load and hold time was 15 seconds. The Vickers indenter was small enough to enable the determination of the hardness of individual phases. The indentation load 0.981N was chosen to

produce indents, which were 24.5µm on average. The resulting indents were large relative to the duplex microstructure. It was therefore necessary to scan the sample surface to locate large colonies of ferrite/austenite and carry out measurements at these locations. As a result of the large indents, error in determining indent width was minimised.

Three regions were tested in each of the base, HAZ and weld metal areas as in figure 3.6. Each phase was tested 10 times in each of the regions, therefore, a total of 30 readings were taken for each phase in the base metal alone.

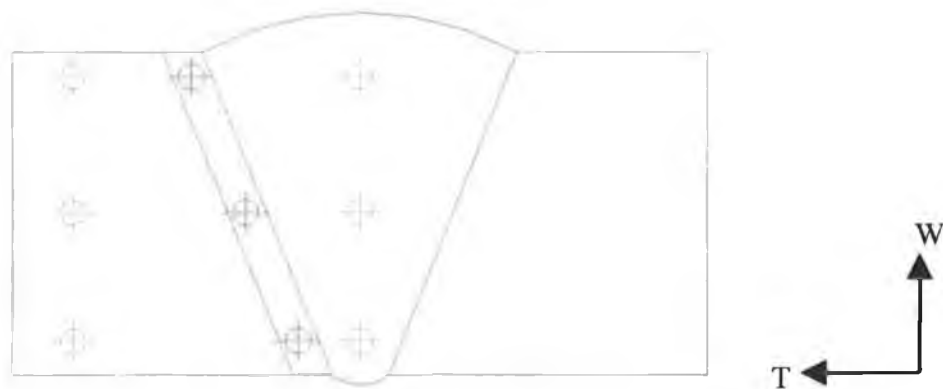


**Figure 3.6 Approximate positions of the 9 microhardness test regions.**

The Vickers hardness number (HV) is obtained by dividing the applied load in gram-force by the surface area of the indentation in square millimetres computed from the mean of the measured diagonals of the indentation. It is assumed that the indentation is an imprint of the undeformed indenter. The Vickers hardness number was computed from tables, which comply with the following equation [113].

$$HV = 1854.4 \frac{P_1}{(d_1)^2} \quad 3.3$$

Where:

$P_1$  = load, (gram-force) gf.

$d_1$  = mean diagonal of indentation, µm.

### ***3.1.5 Non destructive tests (NDT)***

It is common practice to assess weld flaws for critical applications by non-destructive means. The main aim of the current tests is to determine whether flaws are present and to obtain information on their size. This data can then be used to determine if the weldments are “fit for purpose” under current guidelines on acceptable flaw sizes as in BS 7910 [114]. Two types of non-destructive tests were employed for the weldments: radiographic and dye penetrant tests.

The dye penetrant tests were carried out at WMF’s foundry in Manchester. WMF carry out this test on numerous items including impellers, pump casings, valves etc., to BS EN 571-1 [115] specification. This test highlights any external defects such as micro-cracking from where a fatigue crack may propagate, or localised corrosion may occur. If a surface defect is found, it is common practice to remove the defect by grinding.

A representative selection of the weldments (2 of each type) was selected for dye penetrant tests. First, the samples were cleaned using a degreasing agent. Dye penetrant (red) was then applied to the surface of the sample. The samples were left for 15 minutes to allow the dye to enter any microvoids/cracks by capillary action. The samples were then cleaned again ensuring all visible traces of penetrant were removed. The developer (white) was applied, which enticed the penetrant out of any defects, which were present. The samples were left for an hour to see if any indications (red lines/dots) of a defect developed.

Radiographic tests highlight internal defects such as pores and lack of fusion, which may deleteriously affect structural integrity. These tests were carried out at the Royal & Sun Alliance, NDT laboratory, in Manchester.

A single wall single image (SWSI) technique was used on a representative selection of the weldments (2 of each type). Here the radiographic film was placed behind the weldment with the X-ray source at 160 kV placed in front of the weldment. An image quality indicator (IQI) ASTM 1-A was also placed in front of the weldment to ensure adequate sensitivity was obtained. A sensitivity of 1.25% was obtained which means

that defects down to 0.125 mm in width for the 10mm thick weldments were detectable.



## 3.2. Microstructural and Corrosion Assessment of Weld metal

### 3.2.1 Microstructural examination

Once the basic integrity of the weld metals was established, it was necessary to characterise the weld metals in terms of proportion of primary phases present, inclusion content and intermetallic content. These factors may have a bearing on both mechanical and corrosion properties.

Colour metallography was employed to aid characterisation. Since ferrite and austenite contain different quantities of alloying elements, they react differently to a particular etchant. For example, one phase may corrode in preference to the other phase. The corrosion product is typically a distinctive 'new' colour while the unaffected phase remains the same original colour. It is then possible to distinguish between the phases present. This allows:

- Determination of the relative proportions of ferrite, austenite and inclusions present.
- Microhardness testing (as described earlier).

Two transverse samples (figure 3.7) were selected for metallographic analysis, one from the centre of each weldment type. The base metal was also analysed, as significant portions of base metal were present either side of the weldmetal. These samples were assumed representative of conditions along the full length of the weldment. Numerous longitudinal (TL) and normal sections (LW) were also prepared in order to aid visualisation of the three dimensional microstructure.

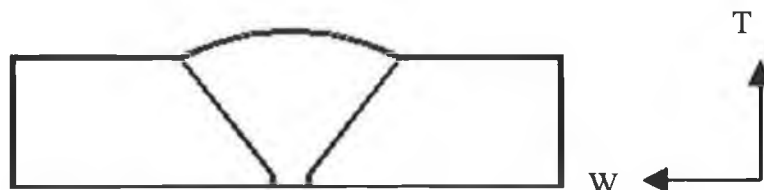


Figure 3.7 Transverse weldment sample

The samples were firstly cut to size using an abrasive cut-off machine with a blade suitable for tough materials. Lubricant was used to minimise burning and

deformation. Because of the abrasion associated with cutting, it was assumed that the structure of the alloy was damaged to a depth of approximately 1mm. Before addressing the damaged layer, the sample was mounted. All samples sectioned were mounted in a non-conducting thermosetting phenolic, which developed a rigid three-dimensional structure upon being heated and held at 300°C.

The mounted samples were subsequently ground down, taking care to minimise mechanical surface damage. The grinding times and relative rotation of abrasive and sample are given in table 3.3. The samples were washed in between each grinding step. From trial and error, this four-step procedure was found to give the best balance between best surface finish achievable, and total grinding time taken.

Procedure number	PAPER GRADE	GRINDING / POLISHING TIME	RELATIVE PLATEN-SAMPLE ROTATION
1	G 240	5 mins	Contra
2	G 600	5 mins	Contra
3	G800	5 mins	Contra
4	G1200	5 mins	Complimentary
5	Perforated Texmet 3µm	8 mins	Complimentary
6	Perforated Texmet 3µm	8 mins	Complimentary
7	Colloidal Silica 0.05µm	4 mins	Complimentary

**Table 3.3 Grinding and polishing procedure.**

Polishing of the metallographic samples involved, both rough and fine polishing (table 3.3, steps 5-7). The rough polishing was carried out using a perforated polishing cloth impregnated with a fine 3µm diamond paste. Rotation of the sample and the polishing cloth was complimentary for polishing in order to ensure that new scratches were not introduced onto the sample surface. Fine polishing was conducted with an unperforated cloth and a 0.05µm Colloidal Silica solution. Finally, samples were degreased in detergent, followed by alcohol and rinsed in water.

Electrochemical attack was used to good effect on the samples to reveal the true microstructure. This was carried out with reference to ASTM E 1558-93 [116].

Firstly, the sample was immersed in an etching solution in a stainless steel beaker (figure 3.8).

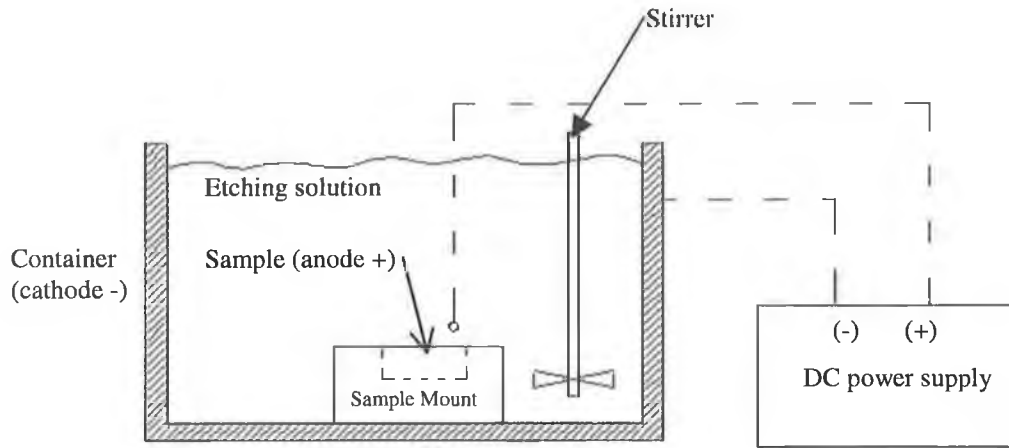


**Figure 3.8 Electrolytic etching cell.**

The beaker was electrically connected to the cathode of a DC power supply. The circuit was completed by a breakable connection between the anode of the power supply and the sample surface. Voltage was applied in five-second bursts until the specimen was satisfactorily etched. Two etchants were used.

- 20wt% sodium hydroxide (NaOH) in distilled water at 5V.
- 10wt% oxalic acid (COOH)<sub>2</sub> in distilled water at 5V.

The sodium hydroxide etch is commonly used for duplex stainless steels, and darkens the ferrite, with little or no effect on the austenite. In contrast, the oxalic acid etch does not generally darken the ferrite, but reveals the ferrite/austenite grain boundaries and sub grain boundaries. Best results were obtained with the samples lying flat in the container.

Digital images were captured at a magnification of 500 using a Reichart optical microscope with digital image capture capability. The TW plane of two additional larger representative samples was prepared and hand polished using facilities at

WMF. The electrochemical etching process was similar to the one described above. The samples were also examined under a high-powered optical microscope at a magnification of 1000 and the images were digitally captured. Macrographs were also captured.

### *3.2.2 SEM & image analysis*

Microstructural examination was also carried out using a scanning electron microscope (SEM). The electrolytically polished (TW) samples described previously were utilised for this purpose. Although more time consuming, high quality digital images can be captured by the SEM. In addition, much higher magnifications can be realised than by an optical microscope.

It was possible to observe the ferrite and austenite phases using a standard secondary electron detector. However, it proved more useful to use a back-scattered electron detector (BSD). Since the intensity of back scattered electrons increases with the atomic number of the elements from which they originate, they can be used to generate an image, which shows compositional variation. This makes the BSD extremely useful when multiple phases are present and differentiation between the phases is required.

Five images were captured at a magnification of 2000 in the top middle of each type of weld metal. Four images were captured at a magnification of 1000 outside the weld fusion line in the heat-affected zone (HAZ) of each type of weld metal. A further five images were captured in the base metal at mid thickness at a magnification of 1000. The small number of fields examined was largely a result of preferential etching of samples particularly in the weld metal. This phenomenon made it difficult to clearly differentiate between the phases in certain regions of the sample. Fields with the greatest clarity between the phases were chosen for examination.

Using Omnimet Enterprise 4 image analysis system, it was possible to quickly determine the approximate quantity of ferrite in the images. This was possible due to a feature on the software, which allows the darker regions on the digital image to be identified and shaded. The shaded area corresponds to the austenite phase, which was darker, than the ferrite phase using BSD imaging. The software can calculate the percentage of shaded area. The remaining area was assumed to consist totally of ferrite. However, a standard approach to finding the percentage ferrite content is employed later.

BSD images were also useful in determining the intermetallic phase content (introduced in the literature review, section 2.2.3), as these phases are exclusively highlighted as illuminated spots on an otherwise relatively dark image [117]. However, it was difficult to locate fields with a significant intermetallic content even at relatively high magnifications. Consequently, five fields were examined in the GTA root and fill weld metal and three were examined in the GTA root SMA fill weld metal at a magnification of 3000.

The image analysis software was also used to quantify the inclusion content in the SMA weld metal, as this had been observed to be significant in optical microscope examinations at a magnification of 500. Four fields from the top centre of the weld metal were examined at a magnification of 2000. These images were obtained using the secondary electron detector as inclusions showed up as black spots on an otherwise bright image.

### ***3.2.3 Calculation of percentage ferrite***

The etched transverse samples (TW plane) as described in the previous section were again used in the calculation of the percentage ferrite. The phase balance was determined in accordance with the standard method described in ASTM E 562-95 [118]. This standard describes a systematic manual point counting procedure for statistically estimating the volume fraction of an identifiable phase from sections through the microstructure by means of a point grid. The point grid was superimposed by means of image analysis software over an image projected by an optical microscope. The number of grid points falling within the phase of interest were counted and divided by the total number of grid points yielding a point fraction, expressed as a percentage for that field. The average point fraction for  $n$  measured fields' gave an estimate of the volume fraction of the phase. After a representative number of different fields were examined, an unbiased statistical estimation of the volume fraction was attained.

Since the ferrite content of the samples was expected to be greater than 20%, a grid size of 16 was selected for optimum efficiency. In addition, due to the regular pattern of the austenite colonies in the ferrite matrix (in the base metal), a circular grid was chosen to minimise bias due to the regular pattern. The grid was superimposed on an image (at a magnification of 500) from an optical microscope by means of image analysis software. The standard recommends the measurement of thirty fields in order to be able to calculate a 95% confidence interval. The 30 fields were measured as arrays. A 5 x 6 array was chosen for the base metal. The arrays for the HAZ, weld metal and base metal can be seen in figure 3.9.

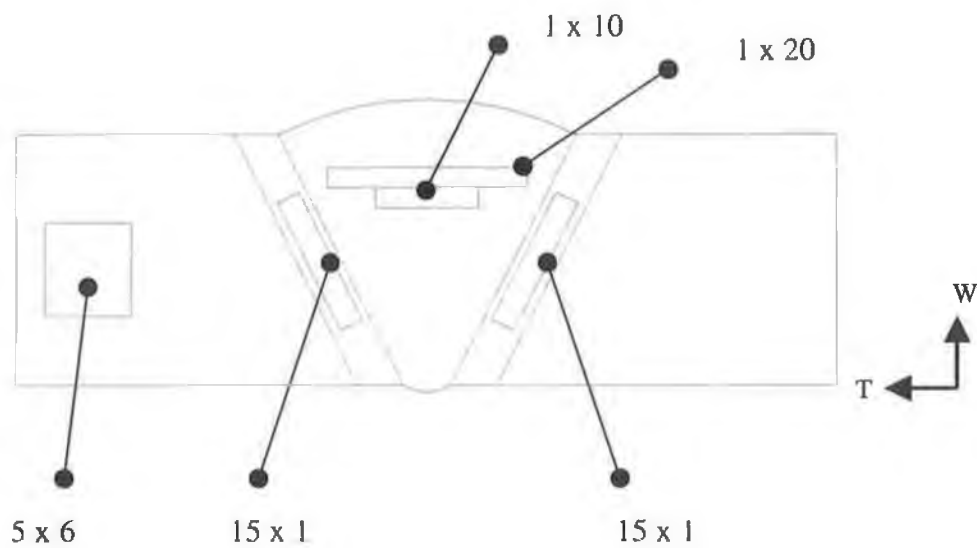


**Figure 3.9** Approximate location of field arrays used for point counting of ferrite content.

A minimum spacing of 0.3 mm was used between the fields, and field positioning was done without viewing the microstructure in order to eliminate operator bias. The following formulae were used in the analysis.

The average percentage of points ( $\bar{P}_p$ ) or % ferrite content of alloy is:

$$\bar{P}_p = \frac{1}{n} \sum_{i=1}^n P_p(i) = \frac{1}{n} \sum_{i=1}^n P_i / P_T \quad 3.4$$

The standard deviation (s) estimate is:

$$s = \left[ \frac{1}{n-1} \sum_{i=1}^n [P_p(i) - \bar{P}_p]^2 \right]^{\frac{1}{2}} \quad 3.5$$



The 95% confidence interval (CI) for  $\bar{P}_p$  is:

$$95\%CI = \frac{2.0s}{\sqrt{n}} \quad 3.6$$

where

$n$  = total number of fields measured

$P_i$  = number of grid points falling within ferrite phase in field  $i$ .

$P_p(i)$  = percentage of grid points falling within ferrite phase in field  $i$ .

$P_T$  = total number of points in test grid

### **3.2.4 Energy dispersive X-ray (EDX)**

Investigation of element partitioning between the austenite and ferrite phases was deemed important, as phase element content is known to determine the relative corrosion resistance of each phase. This was discussed in the literature review. Element content of each phase was determined using an energy dispersive spectrometer in a scanning electron microscope (SEM). This solid-state device distinguishes elements based on X-ray energies.

Quantification of relatively light elements (atomic number less than 12) was not attempted, as these elements were very difficult to detect especially combined with low count rates. As such, quantification of Fe, Cr, Ni and Mo were the only reliable results, as these elements are relatively heavy and count rates were high. Other heavy elements Cu, Mn and W are included, even though count rates were low.

Electrolytically polished transverse samples (TW plane) of each weldment were used for these tests at a working distance of 25mm. In order that counting statistics didn't limit precision, 250,000 counts were obtained for each test. In addition, the tests were repeated twice for each phase in each test region - base metal, HAZ and weld metal.

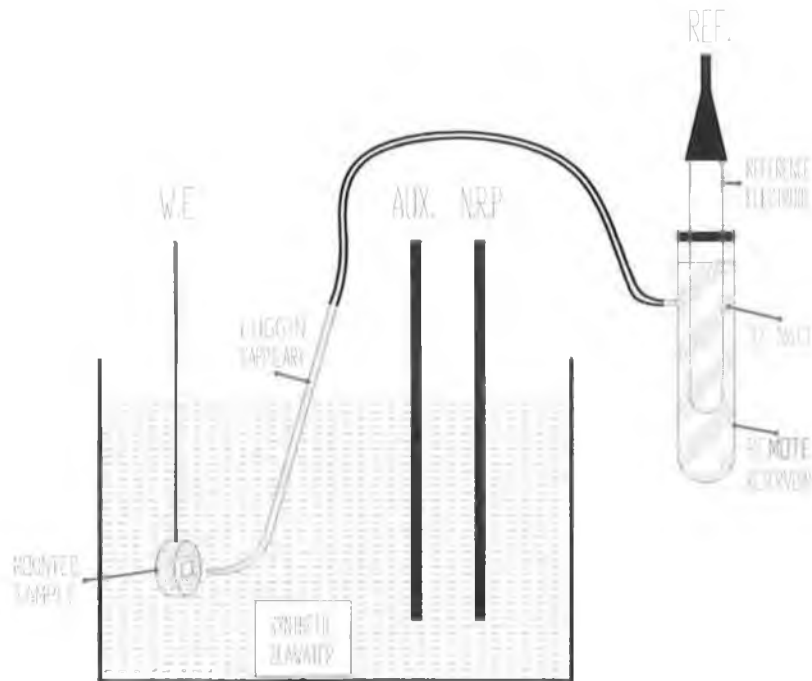
Accuracy of each test was maximised by using a high take off angle of  $35^{\circ}$ , along with an average electron beam voltage of 13.25keV. X-ray detection was by a lithium drifted silicon (Si(Li)) crystal.

The ZAF correction method was employed which is known to produce reliable results for X-ray lines greater than 1keV. The 'Z' factor corrects for atomic number. Elements with high atomic numbers repel the majority of incoming electrons elastically (back scattered electrons). Consequently, fewer X-rays are produced by these elements. 'A' corrects for absorption. Since X-rays are produced beneath the sample surface, some X-rays produced are immediately absorbed and fail to escape from the sample. 'F' corrects for fluorescence. 'F' corrects for those X-rays, which are detected by the detector, but were not generated by the electron beam. These X-rays can cause a low signal to noise ratio.

### ***3.2.5 Localised corrosion***

In order to gain an insight into the corrosion properties of the parent and weldmetal regions, potentiodynamic scans in accordance with ASTM G61-86 [75] in a synthetic seawater (table 3.4) were performed. The test method is a procedure for conducting a polarisation scan, to determine relative susceptibility to corrosion, for iron-based alloys in a chloride-containing environment. The corrosion rate (in the form of current density) at particular electrochemical potentials (ECP's) can be determined from a scan.

The apparatus used in the tests consists of a 1litre cell, luggin capillary, remote reservoir and various electrodes-platinum, noise reduction and, reference (saturated calomel electrode, SCE)(figure 3.10). Electrodes are conducting media, which provide an interface between the electron current in wired electrical circuits and the ionic current of aqueous solutions. The four electrodes are electrically connected to a potentiostat, which is described later. Refer to appendix A for an introduction to electrochemistry.



where:

- W.E. = Working Electrode
- AUX. = Auxiliary Electrode
- N.R.P. = Noise Reduction Probe
- REF. = Reference Electrode

**Figure 3.10 Determination of ECP as a function of corrosion rate - experimental setup.**

The 1 litre cell contained approximately 800ml of synthetic seawater (table 3.4). Deionised water with a resistivity greater than one microsiemen obtained from a Waterman deionising unit was used to make all synthetic seawater in the current project. The synthetic seawater was pH buffered by means of a small quantity of sodium bicarbonate. Presence of the bicarbonate ion ensures that the solution pH won't drift during experiments. Tests were carried out with the synthetic seawater at 20°C and 80°C.

Chemical	Weight per litre (g)
Sodium Bicarbonate	0.2
Calcium Chloride	2.3
Magnesium Chloride	6.0
Magnesium Sulphate	7.7
Sodium Chloride	28.0

**Table 3.4 Synthetic seawater composition [16].**

The corrosion rate of the sample (current density) was determined while the sample was held at a constant potential (ECP). Essentially a voltage was applied between the sample (working electrode) and the auxiliary electrode so that a current flowed through the synthetic seawater by means of ions. As platinum is a relatively noble metal (i.e. it is practically unaffected by the electrochemical reaction taking place), it makes a good auxiliary electrode. The ECP of the sample was referenced to a stable potential (reference electrode). Once the current flowing at a particular ECP had been found, the voltage applied between the sample and auxiliary electrode was changed, and a new reading was recorded. The procedure was repeated until readings had been obtained from  $-1200\text{mV}$  to  $+1200\text{mV}$ .

A luggin capillary, the tip of which was placed no greater than 10 mm from the sample surface, provided a conductive path (salt bridge) from the sample surface to the reference electrode. This enabled the potential of the sample to be referenced accurately against the reference electrode. The luggin capillary was connected to a remote reservoir, which contained the reference electrode. Locating the reference electrode in the remote reservoir ensured that the test solution didn't become contaminated with the concentrated potassium chloride (KCl) solution contained in the reference electrode. The luggin capillary and remote reservoir were filled with 3% NaCl.

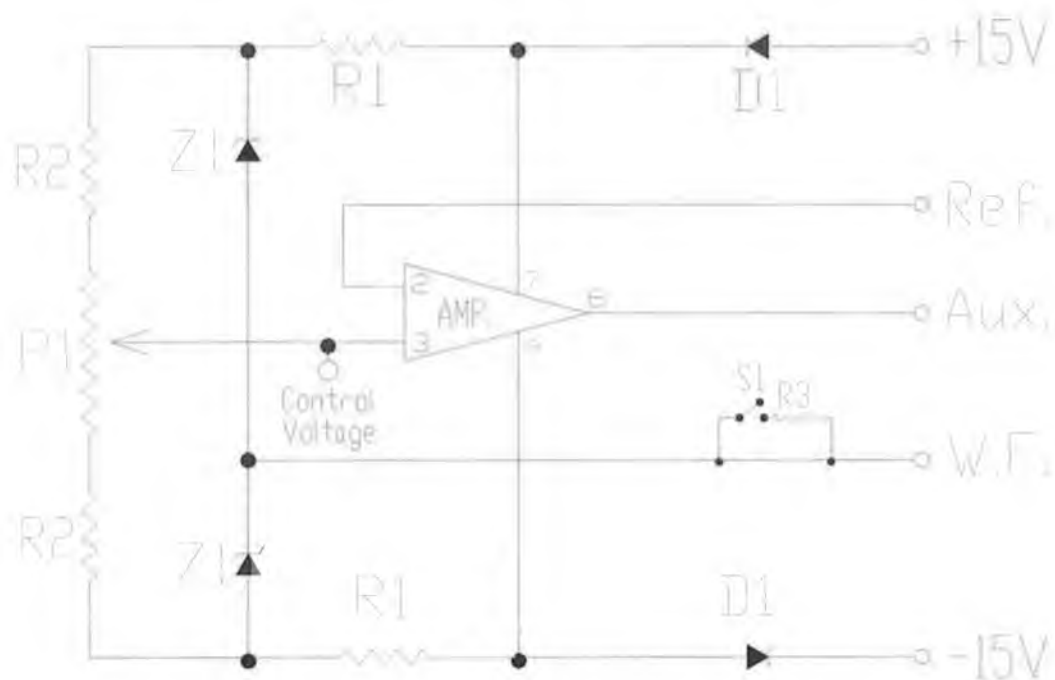
A saturated calomel electrode (SCE) was chosen as the reference electrode. Located in the remote reservoir, it provided a well-defined constant potential from which the potential of the sample could be referenced.

A noise reduction probe provided a low impedance path to earth for unwanted A/C currents induced in the luggin probe and reference electrode. A/C currents occur due to the high impedance path caused by the luggin probe and tubing. The high

impedance path acts as a radio receiver 'picking up' local electromagnetic radiation. The noise reduction probe ensured that the electrode potential of the sample was measured with respect to the reference electrode, and not with respect to the reference electrode plus any induced A/C currents. The noise reduction probe was suspended into the flask and connected to the reference electrode terminal.

A potentiostat was assembled and used to control the ECP of the sample. As mentioned previously, the potential of the sample was referenced to an SCE reference electrode. The basic function of the potentiostat was to hold the ECP of the sample constant. Figure 3.11 is a schematic of the electrical circuit (supplied by WMF) used for the potentiostat. It was powered by a  $\pm 15\text{V}$  power supply. The potentiostat could polarise samples to  $\pm 1200\text{mV}$ , and the potential was set by means of a 10 turn potentiometer.

The actual current flowing through the sample was determined by measuring the voltage drop across a 100ohm resistor connected in parallel with the auxiliary electrode electrical connection. A switch was used to divert the current through the 100 ohm resistor, when a voltage reading was required. The voltage drop across the resistor divided by 100 gave the current in mA. Further dividing by the surface area of the sample gave the current density ( $\text{mA}/\text{mm}^2$ ). The potentiostat had a practical current output of 7mA.



where:

- D1 = IN4001 diode
- Z1 = 6V Zener diode
- R1 = 2.2 kohm resistor
- R2 = 33 kohm resistor
- R3 = 100 ohm resistor
- P1 = 10-turn potentiometer (20kohm)
- Amp = 081 operational amplifier
- S1 = Switch

**Figure 3.11 Schematic of potentiostat electrical circuit [16].**

Sample faces parallel to the LW plane were prepared for the tests. This face was chosen as the crack propagates parallel to the LW plane in the corrosion fatigue crack propagation tests, which are described later. Metallographic preparation was the same as described previously, i.e. including sectioning, mounting, grinding and electrolytic polishing procedures.

However, further sample preparation was required for the tests in question, because an electrical connection was necessary between the sample and the potentiostat. A hole was drilled in the side of the polymer mounting material of the sample until the metallic sample was reached. A self-tapping screw was inserted into the hole until it

touched the metallic sample. A wire was subsequently soldered onto the self-tapping screw. The region where the self-tapping screw entered the polymer mounting material, the self tapping screw and the soldered region were then electrically insulated by heat shrinking a rubber sleeve over them to avoid corrosion. The sample was then immersed in the solution and the wire connected to the working electrode terminal of the potentiostat.

Four polarisation scans were carried out in synthetic seawater at 20<sup>0</sup>C - 1 x GTA weld metal, 1 x SMA weld metal and 2 x base metal. The surface area of each sample tested was measured, to enable the calculation of current densities. The repassivation loop (obtained on reduction of ECP from high positive ECP's) was completed once for each of the base and weld metal samples. One test was carried out on a base metal sample in synthetic seawater at 80<sup>0</sup>C to investigate the effect of solution temperature on the rate of corrosion. Solution pH and the free corrosion potential before turning on the potentiostat were recorded. Polarisation scans commenced at -1200mV with a scan rate of 0.6V/hour until 1200mV was reached. The scan was then either stopped or reversed at the same scanning rate, until the re-passivation loop closed.



### 3.2.6 Residual stress determination

It was deemed critical to assess the residual stresses prevalent in both the GTA and SMA weld metal as residual stresses are widely known to influence local stress levels independent of the applied remote loading. Therefore, residual stresses may be a major factor in resultant crack propagation rates.

Residual stress measurement on the weldments was attempted using the X-ray diffraction technique. The method was chosen due to its non-destructive nature, which allows repetition of tests. Spatial and depth resolution are also orders of magnitude greater than destructive mechanical methods.

Exploratory tests were carried out on a Bruker AXS X-ray diffractometer. Tests were carried out using a KF4KE X-ray diffraction tube with an air insulated Cu anode. The sample used for the investigation is shown below (figure 3.12). X-rays were diffracted from the L-T plane with the weld bead in the horizontal position. As a result the stress in the transverse direction (T direction) would be determined. This procedure was carried out at 10mm intervals across the sample width (L direction).

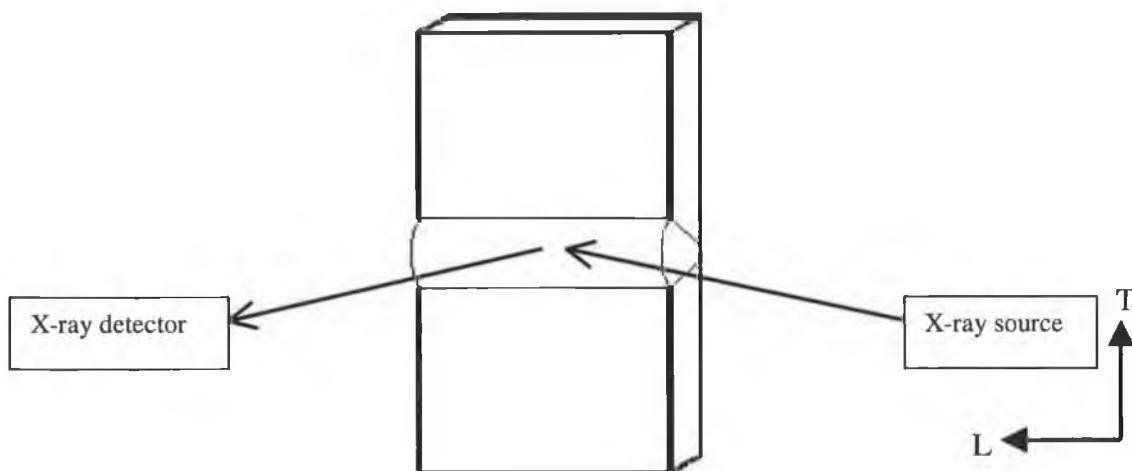


Figure 3.12 Weldment sample, x-ray source and detector - residual stress determination test.

### 3.3 Crack Propagation

#### 3.3.1 Sample type selection

In general, any sample configuration with a known solution for stress intensity factor,  $K$ , can be used in fatigue crack growth rate (FCGR) testing. Some of these are listed below. Samples used in FCGR tests may be divided into three categories: pin loaded (CT), bend loaded (SENB3/4) and wedge gripped (CCT).

- Three-point single edge notch bend (SENB3)
- Four-point single edge notch bend (SENB4)
- Compact tension (CT)
- Centre-Cracked tension (CCT)

The sample type, which appeared most suitable for the purposes of the current research, was either of the bend type samples (SENB3/4). This was largely due to the minimal effect of angular misalignment on resulting crack propagation rates if the loading set-up in bending is as shown in figure 3.13. This is because secondary bending moments, which can be induced due to axial loading on angular misaligned samples, are minimised under bending. CT and CCT samples are loaded axially, therefore the secondary bending moments induced at the crack tip region, due to say angular misalignment could be considerable (figure 3.13). As a result, the data would not be meaningful in general unless the secondary-bending moments could be isolated and quantified.

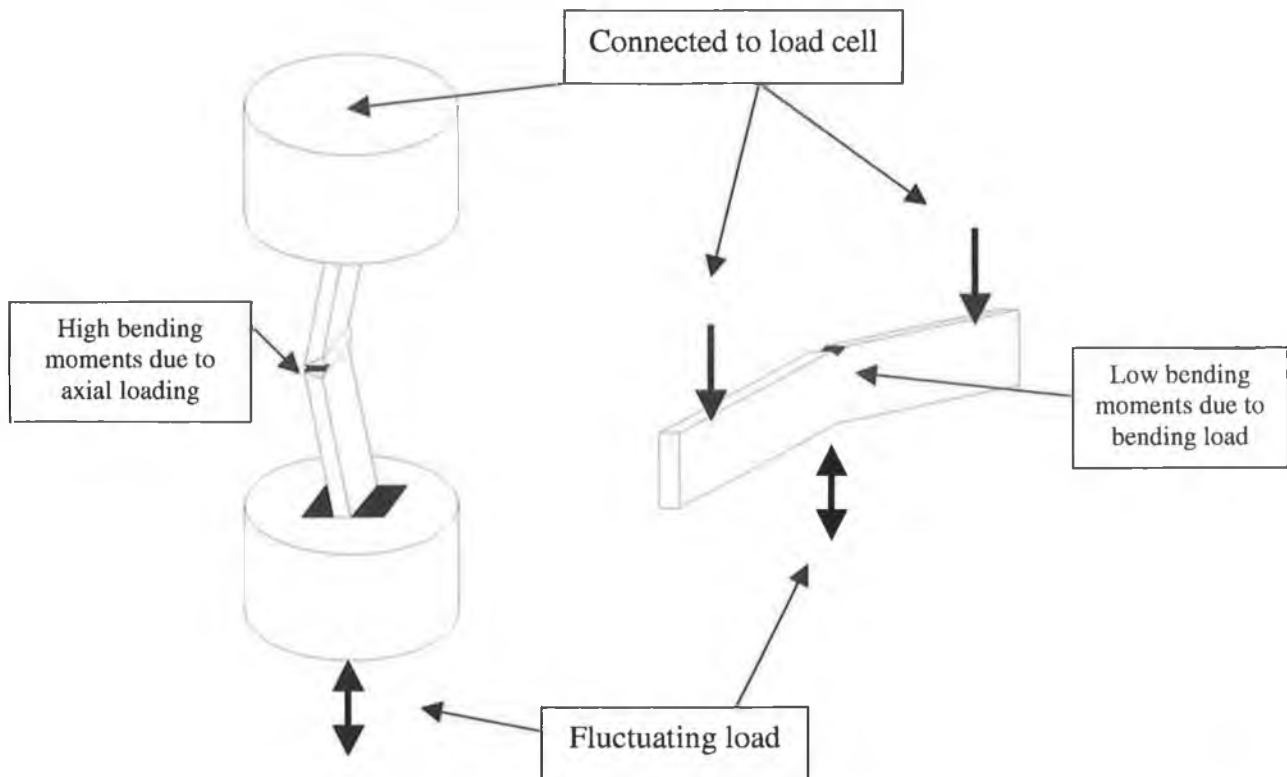


**Figure 3.13 Effect of loading mode on samples with angular misalignment.**

SENB4 specimens which result in a constant bending moment over a length were chosen over SENB3 specimens. A constant bending moment over the weld and heat affected zone (HAZ) was thought to be beneficial as the whole weld region would then experience a relatively high moment at maximum load. In addition, four point loading is more amenable to environmental testing from the view point of fitting an environmental chamber around the weld bead/centre of a sample.

### ***Sample dimensions***

For fatigue crack growth samples, thickness effects and plasticity limitations are not generally issues of major importance as they are in tests for plain strain fracture toughness ( $K_{IC}$ ) applications [119]. Even so, current corrosion fatigue test standards [94, 95] recommend that equation 3.7 be used to ensure adequate constraint during corrosion fatigue crack growth testing.

$$a, (B - a), t \geq 2.5 \left( \frac{K_{MAX}}{\sigma_y} \right)^2 \quad 3.7$$

where:

a = crack length

B = specimen width

t = specimen thickness

For the SENB4 samples at the test parameters used in the current testing, the above equation only holds up to a  $\Delta K$  of 25MPa $\sqrt{m}$ . Data was acquired up to 55MPa $\sqrt{m}$  on average. That does not mean that the tests were invalid, but it is generally considered that the best check is the extent of shear lips on the fracture surface [120]. Preliminary tests produced fracture surfaces with no evidence of shear lips up to the  $\Delta K$  of interest.

However, due to the low sample thickness 10 mm, fracture toughness values obtained are not  $K_{IC}$  values due to the absence of full plane strain constraint conditions. Samples with greater thickness were considered impractical due to increased difficulty in machining and laser cutting of samples. In addition, welding would have been more expensive requiring extra joint preparation and filler metal. Finally, shipping the plate would have been much more expensive.

It is important to note that dimensions for both the SENB4 and CCT specimens (introduced later) were chosen with reference to guidelines on absolute limits, specimen proportions and limits related to mechanical properties as in BS 6835 [96].

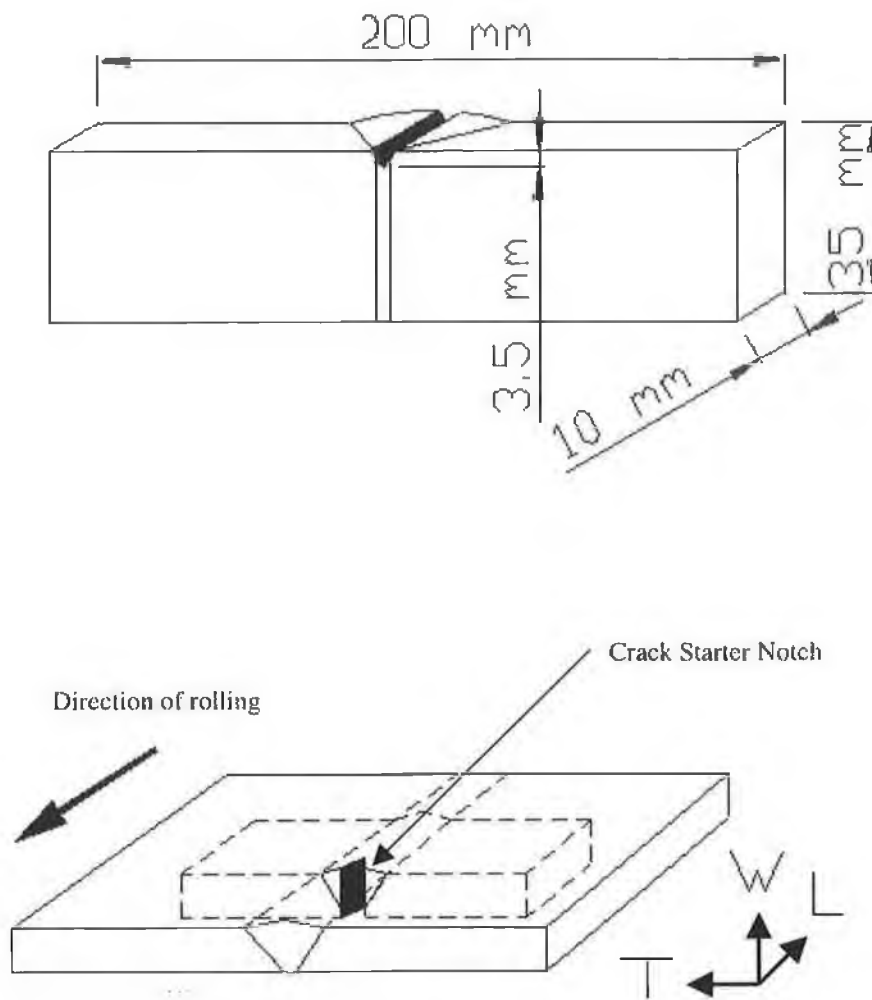


**Figure 3.14 Single edge notched four point bend (SENB4) sample.**

Some plain unwelded base metal samples were also fabricated. Since, it was known that fatigue crack growth rates in Zeron 100 duplex stainless steel in air varied with crack orientation in the wrought banded microstructure by a factor of 3 at 30 MPa√m [103], the orientation of the base metal used in the current research was specifically chosen to produce intermediate crack growth rates.

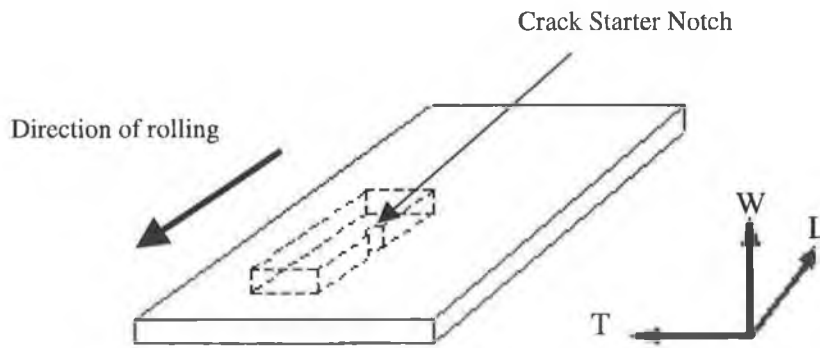


**Figure 3.15 Base metal sample**

A number of CCT samples were also fabricated for the purpose of assessing residual stress effects on crack propagation rates. It is widely known that weldments inherently contain residual stresses. If these stresses act at right angles to a propagating crack, they may decrease or increase the rate of growth depending on whether the stress is compressive or tensile. Residual stresses can be high (approaching material yield) parallel to the weld bead [19]. Transverse to the weld (figure 3.16), they are known to be considerably lower [19]. This case is of main concern in the current research.

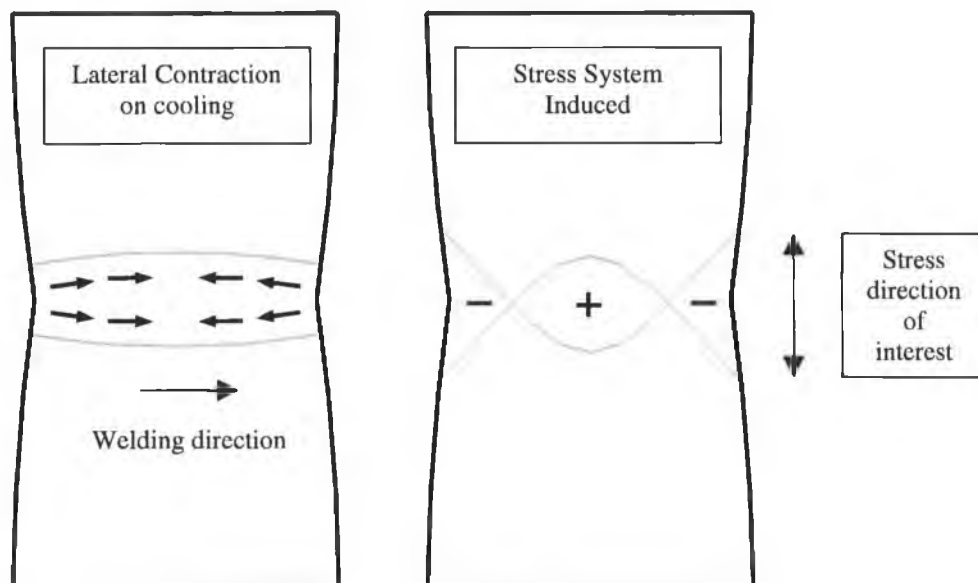


**Figure 3.16 Schematic of residual stress system induced transverse to weld bead in a weldment.**

**Residual stresses are caused by weld bead contraction.**

Two ways were identified to minimise the effect of residual stresses on crack growth through the weld metal in the current tests.

1. Cracks would be grown parallel to the weld bead; therefore, the lower transverse residual stress would act perpendicular to the crack path, with the higher longitudinal stress having negligible effect.
2. SENB4 samples were intentionally designed with a small width or weld bead length ( $W=35\text{mm}$ ), as it has been reported [121, 122] that a sample width ( $W$ ) of greater than 100 mm is required for significant residual stresses to be present.

Due to the location of the crack starter notch in the weld metal of each specimen type, crack propagation rates were determined in areas where compressive (SENB4) and tensile (CCT) residual stresses were assumed negligible. The crack growth rates in the two types of sample under the same test parameters should be similar indicating that the effect of residual stresses is negligible. As such, it would be possible to determine the intrinsic resistance of the weld metal.

The CCT samples were fabricated from the GTA root and fill weldments. This weldment contained the lowest degree of angular misalignment, which could have a major effect on crack propagation rates in CCT type specimens due to the axial mode of loading. CCT specimen size was chosen as 200mm x 48mm x 10mm.

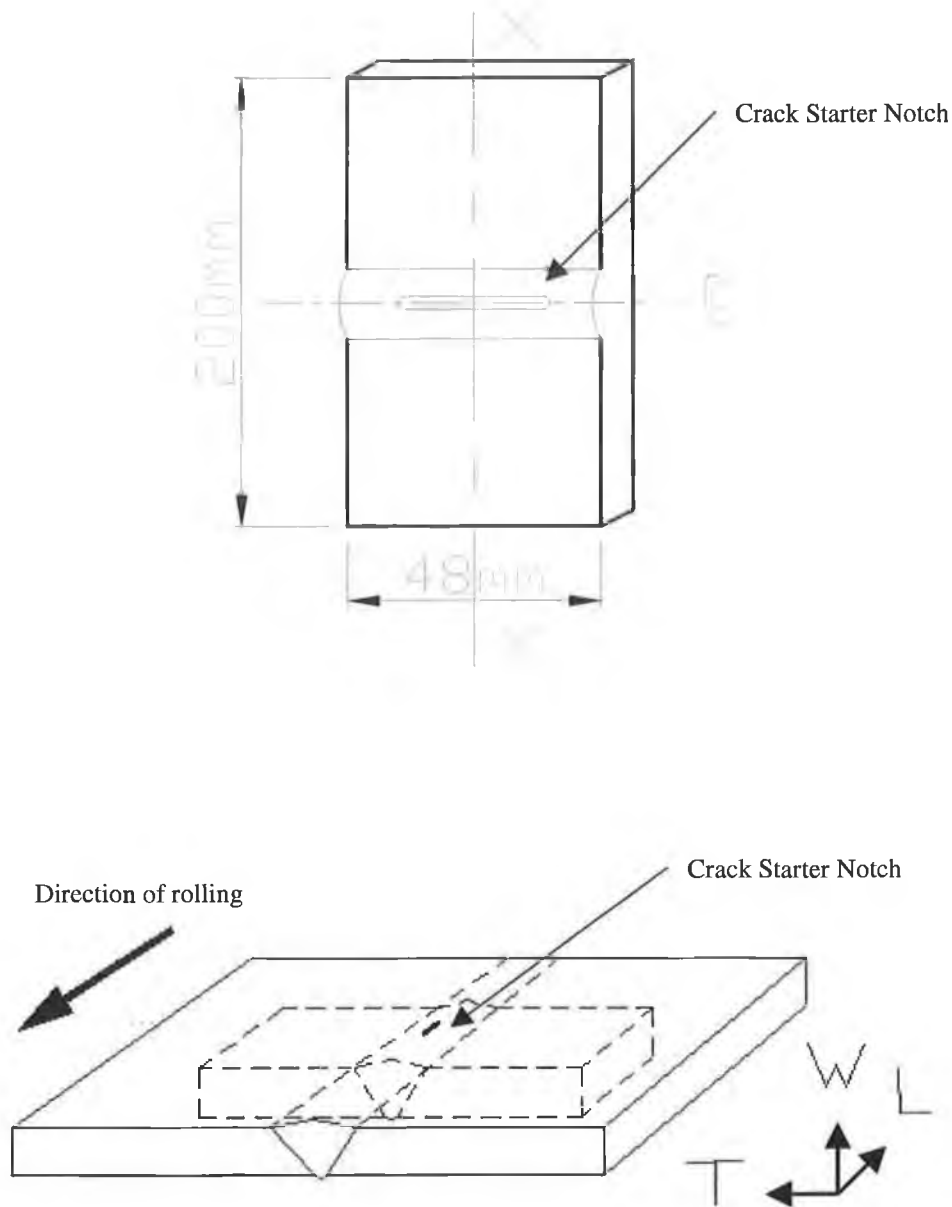


**Figure 3.17 Centre cracked tension (CCT) sample – dimensions in mm.**

The inherent angular misalignment present in the weldments inhibited accurate machining of the samples. Therefore, SENB4 and CCT samples were fabricated by laser cutting. This method was advised by WMF due to the number of samples required, and the high toughness of Zeron 100. Perhaps most importantly, laser cutting produces samples with consistent dimensions. Subsequent machining was not required except for the creation of a crack starter notch. The narrow heat affected zone resulting from the laser cutting operation does not affect crack propagation resistance. This is due to the precracking operation, which ensures crack growth rates



are determined in material, which is a significant distance away from the heat-affected zone.

In the case of weldments, the weld cap and crown were not machined down flush with the specimen surface. However, the majority of the cap and crown were ground down and subsequently polished using methods as described in the specimen preparation section. This was necessary to aid crack visualisation.

### ***Starter notch and crack length measurement***

A notch from which the fatigue pre-crack could be initiated was made by orientating the SENB4 sample at  $45^{\circ}$  and then milling. The notch was located so that a crack would initiate in the centre of the weldmetal and propagate through the centre of the weldmetal under fatigue loading. The depth of the notch as can be seen in figure 3.14 was 3.5 mm. This procedure was not from a relevant standard, but as the purpose of the notch was simply to provide a stress concentration at which a crack would initiate, its geometry was not deemed important enough to deliberate over. In addition, figure 3.14 shows the notch location with respect to the rolling direction.

The notch detail for the CCT specimen can be seen in figure 3.18. Since the notch was a through thickness notch, it had to be spark eroded. Two cracks propagate during a test, one from each apex at the centre of the sample. Crack length on the back and front of the sample was measured from the reference plane X-X.

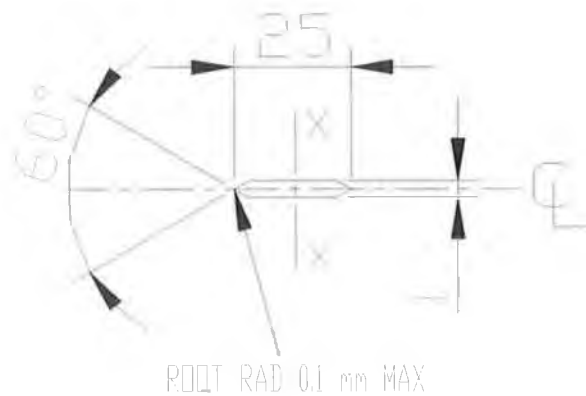


**Figure 3.18 CCT notch detail – dimensions in mm.**

The DC potential difference method has been successfully employed for crack length measurement in corrosion fatigue tests by other researchers. However, it was difficult to apply in the current work as a potentiostat was already being used to control the ECP of the sample. A clip gauge was not available for the compliance method to be utilised. It was decided to measure the crack length by means of an optical microscope complete with a translation stage and digital measuring gauge. The eyepiece was equipped with cross hairs. Resolution of the gauge was 0.01mm, however a resolution of only 0.1mm was required in relevant standards. Magnifications of 30 and 100 were available.

### ***3.3.2 Crack propagation set-up***

#### ***Laboratory air***

The experimental set up in laboratory air was relatively straightforward. All crack propagation tests were carried out on an ESH servo-hydraulic fatigue testing machine. The hydraulic actuator had a capacity of 100kN under static load and  $\pm 80$ kN under fluctuating load.

The actuator was programmed by means of a virtual control panel on a personnel computer. A macro (computer programme consisting of 'English like' instructions) was written to control the actuator from the start of a test until a defined finish point. The test type (load control) and waveform (sinusoidal) were defined in the computer programme. However, the macro required other 'inputs' from the user. These 'inputs' included mean load, load amplitude, loading frequency, number of cycles to complete and failure criterion. The failure criterion consisted of inputting an acceptable displacement range for the actuator. Once this displacement limit was broken, the test automatically stopped.

A four-point bend fixture was designed in order to carry out the crack propagation tests on the SENB4 samples. The bend fixture incorporated an I-beam, which served two purposes. First, the I-beam ensured maximum flexural rigidity during fatigue loading while transferring the applied load to a 100 kN load cell. Secondly, the I-beam supported the upper static loading points. Loading points consisted of tool steel pillars (hardened to greater than 40HRC as per ASTM E813 [123]) and hardened silver steel rollers (figure 3.19). The distance between the roller centres on the upper loading pillars was 150mm.

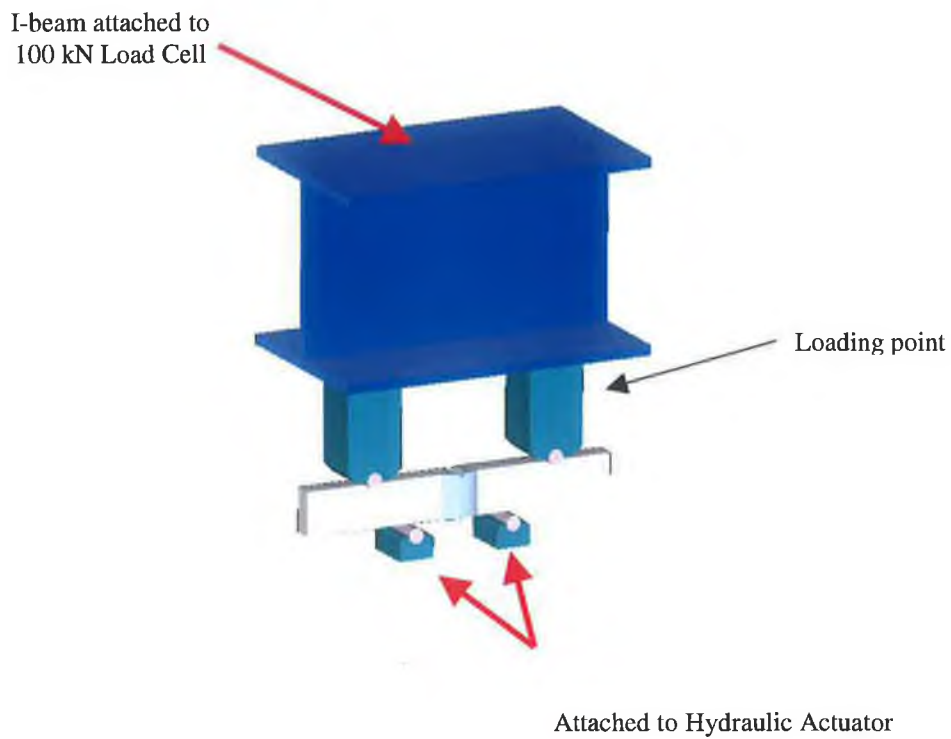


**Figure 3.19 SENB4 sample set-up in laboratory air.**

The distance between the lower loading points was 80mm. The lower loading points were attached to a platen, which was bolted to the actuator. The set up for the CCT samples tested in laboratory air is shown in figure 3.20.

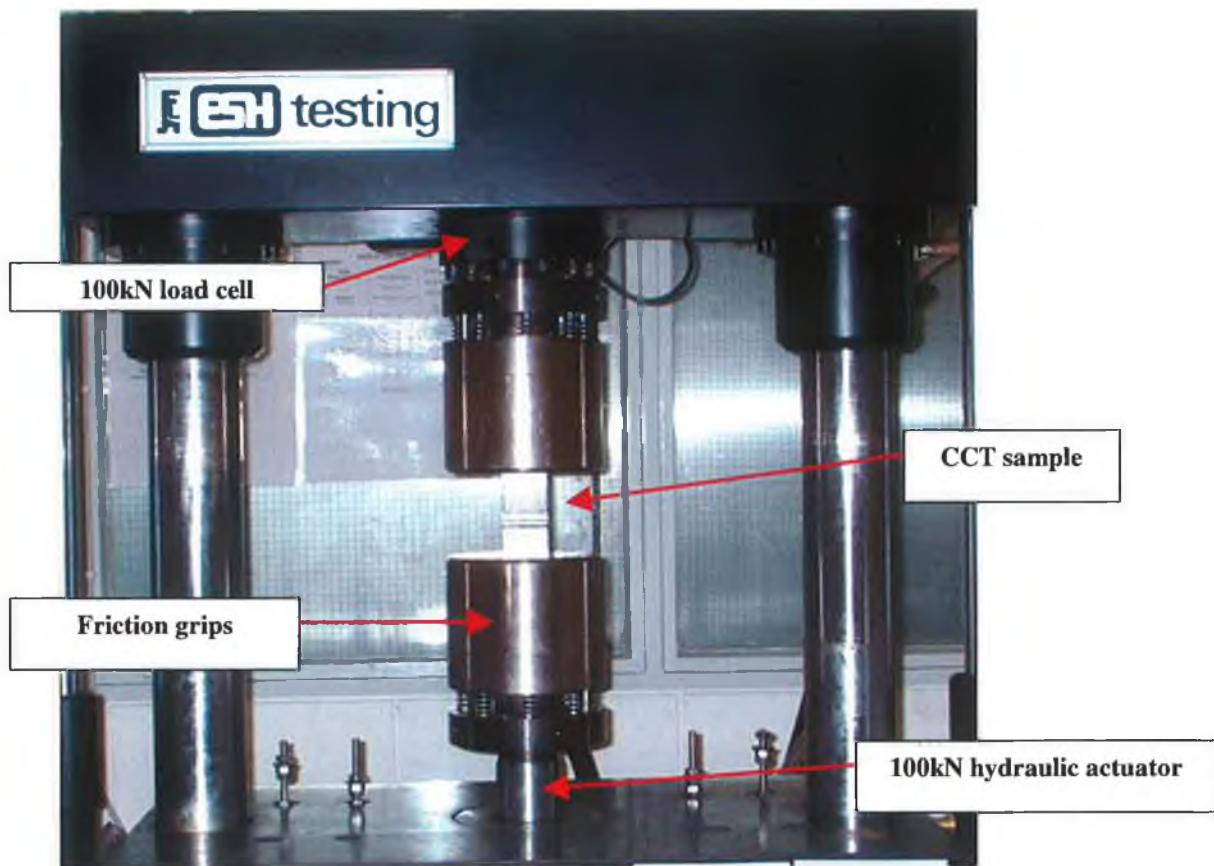


Figure 3.20 CCT sample set up on ESH fatigue machine.

### *Seawater*

The first major problem in performing crack propagation tests in seawater was that the seawater had to be contained around the cracked sample without affecting the load applied. In addition, in order to eliminate any galvanic reactions between dissimilar materials, it was critical that the only alloy in contact with the seawater was the weldment to be tested. However, a watertight seal between the weldment and the environmental chamber wall was then necessary.

An effective seal between the glass reinforced plastic (GRP) environmental chamber and metal sample surface was achieved with a silicone rubber compound, applied on the outside of the chamber. This technique has been used by other researchers [102] with no reported effect on crack propagation rates. Up to fourteen hours was allowed for escape of the acetic acid solvent base each time the seal was formed. Crevice corrosion at the location where the sample and GRP chamber were attached was never

evident. Crevice corrosion may have been a problem due to the tight gap formed between the sample and the wall of the environmental chamber.

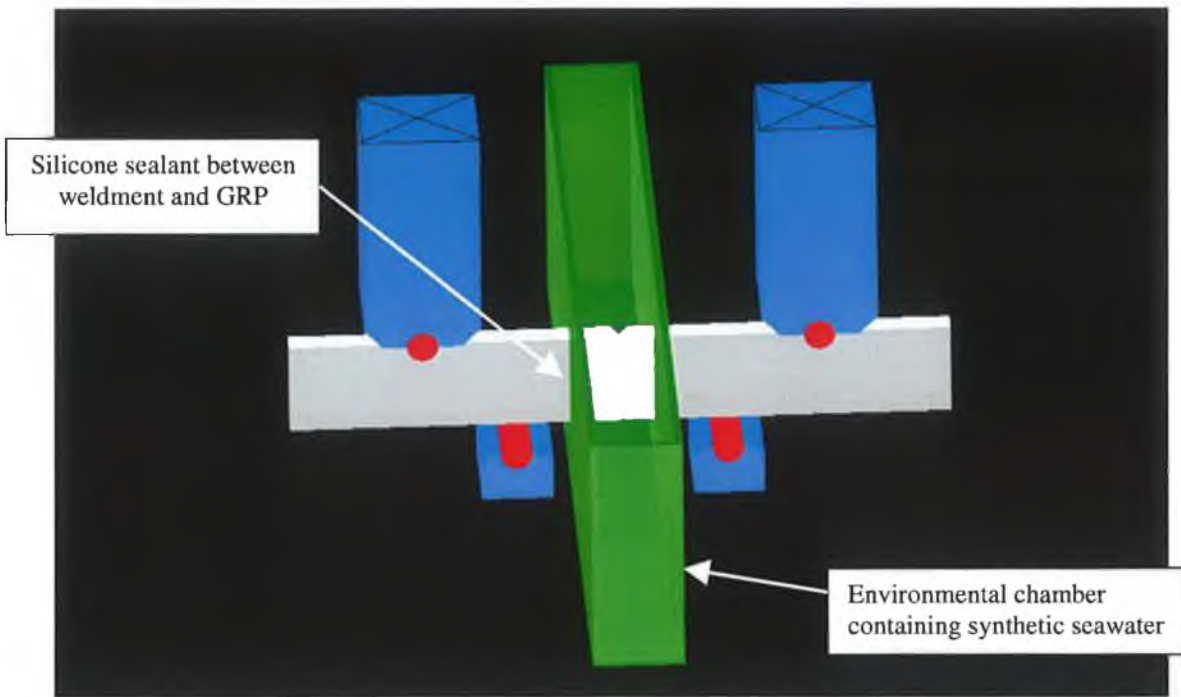


**Figure 3.21 SENB4 sample with environmental chamber attached.**

The environmental chamber was fabricated from hand laid up glass reinforced plastic (GRP) with a volume of approximately 1600 ml. The wetted sample area was  $20 \text{ cm}^2$  giving approximately  $80 \text{ ml/cm}^2$ . ASTM G31 [124] recommends a minimum solution volume to wetted sample area of  $40 \text{ ml/cm}^2$ . This serves to avoid any appreciable change in solution aggressivity during a relatively long-term test.

The second problem encountered was that the crack length had to be measured periodically for calculations of  $\Delta K$  and crack growth rate. In-situ visual crack length measurement was precluded by the test environment solution and the test chamber. The weldment sample had to be removed from the environmental chamber periodically for crack length measurement. The time that the sample was out of the solution was always less than 15 minutes.

In any case, the problem of loss of solution corrosivity over time was minimised by employing a circulation system as seen in figure 3.22. The total solution volume in circulation was 15 litres. This relatively large volume ensured that the effect of minor

contaminants was minimised. The circulation flow rate was in the order of 1.5 litres per hour. High flow rates may have flushed out aggressive species that had built up in the crack tip enclave. A final measure to ensure corrosivity was maximised was by renewing the synthetic seawater at least once per week.

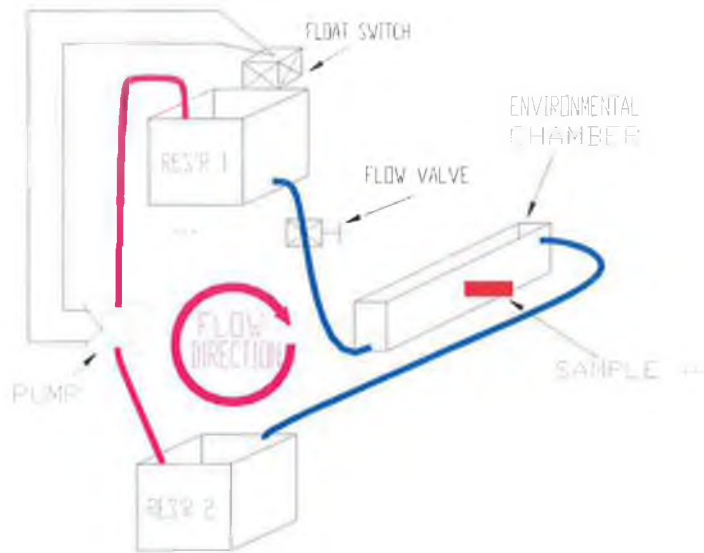


**Figure 3.22 Schematic of synthetic seawater circulation system.**

The sample was polarised by a potentiostat during the fatigue tests. As a portion of the sample was protruding from the environmental chamber, it was possible to electrically connect the sample to the potentiostat by means of an alligator clip. A noise reduction probe (NRP) and an auxiliary electrode were placed in the seawater for the duration of the test and electrically connected to the potentiostat. The tip of the luggin capillary was placed adjacent to the weldment in order to minimise potential drop between the reference electrode and the sample surface. The luggin was connected to a salt bridge, which provided a conducting path (for ions) to the reference electrode. The saturated calomel reference electrode (SCE) was situated in a remote reservoir and also electrically connected to the potentiostat. The corrosion fatigue set up can be seen in figure 3.23. This is an electrochemical cell set-up similar to the set-up described in the section concerning corrosion resistance (section 3.2.5).

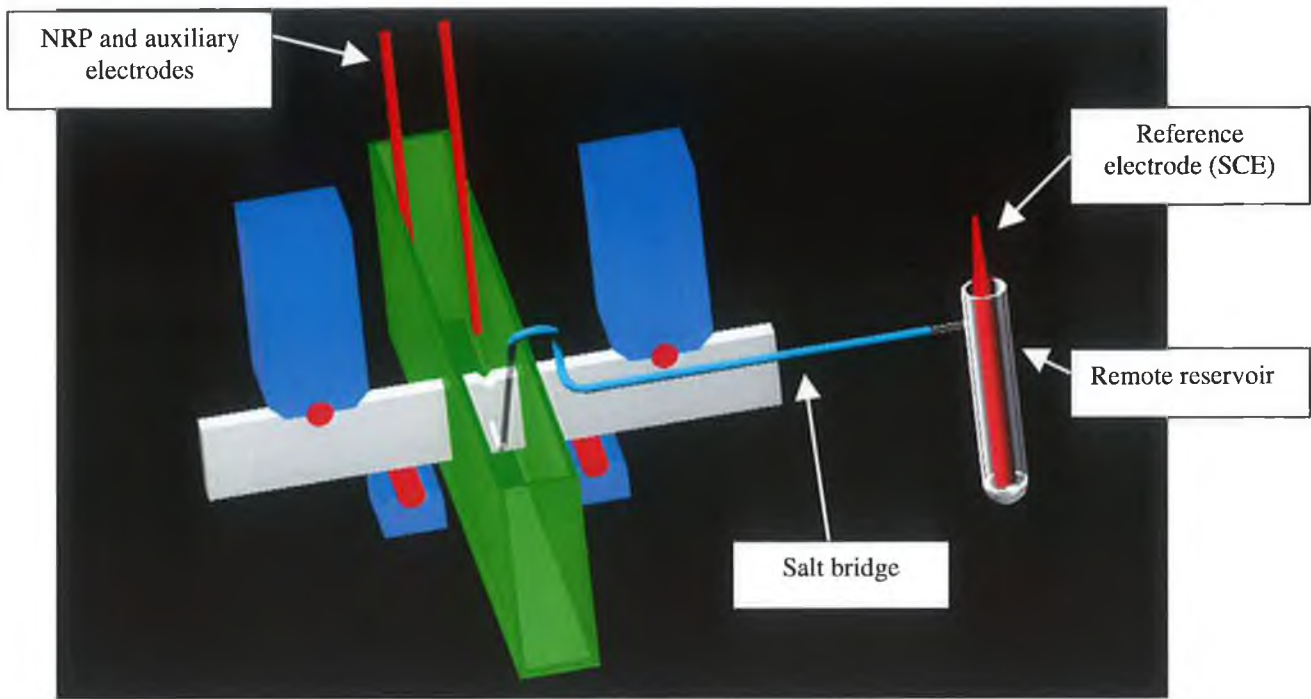


**Figure 3.23 Corrosion fatigue set up showing reference, auxiliary, noise reduction electrodes, remote reservoir and salt bridge.**

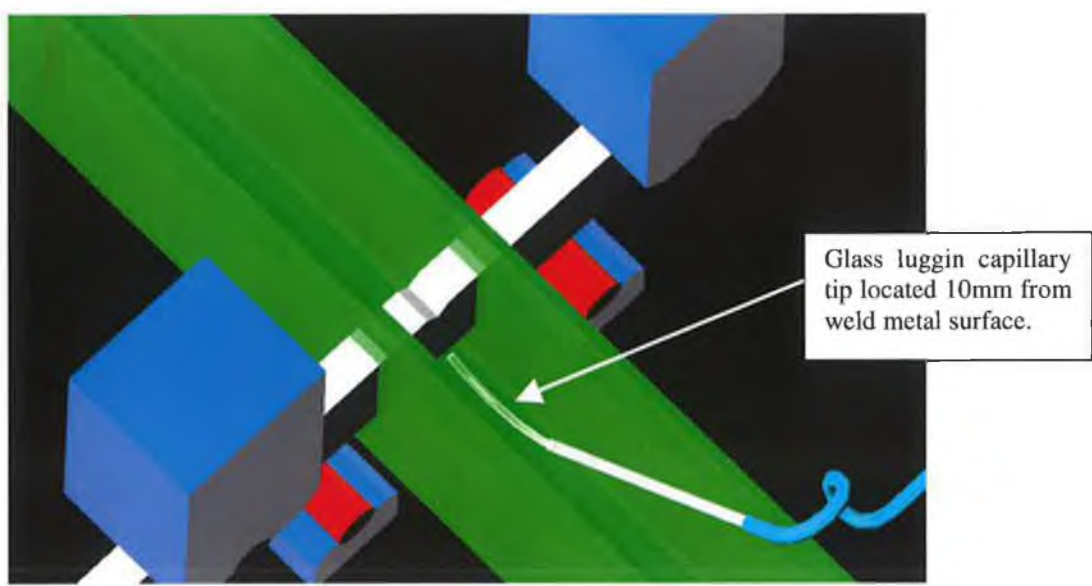


**Figure 3.24 Close up of luggin capillary, the tip of which is located 10 mm from the weld metal.**



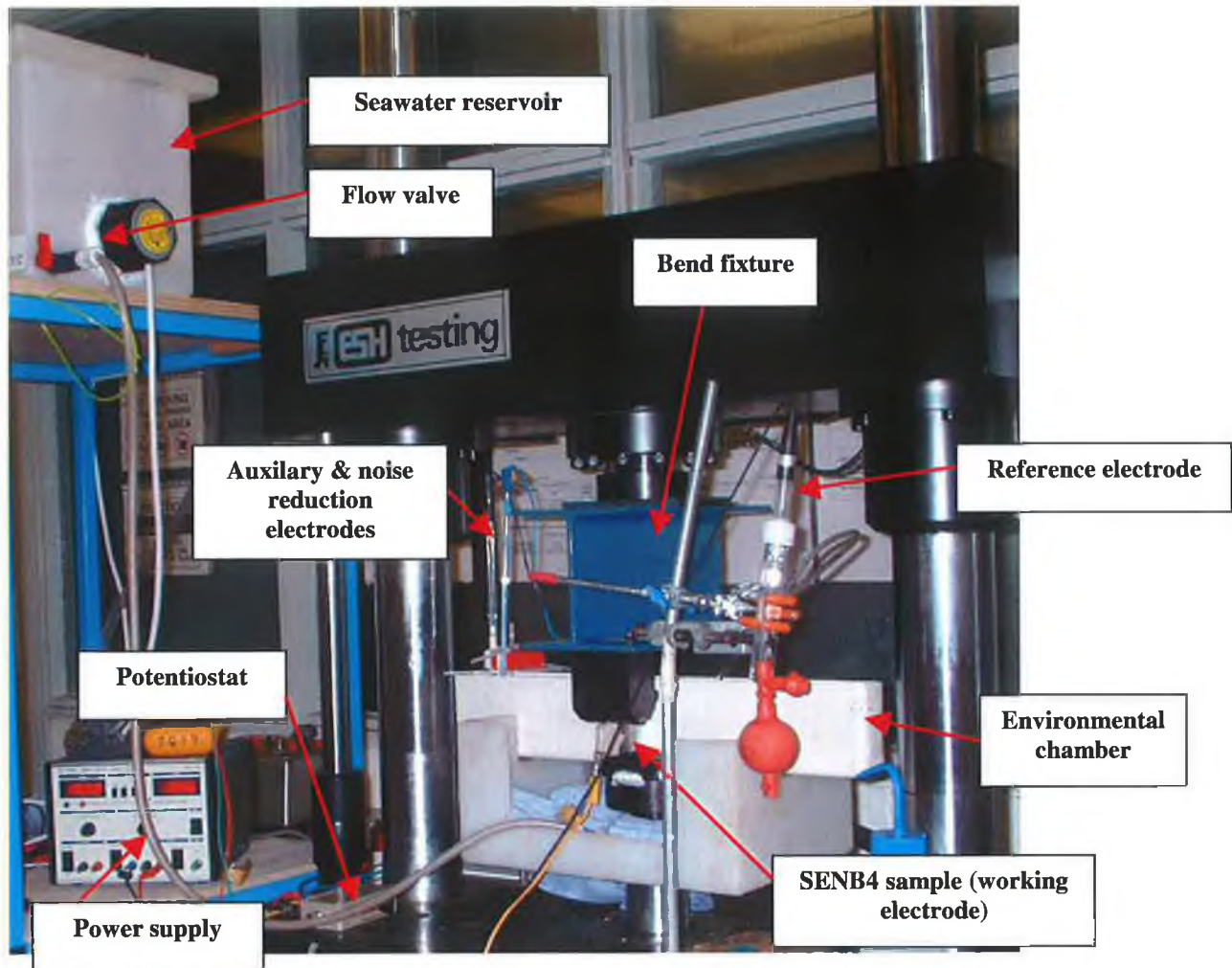


Figure 3.25 Experimental set up for corrosion fatigue.

The potential of the weldment was held constant during the fatigue tests as particular ECP's were of interest. A digital voltmeter with relatively high input impedance was used to ensure the ECP was set at the required value. Since a ground isolated power supply was used, all of the DC current which left the "+" terminal returned to the "-" terminal. Therefore, it was not necessary to electrically isolate the sample from the loading linkage, which typically is necessary when using a potentiostat to impose a specific ECP. Data relating to the synthetic seawater (pH and temperature) was recorded throughout the duration of the tests.

### ***K Calibration***

The stress intensity factor range was calculated for both sample types from equation 3.8 [96].

$$\Delta K = \frac{Y\Delta P}{B\sqrt{W}} \quad 3.8$$

where:

$\Delta K$  = stress intensity factor range

$\Delta P$  = load range

$Y = K$  calibration function

$B$  = sample thickness

$W$  = sample width

For constant load amplitude tests, the rate at which  $\Delta K$  increases as crack extension occurs is given by the geometry function also termed the  $K$  calibration function,  $Y = f(a/W)$ . The  $K$  calibration functions [96] for SENB4 and CCT samples are stated below. The functions are valid for all values of  $a/W$ .

SENB4

$$Y = \frac{3\sqrt{(2 \tan \theta)(0.293 + 0.199[1 - \sin \theta]^4)}}{\cos \theta} \quad 3.9$$

$$\theta = \pi a / 2W \quad 3.10$$

CCT

$$Y = \sqrt{(\theta \sec \theta (0.707 - 0.007\theta^2 + 0.007\theta^4))} \quad 3.11$$

$$\theta = \pi a / 2W \quad 3.12$$

where:

$a$  = crack length

$W$  = sample width

### 3.3.3 FEA analysis of angular misalignment

Since misalignment was prevalent in the weldments, it was deemed prudent to investigate the effect of angular misalignment on the stress intensity factor range,  $\Delta K$  in an SENB4 type sample. It was decided that FEA methods was the most efficient way of carrying out this analysis.

The misaligned weldments were modelled without the weld bead cap and crown. In any case, most of the cap and crown were removed from the SENB4 specimens before physical testing, as the weld metal was ground and polished to facilitate crack visualisation.

Commercial software packages such as ANSYS 5.7 and FRANC 3D use the displacement correlation technique (DCT) to compute stress intensity factors. A study has shown that the DCT technique provides adequate results especially where loading creates only a mode I condition [125]. Not only were adequate results reported but the size of the quarter point elements had little impact on the outcome. The DCT method uses all four nodes present on the crack face (2, 3, 4 and 5 in figure 3.26).

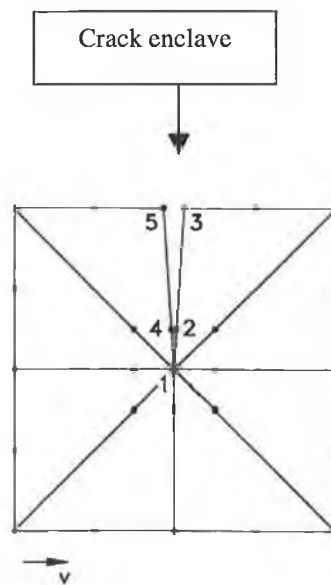


**Figure 3.26 Triangular quarter point elements and nodes used for calculating K.**

The differential displacements of the adjacent nodes across the crack enclave are required for the computation of the stress intensity factor,  $K$ .  $K$  can be calculated from equation 3.13 [125].

$$K = \frac{G}{K+1} \sqrt{\frac{2\pi}{L}} [4(v_2 - v_4) - (v_3 - v_5)] \quad 3.13$$

where

$G$  = shear modulus

$K = (3-4\nu)$  for plane strain

$L$  = element length (radius)

$\nu$  = Poisson's ratio

$v_i$  = transverse displacement with respect to crack direction for the  $i$ th node.

The following nominal material properties for Zeron 100 were used in all of the models described. An isotropic material was assumed. This assumption is true for the weld metal as will be discussed later.

Material Property	Value
Youngs Modulus	190 GPa
Poissons Ratio	0.33

**Table 3.5 Material properties used in FE analysis [112].**

Initially, a 2D model of the SENB4 sample was constructed in ANSYS 5.7. This model was created to find  $\Delta K$  over a range of crack lengths and to assess the results of the model against the values of  $\Delta K$  calculated from equation 3.8 using the appropriate 'Y' calibration function.

In order to simulate the singular stress field occurring at a crack tip, two steps were carried out. First, PLANE2, 2D 6 node triangular quadratic elements were employed.

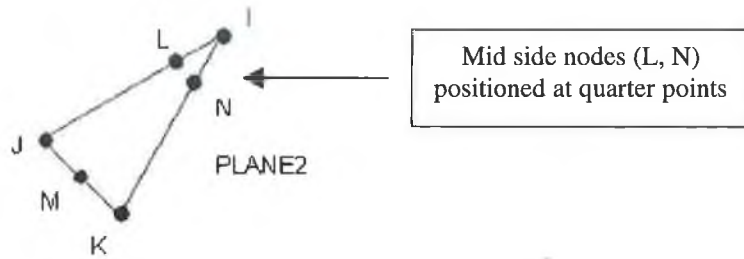
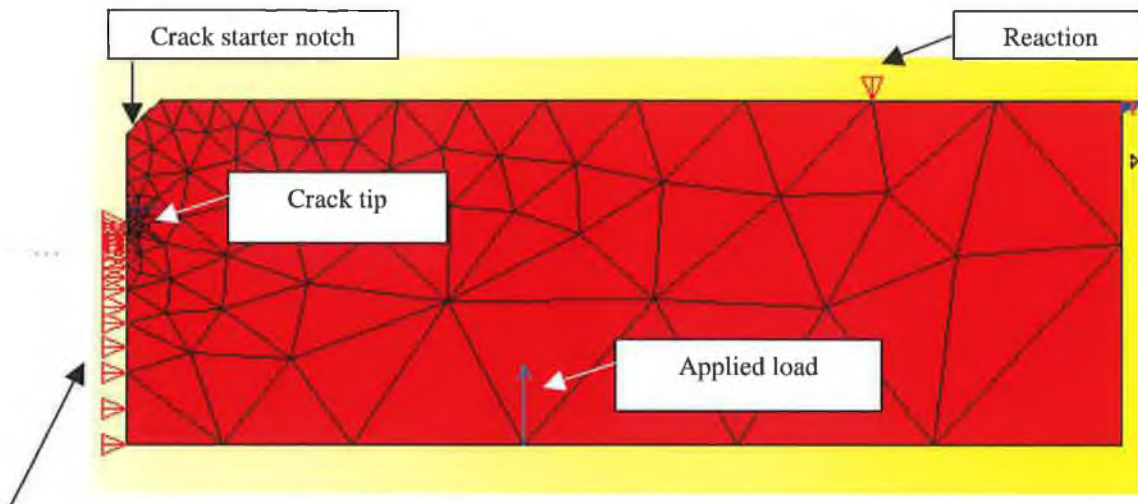


**Figure 3.27 Plane 2, 6 node triangular element.**

Secondly, midside nodes (L, N) were positioned at the quarter points automatically by using the 'KSCON' command, which generated singular elements around a 'keypoint' positioned at the crack tip.



Symmetry boundary conditions

**Figure 3.28 Half model of SENB4 sample.**

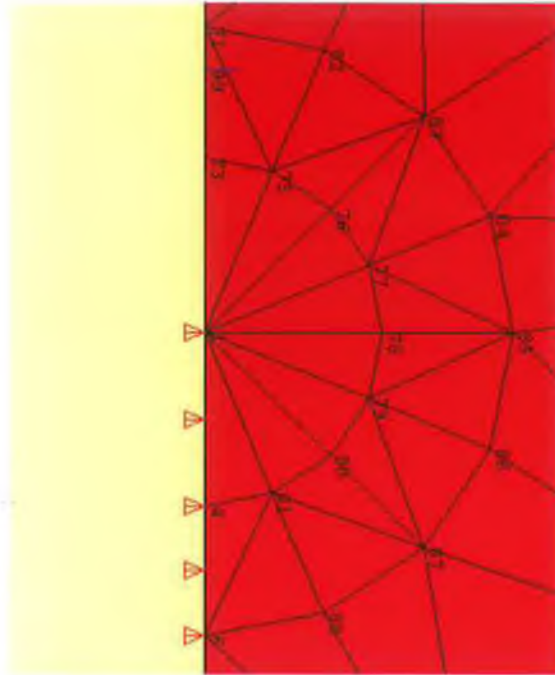


**Figure 3.29 Close up of crack tip showing 8 singular elements (isosceles triangles) with 1 mm radius. Midside nodes are not shown.**

The stress intensity factor  $K$ , was determined at the maximum and minimum loads intended in crack propagation tests at various crack lengths, 10 mm – 21mm.  $\Delta K$  was calculated from  $K_{\max} - K_{\min}$ .

In order to evaluate the effect of misalignment on  $\Delta K$ , a 3D model with angular misalignment was required. First, an aligned 3D model was constructed using the recommended SOLID95 - 3-D 20-Node elements. This model was extruded from the 2D model previously mentioned. Poor correlation between the model and the calculated stress intensity factor was obtained. Refinements of the mesh were tried, but the correlation didn't improve.

In addition, the model was taking significant time to solve and the method of obtaining the stress intensity factor from the software was rather awkward and time consuming. It involved the creation of a crack tip, re-meshing and solving of the model at each new crack front location. In addition, three post processor steps were required at each new crack front location:

- Definition of a local coordinate system at the crack tip.
- Definition of crack path.
- Calculation of K.

As such, a model with angular misalignment was not attempted using ANSYS. It was decided to use a different software package. Crack propagation software FRANC3D was employed for the task. The stress intensity factor could be obtained much quicker and easier from the package as the software was specifically designed to yield stress intensity data.

On insertion of a crack into the sample, singular elements were created near the crack tip automatically on meshing. This crack could then be grown a specified distance and the model re-meshed automatically. Once solved, the stress intensity at the crack tip was immediately available.

A 3D perfectly aligned model was constructed. By subdividing edges of the model into equal divisions, a bi-linear transfinite mapping algorithm could be used. The resulting mesh was composed totally of 4 node quadrilateral elements. Stress intensity factors were obtained across the thickness of the model (10mm) and at crack lengths from 10 to 22 mm. The results correlated well with calculated results using equation 3.8.

The next step was to construct a 3D model with a degree of angular misalignment. A misalignment of  $8^\circ$  was chosen. This is  $1.5^\circ$  greater than the maximum misalignment prevalent on the weldments, which were to be physically tested. The same elements and number of edge subdivisions were used as for the perfectly aligned model. Again, stress intensity factors were obtained across the full thickness of the model and at crack lengths from 10 to 22 mm.

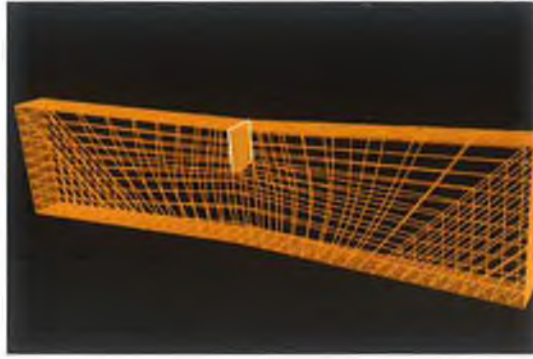
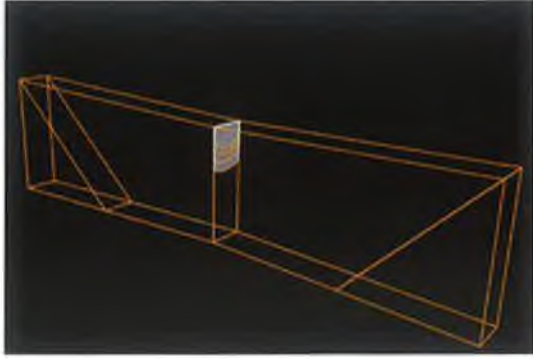


**Figure 3.30 Geometry, mesh and crack in misaligned SENB4 finite element model.**



### **3.3.4 Test procedures**

#### ***Precracking***

Before a precrack was grown in the samples, the region through which the crack would grow was given a mirror finish by metallographic procedures mentioned previously (section 3.2.1) in order to aid crack visualisation. However, due to the relatively large sample size (150 mm x 35 mm x 10 mm)-the grinding and polishing had to be carried out by hand. The majority of the weld cap and crown was removed in the grinding and polishing process, leaving all of the specimens between 10 and 11.5 mm thick at the weld metal. The variation in thickness was accounted for in calculations of  $\Delta K$ .

The K calibration functions (equations 3.9 & 3.11) mentioned previously are only valid for sharp cracks. Consequently, before crack propagation testing commenced, a sharp fatigue crack was grown in a sample by the traditional load shedding technique as recommended in ASTM E 647-95a, BS ISO 11782-2: 98 and BS 6835-1: 98 [94-96]. However, after difficulties obtaining conservative threshold data, a novel method of precracking was employed. This new method was more effective for obtaining data near threshold than the traditional load shedding method. Both methods are described below.

The standard method for precracking involves the application of a relatively high  $\Delta K$  using a positive load cycle so that a crack initiates at the apex of a machined notch. Once a crack initiates, load is reduced in steps until a satisfactory low  $\Delta K$  (below required  $\Delta K$  at test start) is obtained. A  $\Delta K$  of around 40 MPa $\sqrt{m}$  was applied at the notch apex. A crack was grown 2.5mm in length before the applied load range was manually reduced. Load was reduced in increments as uniformly as possible to avoid load sequence effects. The step size of the load during precracking was minimised to 22% on average. The amount of crack extension between each step was also controlled. If the step was too small, crack propagation may have been affected by the influence of the relatively large plastic zone present from the previous load cycle. The crack increments were at least greater than 0.75 mm in all cases. At the end of

precracking,  $K_{max}$  was less than the  $K_{max}$ , which was to be applied at the start of the constant amplitude  $\Delta K$  increasing type test.

An improved method of initiating a crack similar to the method described by Suresh and Forth [86, 126], was used to obtain conservative threshold values. A cyclic compressive four-point load was applied to SENB4 specimens such that instead of the stresses normal to the intended crack propagation direction being tensile, they were compressive.

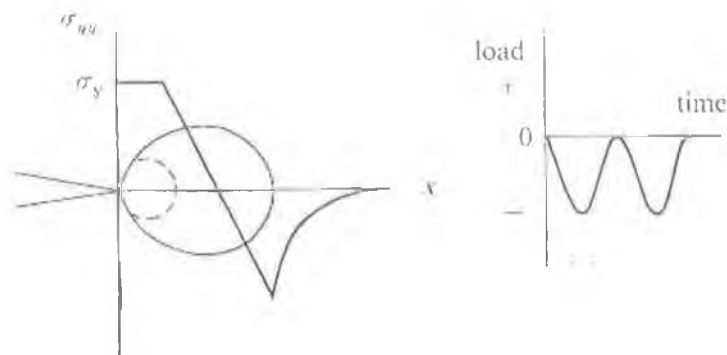


**Figure 3.31 Development of residual tensile stresses ahead of a crack tip due to the application of fluctuating compressive loading [86].**

The reason a crack initiates under fluctuating compressive loading is due to the fact that residual tensile stresses are induced ahead of the notch tip during unloading as evident in figure 3.31. A residual tensile field may only be generated ahead of a notch as closure cannot occur in the wake of a notch tip. Closure due to crack face contact in the wake of a propagating crack inhibits the formation of a tensile residual stress field.

A  $\Delta K$  of about  $40 \text{ MPa}\sqrt{\text{m}}$  was again used to nucleate and propagate the precrack. Using the cyclic compression method there was no need to progressively reduce the applied load, as the precrack propagated at a progressively slower rate due to increased crack closure until complete arrest took place at a particular crack length  $a^*$ . The sample was then ready for a constant amplitude  $\Delta K$  increasing type test.

### ***Crack Opening Load***

As mentioned in the previous section, crack closure typically occurs due to contact between crack faces (in the wake of the crack tip). Relatively rough fracture surfaces come into contact during the unloading portion of a load cycle and load is transferred across the crack [86]. Corrosion product can have a similar wedging effect [86]. As a consequence of crack closure the effective stress intensity factor range near the crack tip ( $\Delta K_{EFF}$ ) is less than the nominally applied  $\Delta K$ . This phenomenon is important because it has the potential to mask the true stress intensity factor range. Closure can cause non-conservative threshold stress intensity values to be obtained, which is to the detriment of structural design.

It was deemed important to determine the load required to obtain a fully open crack as fatigue load is widely known to be most damaging under fully open conditions. Subsequently  $\Delta K$  could be modified to take account of the fact that the crack was closed during a portion of the applied  $\Delta K$  range. Essentially  $\Delta K$  applied would be replaced by an effective  $\Delta K$  ( $\Delta K_{EFF}$ ). Resulting crack propagation data would be conservative.

The most widely used approach for determining the crack opening load (compliance technique) was used in the current research, and is similar to the standard practice described in ASTM E 647 [94]. However, since a clip gauge was not available, an LVDT was utilised to measure displacement across the crack mouth of an SENB4 sample. The LVDT was fixed across the crack mouth using two purposely-designed nylon mounts. A fluctuating load was applied to the sample oscillating between 2 and 20kN giving an R-ratio of 0.1. This was carried out at a crack length of 12mm on average. Three load versus displacement data sets were obtained for each sample: base, GTA and SMA weld metal.

Unfortunately, it was not possible to determine the crack opening load defined by an offset criterion of 2% as outlined in ASTM E647 [94]. This was due to high variability in the compliance offset data as a result of the relatively poor sensitivity of the LVDT. An attempt was made to determine the opening load using a strain gauge attached to the back face of a four-point bend sample. However, difficulty was

encountered correlating the load-strain readings. As a result, it was not possible to calculate the crack opening load.

***$\Delta K$  increasing/decreasing type tests***

$\Delta K$  increasing fatigue crack propagation tests were the main type of test used in the current research to assess the rate at which subcritical cracks propagate due to constant amplitude fluctuating loads. This type of test is suitable for crack growth rates  $>10^{-5}$ mm/cycle [94]. In constant load amplitude tests, the stress intensity factor range  $\Delta K$ , increases with increase in crack length leading to faster propagation rates as the crack progresses.

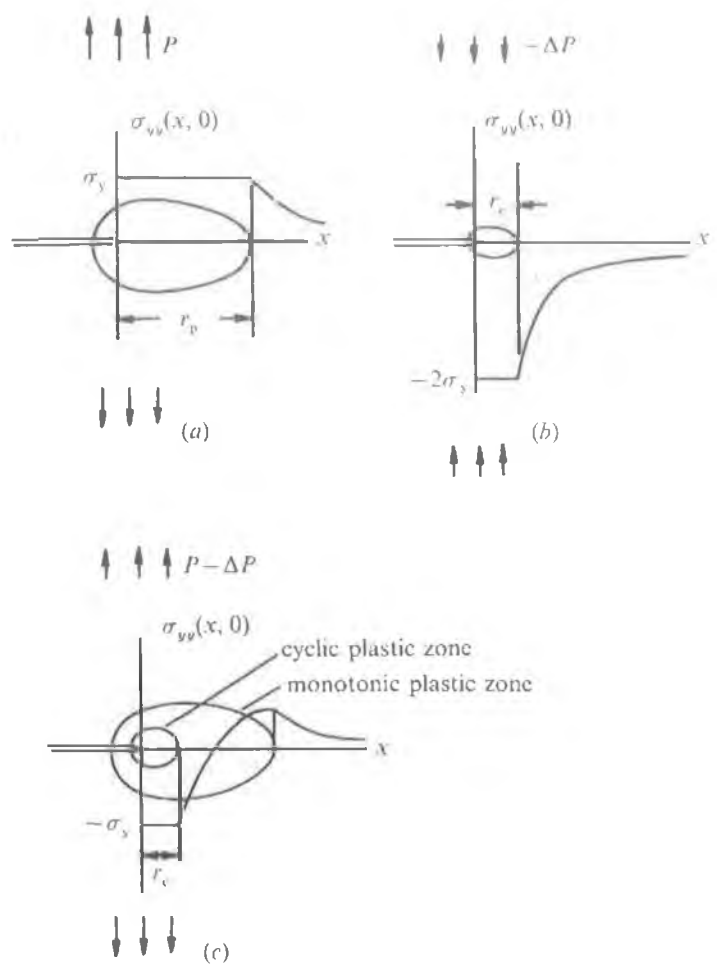


**Figure 3.32 Development of a monotonic and cyclic plastic zone ahead of a crack tip [86].**

The development of a monotonic and cyclic plastic zone at the tip of a fatigue crack is illustrated in figure 3.32. An important point to note about  $\Delta K$  increasing type tests is that the size of the monotonic and cyclic plastic zones increase as  $\Delta K$  increases. Consequently as the fatigue crack propagates, it is continuously sampling material without a prior load history. Therefore, crack propagation rates determined are the

worst-case scenario under the particular testing conditions. In contrast, in  $\Delta K$  decreasing tests, the crack may propagate through material, which has a prior load history. This is a consequence of the nature of a  $\Delta K$  decreasing test, which requires a progressive reduction in load. If the load reduction is carried out uniformly in relatively small steps and the crack is allowed to propagate a critical distance at a particular load level, then the effects of prior load history can be minimised.

Constant load amplitude  $\Delta K$  increasing fatigue crack growth rate tests were carried out with reference to both US and British standards, ASTM E 647-95a and BS 6835-1: 1998 [94, 96] respectively. Corrosion fatigue crack propagation tests were carried out with reference to BS ISO 11782-2:1998 [95] and ASTM E 647-95a [94].

In order to determine crack growth thresholds in laboratory air, a  $\Delta K$  decreasing or 'constant R load reduction' test was employed as recommended for crack growth rates  $<10^{-5}$  mm/cycle [94]. The rate of load shedding was controlled by limiting the normalised K-gradient 'C' to a constant  $-0.08\text{mm}^{-1}$  in accordance with ASTM E647 [94]. The following relationship between  $\Delta K$  and crack length (a) for a constant C test was employed [94].

$$\Delta K = \Delta K_0 \exp[C(a - a_0)] \quad 3.14$$

where  $\Delta K_0$  and  $a_0$  are the initial  $\Delta K$  at the start of a test and the corresponding crack length. As step shedding was carried out manually, the reduction in maximum load ( $P_{\max}$ ) did not exceed 10% of  $P_{\max}$  for adjacent load steps. In addition, a crack extension of at least 0.5 mm was obtained before the load was reduced. These precautions were in keeping with the relevant standards.

When determining crack growth thresholds from samples precracked using the cyclic compression technique, it was necessary to begin a  $\Delta K$  increasing type test at about  $1\text{MPa}\sqrt{\text{m}}$ . If a crack did not propagate after 2.5 million cycles,  $\Delta K$  was increased to  $1.5\text{MPa}\sqrt{\text{m}}$ . This procedure continued until crack growth was obtained.

It was decided to use a relatively high mean stress (R-ratio =0.5) for all tests in order to try to minimise crack closure effects due to rough fracture surfaces (large grain sizes in welded samples and corrosion product in corrosion fatigue tests) at relatively low  $\Delta K$ . In addition, some crack propagation data was available for Zeron 100 and other superduplex stainless steels at this R-ratio [26, 102, 98]. A sinusoidal waveform was employed for all tests, because as mentioned in the literature review, it is known to be the most severe for corrosion fatigue type tests.

Since a range of frequencies up to 50Hz are widely known to have little effect on crack propagation rates in laboratory air for given loading conditions, relatively high frequencies were preferred to speed up testing time. In corrosion fatigue tests, loading frequency is a major variable and frequencies as close to those encountered in reality (wind/wave loading) are essential. Initial  $\Delta K$  increasing tests in air were carried out at 5 Hz so that the frequency difference between environmental tests carried out at 0.1Hz was minimal and yet the test duration was relatively short at 9.6 hours. However, precracking time was significant at 10 hours. Therefore, total test time for each sample was in the region of 20 hours. Tests on the base and two weld metals started around 20 MPa $\sqrt{m}$  and terminated at the point of fast fracture. Information for all crack propagation tests carried out is listed in table 3.6.

Test	Test type	Sample type	Environment	Loading frequency	$\Delta K$ range considered	Sample tested			Test time
						Base	SMA	GTA	
				(Hz)	(MPa√m)				(hours)
A	$\Delta K$ inc'g	SENB4	air	5	20 → fracture	*	*	*	20 x3
B	$\Delta K$ inc'g	CCT	air	25	1 → 20			* x2	64 x2
C	$\Delta K$ dec'g	SENB4 <sup>1</sup>	air	10	20 → crack arrest	*	*	*	60 x3
D	$\Delta K$ inc'g	SENB4 <sup>2</sup>	Air/sea -1040mV SCE	25 in air/0.1 in seawater	1 → onset of EAC	*	*	*	225 x3
E	$\Delta K$ inc'g	SENB4	Sea -1040mV SCE	0.1	20 → fracture	*	*	*	100 x3
F	$\Delta K$ inc'g	SENB4	Sea -1040mV SCE	0.02	18 → 24	*			673
G	$\Delta K$ inc'g	SENB4	Sea +600 → 1040 mV SCE	0.1	20 → fracture	*	*		247 x2
H	$\Delta K$ dec'g	SENB4	Sea -1040mV SCE	0.1	20 → crack arrest	*		*	512 x2

Notes on table:

- Specimens in tests B and D were precracked using the cyclic compression technique. All other specimens were precracked using the traditional load shedding technique.
- With regard to test G, oxygen was bubbled into the seawater to ensure that a supply of oxygen was not the limiting factor on the dissolution mechanism.
- A  $\Delta K$  increasing test was carried out on CCT samples (figure 3.17) in order to assess the influence of residual stress fields on crack propagation rates.

**Table 3.6 Summary of crack propagation tests carried out in the current research.**

The precracking procedure in synthetic seawater was identical to the previously described test procedures in laboratory air. However, the constant amplitude load tests were conducted in an environmental chamber with environment controlling

<sup>1</sup> A  $\Delta K$  increasing test was subsequently performed on GTA sample.

<sup>2</sup> The base and SMA samples were periodically subjected to synthetic seawater (-1040mV SCE) at 0.1Hz to investigate if the EAC thresholds obtained from the  $\Delta K$  decreasing tests in synthetic seawater were conservative. The synthetic seawater in these tests consisted only of 3.5% NaCl to eliminate calcareous deposit formation which may have resulted in non-conservative EAC thresholds.



accessories fitted around the sample crack growth region as described in section 3.3.2. This meant that the sample had to be removed periodically from the test chamber in order to record crack length. A full 1 mm of crack growth was allowed under full test conditions after precracking before data was recorded to ensure non steady state or transient effects were minimised.

Free corrosion potential or tests without the aid of a potentiostat were not carried out as under these conditions the ECP of the alloy is typically somewhere between the cathodic ECP and anodic ECP considered in the current research. The 'limits' considered in the current research are the worst-case scenario and therefore data at free ECP was of secondary concern.

### ***3.3.5 Fracture surface analysis***

Striation measurement was carried out on the fracture surfaces of samples tested in laboratory air and in seawater under cathodic overprotection using a scanning electron microscope (SEM). For samples tested in synthetic seawater, a combination of nitric and hydrochloric acid was used to dissolve the calcareous deposits formed on the fracture surfaces.

Seven to eighteen ductile striations measurements were made at four  $\Delta K$  values between  $\Delta K = 23$  to  $46 \text{ MPa}\sqrt{\text{m}}$  on the base, GTA and SMA samples in laboratory air but only on the base metal and GTA samples in seawater. With regard to brittle striations, ten to twenty measurements were made at six  $\Delta K$  from  $\Delta K = 21$  to  $52 \text{ MPa}\sqrt{\text{m}}$  on the base and GTA weld metal. Eleven to fourteen measurements were carried out at three  $\Delta K$  values on the base metal sample tested in seawater ( $-1040 \text{ mV SCE}$ ) at  $0.02 \text{ Hz}$ .

With regard to samples tested in synthetic seawater at  $-1040 \text{ mV SCE}$ , the percentage of area cleaved was also determined. This was done using image analysis software to determine the percentage area cleaved on a micrograph digitally captured on the SEM at a magnification of between 100 to 600. Six base metal, fifteen GTA, and sixteen SMA images were assessed at  $\Delta K$  ranging from  $21 \text{ MPa}\sqrt{\text{m}}$  to  $53 \text{ MPa}\sqrt{\text{m}}$ .

## **4. RESULTS & DISCUSSION**

Chapter four comprises four sections, which correspond to the sections outlined in the previous chapter concerning experimental work. First of all, the results of the basic integrity tests on the weld metals are presented. These results are assessed and discussed with reference to results for the base metal and results available in the literature. This preliminary work is followed by results concerning the characterisation of both weld metals in terms of metallurgy, corrosion resistance and residual stress levels prevalent and their possible influence on the rate of crack propagation.

The third section is the main focal point of the project, as it concerns the corrosion fatigue crack propagation tests. Here, the results of the crack propagation tests carried out in laboratory air and in seawater under cathodic overprotection are presented. Subsequently, a comprehensive discussion of these results is divided into two sections relating to tests carried out in laboratory air and tests carried out in seawater.

The fourth section investigates the fracture mechanisms responsible for the crack propagation data produced under the different testing conditions. Here, microscopic features on the fracture surface are used to explain the variation in macroscopic crack growth rates under different testing conditions. Finally, a model based on the experimental data, capable of predicting the fatigue life of the weld metals is presented. In addition, a new mechanistic model for subcritical brittle crack growth is proposed.

### **4.1 Weldment Fabrication and Basic Integrity Assessment**

The objective of this section is to assess the performance of the weld metals in fundamental mechanical tests such as tensile and impact tests. In this way, any major flaws in the weld metals will be identified early before subsequent thorough microstructural characterisation is performed.

#### 4.1.1 Weldment fabrication

It was noted that each of the three plates exhibited a degree of angular misalignment. This was attributed to both the single V geometry of the weldments, and the inexperience of the fabrication shop in welding superduplex stainless steels.

The maximum angular misalignment was found in the GTA root, SMA fill weldment. The average misalignment angles are given in table 4.1.

Weldment	Misalignment Angle ( $^{\circ}$ )
GTA root & fill a	5.5
GTA root & fill b	2
GTA root, SMA fill	6.5

Table 4.1 Angular misalignment in weldments.

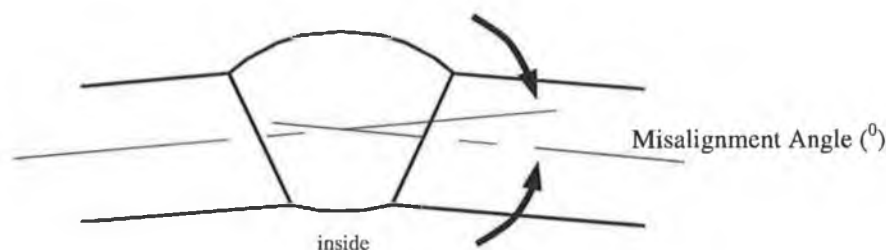


Figure 4.1 Angular misalignment in weldments.

The 300 series stainless steels, duplex and superduplex stainless steels tend to show greater angular and lateral distortion than carbon-manganese steels, because of the higher coefficient of thermal expansion associated with austenite. Superduplex stainless steels have a coefficient of expansion intermediate to that of carbon manganese steel and of austenitic stainless steels.

It is known that butt joints subjected to bending are not sensitive to angular misalignment [19]. This fact is accounted for in BS 7910 [114] (which defines quality categories for weldments depending on the type and severity of weld flaw), where an angular misalignment stress magnification factor is only applied, when an axial load

is present. Therefore, the weldments in the current project can be used to gather conservative crack propagation data provided that the mode of loading is bending. However, account is taken of the effect of angular misalignment where possible.

In hindsight, a double V butt weld, where alternate weld passes each side of the joint would have had a balancing effect minimising distortion, may have been more appropriate.

### 4.1.2 Tensile strength

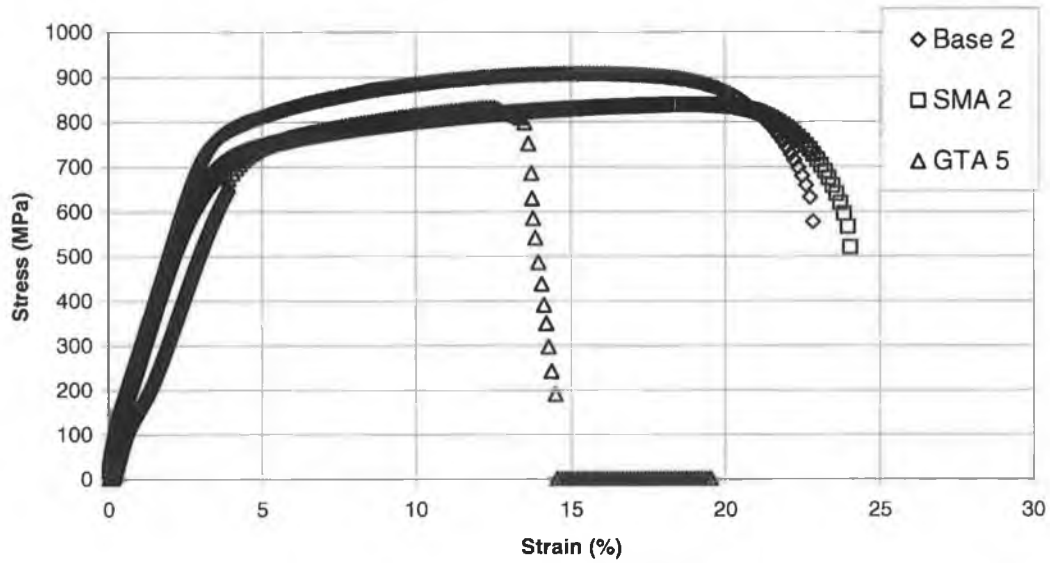


Figure 4.2 Worst case strength for cross weld tensile samples

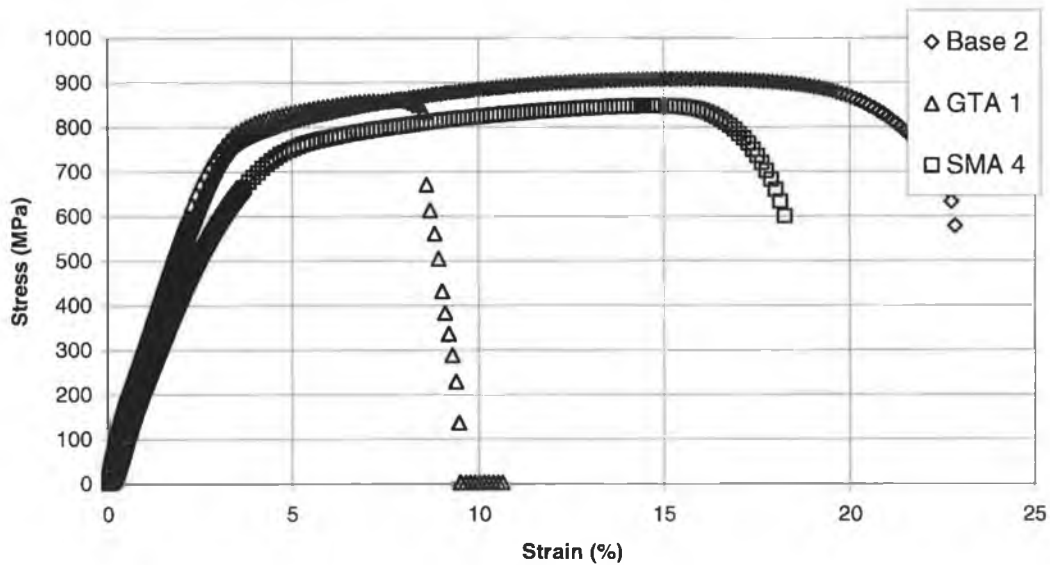


Figure 4.3 Worst-case ductility for cross weld tensile samples.

As can be seen in figure 4.2, yield and tensile strengths were well above the design limits (550MPa and 750MPa respectively) for Zeron 100 base metal, even for the worst-case weld samples. Five weldments were tested in each case (table 4.2).

Minimum values were 698 MPa and 853 MPa for yield and tensile strength respectively. The GTA root SMA fill cross weld samples all failed in the base metal showing the good integrity of the weld metal. The lowest ductility of these samples was 18% (table 4.2). The fully GTA cross weld specimens all failed through the centre of the weld metal and exhibited the lowest ductility. The minimum ductility was 10%. A fully base metal sample showed a ductility value of 27%. This compares favourably with the design value (25%) for Zeron 100 base metal.

Table 4.2 lists the data acquired from the tensile tests carried out. In addition, the percentage scatter is shown.

<b>Sample</b>	<b>Yield strength (MPa)</b>	<b>Ultimate tensile strength (MPa)</b>	<b>Elongation (%)</b>
Base 1	787	868	--
Base 2	739	898	27
GTA 1	770	853	10
GTA 2	737	898	27
GTA 3	757	838	11
GTA 4	748	894	16
GTA 5	699	841	15
SMA 1	713	881	24
SMA 2	710	838	24
SMA 3	698	892	32
SMA 4	721	847	18
SMA 5	717	916	30
<b>Average</b>	<b>733</b>	<b>872</b>	<b>21</b>
<b>% scatter</b>	<b>7</b>	<b>5</b>	<b>52</b>

**Table 4.2. Tensile test results including percentage scatter.**

These results are in agreement with the literature, where it is seen that yield and tensile strengths of superduplex weld metals are always greater or equal to base metal design values [28, 29, 31,45, 51], but ductility may be reduced [29]. In addition, it has been stated in the literature that ductility decreases with a decrease in austenite content [127]. As will be seen in section 4.2.4 the GTA weld metal showed slightly lower austenite content than the base metal whereas the SMA weld metal showed slightly higher austenite content than the base metal. This may be the main reason why the fully GTA welds failed in the weld metal. In addition, the degree of angular

misalignment present in the weldments may have influenced the location of failure. The effect of misalignment on the tensile test results was not quantified, as the main purpose of the tensile tests was to ensure the weldments exhibited integrity similar to the base metal.

Other factors may have also influenced ductility. Strain hardening present in the weld metal discussed in section 4.1.4 is probably the main reason for the low ductility values obtained in the GTA weld metal.



### 4.1.3 Toughness

Results for the Charpy impact tests are listed in the table below with the average values in bold. The maximum percentage scatter in the base metal was 25%. This relatively high scatter is due to the fact that both TL and LT type samples were tested (figure 3.5). Two samples were tested for the GTA weld metal and four for the SMA weld metal.

<b>Base metal</b>	<b>GTA weld metal</b>	<b>SMA weld metal</b>
Joules	Joules	Joules
203 (LT)	60	44
170 (LT)	78	51
193 (LT)		45
170 (LT)		47
198 (LT)		
129 (TL)		
142 (TL)		
<b>Average</b>	<b>172</b>	<b>69</b>
<b>Max % scatter</b>	<b>25</b>	<b>8.5</b>

**Table 4.3 Charpy V Notch experimental values, average values in bold.**

Comparing the average experimental values to the design values in figure 4.4, it appears that the experimental GTA value (69J) is some 14% below the design value (80J) at  $-40^{\circ}\text{C}$ . Further, the experimental base metal value (172 J) is 41% below the design value (290J). However, the design values quoted by WMF are not conservative when compared to data available in the literature. Values of 69J (GTA) and 36J (SMA) have been found for the weld metal of a superduplex stainless steel UR 52N+ [32]. Further, impact tests carried out on base Zeron 100 yielded values of between 150 and 250 Joules in the TL and LT orientations respectively [28].

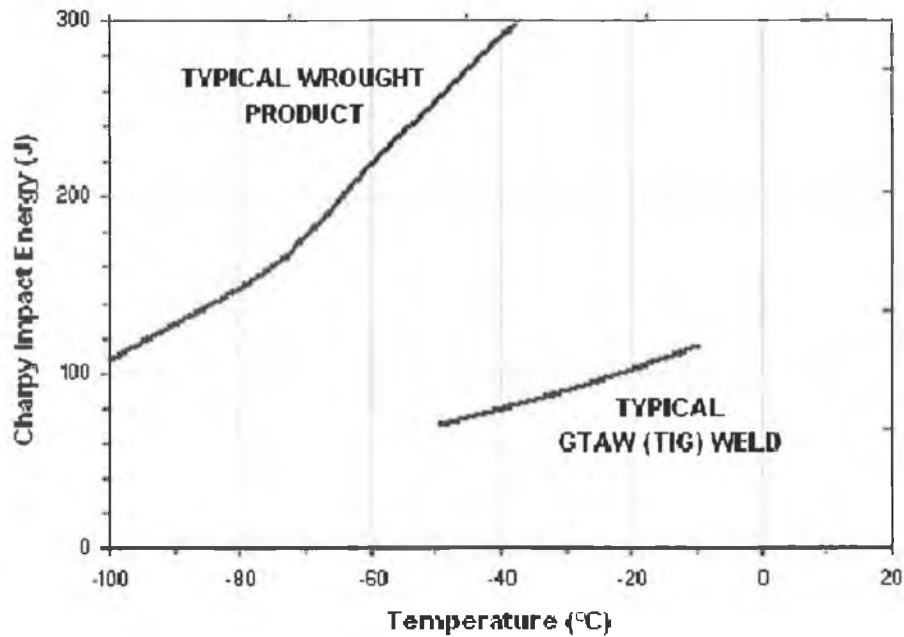


Figure 4.4 WMF Charpy impact toughness design values [112].

With regard to a threshold impact level required for service, a particular researcher considering substantial amounts of data stated that an impact value of 27J is necessary at  $-40^{\circ}\text{C}$  for superduplex stainless steels [30]. However, as mentioned previously, the NORSOK acceptance criteria for wrought superduplex base metal operating offshore requires a charpy impact value of 45J at  $-46^{\circ}\text{C}$  [12]. Values for weld metal also need to be above this value. With these values in mind, it can be seen that the base and weld metals performed adequately in the impact tests and are fit for purpose.

#### 4.1.4 Hardness

The average hardness value obtained for the base metal was  $26.5 \pm 0.6$  HRC, which is slightly below the design value given by WMF (28 HRCmax) for wrought Zeron 100 [112] and the limit proposed by NACE (NACE MR0175) (28-34HRC) and NORSOK (28HRC) [12].

Figures 4.5 and 4.6 show the microhardness results for the base, GTA and SMA HAZ and weld metals.

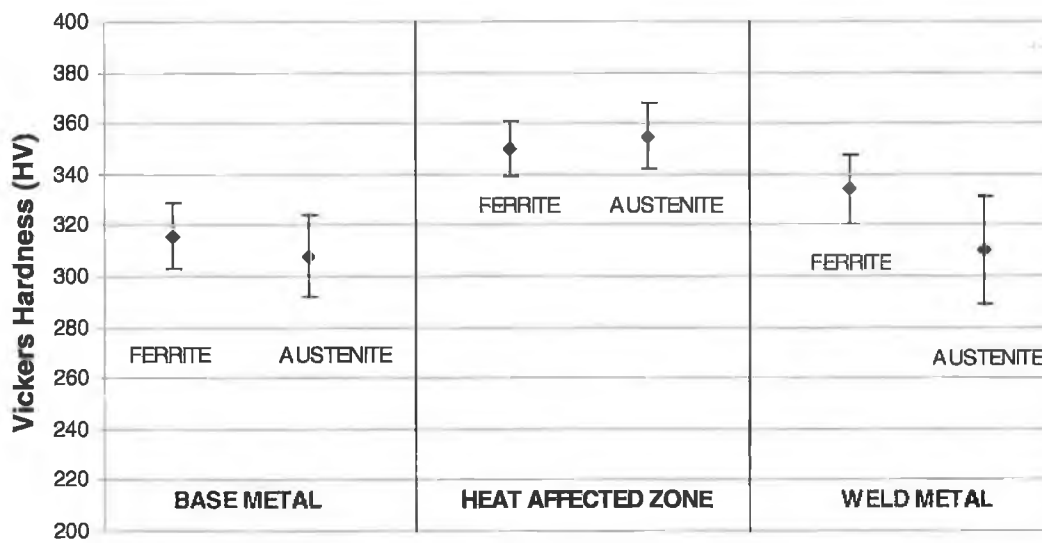


Figure 4.5 GTA microhardness and 95% confidence interval.

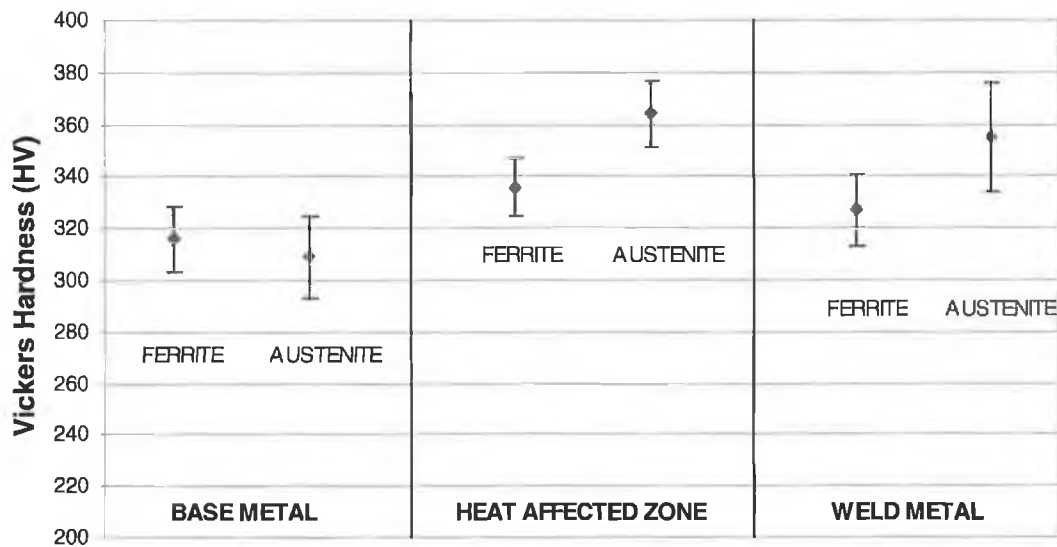


Figure 4.6 SMA microhardness and 95% confidence interval.

The highest hardness value found in the weldments was 350 HV (average of austenite and ferrite in HAZ of SMA weld metal). To convert to HRC the following conversion has been proposed for duplex stainless steels weldments [cited in 12].

$$\text{HRC} = 0.091 \text{ HV} - 2.4 \quad 4.1$$

Therefore, the highest hardness value in the weldments is 29 HRC. This value is still below the limit proposed by NACE for base and weld metal but is 4% greater than the more stringent NORSOK requirements (28HRC) for base metal operating offshore.

Microhardness results are of critical importance with regard to crack propagation. Depending on the relative hardness of each phase, a crack may propagate preferentially through one particular phase, perhaps following the grain boundary of the harder phase. If the phases are of similar hardness, a crack may propagate through both phases.

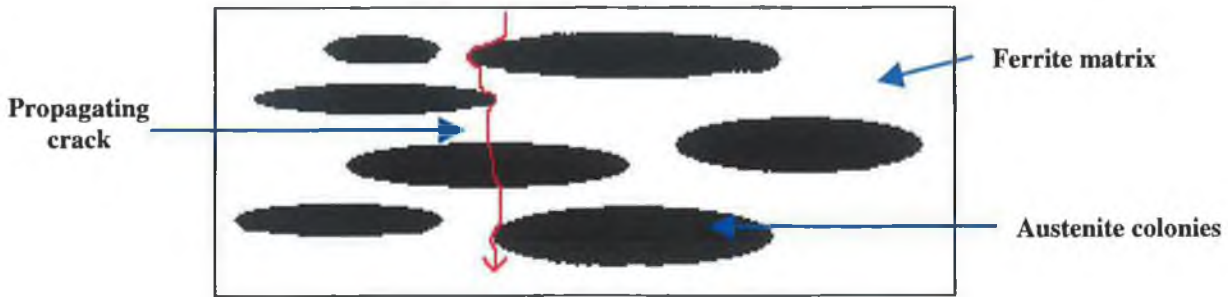


**Figure 4.7 Interaction of propagating crack with phases of different hardness.**

With regard to the base metal, it was noted that the phases have similar hardness levels. This result is in agreement with commercial austenitic and ferritic alloys where similar hardness levels are observed (table 2.1). The similar hardness levels of the phases in Zeron 100 base metal are thought to be due to two reasons. First, the base metal undergoes thermomechanical treatment in a controlled factory environment, which allows a balance of alloying elements to be obtained between ferrite and austenite. Secondly, annealing reduces any work hardening of the phases caused by the mechanical rolling process.

In figures 4.5 & 4.6, it can be seen that the SMA and GTA weld metals exhibited higher hardness averages relative to the base metal. The HAZ regions were also noted to be harder than the weld metal regions. The main reason for the higher hardness of the weld metal relative to the base metal is strain hardening induced as a result of the welding process [54] as discussed in the literature review (section 2.2.3).

Differences evident in relative phase hardness are thought to be due to either of two reasons. As just mentioned, strain hardening is a major factor. It appears possible that one phase may strain harden by a greater amount relative to the other phase. Secondly, the weld thermal cycle or more precisely the cooling rate (which is a function of the heat input/weld speed used) is known to control the diffusion rates of interstitials such as nitrogen. It is possible that the SMA weld cooled slower than the GTA weld allowing a high percentage of nitrogen to preferentially diffuse to the austenite.

With regard to the GTA weld metal, similar hardness values of the ferrite and austenite can be seen in the HAZ region, which is also the case in the base metal. Therefore, the HAZ was not affected by the weld thermal cycle. It is thought that the weld region experienced a faster cooling rate than the HAZ with the ferrite noted to be harder than the austenite by 7 to 8%. Preferential solid solution hardening by nitrogen in the austenite didn't occur due to the relatively fast cooling rate. However, the ferrite may have strain hardened to a greater extent than the austenite.

The SMA weld region is thought to have experienced a slower cooling rate than the GTA weldment. Therefore, preferential interstitial solid solution hardening by nitrogen in the austenite occurred. It is noted that in the SMA HAZ and weld metal the austenite is 7-8% harder than the ferrite.

In a study on welded joints of the superduplex stainless steels (UNS S32760) using the GTA root and SMA fill welding process [33], hardness was similar in the root, fill and weld cap averaging at 305HV. The weld metal was about 33HV harder than the base metal. These observations agree with the current research. In another study, hardness values did not have large variation between the SMA weld deposit (285 HV) and the Duplok A4 base material [128].

Overall it is clear from the current research that the difference in hardness between the austenite and ferrite phases in the base metal (2%) should not have a significant effect on crack path. However, the difference in phase hardness in the weld metal regions is approximately 8%. Therefore, the path of crack propagation may be influenced by relative phase hardness in the weld metal.

#### 4.1.5 Non destructive tests (NDT)

Engineering critical assessment of weld flaws is performed to define acceptable, harmless flaws in a structure that will not sacrifice weldment reliability. "Fitness for purpose" is a rationale for considering whether an imperfections presence is acceptable provided its presence does not reduce the fatigue life of the joint below that required for service. It seeks a balance among quality, reliability and economy of welding procedure.

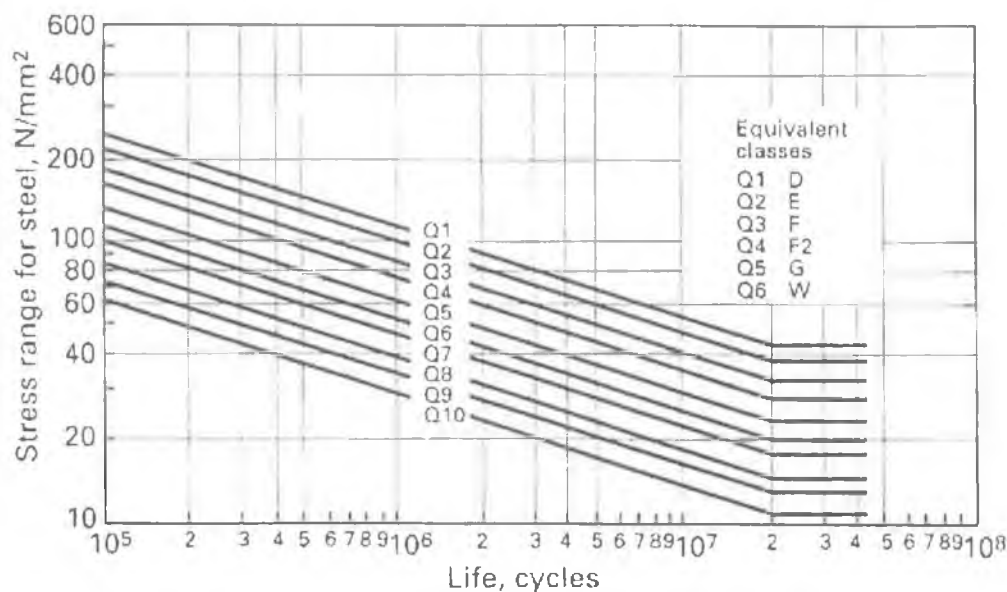


**Figure 4.8 S-N quality curves for steel weldments [19]. To qualify in a category, the type and severity of weld flaw must be assessed. Q1 is the highest quality category.**

In decreasing order of harmfulness, weld flaws may be classified as crack/crack-like, geometric (weld toe undercut between weld metal and base metal on weldment surface), lack of fusion/lack of penetration, inclusions and porosity [129].

#### Dye Penetrant

Surface planar (crack-like) or non-planar flaws were not found using the dye penetrant method. Of particular concern was the presence of crack like defects in the weld metal. A maximum undercut depth of only 0.25mm is allowed for the most stringent quality category (Q1) for a 10mm butt weld according to BS 7910 [114]. In industry, such flaws are removed by grinding, since a planar flaw is a good site for

crack initiation and/or crevice corrosion. However, grinding of the base metal or weld region was not required in the current work.

### Radiographic Technique

Isolated gas pores and a tungsten inclusion were present in the GTA root and fill weldments using the radiographic technique. Just isolated gas pores were detected in the GTA root SMA fill weldments. The percentage area of weld metal on the radiograph taken up by porosity was visually determined to be much less than the 3% maximum limit prescribed by BS7910 [114] for a top quality (Q1) butt weld.

Further information was acquired on flaws present in the weld metal including inclusions and is presented later in the section on defect assessment (section 4.2.2). Here, a scanning electron microscope is used to examine the fracture surfaces of weld metal. The weld metals in the current research appear to be of the highest quality (category Q1) with regard to the presence of weld flaws, determined by dye penetrant and radiographic tests. However, further analysis is required to determine if flaws such as lack of fusion and lack of penetration exist in the weldments

Overall, the basic mechanical properties of the weld metals can be summarised as follows:

	Base metal	GTA weld metal	SMA weld metal
Misalignment ( <sup>0</sup> )	N/A	5.5	6.5
Misalignment Assessment (BS 7910)	N/A	Q1* in bending	Q1 in bending
Yield/UTS (MPa)	750/910	700/825	700/830
Ductility (%)	23	9	18
Toughness (Joules)	172	69	47
Average Hardness (HV)	315 $\alpha$ /310 $\gamma$	335 $\alpha$ /310 $\gamma$	328 $\alpha$ /355 $\gamma$

**Table 4.4 Summary of base and weld metal mechanical properties.**

---

\* Q1 is the highest quality category for butt welds.



## **4.2 Microstructural and Corrosion Assessment of Weld metal**

This section concerns the characterisation of both weld metals in terms of structure, composition, local stresses prevalent and corrosion resistance. This analysis is necessary as corrosion fatigue crack propagation behaviour may depend on a number of factors. These factors are now briefly introduced.

Firstly, from a mechanical viewpoint, both the macrostructure and microstructure need to be characterised as crack propagation resistance may depend on one or both of these elements. Of major concern is the presence of residual stresses, which may influence the rate of crack propagation locally and lead to non-conservative crack propagation rates and thus mask the intrinsic microstructural resistance to crack propagation. Assessment of flaws present in the weld metals is also critical so that the possibility of crack initiation can be assessed. Finally, the presence of inclusions must be investigated, as inclusions are known to influence the onset of fast fracture whereas the presence of appreciable intermetallic content may lead to a loss in ductility.

Secondly, the relative proportions of ferrite and austenite their distribution and alloying content may affect corrosion resistance and mechanical properties. In addition, it has been discussed in the literature review that austenite content is critical with regard to hydrogen embrittlement resistance. The presence of appreciable inclusions and intermetallics may also affect corrosion resistance as they leach corrosion-resisting alloying elements from neighbouring regions. Subsequent to microstructural characterisation, corrosion resistance is assessed for both weld metals over a range of ECP's in seawater.

#### 4.2.1 Microstructural examination

From observation of a macro transverse sample (figure 4.9) of each weldment it was possible to determine the number of weld passes required to complete each weldment. Also, evident is the fact that the weld beads are approximately 3 mm thick. Beads 3-3.5 mm thick (GTA welding) are recommended in WMF welding guidelines [111].

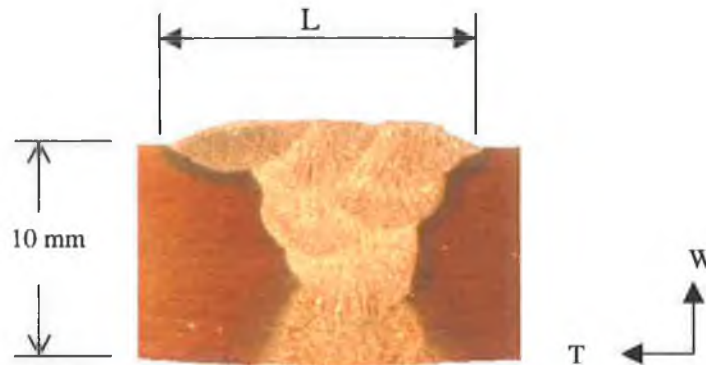


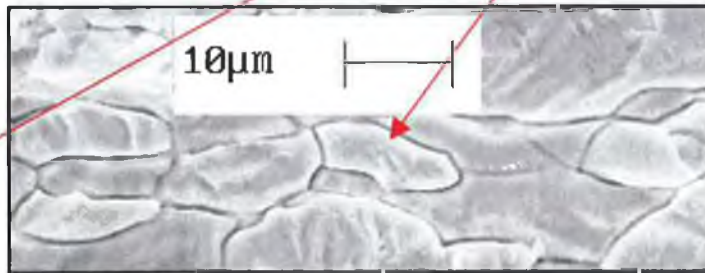
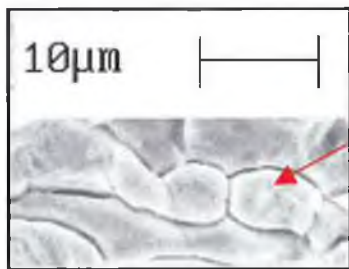
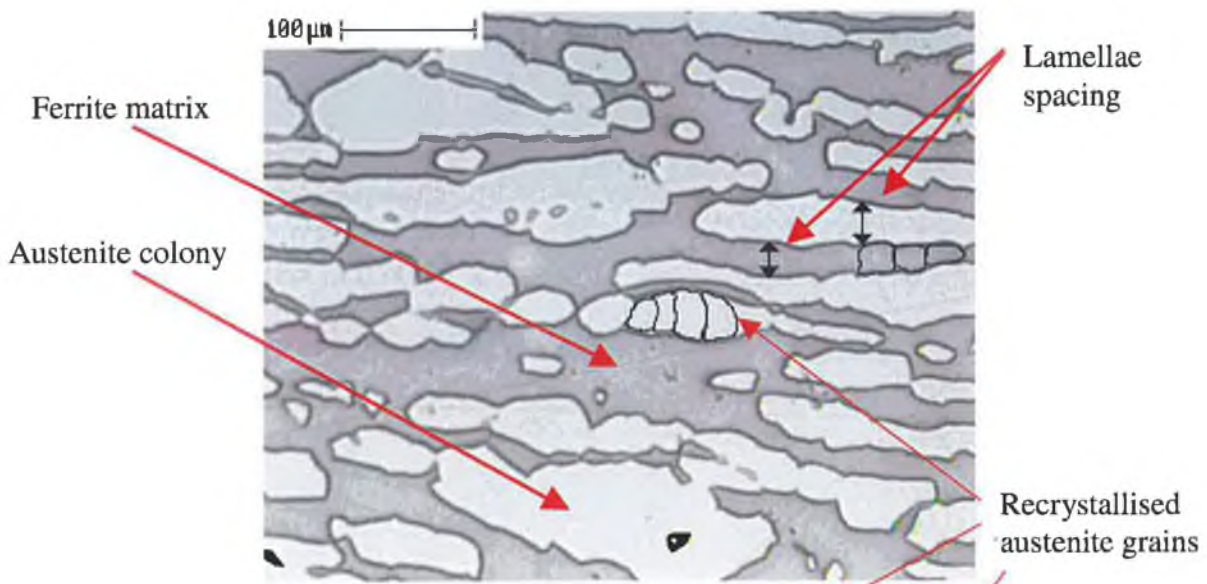
**Figure 4.9 Macrograph of SMA weld metal etched using 20% NaOH. Attachment length 'L' also shown.**

As can be seen in table 4.5 below, completion of both welds required a similar number of passes.

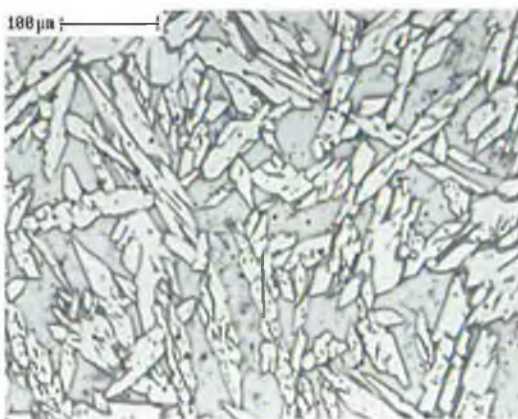
Weldment	Number of Passes
GTA (a)	1 root / 8 fill
GTA root / SMA fill	1 root / 9 fill

**Table 4.5 Number of passes required to complete weldments.**

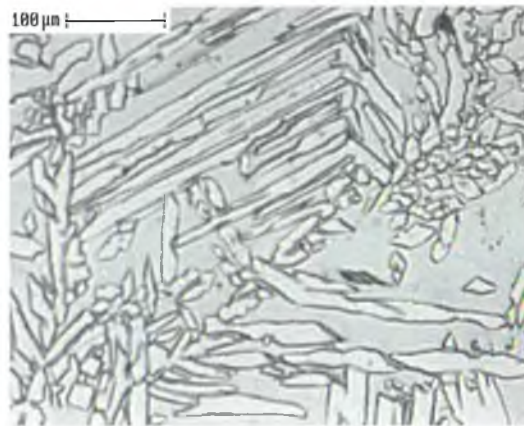
Further observation of the transverse weldmetal samples at a magnification of 500 and 1000 revealed that the microstructures of the base and GTA root and fill welds were very clean, with no evidence of inclusions or slag entrapment. However, the GTA root SMA fill weld exhibited a significant inclusion content, which was easily visible at a magnification of 1000.



**BASE METAL**



**SMA**



**GTA**

**Figure 4.10 Micrographs of base, GTA and SMA weld metals.**

From the micrographs above, it is possible to approximate the size of the austenite colonies prevalent in the base and weld metals. In the base metal the aligned austenite colonies average about 100 by 25 microns on the TW plane. The weld metals exhibit randomly orientated austenite colonies approximately 100 by 15 microns. The austenite colonies consist of several austenite grains (figure 4.10). In fact both the ferrite and the austenite are comprised of recrystallised grains and, in most cases, the ferrite and austenite lamellae spacing may be considered to a good approximation as the grain size [43]. Therefore, from the above micrographs (considering the thinner lamellae) the approximate grain sizes are:

	Ferrite ( $\mu\text{m}$ )	Austenite ( $\mu\text{m}$ )
Base metal	5	5
GTA weld metal	Not determinable	5
SMA weld metal	Not determinable	5

**Table 4.6 Grain size in base and weld metals.**

It is also important to note that a specific macrostructure was also present in the weld metals in addition to the microstructure discussed above. The macrostructure was dominated by the primary ferrite grains, which solidified first during cooling from molten metal. Although an etched sample of this structure was not obtained in the current research, the macrostructure and its formation can be appreciated in figure 4.11 [12].

However, evidence of the macrostructure was prevalent on the fracture surfaces resulting from corrosion fatigue crack propagation tests where hydrogen embrittlement took place. This will be discussed in more detail later, but suffice to say here that a proportion of the primary ferritic grains were embrittled. The embrittled grains were easily identified on the fracture surfaces and approximate dimensions were obtained.

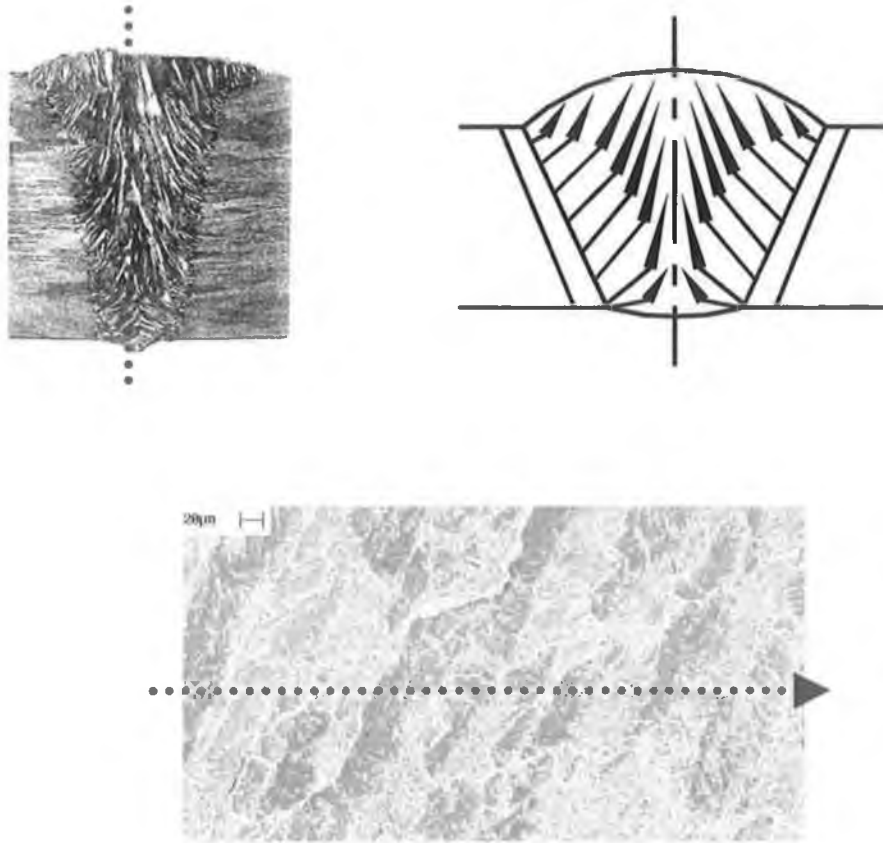


**Figure 4.11 Top left is the superstructure of weld metal [12] and schematic of primary ferrite grain growth (top right). Lower figure shows direction of welding and embrittled primary ferrite grains.**

The columns of primary ferrite varied in size, the smallest columns being at the root pass. With regard to the centre of the weld metal, column width was approximately 30 microns (also see figure 4.41). The length of the columns was difficult to approximate but appears to be in the range 0.1mm to 2 mm for the weld metals considered. In addition, it is interesting to note that the primary ferrite grains were not perpendicular to the crack growth direction (red arrow). They were angled at about  $65^{\circ}$  to the crack growth direction, which is the same direction that the welding torch was moving during welding. As such, the primary ferrite grains solidified in the direction of the thermal gradient. The angle was very similar in the GTA weld metal, suggesting that both welding processes were carried out at similar welding speeds.

## 4.2.2 SEM and image analysis

### Flaw Assessment

Although not evident on the etched samples, welding flaws were noted on micrographs of weld metal fracture surfaces (figures 4.12 - 4.15). It was decided to analyse the flaws present to supplement the information gathered by the non-destructive tests carried out earlier. It is important to note that the planar flaws depicted are parallel to the applied load direction (perpendicular to the fracture surface). Therefore, it is unlikely that cracks would initiate from these flaws and propagate to failure. However, they are indicative of the flaws possibly present in the current weldments.

First, with regard to the GTA weld metal, it is clear from the fractograph below that both inclusions and porosity were prevalent in the weld metal. This observation is in agreement with the radiographic results presented earlier. The inclusion is tungsten as determined from the radiographic tests and is non-planar approximately 50 $\mu\text{m}$  in diameter. Of more concern is the gas pore, which appears planar and is just over 400 $\mu\text{m}$  in length.

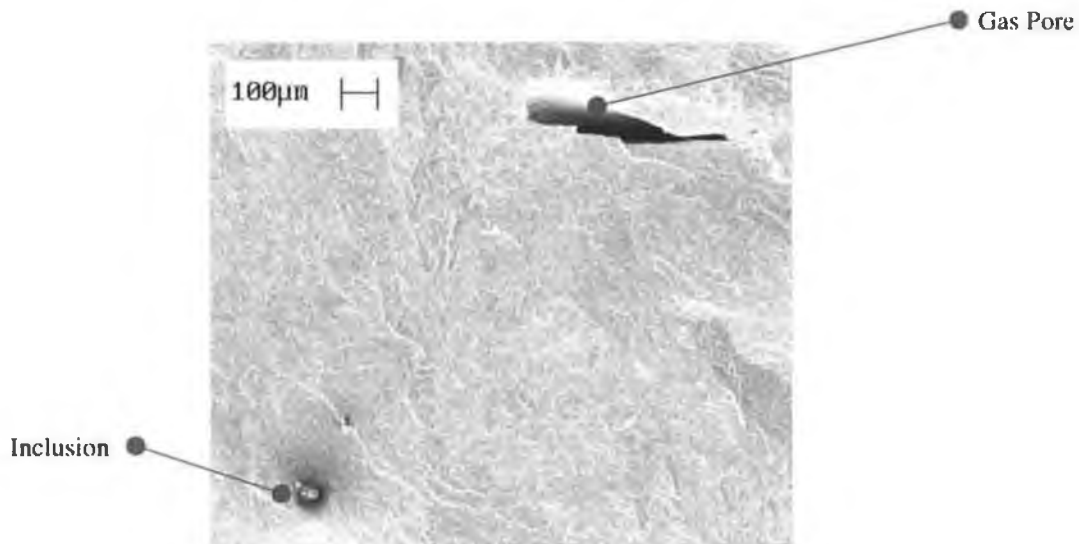
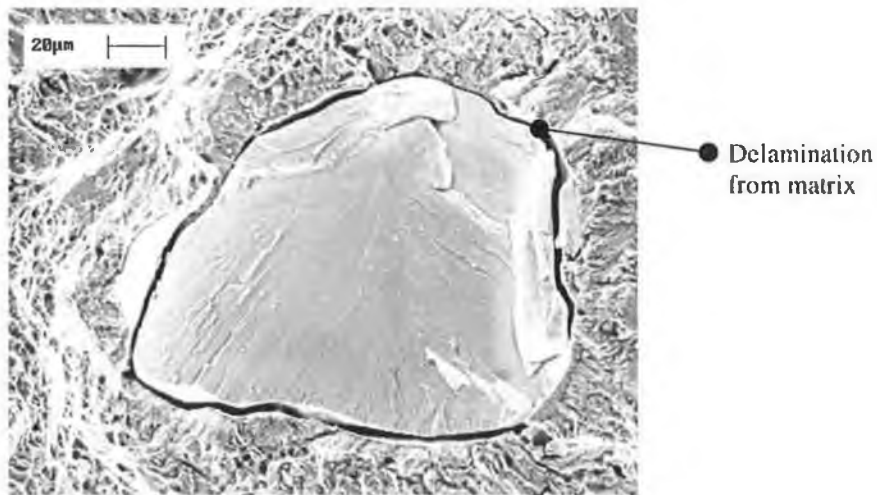


Figure 4.12 GTA fracture surface.

Evidence of welding defects was also found on the fracture surface of the GTA root, SMA fill weld metal. These flaws consisted of inclusions and slag entrapment. Slag entrapment is a typical consequence of the flux shielded SMA welding method. This welding flaw was not evident on the radiographs presented earlier. In addition, porosity and lack of fusion between the GTA root pass and the SMA weld metal were found.



**Figure 4.13 SMA fracture surface**



**Figure 4.14 Fractured brittle inclusion.**

It is quite normal for weld metal to contain flaws such as those described above. In addition, it is important to note that only a small number of instances of the typical

defects mentioned above (inclusions, porosity, slag entrapment) were found in the weld metals.

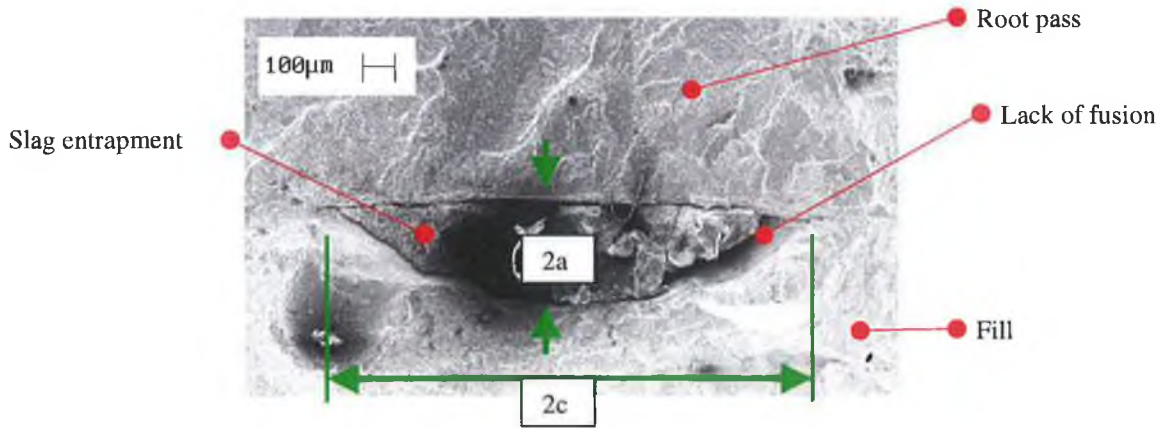


**Figure 4.15 Lack of fusion between GTA root pass and SMA weld metal**

Figure 4.15 shows a lack of fusion flaw between the GTA root pass and the SMA fill due to the presence of slag. This flaw was found by systematically scanning the fracture surfaces of both types of weld metal. It was identified as the most deleterious flaw present. The flaw was assumed to be planar in the plane of the fracture surface and as such crack-like. This was a worst case scenario. At  $2c = 1.5\text{mm}$  and  $2a = 0.3\text{mm}$ , it is clear that such a flaw could lead to premature crack initiation in the weldment in the absence of other more deleterious flaws. A conservative approach to assessing the severity of the flaw was to consider the flaw as a planar defect and analyse it using a technique for assessing weld flaw severity in BS 7910 [114]. It was determined that for  $2c = 1.5\text{mm}$ ,  $2a$  could be up to  $1\text{mm}$  for a category Q1 butt weld. Therefore, the flaw does not compromise weldment quality.

A macro flaw was detected on the fracture surface of the fully GTA centre cracked tension sample. The CCT samples were fabricated from weldment (b) whereas the flaws analysed up to this point were all present in samples from GTA weldment (a). The flaw in question was considered more deleterious compared to any of the flaws found up to this point. The flaw was located at the interface between the root pass and the filler metal. It was practically continuous in length, with  $2a = 0.5\text{mm}$ , running parallel to the welding direction.



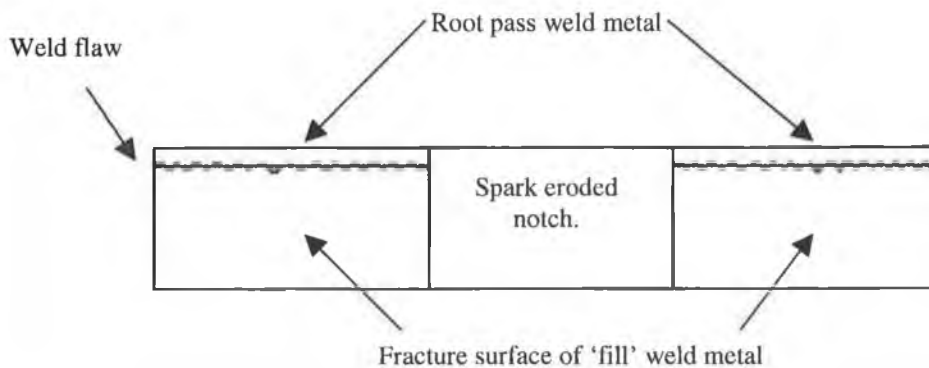


**Figure 4.16 Schematic of flaw on fracture surface of CCT GTA weld metal sample.**

Two possibilities were considered. The first was that the flaw was slag inclusion, non planar in nature. Continuous slag inclusion would reduce the quality category of the fully GTA weldments significantly from category Q1 to Q5. However, since flux is not utilised in the GTA welding procedure, slag should not be present. The second and more conservative option was to consider the flaw as a planar defect and analyse it using methods presented in BS 7910 [114] as carried out previously. It was determined that an embedded planar flaw of practically continuous length was allowed in a 10mm thick category Q1 butt weld provided its width was less than 2.5mm. Therefore, the weldment was fit for purpose in the highest quality category, Q1.

With regard to the occurrence of such a flaw in the GTA weldment, it is thought that it may have been difficult for the molten weld metal to penetrate into the acute angle of the V weld. In addition, the time lapse between filling the weldment and forming the root from the other side may have been an influencing factor.

Despite these typical weld flaws, both weld metals had sufficient integrity to perform well in the tensile and impact tests. However, the investigation is revealing as to the size and type of defects present in a particular weld metal type. Further, it is clear that the likelihood of crack initiation is greater in the weld metals than in the base metal where such 'large' flaws were not found.

**4.2.3 Intermetallic and inclusion content**

Small amounts of the intermetallic sigma phase (gold colour) were observed on the micrographs taken using an optical microscope but were not quantified. The micrographs were compared to micrographs of high quality weld metals fabricated by WMF’s own proficient welders. The weld metals were observed to be similar, with no deleterious points prominent. Table 4.7 below shows results obtained for the intermetallic content in the two weld metals from images obtained using back-scattered electrons on the SEM.

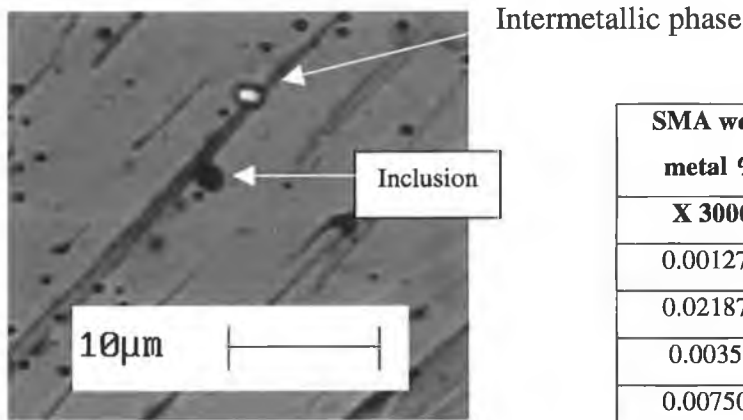


**Figure 4.17 Intermettalic at ferrite/austenite grain boundary in SMA weld metal.**

SMA weld metal %	GTA weld metal %
<b>X 3000</b>	<b>X 3000</b>
0.001272	0.006994
0.021871	0.005722
0.00356	0.006739
0.007503	
0.025177	

**Table 4.7 Intermetallic contents in weld metals**

Even though illuminated spots (figure 4.17) which correspond to intermetallic phases were located after scanning systematically around both weld metals, the intermetallic content was negligible. Highest estimates using the image analysis software were in the region of 0.03%. Intermetallics are extremely hard and brittle phases, which typically precipitate in high alloy, weld metal when the cooling rate is too slow during welding. They have the ability to either fracture or disbond from the surrounding ferrite and austenite, act as local stress raisers and encourage cleavage through the ferrite phase [50]. Further, precipitation can reduce corrosion resistance and toughness significantly [110]. The lack of appreciable intermetallic content in the current weld metals indicates that the weldments were fabricated using appropriate welding procedure. In addition, mechanical and corrosion properties will not be compromised by brittle behaviour, or preferential corrosion at intermetallic sites.

In contrast to intermetallics, inclusions occur when oxygen reacts with elements in the weld metal. Advanced gas shielded welding processes (GTA) can typically deny oxygen to the weld metal, but flux shielded methods (SMA) allow trace concentrations which give rise to inclusions. The inclusion content was on average 0.3% in the SMA weld metal (table 4.8). This figure may appear quite low, but in comparison to the base and GTA weld metal which have practically zero inclusion content, it is a significant quantity. All inclusions observed were spherical in nature. Inclusions typically have a major role to play in the early onset of microvoid coalescence (MVC) and can determine the size and form of dimples on a fracture surface [130].

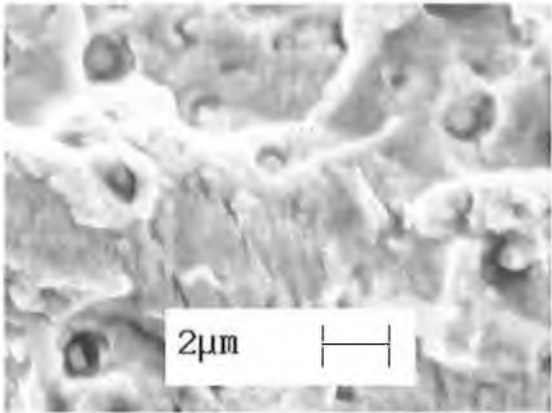


**Figure 4.18 Inclusions on SMA weld metal fracture surface.**

SMA weld metal %
X2000
0.2013
0.2554
0.2730
0.3712

**Table 4.8 Inclusion content in SMA weld metal.**

Figure 4.19 shows a spectral analysis for an inclusion found on the fracture surface of an SMA sample, fatigue tested in laboratory air. Two other inclusions were analysed and the major elements present quantified. Content by weight % is given in table 4.9.

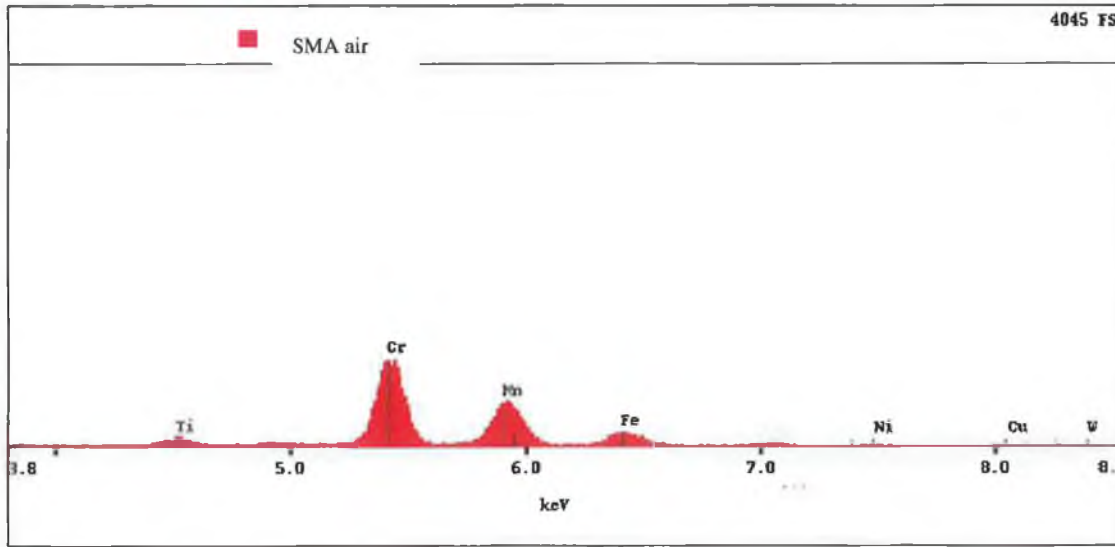


**Figure 4.19 Spectral analysis of inclusion found on SMA fracture surface.**

Element	Inclusion 1	Inclusion 2	Inclusion 3
Cr	54.5	48	30
Mn	26	19	25
Fe	12.5	20	38.5

**Table 4.9 Wt % of heavy elements in three inclusions.**

The inclusions may be of the form CrO-MnO-FeO. An important point is that the inclusions contain a high percentage of Cr. This implies that regions surrounding the inclusions may be depleted in Cr and, as such, subject to chemical attack as the crack front comes into contact with these regions during corrosion fatigue crack propagation. Finally, it must be pointed out that the likelihood of crack initiation in the SMA weld metal is higher than in the fully GTA weld metal, due to the presence of inclusions, which increase the probability of crack initiation for a given cyclic load.

#### 4.2.4 Calculation of percentage ferrite

The following tables show the results of the ferrite measurements using SEM images and image analysis software. These values were obtained relatively quickly and are a good indicator of phase content in the various regions of the weldment.

Base 1000X	HAZ 1000X		Weld Metal 2000X	
	GTA	SMA	GTA	SMA
42.5	46.8	48.8	36.3	32.2
44.3	47.6	44.2	43.8	35.8
43.8	36	49.2	45	34.4
46.5	40.8	41.1	53.4	36.7
49.8			42.8	30
			47.3	

SAMPLE	Average % ferrite	Max. % scatter
Base metal	45	11
GTA root GTA fill (HAZ)	43	16
GTA root SMA fill (HAZ)	47	13
GTA root GTA fill (weld)	44	22
GTA root SMA fill (weld)	35	14

**Table 4.10 Average % ferrite determined by image analysis.**

The results for the ferrite phase content determined by the point count method are presented in figure 4.20. In addition, the graph includes the results of the ferrite content obtained using SEM images and image analysis software for comparison purposes.

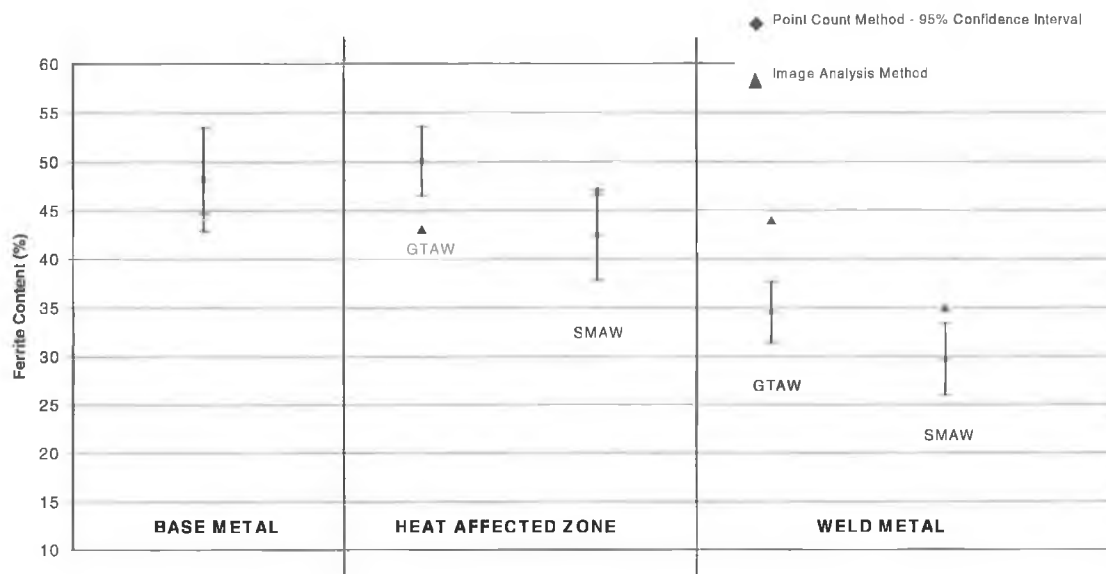


**Figure 4.20 % ferrite content of weldment regions - point count method & image analysis method.**

Good correlation between the average values obtained from the image analysis method and the point count method was obtained for the base metal and SMA HAZ. However, the correlation was poor for the GTA HAZ and weld metal, while the correlation for the SMA weld metal was intermediate. Similarly, the scatter bands (table 4.10) are largest for the GTA HAZ ( $\pm 16\%$ ) and weld metal ( $\pm 22\%$ ) and lowest for the base metal ( $\pm 11\%$ ) while the scatter bands for the SMA samples was intermediate.

The good correlation obtained between the two test methods for the base metal was due to the fact that the etched base metal samples had good phase boundary definition. The phase boundaries were clearly defined due to the different colours of the electrolytically etched phases. Under these conditions the image analysis method yields more accurate results than the point count method as the software employs a much finer grid than the coarse radial grid employed in the manual point method.

The main reason for the poor correlation between the two methods for the HAZ and weld metals was the imperfect etching of the samples in the weld metal region. In

particular, poor phase boundary definition made it difficult for the software to differentiate between the phases in the weld metal.

Therefore, for the HAZ's and the weld metals, the point count method is considered to have produced the most reliable results as:

- good judgement was invoked to decide if a grid point was actually in a particular phase.
- At least thirty fields were considered using the point count method whereas only five were considered using the image analysis software.

Evident from the results is the fact that the base metal exhibited a ferrite content within limits stated by WMF ( $50\pm 15\%$ ). Gunn used the point count method to assess the ferrite content in the duplex stainless steel UNS S32750 [50]. A content of  $48.4\pm 2.8\%$  was found for the base metal, which is in excellent agreement with the current results.

Ferrite contents for Zeron 100 GTA root and fill and GTA root and SMA fill weld metals have also been reported [45]. Average % ferrite was 41.5 for the fully GTA weld metal and 45 for the SMA weld metal. The fully GTA weld is approximately 6% greater than that found in the current work while the GTA root SMA fill weld is 15% greater. Other researchers report even higher ferrite contents [32]; the SMA method produced weld metal with 50% ferrite, and the GTA method produced welds with 51% ferrite. The superduplex grade under investigation was UR 52N+.

With regard to the current results, the phase contents in all regions (base, HAZ and weld metal) fall into the typical limits of at least 50 % austenite and 30% ferrite [16]. Evident from the current results is that a greater percentage of austenite reformed in the SMA HAZ and weld metal relative to the corresponding GTA weld regions. This difference in phase content may have caused the observed difference in tensile failure location observed earlier in the tensile tests. (It was seen in the literature review that austenite increases ductility.) In addition, weld metals with relatively high austenite contents are essential under hydrogen embrittlement conditions where austenite acts

as a hydrogen sink counteracting extensive embrittlement. This will be discussed in further detail later.

#### *Influence of welding parameters on phase contents*

Since HAZ and weld metal chemical compositions are crucial to ensure mechanical and corrosion properties similar to the base metal, it is current practice to use consumables with increased levels of austenitic alloying elements. This measure ensures adequate austenite reformation (>50%) on cooling. The welding consumables used in the GTA and SMA welding processes in the current research contained similar amounts of austenite promoting elements (Ni & N). Therefore, alloy content does not explain why more austenite reformed in the SMA weld metal.

However, it must be noted that austenite nucleation and growth is controlled by the diffusion of the interstitial elements C and N [55], and thus the cooling rate is of major importance in determining the extent of transformation. Slower cooling implies increased austenite reformation.

Therefore, as mentioned in the section on hardness (4.1.4), it is thought that the SMA weld metal cooled more slowly than the GTA weld metal. It was stated previously that the welding speed for both processes was similar. In addition, the number of weld passes required to complete both joints was similar, implying deposition rates were similar. From these observations it appears that the relatively high current used in the GTA method induced a high wire feed rate promoting cooling rates approaching optimum and subsequently a 65/35 % austenite ferrite phase balance.

The welding current for the SMA welding method was between recommended limits. However, SMA welding speeds are typically significantly faster than GTA welding speeds. In the current research, it appears the welding speed used for the SMA method was similar to the GTA welding speed. Therefore, the SMA welding speed was too slow inducing excessive temperatures in the weld metal. A greater angular distortion in the SMA weldment is a good indicator that this was the case. Subsequently cooling was slow and austenite reformation greater than in the GTA weld metal.



#### 4.2.5 Energy dispersive X-ray

Figure 4.21 shows EDX spectra for the ferrite and austenite of base Zeron 100. Relative intensities of the K $\alpha$  lines of elements from Cr to Ni are clearly visible. Detector efficiency was 100% above about 2.5keV [131]. Below this energy, absorption of X-rays in the detector window was significant [131]. Therefore, data below 2.5keV was not taken into account. Clearly evident from the spectra is the fact that the Cr/Ni ratio is higher in ferrite than in austenite.

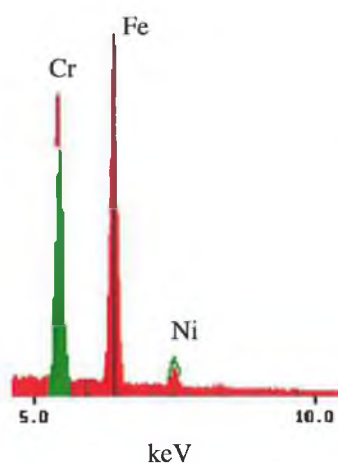


**Figure 4.21 EDX spectrum of ferrite (red) with austenite spectrum superimposed (green).  
Evident is higher Cr/Ni ratio of ferritic phase.**

With regard to superduplex stainless steels, it is widely known that the corrosion properties of both ferrite and austenite depend strongly on the chemical composition. The main alloying elements chromium, molybdenum, nickel and nitrogen are not equally distributed in ferrite and in austenite. In superduplex stainless steels, molybdenum enriches significantly in ferrite while nitrogen and nickel enrich in austenite [74]. Chromium is slightly enriched in ferrite. The partitioning of these elements affects the corrosion resistance of both, the single phases and the entire alloy. Results from the EDX analysis carried out in the current research are tabulated below.

Element	BASE		HEAT AFFECTED ZONE		WELD METAL	
	Ferrite (wt %)	Austenite (wt%)	Ferrite (wt %)	Austenite (wt%)	Ferrite (wt %)	Austenite (wt%)
Fe	61.1	61.6	61.5	60.5	60.4	60.4
Cr	25.8	22.3	24.9	23.0	23.7	23.2
Ni	6.3	9.6	7.7	10.1	9.6	10.8
Mo	1.9	1.9	1.5	1.5	2.0	1.3
Cu	0.5	0.5	0.7	0.5	0.5	0.5
W	1.7	1.7	1.9	2.1	1.5	1.9
Mn	1.4	1.4	1.2	1.4	1.2	1.3

**Table 4.11 Element content of GTA weld metal determined by EDX analysis.**

Element	BASE		HEAT AFFECTED ZONE		WELD METAL	
	Ferrite (wt %)	Austenite (wt%)	Ferrite (wt %)	Austenite (wt%)	Ferrite (wt %)	Austenite (wt%)
Fe	61.5	62.4	61.8	60.9	58.9	58.8
Cr	26.6	21.9	24.2	21.8	25.6	23.8
Ni	6.3	9.2	6.9	11.4	7.3	11.0
Mo	2.1	0.8	2.4	1.8	1.7	1.8
Cu	0.0	0.0	0.0	0.0	0.0	0.0
W	0.7	0.7	0.9	0.5	2.3	1.3
Mn	1.6	2.7	1.3	2.0	2.0	0.9

**Table 4.12 Element content of SMA weld metal determined by EDX analysis.**

Element	Cr	Ni	Mo	Cu	Mn	W
<b>GTA</b>	24.8	9.35	3.8	0.61	0.69	0.6
<b>SMA</b>	25	9.5	3.6	0.8	0.7	0.7
<b>BASE</b>	26	8	4	1	1	1

**Table 4.13 Selection of elements present in base metal & weld metal consumables [16, 112].**

With regard to the wt% of elements presented in the tables above, caution was exercised in their significance. The results obtained for Fe, Cr and Ni are considered the most accurate and are considered further. This is due to three reasons:

- These elements are relatively heavy.
- They are present in relatively high quantities in the base and weld metal.
- Quantities obtained in the two base metal samples correlate well with the levels reported in Weirs datasheet [112].

In order to secure good corrosion properties in superduplex stainless steel welds, the alloying elements chromium, molybdenum and nitrogen must be kept at the highest possible level [58]. However, over alloying can lead to an acceleration of intermetallic precipitation rates [53]. From the results, it is evident that Cr is present in sufficient quantities in the HAZ's and weld metals. In addition, the fact that nickel is present in the ferrite phase in both base and weld metal suggests that the ferrite phase is susceptible to stress corrosion cracking. In commercial ferritic alloys, nickel is not present and these alloys display excellent resistance to SCC.

With regard to the weld metals, it is evident that similar amounts of nickel are present in the austenite phase. This suggests that nitrogen partitioning had the largest effect on austenite reformation. As seen earlier, more austenite reformed in the SMA weld metal due to a relatively slow cooling rate. In addition, one can see the high percentage of nickel in the HAZ's and weld metals relative to the base metal. This is due to the filler metal being over alloyed in nickel, which promoted austenite reformation.

With regard to the SMA weld metal, the nickel content in the austenite is significantly higher than in the ferrite. This, coupled with the hardening effect of N, could be responsible for the higher microhardness of the austenite compared to the ferrite (figure 4.5). In the case of the GTA weld metal the difference between Ni levels in both phases is less. This fact, coupled with a faster cooling rate, rendered phases with similar hardness (figure 4.6).

#### 4.2.6 Localised corrosion

Figure 4.22 shows polarisation curves for two base metal samples and weld metals tested in synthetic seawater at 20°C.

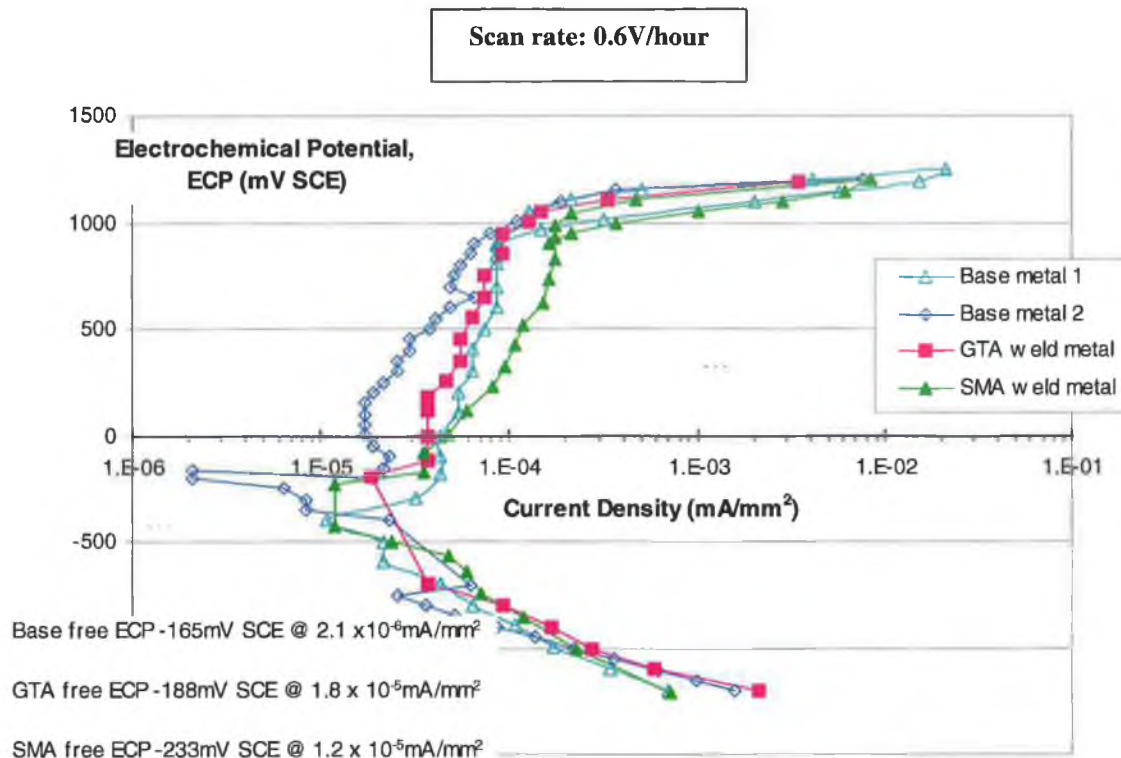


Figure 4.22 Average ECP v current density curves for base and weld metals at 20°C.

The average free corrosion electrochemical potential (ECP) for the base and weld metals at 20°C was -195 mV SCE at a current density of  $1.1 \times 10^{-5}$  mA/mm<sup>2</sup>. This free ECP is in good agreement with the generally acknowledged value of -200mV SCE for stainless steels in seawater [12]. In addition, it is clear that the passive film of the base and weld metals breaks down at approximately 895mV SCE at 20°C. Tavera reported a free corrosion potential of -245mV SCE and a breakdown potential of 1050mV SCE for a duplex stainless steel weld metal (Ferralium 255) [132].

In addition, it is evident that the time required to repassivate or restore the damaged passive film is minimal at 20°C. On reducing the applied ECP of base metal sample one from approximately 1200mV SCE, the corrosion rate reduces rapidly. A

hysteresis loop with a relatively small surface area is produced. A similar loop was produced for the SMA and GTA (not shown for clarity) weld metal.

The hysteresis loops just described are in stark contrast to results obtained for the base metal in seawater at 80°C. Figure 4.23 shows the effect of an increase in temperature on the polarisation curve for the base metal.

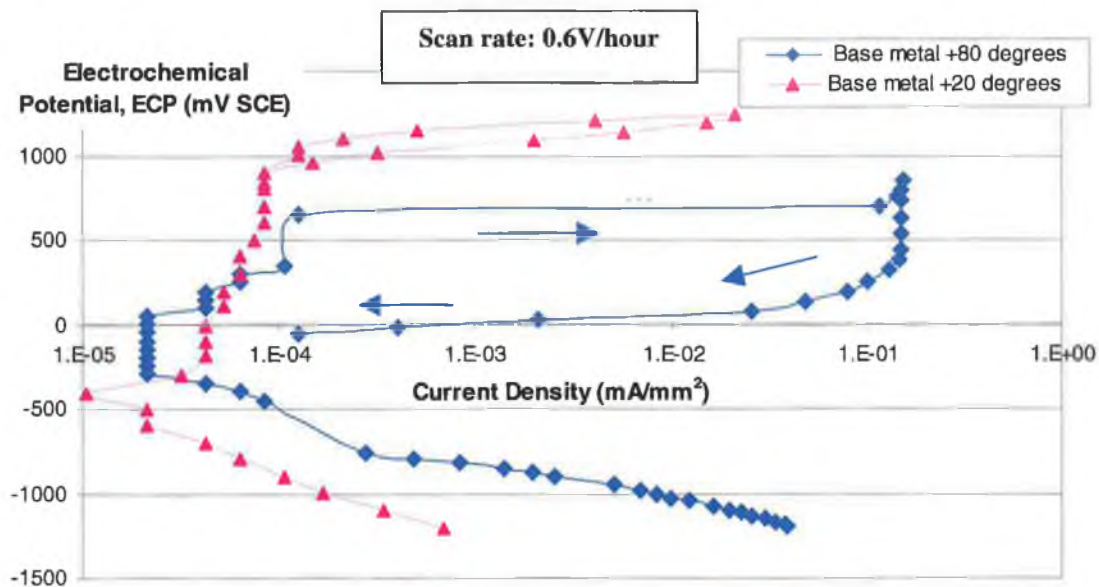
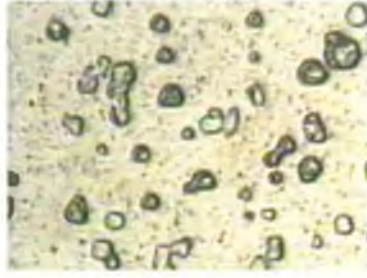


Figure 4.23 ECP as a function of current density for base metal in seawater at 20°C and 80°C.

The free ECP was noted to move in the active (positive direction) due to the higher solution temperature. A value of  $-73\text{mV SCE}$  was obtained for the base metal at  $2.1 \times 10^{-5} \text{mA/mm}^2$ .

In addition, it is evident from the graph that the breakdown/pitting potential is reduced significantly from 895mV at 20°C to 650mV at 80°C. This temperature dependent behaviour is backed up by research reported in the literature. Critical pitting temperature (CPT) values were determined for type UNS S 32750 weld metals in ferric chloride solution (which is much more aggressive than seawater) [31]. Joints completed by GTA root and fill and GTA root, SMA fill exhibited CPT's greater than 40°C. In addition, a minimum CPT of 55°C has been measured in the HAZ of Zeron 100 [133]. Therefore, solution aggressivity and temperature have a major influence on the onset of dissolution.



**Figure 4.24 Pitting on base metal sample at 20<sup>0</sup>C, +1100mV SCE.**

Repassivation is significantly slower at 80<sup>0</sup>C, as evident from the relatively large hysteresis loop (figure 4.23). At 20<sup>0</sup>C, the alloy repassivates almost instantaneously, whereas there is a significant time lag at 80<sup>0</sup>C. During this time lag, significant chemical damage may occur on the alloy. In addition, the corrosion rate is almost 50 times greater at 80<sup>0</sup>C than at 20<sup>0</sup>C at -1000mV SCE. This is a key point with regard to cathodically protected components showing that high solution temperature is highly deleterious.

From the curves just described it is evident that crack growth rates of Zeron 100 base and weldmetal in seawater will be highly dependent on the temperature of the seawater. A short-term temperature upset could dramatically increase crack growth rates due to a delay in repassivation/increased hydrogen evolution.

This is supported by research regarding crevice corrosion of Zeron 100 in artificial seawater, which revealed that the alloy had a 50% chance of suffering crevice corrosion during short-term (24 hours) temperature upsets at 70<sup>0</sup>C [134]. Repassivation occurred only after a few hours when the temperature was restored to normal. Good resistance to HCl, which is present in crevices, was cited as the reasonable performance of Zeron 100. The presence of copper and tungsten was thought to be largely responsible. Five years service experience supported the laboratory results.

It has also been reported that pitting did not occur for SAF 2507 in natural seawater. Seawater coolers have been working in natural seawater at 95<sup>0</sup>C since 1987 [65]. However, it was not stated whether the alloy was cathodically protected or not.

#### 4.2.7 Residual stress measurement

The measurement of residual stresses by X-ray diffraction was unsuccessful mainly due to the alloy in question. First, it was decided to carry out a measurement on base Zeron 100 and use this data as reference data to calibrate subsequent measurements on the weldmetal. The base metal sample was positioned and aligned by performing standard Z Scan and Rocking Curve Scans as shown in figure 4.25. This was to ensure X-ray detection was maximised.

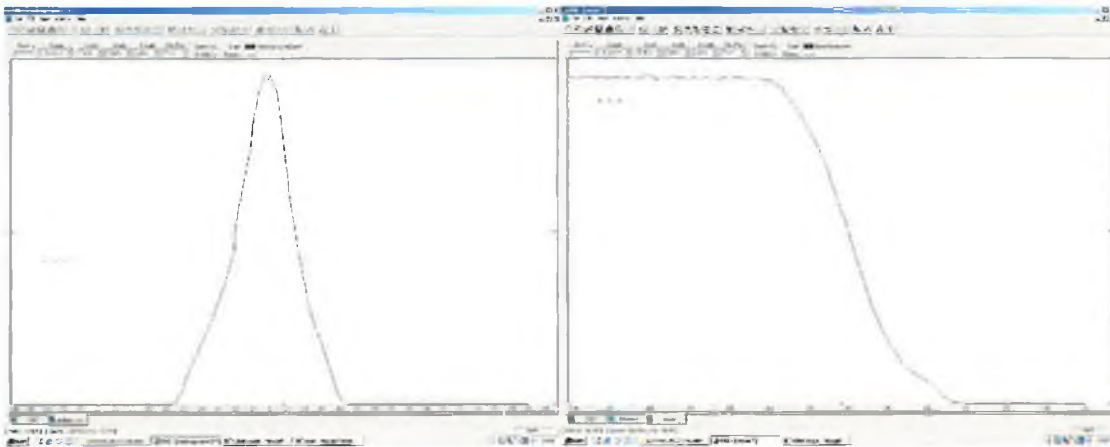
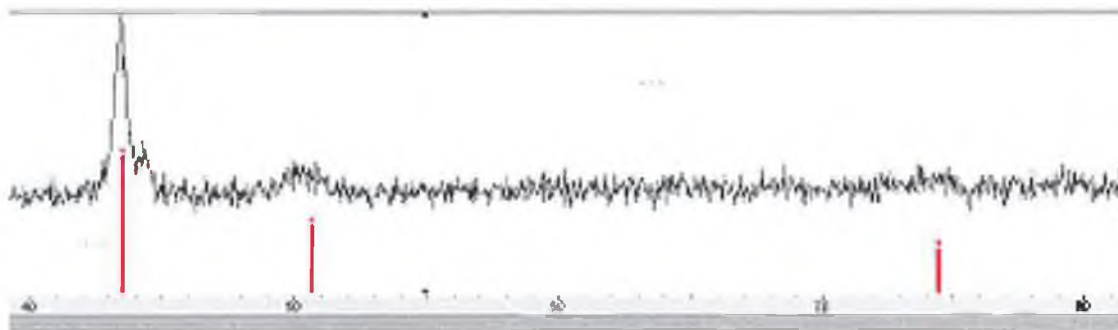


Figure 4.25 Snapshot of rocking curve scan and Z scan from X-ray diffractometer software.

Subsequently, a Locked Couple Scan was performed between  $20^{\circ}$  and  $90^{\circ}$  as shown in figure 4.26. This scan essentially exhibits a set of peaks corresponding to elements present in the alloy, each at a characteristic diffraction angle. One particular peak is then chosen for closer measurement, ultimately leading to a stress measurement. Practical techniques require that the peak chosen for analysis must be greater than  $55^{\circ}$  to ensure accurate stress measurements. As can be seen, only Cr and Fe (indicated by the red lines) exhibit discernable peaks on the scan. Both of these are less than  $55^{\circ}$ . In addition; the intensity of these two peaks was very low. The third red line corresponds to Mo. A peak is not evident.

A very low signal to noise ratio on the locked couple scan made it impossible to distinguish any peaks greater than  $60^{\circ}$ . As a result residual stress measurement was impossible. The reason for the poor scan quality was attributed to the scintillation

counter type detector used in the XRD set-up. This type of detector is ineffective when alloys with high Fe and Cr content are being examined such as in the current research. Fluorescence caused a very low signal to noise ratio and subsequently poor scan quality. A Si(Li) solid state detector as used in the EDX system (section 3.2.4) is required to overcome this problem.



**Figure 4.26 Snapshot of locked couple scan showing peaks for Fe, Cr and Mo.**

Therefore, it was decided to investigate residual stresses in a more direct way by carrying out crack propagation tests on CCT weld metal samples. Crack propagation is in a field of residual tensile stress whereas crack propagation is in a field of residual compressive tensile stress in SENB4 weld metal samples. By comparing the results, the presence or absence of significant residual stresses should be apparent.



	<b>Base metal</b>	<b>GTA weld metal</b>	<b>SMA weld metal</b>
<b>Inclusion content (%)</b>	Negligible	Negligible	0.3
<b>Intermetallic content (%)</b>	Negligible	Negligible	Negligible
<b>Weld Flaw Assessment (BS 7910)</b>	Not applicable	Q1	Q1
<b>Phase balance (%)</b>	48 $\alpha$ /52 $\gamma$	35 $\alpha$ /65 $\gamma$	30 $\alpha$ /70 $\gamma$
<b>Average Cr/Ni content (%)</b>	24Cr/8Ni	24Cr/10Ni	25Cr/9Ni
<b>Free ECP (mV SCE) @20°C</b>	-165	-188	-233
<b>Pitting ECP (mV SCE) @20°C</b>	895	895	895

**Table 4.14 Summary of Microstructural investigation of weld metals.**

### **4.3. Crack Propagation**

In the previous two sections, the fundamental mechanical and corrosion properties of the GTA and SMA weld metals have been reported. In addition, a thorough analysis has been carried out on the weld metal structure including both the micro and macrostructure. The focus in this section is on the crack propagation resistance of the weld metals relative to the base metal and other relevant published data. Reference is made where appropriate to characterisation results reported in the previous two sections. However, before crack propagation results are reported, it is necessary to assess the effect of angular misalignment on the stress intensity factor range  $\Delta K$ , to ensure it is rational to compare weld metal results with base metal results.

#### ***4.3.1 FEA analysis of angular misalignment***

With regard to the 2D perfectly aligned model developed in ANSYS 5.7, good agreement was found between the stress intensity factor ranges obtained from the model and the 'hand calculated' stress intensity factor ranges (equation 3.8). This was to be expected. The hand calculation for  $\Delta K$  serves as a reference line. Results are shown in figure 4.27.

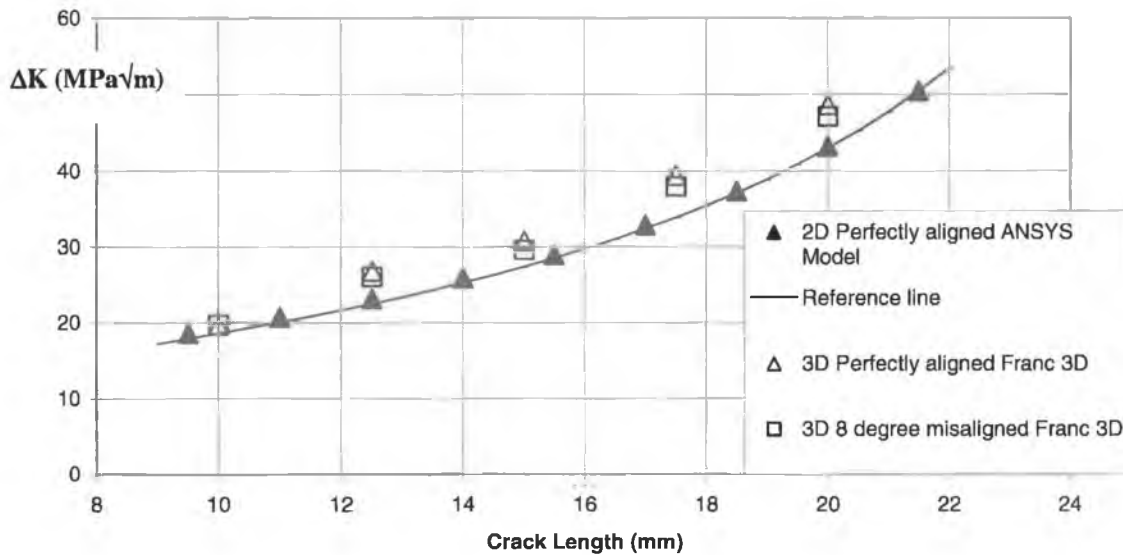
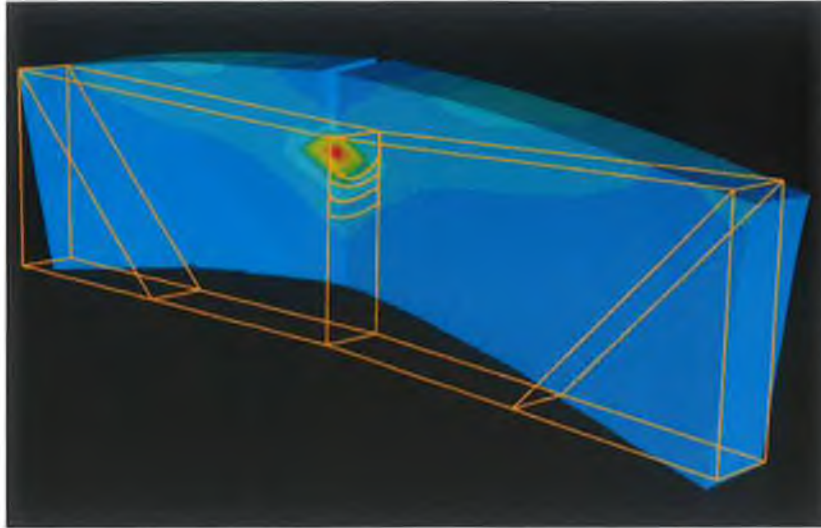


Figure 4.27  $\Delta K$  versus crack length for SENB4 sample.

Figure 4.27 also shows the stress intensity factor range for the 3D models created using FRANC 3D. The average  $\Delta K$  across the sample thickness for the perfectly aligned model at a given crack length was slightly greater than obtained from the hand calculated reference line values. However, the trend of the results is very similar. In addition, the fact that the models were relatively simple involving solving time of only a couple of minutes must also be taken into account. The accuracy of the 3D aligned model was considered adequate to serve as a reference line for the misaligned FRANC 3D model.

Using the FRANC 3D misaligned model, it was found that the stress intensity factor range across the sample thickness was on average 4% less than the average stress intensity factor range value obtained from the perfectly aligned model at the same crack lengths. The  $\Delta K$  values for the weld metal samples were corrected accordingly by reducing the  $\Delta K$  value calculated from equation 3.8.



**Figure 4.28 FRANC 3D model of misaligned SENB4 sample (undeformed & deformed) at  $\Delta K = 38\text{MPa}\sqrt{\text{m}}$ .**

The results from the misaligned model also highlight the fact that the stress intensity factor range would always be higher on the inside (defined in figure 4.1) of the misaligned weldment than on the outside. For the misaligned model, the lowest stress intensity factor range across the sample thickness at a given crack length was found to be located off centre by up to 1.5 mm. This resulted in the crack front shape being distorted. The typical symmetrical thumbnail type curve obtained in perfectly aligned samples remained but was offset to the inside (defined in figure 4.1) of the misaligned weldment as evident in figure 4.29. This was found to be the case when the actual weldments were physically tested (figure 4.29).

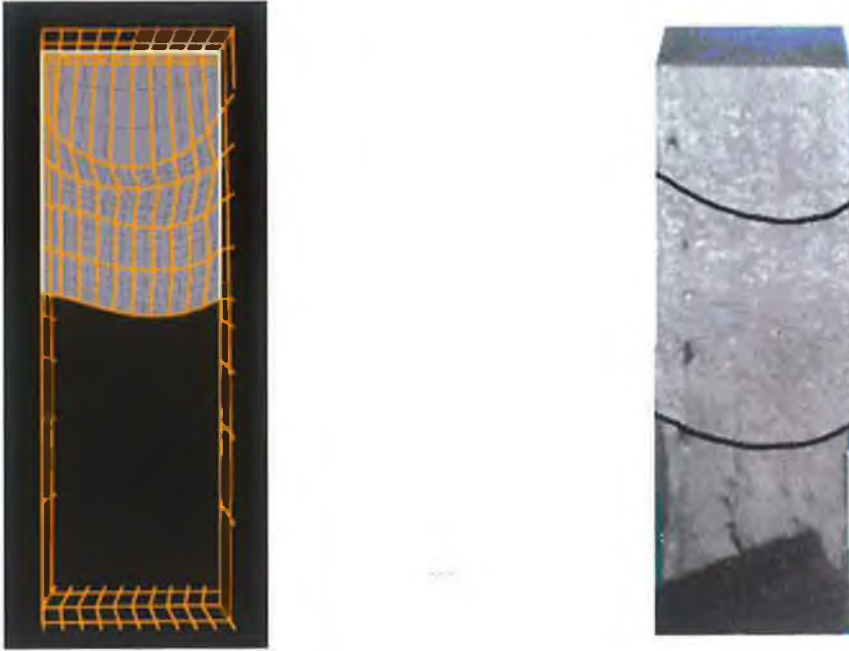


**Figure 4.29 Crack front curvature prevalent on misaligned model & actual SENB4 sample.**

### 4.3.2 Fatigue precracking and crack growth thresholds

Figure 4.30 shows the behaviour of a pre-crack formed by the cyclic compression technique. The curve is an average of three samples, i.e. base and two weld metals (test D in table 3.6).

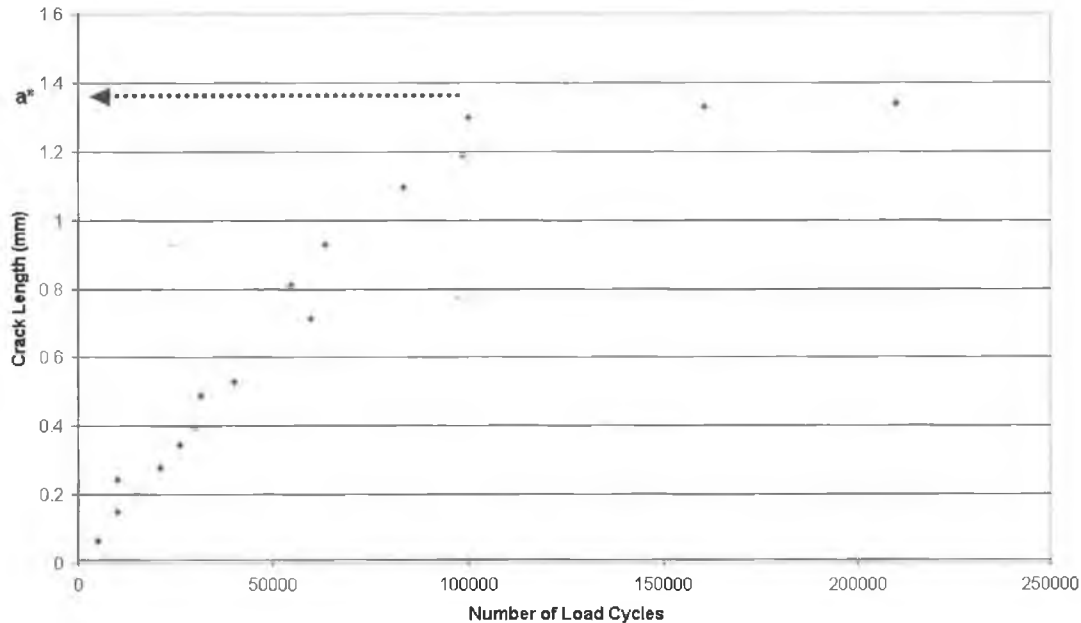


**Figure 4.30 Pre-crack data points for base, GTA and SMA SENB4 samples using cyclic compression technique. Total crack length = notch length (3.5mm) + crack length.**

As can be seen from the graph, precracks arrested at about 1.4mm in Zeron 100 and weld metals under the given loading conditions. Pre-cracks formed by the traditional load shedding techniques were relatively long (>7mm). This has major disadvantages, especially with regard to obtaining threshold values for the onset of crack growth.

Table 4.15 shows threshold values for the onset of crack growth in the base metal and two weld metals tested in laboratory air. Pre-cracks were formed by the load shedding technique in  $\Delta K$  decreasing tests and by the cyclic compression technique in  $\Delta K$  increasing tests.

	$\Delta K_{th}$ ( $\Delta K$ decreasing)		$\Delta K_{th}$ ( $\Delta K$ increasing)	
	(MPa $\sqrt{m}$ )	@ crack length (mm)	(MPa $\sqrt{m}$ )	@ crack length (mm)
Base	8.5	20.2	3.5	5.1
GTA	9.0	18.0	3.5	5.4
SMA	6.7	20.3	3.1	4.3

**Table 4.15** Threshold values obtained by  $\Delta K$  increasing and  $\Delta K$  decreasing tests, R-ratio =0.5.

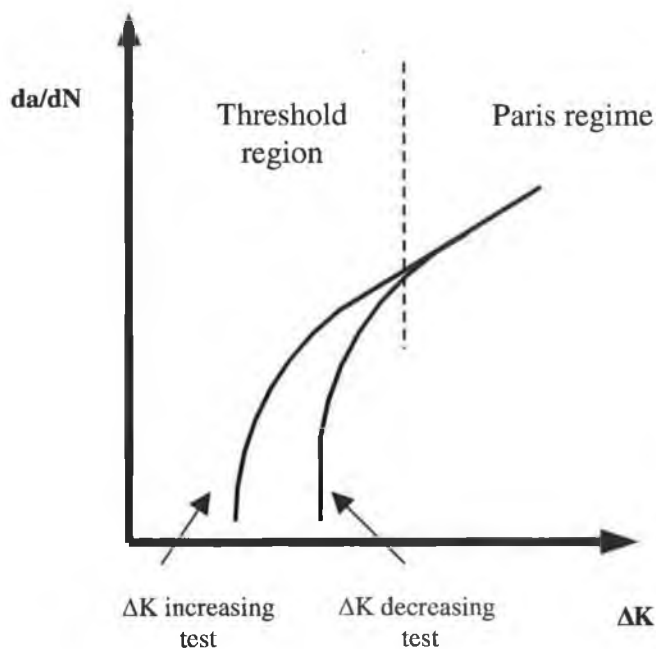


**Figure 4.31** Schematic of threshold behaviour which depends on test type.

It is evident from table 4.15 that the  $\Delta K$  increasing tests yielded the most conservative values. It is thought that the main reason for the discrepancy between the two test methods ( $\Delta K$  increasing and  $\Delta K$  decreasing) was the influence of crack closure. It has recently been concluded that constant R load reduction tests generate artificially high threshold values when compared to steady state data from  $\Delta K$  increasing type tests [126]. With regard to the  $\Delta K$  decreasing technique, thresholds were unavoidably found at a relatively long crack length. Hence, closure due to contact between the fracture surfaces in the wake of the crack tip was significant. The low loads required to obtain threshold exacerbated the closure effect. Therefore,  $\Delta K$  effective was

reduced, and relatively high non-conservative threshold values were obtained. Reductions in imposed  $\Delta K$  with increasing crack length lead to the determination of a 'crack growth arrest threshold' rather than a 'threshold for the onset of crack growth', which was the crucial objective.

Thresholds obtained using the  $\Delta K$  increasing technique were more conservative for two reasons. First, unlike precracking using positive load cycling, a zone of residual tension remains after cyclic compression. Therefore, the crack will propagate easier than through a zone of residual compression. Secondly, the precrack is relatively short. Therefore, contact between fracture surfaces is minimised. Mayaki [25] determined threshold values for Zeron 100 base metal in laboratory air using the constant R load reduction method. Two R-ratio values were investigated, R= 0.1 and R = 0.8. Threshold values of 8 and 3.5MPa $\sqrt{m}$  at  $1 \times 10^{-8}$  mm/cycle were found respectively. Mayaki's threshold values show the effect of R-ratio on threshold behaviour. Secondly, if the threshold obtained at R=0.8 (3.5MPa $\sqrt{m}$ ) is compared to the value obtained for the base metal in the current work (R=0.5, 3.5MPa $\sqrt{m}$ ) it is clear that closure played a role in the determination of Mayaki's values, as one would expect a lower threshold at R = 0.8. This fact highlights the importance of the method used to obtain threshold values.

However Linder [102], using the  $\Delta K$  increasing technique reported a relatively high threshold value (17.5 MPa $\sqrt{m}$ ) for the superduplex alloy SAF 2507. As in the current research, the R-ratio employed was 0.5. Linder proposed that compressive residual stresses were present in the SAF 2507 sample and these stresses reduced the effective  $\Delta K$  resulting in a high threshold value.

Further research has been carried out demonstrating the importance of the effect of R-ratio and crack closure on thresholds. Tie line alloys were fatigue tested where the ferrite and austenite phases each had constant chemical composition in the whole series [127]. The compositions resembled those found in the duplex stainless steel SAF 2205. Five mixtures were investigated, 100% ferrite, 65% ferrite/35% austenite, 40% ferrite/60% austenite, 25% ferrite/75% austenite and 100% austenite. At low R-ratios, the crack growth thresholds were similar for all materials. However, at higher R-ratios, the single-phase alloys were found to have a relatively low intrinsic



resistance to crack propagation compared to the duplex alloys. This was due to the absence of the retarding effect provided by the ferrite/austenite grain boundaries. At low R-ratios this grain boundary retarding effect was balanced by the increased crack closure in the single-phase alloys due to the larger grain size. At high R-ratios the crack closure effect was minimised, and the duplex alloys displayed better crack propagation resistance.

Recent research using a 'Unified Approach' indicates that for low carbon steels at least,  $\Delta K$  threshold is independent of material and is the order of  $2.6 \pm 0.2 \text{ MPa}\sqrt{\text{m}}$  [135]. It is  $K_{\text{max}}$  varying between 2.6 and 10  $\text{MPa}\sqrt{\text{m}}$  that determines the onset of growth being a function of yield stress, grain size, microstructure etc. As such, the threshold values obtained in the current research for Zeron 100 base and weld metals are similar to threshold values for carbon steels.

### ***4.3.3 Stage II crack propagation and effect of residual stress fields***

#### *Laboratory Air Tests*

Stress intensity factor range (SIFR)/ $\Delta K$  increasing and decreasing test results are reported in the following sections. Precracking is by the traditional load shedding method for the SIFR decreasing tests (test type C, table 3.6). The SIFR increasing tests are divided into two sub groups:

- SIFR increasing tests (precracking by the cyclic compression technique (test type B and D). These tests allowed crack growth data to be obtained at low  $\Delta K$ .
- SIFR increasing tests (precracking by the traditional load shedding technique (test type A).

Initial tests carried out on the base and weld metals in laboratory air were  $\Delta K$  increasing type tests (test type A in figures 4.32 – 4.34). The crack growth rates for the base and two weld metals were comparable (within the limits of statistical scatter associated with steady state crack propagation) from  $\Delta K = 20\text{MPa}\sqrt{\text{m}}$  up to approximately  $40\text{MPa}\sqrt{\text{m}}$  (figure 4.35). The main difference between the data for the three samples occurred after this point as the SMA weld metal fractured while the base metal continued to propagate with the same slope. The crack growth rate for the GTA weld metal started to increase relative to the base metal.

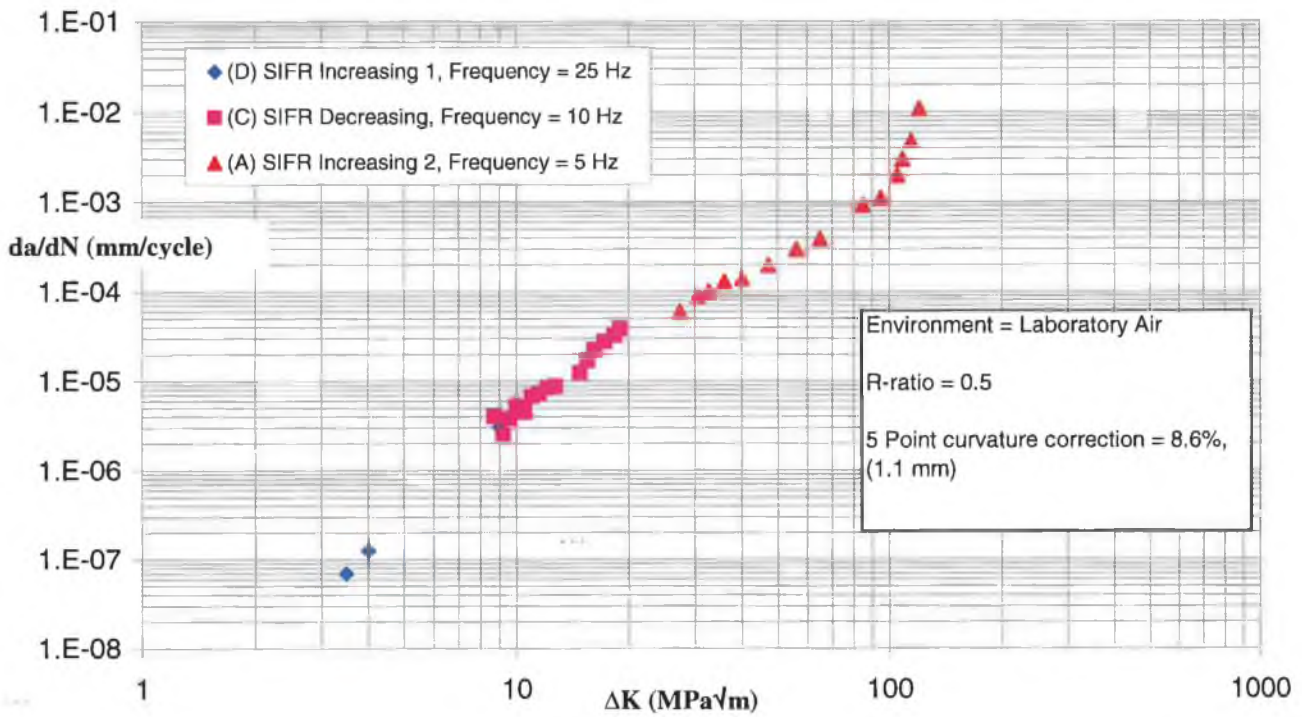


Figure 4.32 Three tests on the base metal in laboratory air.

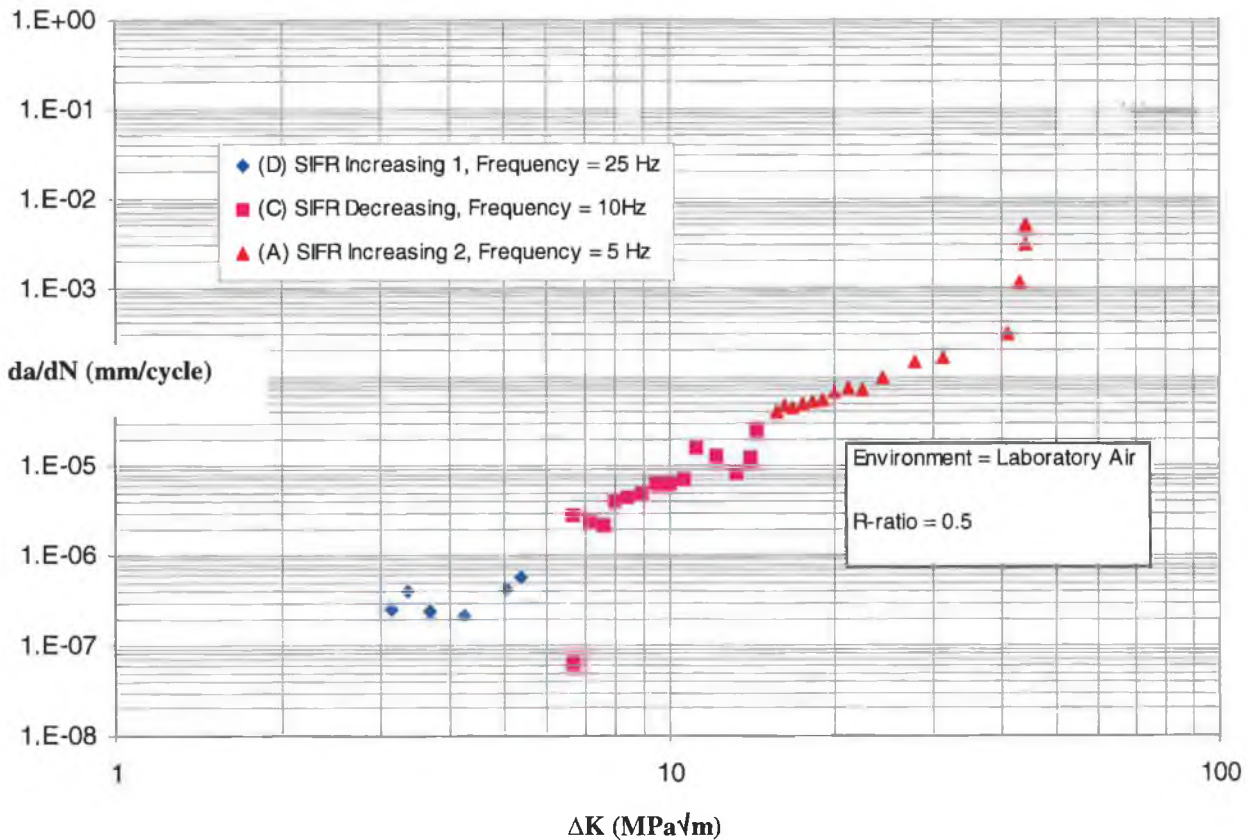


Figure 4.33 Three tests on the SMA weld metal in laboratory air.

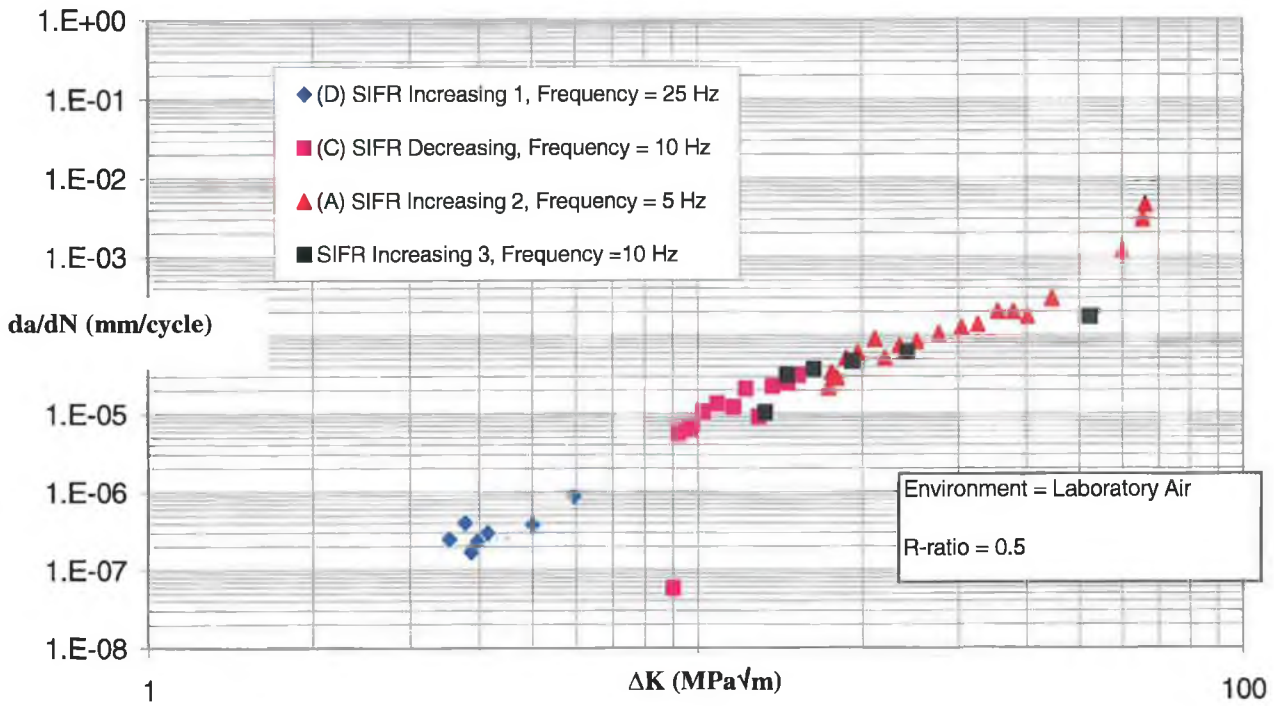


Figure 4.34 Four tests on the GTA weld metal in laboratory air.

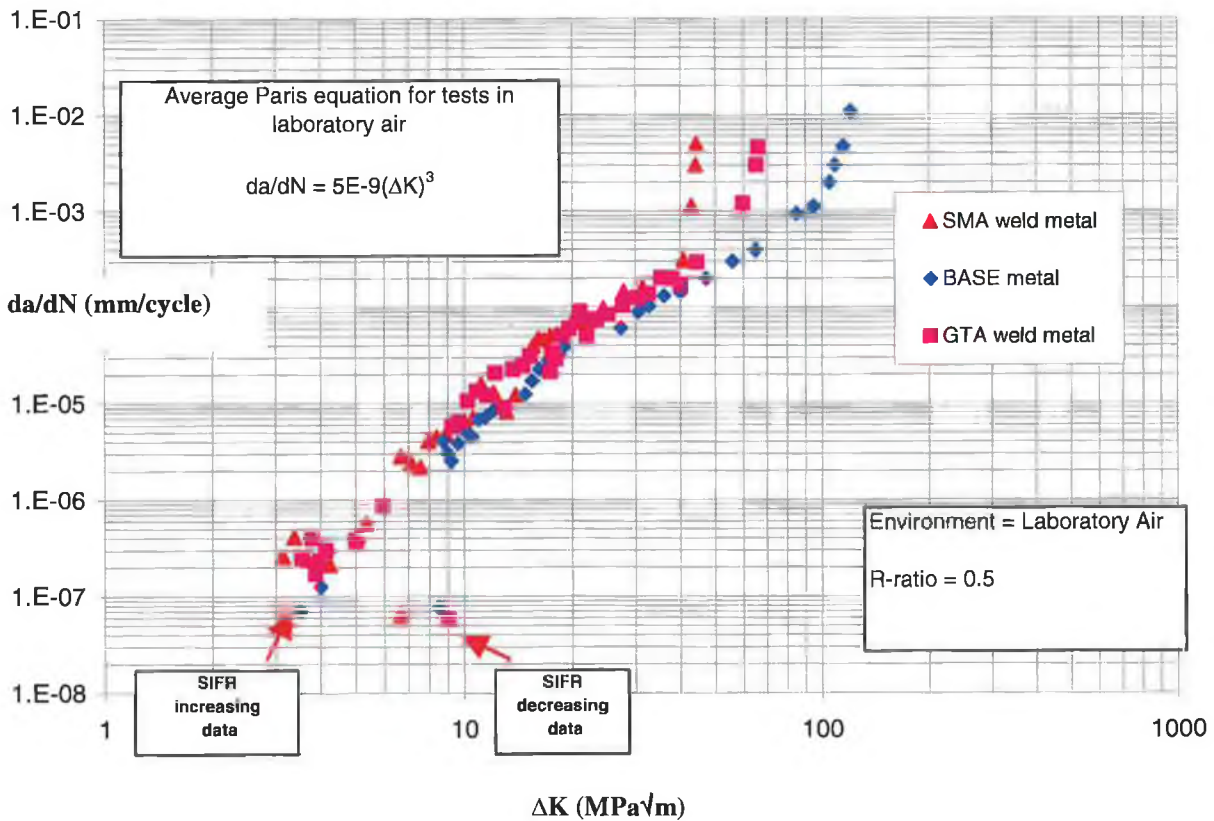


Figure 4.35 Results from nine tests carried out in laboratory air.

The critical  $\Delta K$  ( $\Delta K_C$ ) at failure are presented in table 4.16. These results are averages based on two tests in the case of the base and GTA weld metal and three tests in the case of the SMA weld metal. Values for fracture toughness are also presented based on an R-ratio of 0.5.

Sample	$\Delta K_C$ (fast fracture)	$\Delta K_C$ scatter	$K_{Ic}$ (sample thickness = 10mm)
	MPa $\sqrt{m}$	%	MPa $\sqrt{m}$
Base metal	94	$\pm 1$	188
GTA weld metal	56	$\pm 6.5$	112
SMA weld metal	41	$\pm 4.5$	82

**Table 4.16 Fast fracture average values for base and weld metal samples.**

Subsequent to fracture the fracture surfaces were examined, and digital images captured. Using image analysis software, crack length measurements were performed at five points across the thickness of the samples with the aid of beachmarks, which highlighted the shape of the crack front after precracking and before fast fracture. The average values were used to correct for crack front curvature of the base metal samples.

The crack propagation data acquired during  $\Delta K$  decreasing tests for the three samples were comparable over a  $\Delta K$  range from 18MPa $\sqrt{m}$  to 9MPa $\sqrt{m}$  (test type C in figure 4.32 – 4.34). Consistency is noted between the  $\Delta K$  decreasing and  $\Delta K$  increasing data (test types A & C) for each sample. This was further verified by performing a  $\Delta K$ -increasing test on the GTA sample (figure 4.34). However, data below 13 MPa $\sqrt{m}$  was not obtained.

The data from the third type of test (D) is also consistent with the tests just mentioned (figure 4.32 – 4.35). These tests were  $\Delta K$  increasing type tests and, as such, confirmed that the linear data obtained from the  $\Delta K$  decreasing tests was conservative. Precracking using the cyclic compression precracking method allowed crack growth rates to be determined at very low  $\Delta K$ ; much lower than  $\Delta K$  decreasing type tests. Since the linear data from the three test types was consistent for each sample, confidence in the data generated is high.

Finally, and perhaps most importantly, the effect of residual stresses (possibly present in the weld metal) on crack propagation rates was investigated (test type B). Tests using CCT samples were performed only on the GTA samples extracted from weldment b (table 4.1) as this weldment had the lowest degree of angular misalignment. When angular misalignment is present in samples, which are loaded axially, it is typical to account for the increase in stress due to induced bending moments by means of a stress magnification factor. For a butt weld with angular misalignment as in the current case, the appropriate stress magnification factor is determined from the ratio of the attachment length (figure 4.9) to the sample thickness [19, 114]. Therefore, the stress magnification factor in the current work is 1.4.

However, it was assumed that the effect of the angular misalignment present ( $2^0$ ) on  $\Delta K$  was negligible. Detailed analysis of the effect of the angular misalignment on  $\Delta K$  would only be carried out if the CCT samples exhibited significantly higher crack propagation rates compared to the SENB4 samples.

Results from the tests on CCT samples can be seen in figure 4.36. Evident is the fact that any possible residual stresses present and any increases in local  $\Delta K$  due to angular misalignment did not increase crack growth rates above those found for the SENB4 type samples. Since the data for SENB4 and CCT samples is coincident, it was not deemed critical to carry out further analysis on the effects of angular misalignment/residual stresses on the CCT weld metal samples. It appears likely that the angular misalignment present and residual stress fields (possibly present) had little effect on crack propagation rates.

Therefore, the crack propagation data in the current research is thought to represent the intrinsic resistance of the weld metals. Also evident from figure 4.36 is the fact that both sample types (SENB4 GTA and CCT GTA) yielded the same crack growth threshold value of  $3.5\text{MPa}\sqrt{\text{m}}$ .

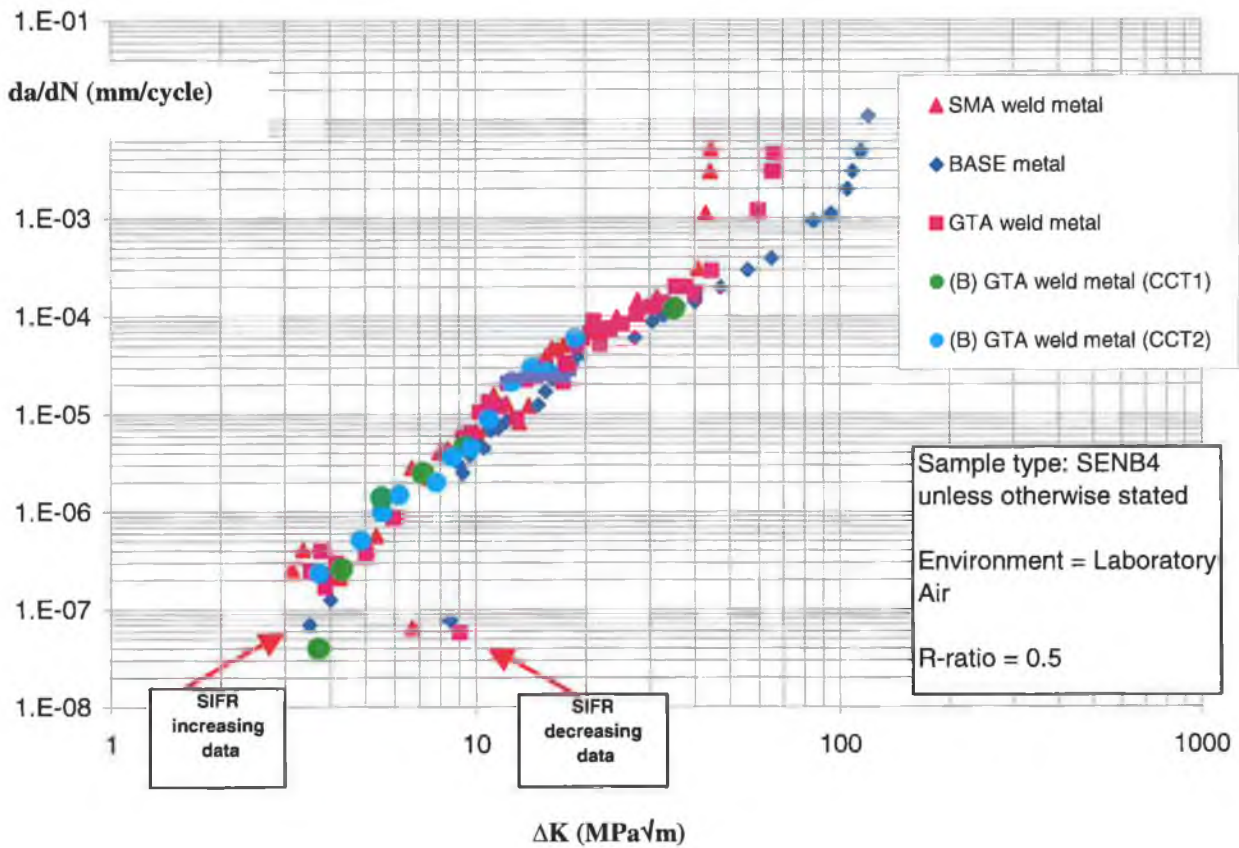
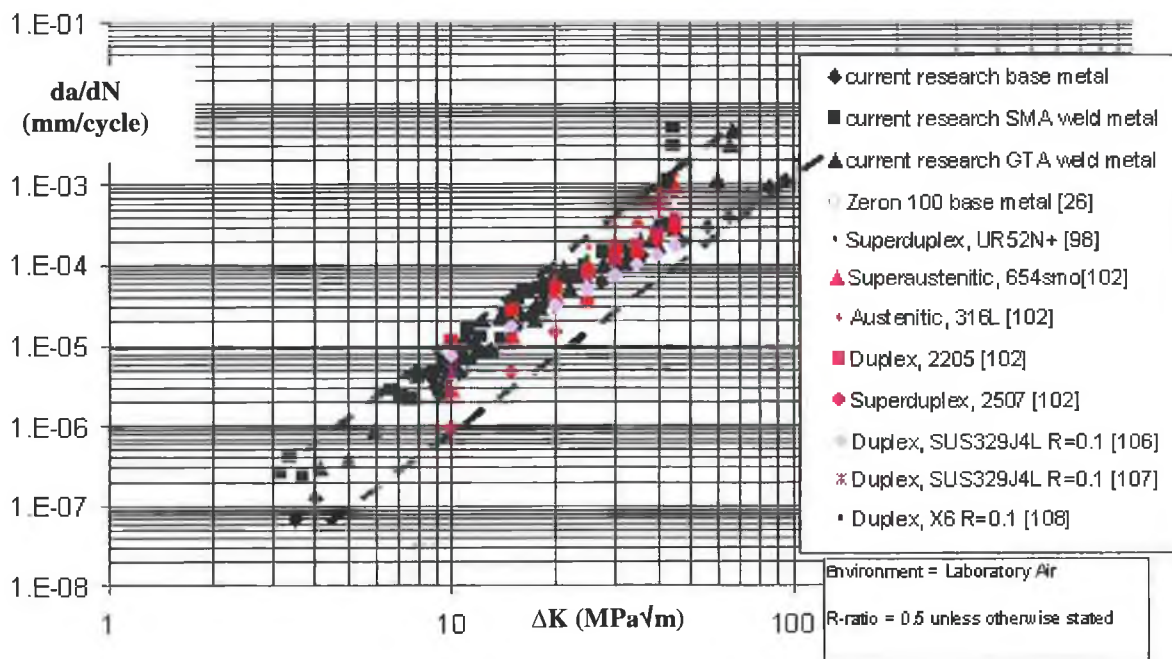


Figure 4.36 Test results in laboratory air from nine tests using SENB4 type samples and two tests using CCT type samples.

The Paris law constants ( $C$  &  $m$ ) and the co-efficient of determination calculated using the accumulated data from the three individual (SENB4) tests on each sample were determined.

Sample	C	m	R <sup>2</sup>
Base metal	4E-9	3.0	0.96
GTA weld metal	6E-9	3.0	0.97
SMA weld metal	5E-9	3.1	0.97

Table 4.17 Paris equation coefficients and the coefficient of determination for data obtained in laboratory air.



**Figure 4.37 Current test data in laboratory air and data available in literature.**

The slope of the Zeron 100 base and weld metal data found in laboratory air (table 4.17) was on average 3.0 which is the generally acknowledged value for alloys fatigue tested in benign environments such as laboratory air. The current crack propagation data was then compared to other researcher's data on Superduplex, duplex and austenitic stainless steels (figure 4.37). As can be seen from this graph, good agreement between the data for the superduplex stainless steels considered was obtained at high  $\Delta K$ . Crack propagation rates for Zeron 100 base and weld metals, Uranus UR52N+ and SAF 2507 superduplex alloys differed by a factor of 7 at  $10\text{MPa}\sqrt{\text{m}}$  and by a factor of 3 at  $40\text{MPa}\sqrt{\text{m}}$ . Data from lower alloyed duplexes (SAF 2205, SUS 329, X6) and super-austenitics (SMO 654) did not increase the scatter band further. The crack propagation resistance of Zeron 100 base and weld metal is similar to that for 316L at  $10\text{MPa}\sqrt{\text{m}}$  but greater only by a factor of 3 at  $\Delta K = 40\text{MPa}\sqrt{\text{m}}$ . Therefore, the higher UTS and yield strength of the superduplex stainless steels appears to have little benefit with regard to resistance to crack propagation in the range  $\Delta K = 10\text{-}40\text{MPa}\sqrt{\text{m}}$ . This observation is commonly acknowledged [19]. The benefit of high tensile strength is associated with crack initiation resistance as discussed in the literature review.



At this point, it is important to assess how superduplex stainless steels achieve their resistance to crack propagation. Previous research on Zeron 100 [25, 103] and simulated HAZ microstructures [136] shows that crack propagation rates in air depend partly on effects such as roughness-induced closure at low R and  $\Delta K$ . It is also commonly appreciated that residual stresses can influence crack propagation rates. Since the aim of the current research is to conservatively assess the intrinsic resistance of the base and weld microstructures to crack propagation, it was desirable to negate/minimise factors such as closure, which tend to increase the crack propagation resistance, making it difficult to conservatively ascertain the microstructures resistance to crack propagation.

With regard to the current research, key factors in minimising crack closure included the relatively high R-ratio used and the utilisation of the cyclic compression precracking technique, which allowed  $\Delta K$  increasing type tests to be performed from the onset of crack growth to failure. Further, an attempt was made to indirectly assess the effect of residual stress fields (which were assumed to be present) on crack propagation rates in GTA weld metal by carrying out crack propagation tests in laboratory air on GTA weld metal CCT and SENB4 samples. Since the results for the two sample types were comparable and considering the test parameters and test methods just mentioned, it is thought that the linear crack propagation data for the three samples base metal, GTA and SMA weld metal represents the intrinsic crack propagation resistance of the samples.

Earlier FEA work sought to assess the effects of misalignment on the welded samples. Again, this was an attempt to minimise extrinsic factors. This measure was supplemented by assessing crack curvature to ensure crack growth rates were determined at the correct  $\Delta K$  values.

In order to comprehensively assess the intrinsic resistance of the base and weld metals, it was necessary to examine the evidence available from the fracture surfaces of each sample. Striations were ductile in nature on samples tested in laboratory air. Good correlation was obtained between the striation size and macro crack growth rate at  $\Delta K = 23$  to  $50\text{MPa}\sqrt{\text{m}}$  (figure 4.38). This clearly indicates that a subcritical ductile

mechanism was controlling the rate of crack propagation. A ductile striation was formed on each load cycle.

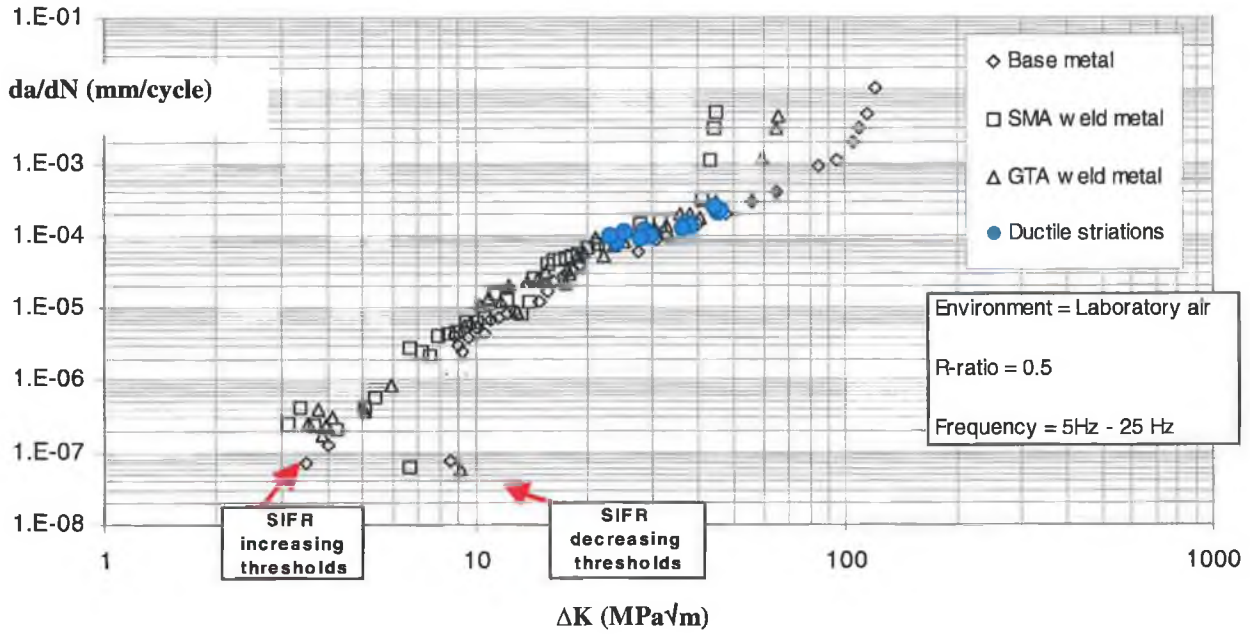


Figure 4.38 Ductile striation spacing compared to macrocrack growth rates in laboratory air.

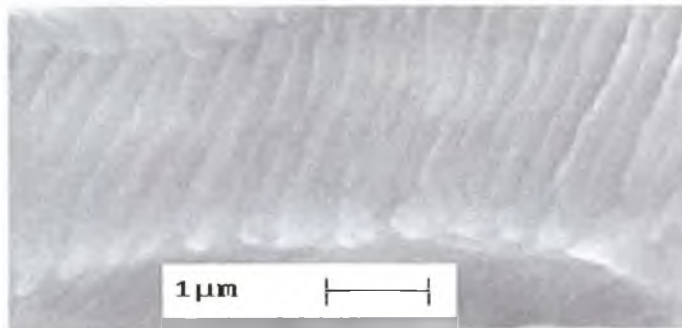


Figure 4.39 Ductile striations at  $45MPa\sqrt{m}$ .

Secondly, it was noted that there was no preferential cracking of the phases during the growth of a macrocrack through the samples. This is in agreement with other researchers' observations [137] and is a result of the plastic zones prevalent ahead of the macrocrack crack tip. Once the monotonic plastic zone (mpz) and reversed plastic zone (rpz) size calculated from [86]:

$$mpz = \frac{1}{\pi} \left( \frac{K_I}{\sigma_y} \right)^2 \quad 4.2$$

$$rpz = \frac{1}{\pi} \left( \frac{\Delta K_I}{2\sigma_y} \right)^2 \quad 4.3$$

where:

$K_I = K_{max}$  in mode 1 loading

$\sigma_y$  = yield stress

become equal to and greater than the characteristic microstructural size (which occurred at approximately  $\Delta K \geq 1$  MPa $\sqrt{m}$ ), preferential cracking of either austenite or ferrite is not observed.

However, it has been established [103] that macrocrack growth rates decrease with increasing frequency of ferrite/austenite (BCC $\rightarrow$ FCC) grain boundaries encountered by the crack tip. For example, crack propagation rates differed by up to a factor of four in Zeron 100 base metal samples tested in different orientations (TL, LT and TW) [103]. Crack tip deflection was commonly observed in the current research on micrographs of both base and weld metal. Figure 4.40 shows how the austenite phase causes the macrocrack to deflect and subsequently follow the grain boundary of the austenite phase. However, once around the austenite phase, the crack can propagate apparently without deflection through the ferrite.

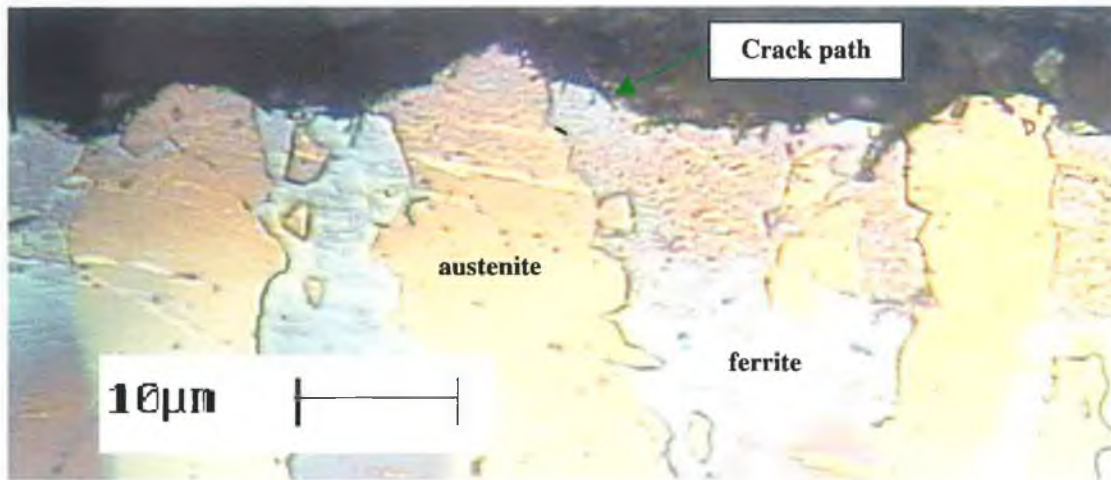


**Figure 4.40 Crack path in base metal showing deflection at ferrite/austenite grain boundaries. Propagation direction, left to right. Etch 20% NaOH.**

Other researchers agree that crack retardation at ferrite/austenite grain boundaries is possible. For example, non-propagating cracks were noted in run out specimens (S-N type tests) on a duplex stainless steel SAF 2304 [138]. Cracks arrested at austenite grains and subsequently followed grain boundaries. This highlights the crack arresting ability of the dual phase structure at low stress levels. Indeed, it is now known that interphases such as grain boundaries are only effective microstructural barriers until the crack length exceeds 5-10 times the grain size [139]. Therefore, microstructural barriers are effective for microcracks up to approximately 50 microns in Zeron 100.

It is plausible that microstructural barriers can have an effect on macrocrack growth rates at low  $\Delta K$ . However, the effect at relatively high  $\Delta K$  ( $>15\text{MPa}\sqrt{\text{m}}$ ) is minimal, as seen earlier in the similar crack propagation performance of a single-phase austenitic stainless steel and the current superduplex alloy Zeron under similar loading conditions (figure 4.37).

At this stage, it is clear that the dual phase microstructure is of greatest benefit at low  $\Delta K$  or in the high cycle regime. Therefore, morphology is a very important parameter affecting crack propagation resistance around threshold [140]. With decreasing morphological scale microcrack growth is impeded. Therefore, propagation resistance increases with increasing morphological anisotropy and decreasing morphological scale.

The two decisive parameters which influence the phase morphologies of the individual phases i.e. their volume fractions, distribution, scale and crystallographic texture are the processing history and the chemical composition [140]. Rolling produces a strong crystallographic texture in the ferrite and a weaker crystallographic texture in the austenite phase and a general alignment of the austenite rods in the rolling direction [140] (figure 4.10).

Cast DSS exhibit a phase morphology characterised by coarse ferrite grains within which the austenite phase forms randomly oriented single crystals [140]. This is similar to the microstructure found in weld metal (figure 4.10). This morphological anisotropy in the as-cast steel is confined within individual ferrite grains whereas the alloy as a whole is isotropic.

As stated previously, macrocracks as characterised in the current work extend by the coalescing of discreet narrow channels or microcracks ahead of the crack tip. Resistance to the initiation of these microcracks governs the macrocrack propagation resistance. As such, it is the cyclic plastic properties of the individual ferrite and austenite phases that govern propagation behaviour.

With regard to microcrack initiation, it has been found that ferrite content is a decisive controlling factor. At high strains, the deformation in the ferritic phase of a duplex stainless steel 22Cr, 7Ni, 2.5Mo, 1.7Mn was found to be the largest influencing factor on crack initiation [97]. Twinning promoted early crack initiation in the ferritic phase reducing the fatigue strength.

Another researcher showed that at plastic strain amplitudes above 0.002, crack initiation occurs preferentially in the ferrite phase in duplex steels [137]. Twinning occurs relatively early in the ferrite, leading to early crack nucleation [141]. Austenite has little influence at high strains [141]. In addition, a general fatigue life increasing effect of nitrogen has not been detected for DSSs. [140]. The fatigue life curves of DSSs with comparable morphological anisotropies and morphological scales, but with different N contents didn't reveal a consistent pattern. Since nitrogen preferentially dissolves in austenite, it appears that ferrite is controlling fatigue resistance.

Cyclic stress-strain type tests were performed on tie line alloys where the ferrite and austenite phases each had constant chemical composition in the whole series resembling those found in the duplex stainless steel SAF 2205 [127]. Five mixtures were investigated, 100% ferrite, 65% ferrite/35% austenite, 40% ferrite/60% austenite, 25% ferrite/75% austenite and 100% austenite. The cyclic yield strength was found to increase linearly with the volume fraction of ferrite, thus following the classical law of mixtures.

Evident from the literature is the controlling influence of ferrite on microcrack initiation in duplex stainless steels. This factor is thought to subsequently govern the macrocrack propagation resistance. It is clear that a high ferrite content is desirable with regard to microcrack initiation as austenite is ineffective in resisting high strain induced damage. In the current work, the base metal had the highest ferrite content at 48%. The weld metals exhibited ferrite contents just above 30% (figure 4.20). Therefore, one would expect the base metal to have better crack propagation resistance than the weld metals. Since the difference in ferrite contents between the base and weld metals is relatively low at 18%, the effect of ferrite content is consequently low. However, evident from table 4.17 is the fact that the Paris C coefficient for the base metal is less than either of the weld metals while the slopes are comparable.

Aside from ferrite content, it is thought that a number of other factors were responsible for the slightly lower crack propagation resistance of the weld metals relative to the base metals. Perhaps the most important intrinsic factor in the crack propagation resistance of the weld metals is the presence of a macrostructure (figure 4.11). In multipass welds, a through thickness notch is known to coincide with both the weakest planes of the coarse columnar solidification structure and the greatest concentration of weak grain boundary segregates [61]. In both SENB4 (GTA and SMA) and CCT (GTA) samples, the macrocrack regularly followed what is thought to be the grain boundaries of the columnar grain macro-structure at least up to a  $\Delta K$  of  $10\text{MPa}\sqrt{\text{m}}$ . It is thought that the columnar grain boundaries provide a path of least resistance to crack growth at low  $\Delta K$ . Figure 4.41 shows the macrocrack path at low  $\Delta K$ . The macrocrack path is thought to highlight the columnar weld grains. The

average width (30 microns) of the columnar weld grains agrees with measurements recorded in section 4.2.1.

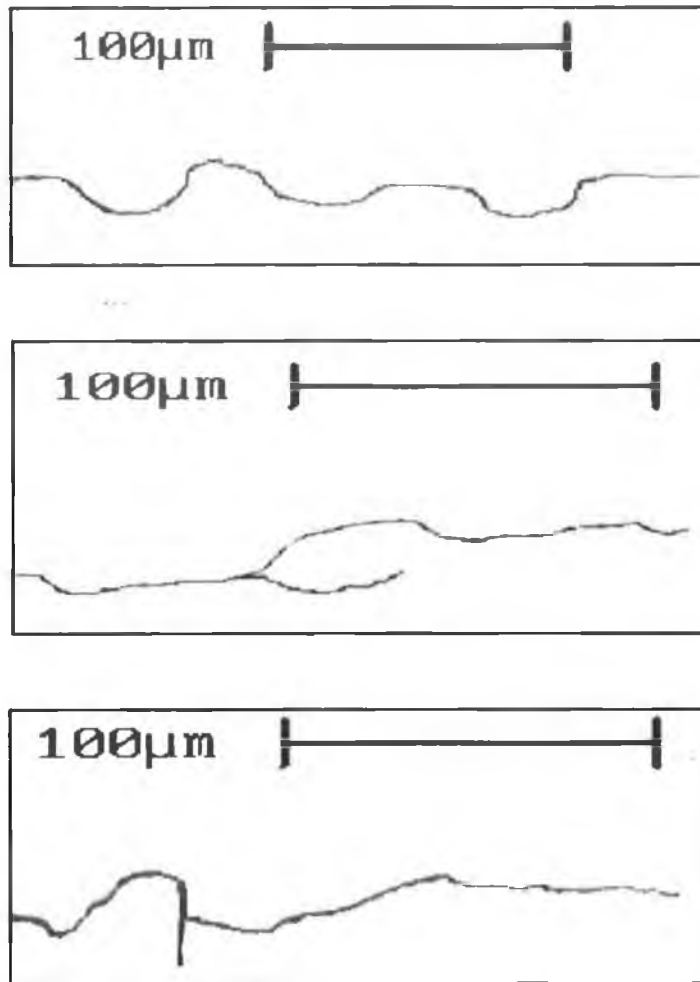


**Figure 4.41 Macrocrack propagation around columnar weld grains at  $\Delta K < 10 \text{ MPa}\sqrt{\text{m}}$ .**

A similar phenomenon (reported as mode II type crack propagation) has been reported for the weld metal of an SAF 2304 duplex stainless steel under high cycle S-N type fatigue tests [138].

It has been observed that the centre of the weld metal, as opposed to the heat affected zone (HAZ), exhibits the lowest toughness with regard to superduplex stainless steel weldments [33, 29, 30, 32]. In general, low toughness at the centre of weld metals has been attributed to the highly restrained conditions under which solidification and

cooling take place [61]. However, as seen in the current research, the grain boundaries of the weld macrostructure appear to be preferred paths for crack growth and probably lead to low toughness values in the weld metal. Low toughness or resistance to crack propagation is probably due to the presence of weak grain boundary segregates.

A secondary factor in crack propagation resistance of the weld metal is thought to be the microstructure, that is the structure that is present in a columnar grain. As seen earlier, both weld metals consisted of randomly orientated austenite colonies relative to the aligned colonies in the base metal, ensuring a higher degree of morphological anisotropy relative to the base metal. In addition, a difference in phase hardness was evident in both weld metals (8%) as opposed to the base metal (2%) (figure 4.5 and 4.6) ensuring microcrack tip deflection at phase boundaries was maximised. However, these factors are only significant when the macrocrack propagates through the columnar weld grains as opposed to around them.

The intrinsic factors just discussed can also be invoked to explain the threshold performance of both weld metals in the  $\Delta K$  increasing tests (type B and D in figure 4.36). Although the  $\Delta K$  required for crack propagation was similar for the base and weld metals, the crack growth rate observed at this threshold  $\Delta K$  was higher for the weld metals by a factor of 3.6 (figure 4.36). (However, one of the CCT samples exhibited similar crack growth rates to the base metal). Again, this was probably due to the easier path provided by the columnar grain boundaries. The GTA weld metal showed a slightly higher threshold compared to the SMA weld metal, probably due to the absence of appreciable inclusions in the GTA weld metal.



### *Synthetic Seawater Tests*

Similar to the tests carried out in laboratory air, both  $\Delta K$  increasing and  $\Delta K$  decreasing type tests were carried out in synthetic seawater.  $\Delta K$  decreasing type tests (test type H) and  $\Delta K$  increasing type tests (test types E, F and G) were all carried out on samples precracked using the load shedding method. Two samples precracked using the cyclic compression technique (test type D) were periodically subjected to a salt-water solution to determine the most conservative point for the onset of environmental assisted crack growth.

Research has shown that environmental assisted cracking in aqueous environments is strongly related to the electrochemical potential (ECP) of a steel component [20]. This fact inspired the environmental tests in the current research to be carried out at constant low and high ECP's (-1040 and +1040mV SCE) in order to assess the resistance of Zeron 100 base and weld metals in such circumstances. High positive potentials can be assumed by stainless steels in seawater (especially at local locations such as crack tip enclaves, crevices etc.) depending on the local seawater condition (section 2.4.1). Low potentials are often imposed on components in service subsea to inhibit general corrosion.

### High positive ECP stage II crack propagation

These tests were necessary to investigate the ability of the anodic dissolution mechanism to augment crack propagation rates in aqueous solution. Figures 4.42 – 4.44 show results for the two tests carried out in synthetic seawater at positive potentials (test type G). The tests commenced at a  $\Delta K$  of  $20\text{MPa}\sqrt{\text{m}}$  and continued until fracture. Crack growth rates obtained from the tests were slightly greater than crack growth rates obtained in laboratory air (figure 4.44). The crack growth rates in synthetic seawater were 2.3 times greater than rates in air at  $\Delta K = 30\text{MPa}\sqrt{\text{m}}$ . The crack growth data for the base metal in synthetic seawater converged with the data for the base metal tested in air at  $85\text{MPa}\sqrt{\text{m}}$ . Fast fracture levels are the same as in air.

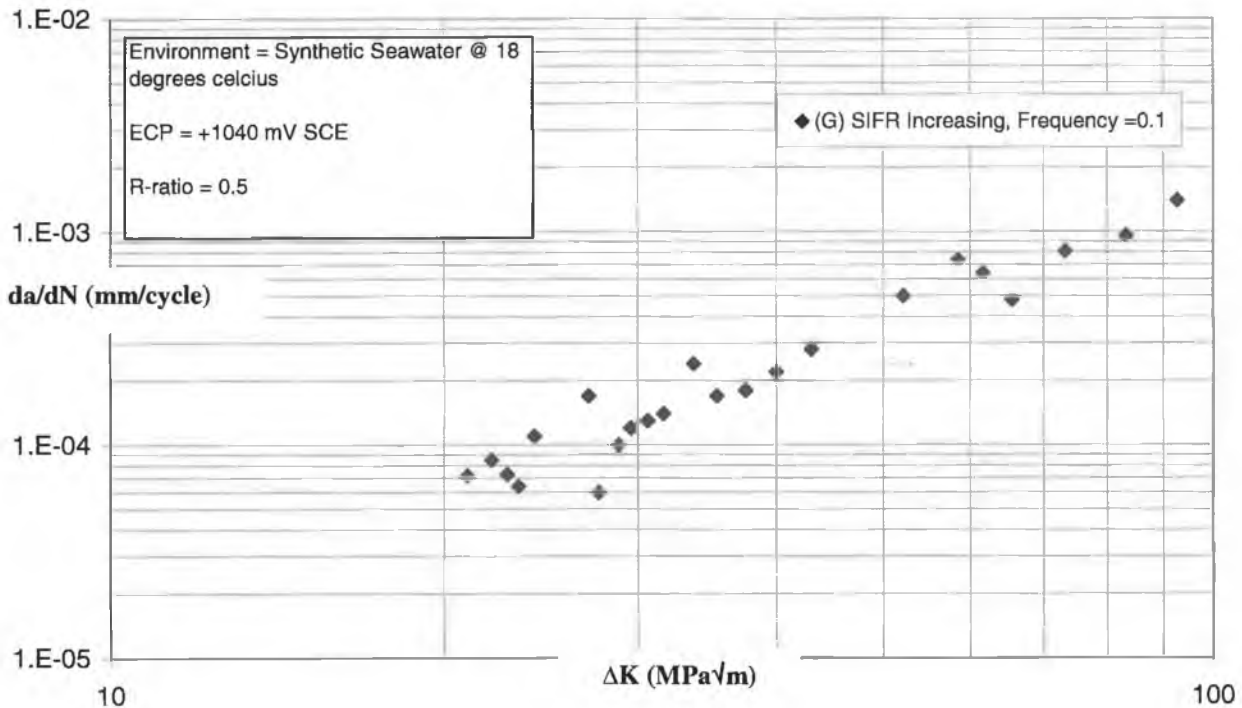


Figure 4.42 Base metal tested in synthetic seawater (+1040mV SCE).

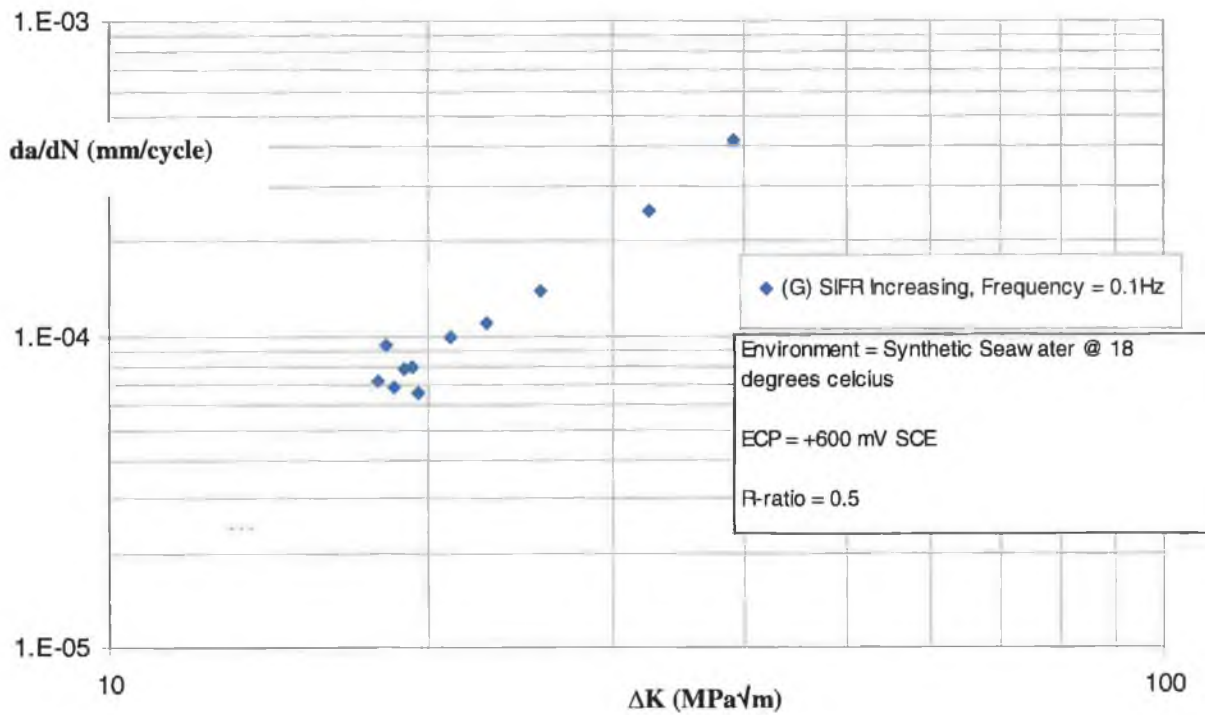


Figure 4.43 SMA weld metal tested in synthetic seawater (+600mV SCE).

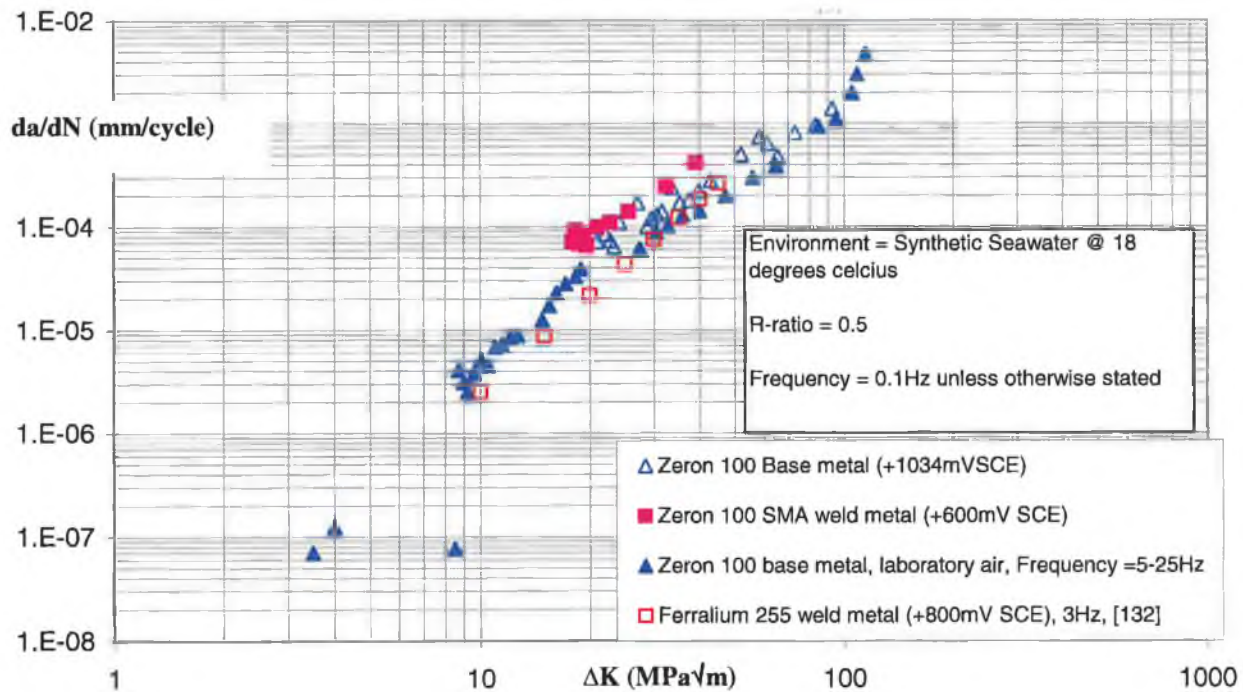


Figure 4.44 Base and weld metal at high potential in seawater and in laboratory air.

Paris law constants and relevant data are given below.

Sample	C	m	R <sup>2</sup>	Average Corrosion Cell Data			
				pH	ECP v SCE (mV)	Current Density (mA/mm <sup>2</sup> )	Solution Temp (°C)
Base metal	1E-7	2.0	0.94	8	+1034	1.0 x 10 <sup>-3</sup>	22
SMA weld metal	1E-7	2.2	0.96	8	+600	1.2 x 10 <sup>-6</sup>	19

**Table 4.18 Paris equation coefficients, coefficients of determination and corrosion cell data for tests in synthetic seawater (+600mV SCE). R-ratio =0.5. Oxygen bubbled into seawater.**

With reference to figure 4.22, the base metal was polarised to +1034 mV SCE, which implied the corrosion rate or current density was approximately  $2 \times 10^{-4}$  mA/mm<sup>2</sup>. Therefore, metal was actively dissolved at the crack tip during the crack propagation test. Figure 4.44 shows that the rate of dissolution at the crack tip is too slow to significantly influence crack propagation rates at 0.1Hz. Tavara [132] also observed the negligible influence of a high positive potential on a duplex weld metal (figure 4.44). However, it must be noted that a relatively high loading frequency (3Hz) was utilised.

The low influence of dissolution is backed up by research carried out by Wei [142]. Here, scratching electrode experiments were used to find that the bare surface anodic dissolution current on an austenitic type 304 stainless steel resulted in the dissolution of only a few atomic layers per second, which confirms that the dissolution mechanism is not effective in increasing crack propagation rates dramatically at 20°C.

With regard to the fractography, the appreciable inclusion content in the SMA weld metal may have contributed to the increase in crack propagation rates by a factor of 2 (at  $\Delta K = 30\text{MPa}\sqrt{\text{m}}$ ) over rates in air at +600mV (figure 4.10). With regard to the base metal sample, it was evident that dissolution selectively attacked the grain boundaries (figure 4.45).

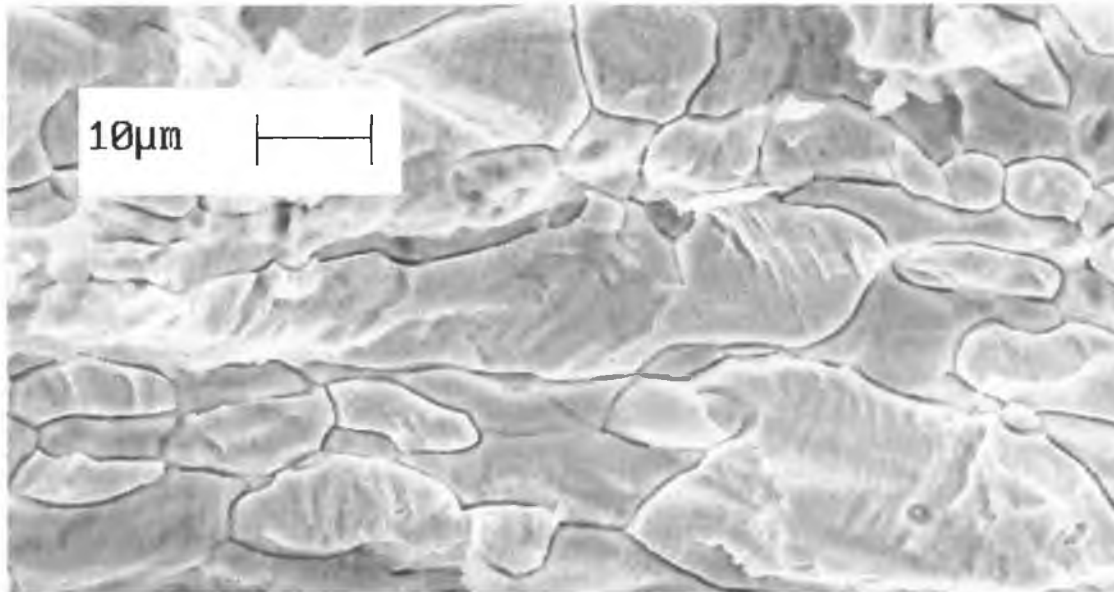


**Figure 4.45 Dissolution of grain boundaries evident on base metal fracture surface tested in synthetic seawater (+1034mV SCE).**

Perdriset reported that dissolution facilitated crossing of the ferrite /austenite phase boundaries, increasing crack propagation rates [141]. Further, the dissolution behaviour of duplex stainless steel 2205 and SAF 2507 has been studied in acidic chloride solutions (4M H<sub>2</sub>SO<sub>4</sub> + 1M HCl) [143]. Selective dissolution of boundary regions between ferrite and austenite phases and of ferrite grains was clearly observed. Ferrite grains dissolved at lower ECPs than austenite grains. Preferential dissolution in boundary regions was much less on SAF 2507 compared to 2205. A well-balanced high content of alloying elements Cr, Mo and N appeared effective in minimising selective dissolution.

The grain boundary dissolution phenomenon gives rise to fracture surfaces taking on a “mud pattern” type appearance as evident in figure 4.45. This effect has been seen before in corrosion fatigue type tests similar to the current work. These tests were carried out on mild steel CCT and SECT specimens at low frequencies (0.17Hz) at free ECP in synthetic seawater [122].

### *Effect of solution temperature on crack propagation rates.*

With regard to the effect of solution temperature on crack propagation rates, Linder [102] working on duplex and superduplex stainless steels carried out crack propagation tests in synthetic seawater at free ECP. Using a loading frequency of 0.2Hz, he observed the temperature independence of corrosion fatigue crack propagation rates suggesting that crack propagation rates are negligibly influenced by anodic dissolution mechanisms at 80<sup>0</sup>C.

In the current research, it was observed from the cyclic polarisation results (figure 4.23) that an increase in temperature from 20<sup>0</sup>C to 80<sup>0</sup>C results in a reduction of the breakdown potential, meaning the passive film is extremely unstable at +650 mV SCE. This is unlike the situation at 20<sup>0</sup>C, where a crack propagation test carried out on the SMA weld metal at +600 mV SCE showed that the passive film was highly stable and/or reformed rapidly when damaged at this potential. In addition, perhaps more importantly, a significant delay ensues at 80<sup>0</sup>C before the passive film can reform once damaged. During this time lag, dissolution on a greater scale than achievable at +20<sup>0</sup>C could occur.

Therefore, it appears possible that solution temperature could have a deleterious effect on crack propagation rates at high positive potentials provided the loading frequency is less than 0.2Hz. However, with reference to figure 4.23, it is also evident that the rate of the corrosion mechanism active at very low potentials increases dramatically by a factor of fifty at -1000mV SCE at 80<sup>0</sup>C. Therefore, it is thought that the corrosion mechanism active at low potentials will still be the most deleterious at 80<sup>0</sup>C. Tests were not carried out in solution at high temperatures as part of the current work due to the requirement to significantly modify the corrosion fatigue test bed, and the availability of published data from tests carried out in seawater at 70<sup>0</sup>C [108]. This data is discussed later.

Overall, from the macrocrack growth rates obtained, it is clear that dissolution was ineffective in increasing crack propagation rates significantly at a loading frequency of 0.1Hz in synthetic seawater (+1034 / 600 mV SCE) at 20<sup>0</sup>C.

### Cathodic overprotection (negative ECP).

The damaging mechanism operating at this ECP proved the most detrimental for the loading and environmental conditions considered in the current research. Evident from figure 4.46 is the fact that the dissolution mechanism only increases the crack propagation rate of the base metal over rates in air by a factor of 1.7 at  $\Delta K = 30\text{MPa}\sqrt{\text{m}}$ . The corrosion mechanism operating at  $-1040\text{mV SCE}$  is twice as damaging with crack growth rates increased by a factor of 4 at  $\Delta K = 30\text{MPa}\sqrt{\text{m}}$ .

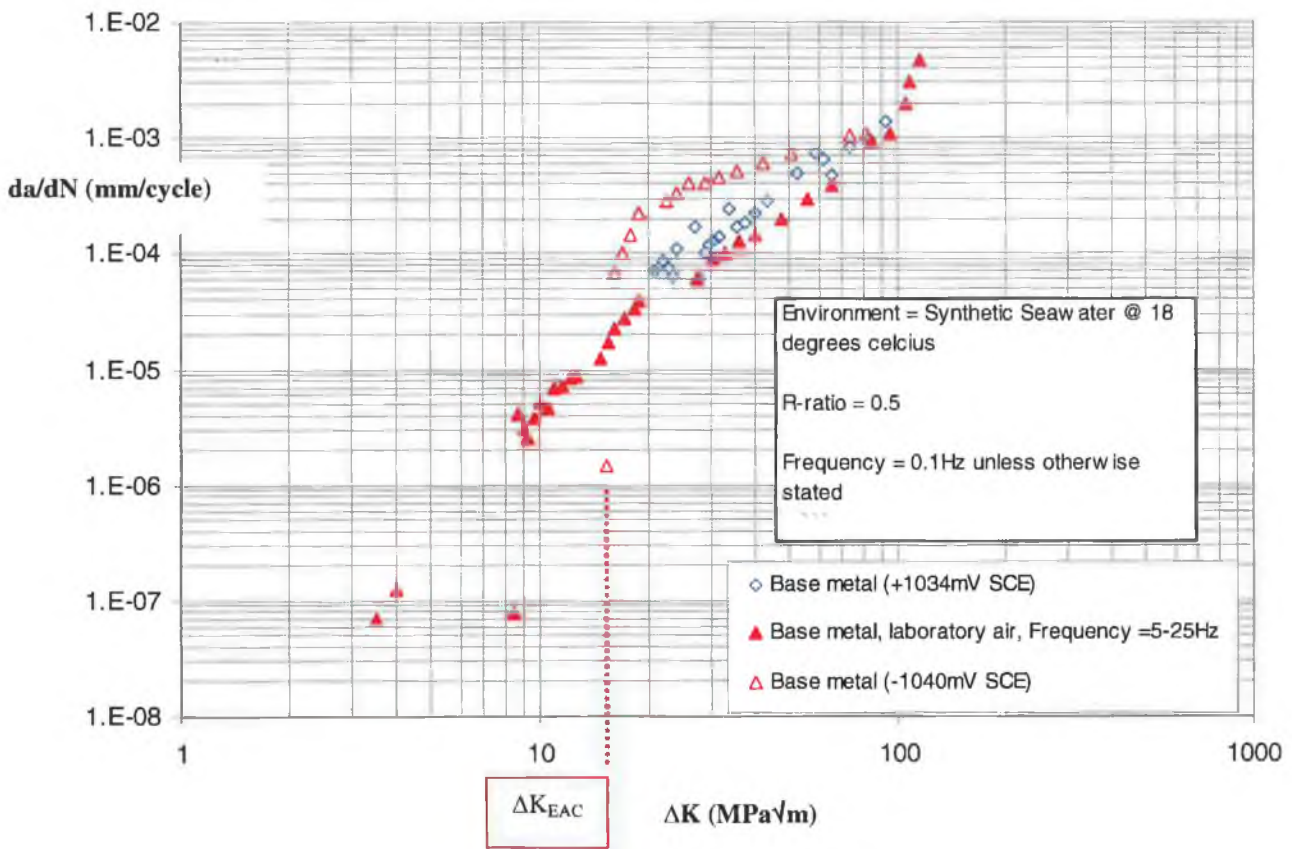
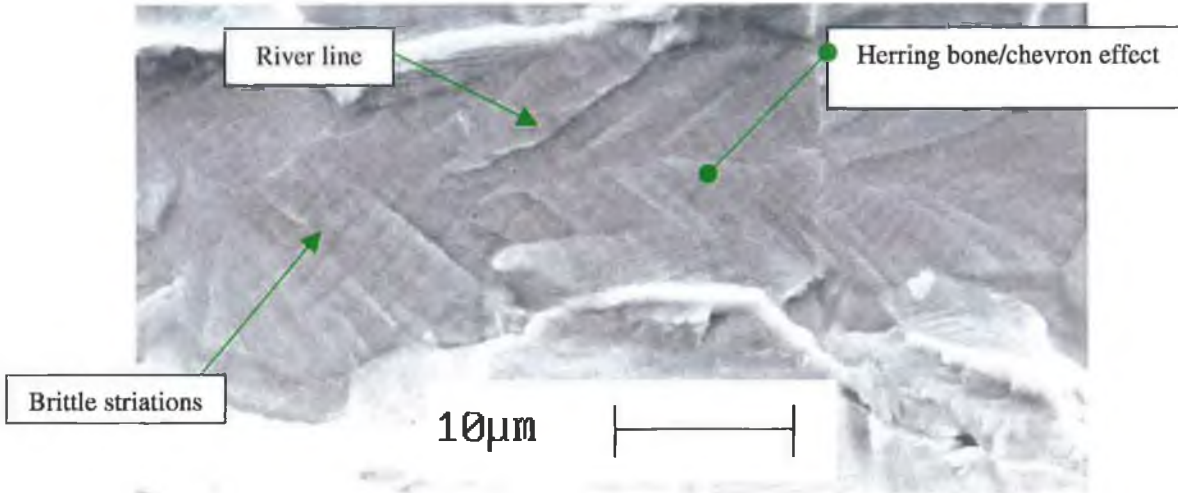
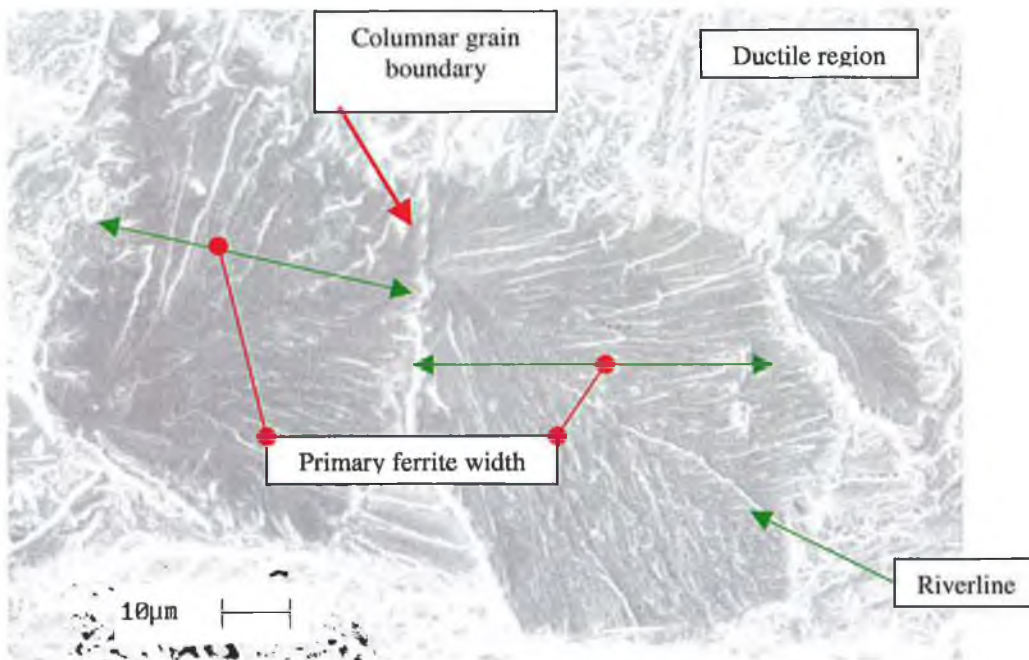


Figure 4.46 Base metal in seawater at positive and negative potentials.

Two key facts point towards a hydrogen assisted damage mechanism. First, the dramatic increase in crack propagation rates above an environmentally assisted cracking threshold  $\Delta K_{EAC}$  (figure 4.46). Second, the classic features prevalent on the fracture surfaces such as fanned cleavage facets, riverlines and brittle striations.



**Figure 4.47** Riverlines and brittle striations evident on base metal fracture surface tested in synthetic seawater (-1040 mV SCE). Propagation direction, left to right.



**Figure 4.48** Brittle cleavage facets fanning out in the direction of crack propagation (left to right) on the fracture surface of SMA weld metal tested in synthetic seawater (-1040mV SCE).

The hydrogen mechanisms responsible for the dramatic increase in crack propagation rates will be discussed later. First, the crack propagation results are presented and discussed.



**Threshold for the onset of hydrogen assisted fatigue crack propagation**

First,  $\Delta K$  decreasing tests (test type H, table 3.6) were carried out on a polarised (-1040mV SCE) base metal and GTA weld metal sample (figure 4.49 & 4.50). The tests commenced at 20MPa $\sqrt{m}$ . Even though the tests were performed at relatively high  $\Delta K$  and R-ratio (0.5), closure due to calcareous deposit formation was thought to result in non-conservative data using the  $\Delta K$  decreasing tests. The crack growth rate dropped below the average laboratory air data very quickly subsequent to load shedding for both samples.

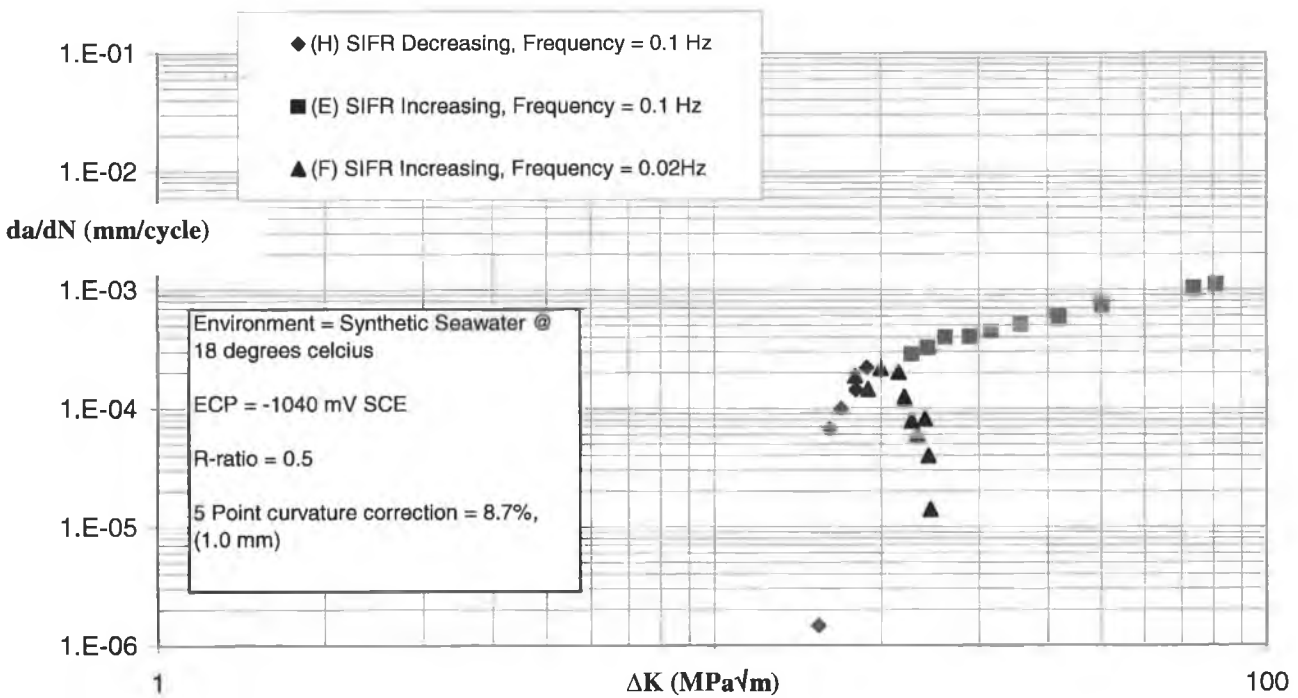


**Figure 4.49 Three tests on base metal cathodically overprotected in synthetic seawater.**

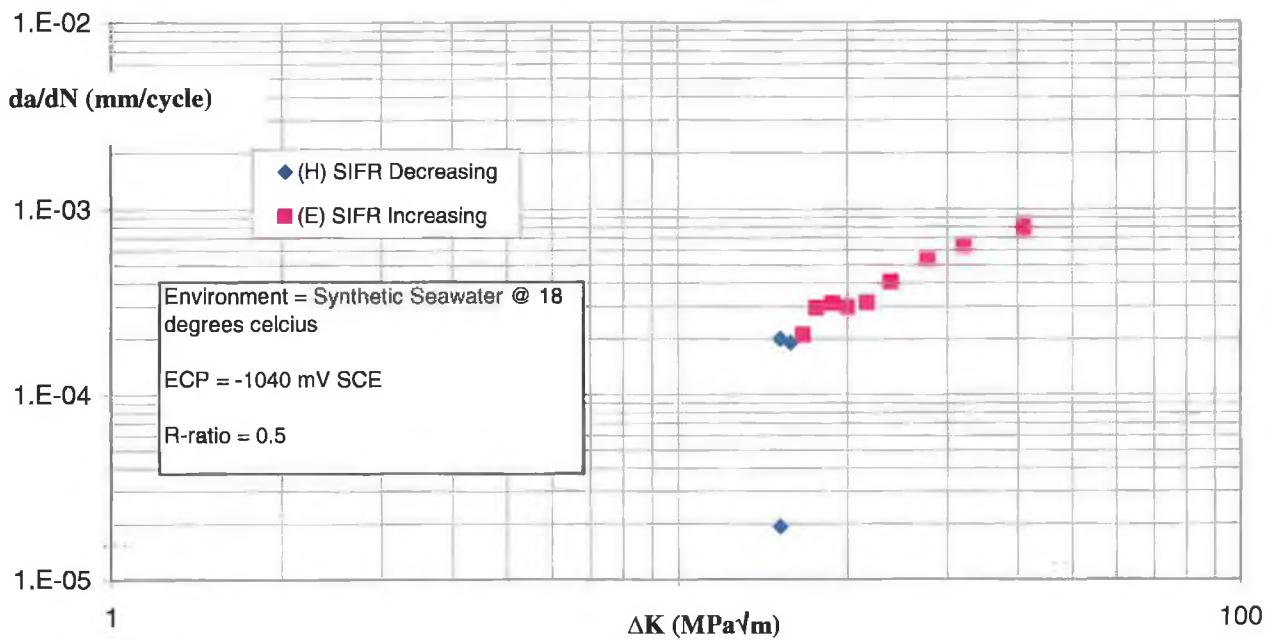


Figure 4.50 Two tests on GTA weld metal cathodically overprotected in synthetic seawater.

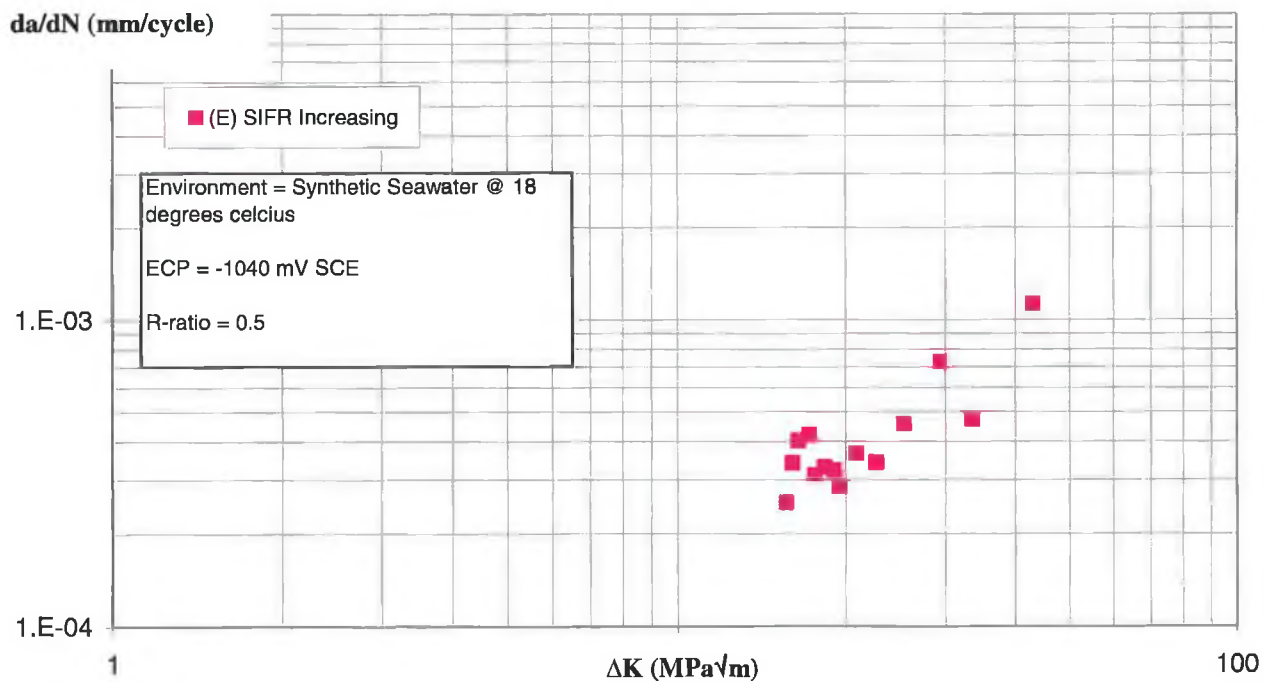


Figure 4.51 SMA weld metal cathodically overprotected in synthetic seawater.

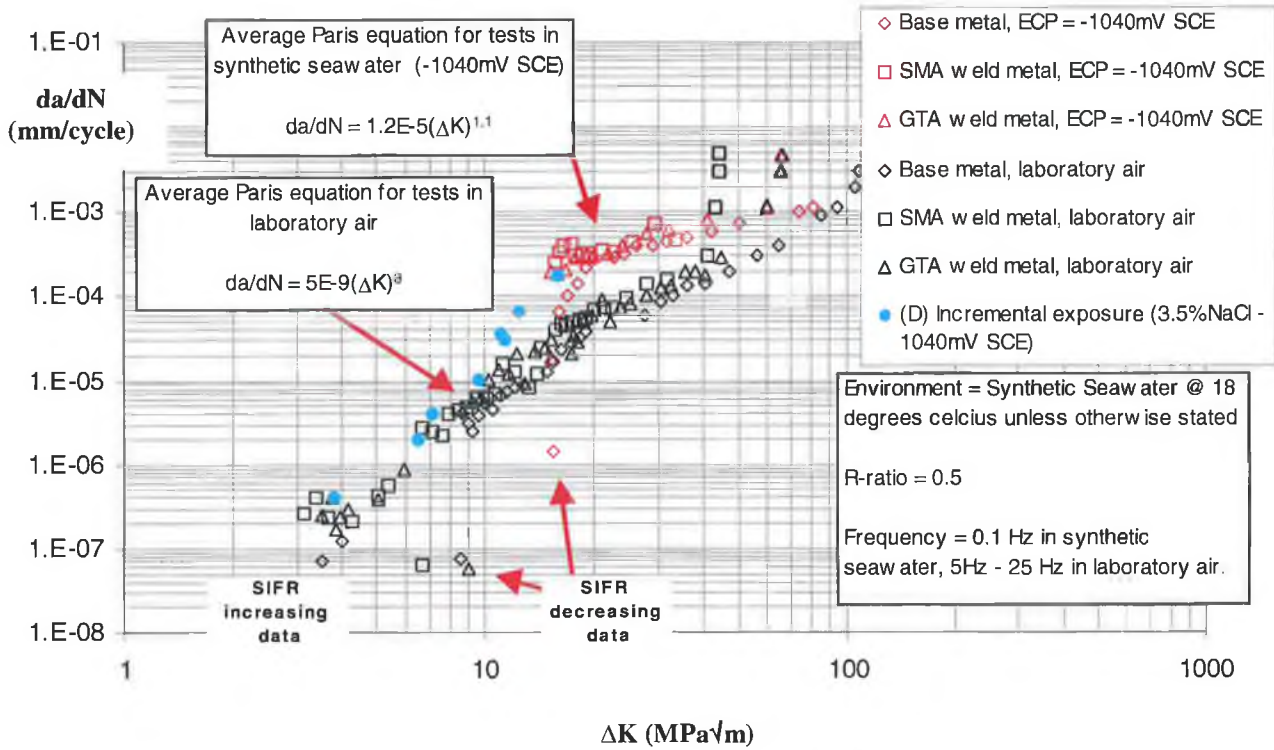


Figure 4.52 Test results in synthetic seawater at -1040mV SCE.

$\Delta K_{EAC}$  values obtained from  $\Delta K$  increasing type tests were lower than values found with  $\Delta K$  decreasing tests (table 4.19). This was mainly because the 3.5% NaCl solution used in these tests inhibited calcareous deposit formation. Crack closure was consequently minimised (figure 4.52). Therefore, the lifetime of a component can be dramatically reduced in the presence of hydrogen on the attainment of a critical stress intensity factor range (11MPa√m for R-ratio =0.5). In addition, the lowest  $\Delta K$  at which hydrogen contribution to sub critical failure processes is maximised is approximately 15MPa√m (figure 4.52).

Sample	Threshold in Seawater ( $\Delta K_{EAC}$ )	
	$\Delta K$ decreasing (MPa√m)	$\Delta K$ increasing (MPa√m)
Base metal	15.4	11
GTA weld metal	15.2	---
SMA weld metal	---	11

Table 4.19 Thresholds obtained in synthetic seawater (-1040mV SCE).

*Stage II Crack Propagation*

The crack growth rates obtained from  $\Delta K$  increasing type tests (where samples were precracked using the traditional load shedding technique (test E) and polarised at -1040 mV SCE) were similar, exhibiting a linear trend on a log-log scale (figures 4.49-4.52). Fast fracture values obtained were the same as those obtained in laboratory air. However, crack growth rates were greater than in laboratory air by a factor of approximately 5 at  $\Delta K = 20\text{MPa}\sqrt{\text{m}}$ , reducing uniformly to a factor of 3.5 at  $\Delta K = 40\text{MPa}\sqrt{\text{m}}$ .

The Paris law coefficients for the linear portion of the data are given below.

Sample	C	m	R <sup>2</sup>	Average Corrosion Cell Data			
				pH	ECP v SCE (mV)	Current Density (mA/mm <sup>2</sup> )	Solution Temp (°C)
Base metal	2E-5	0.9	0.97	8	-1045	3.1 x 10 <sup>-4</sup>	22
GTA weld metal	5E-6	1.3	0.96	8	-1044	3.0 x 10 <sup>-4</sup>	21
SMA weld metal	1E-5	1.1	0.72	8	-1024	2.5 x 10 <sup>-4</sup>	20

**Table 4.20 Paris equation coefficients, coefficients of determination and corrosion cell data for tests in synthetic seawater (-1040 mV SCE), R-ratio =0.5.**

The coefficient of determination is relatively low for the SMA weld metal, but the data, while more scattered, is consistent with the data for the base and GTA weld metal (figure 4.52). Consequently, the test was not duplicated. The deviation from linearity of the SMA sample may be a result of residual hydrogen concentration present from the SMA welding process as mentioned in the literature review.

It is appropriate to compare the data obtained in the current research with data obtained by other researches which is available in the literature. Other researchers data includes some tests which were carried out with cathodic protection. However, most of the test data is at free ECP.

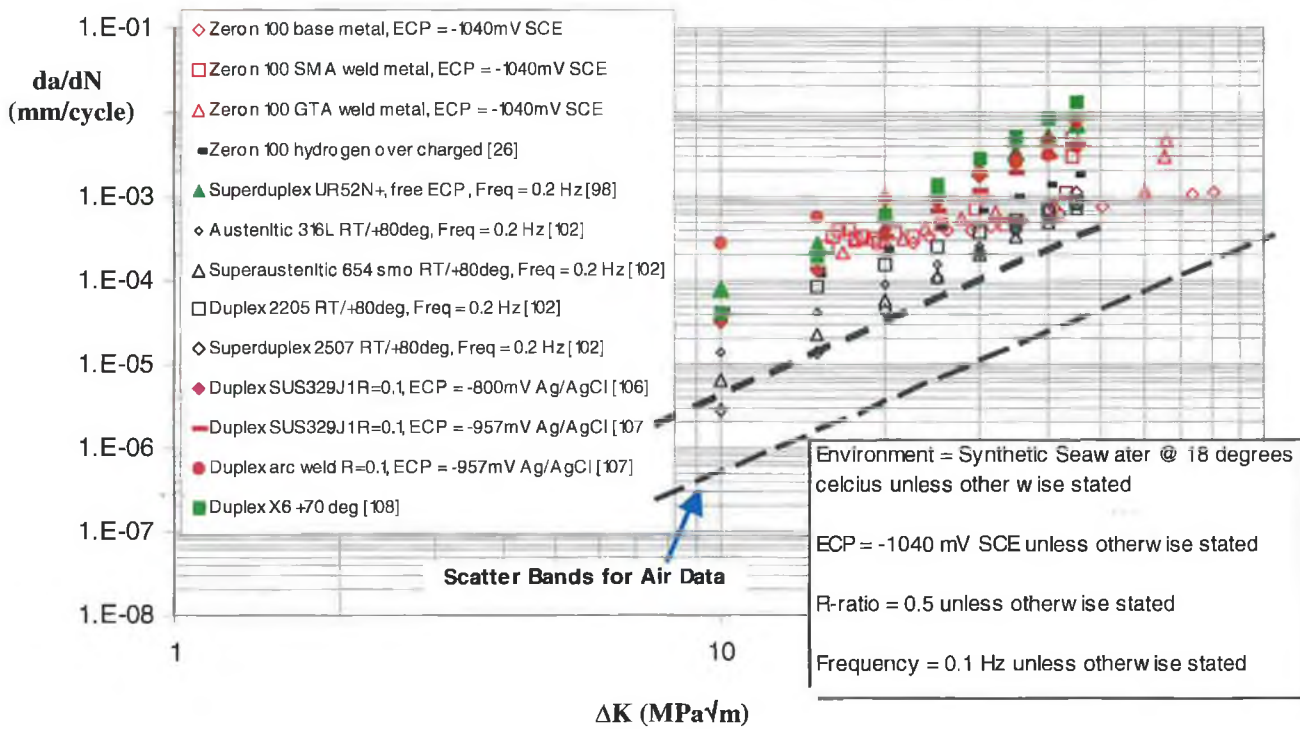


Figure 4.53 Current data and other researchers corrosion fatigue data.

First, the better performance ( $\Delta K > 20MPa\sqrt{m}$ ) of the current base and weld metals relative to the duplex stainless steel SUS329 is clearly evident in figure 4.53. These tests were carried out at the same frequency (0.1Hz) under cathodic protection. This is to be expected as the current superduplex material has a significantly higher alloy content which promotes corrosion resistance.

It is also clear in figure 4.53 that tests carried out at 0.2Hz don't show a significant increase in crack propagation rates over the scatter band in air. Therefore, it is not a fair comparison between this data and the current results. However, data for the superduplex alloy UR52N+ contradicts this point as the crack propagation rate is similar to the rates found in the current research at  $\Delta K = 15MPa\sqrt{m}$ . The crack propagation rate for UR52N+ subsequently increases with a slope of 3. In contrast, the current data only increases with a slope of 1.1. The reason thought responsible for this trend is discussed later.

Finally, the good correlation between Marrows results [26] for Zeron 100 hydrogen charged in 3.5%NaCl and the current data suggests that the current data represents an upper bound for environmentally assisted crack propagation in seawater.

A  $\Delta K$  increasing test (test F) was performed on a base metal sample (-1040mV SCE) at 0.02Hz, commencing at  $18\text{MPa}\sqrt{\text{m}}$  (figure 4.49). The initial four data points correspond well with the data obtained from the base metal test at 0.1Hz. Subsequent data dropped below data obtained in laboratory air. This occurred at a  $\Delta K$  of  $25\text{MPa}\sqrt{\text{m}}$ . In order to assess the contribution of time dependent corrosion processes the  $da/dN$  data was converted to  $da/dt$  data (figure 4.55), which represents crack growth on a time basis as opposed to crack growth per load cycle.

The effect of a relatively low loading frequency (freq. 2) is thought to give rise to three possible scenarios as shown in figure 4.54. The first scenario occurs if the corrosion mechanism is capable of increasing the crack propagation rate independent of the fluctuating load applied (red line, long dash). Therefore, corrosion fatigue crack propagation is time dependent. This situation approaches stress corrosion cracking (SCC) behaviour where crack propagation is possible in the presence of an applied static load and an aggressive environment. The second scenario is cycle dependent. Here the crack growth rate at the lower loading frequency (continuous red line) is reduced by a factor which corresponds to the ratio of the loading frequencies. The third scenario is when the corrosion mechanism impedes the corrosion fatigue crack propagation mechanism (red line, short dash). A typical example is the corrosion product wedging effect.

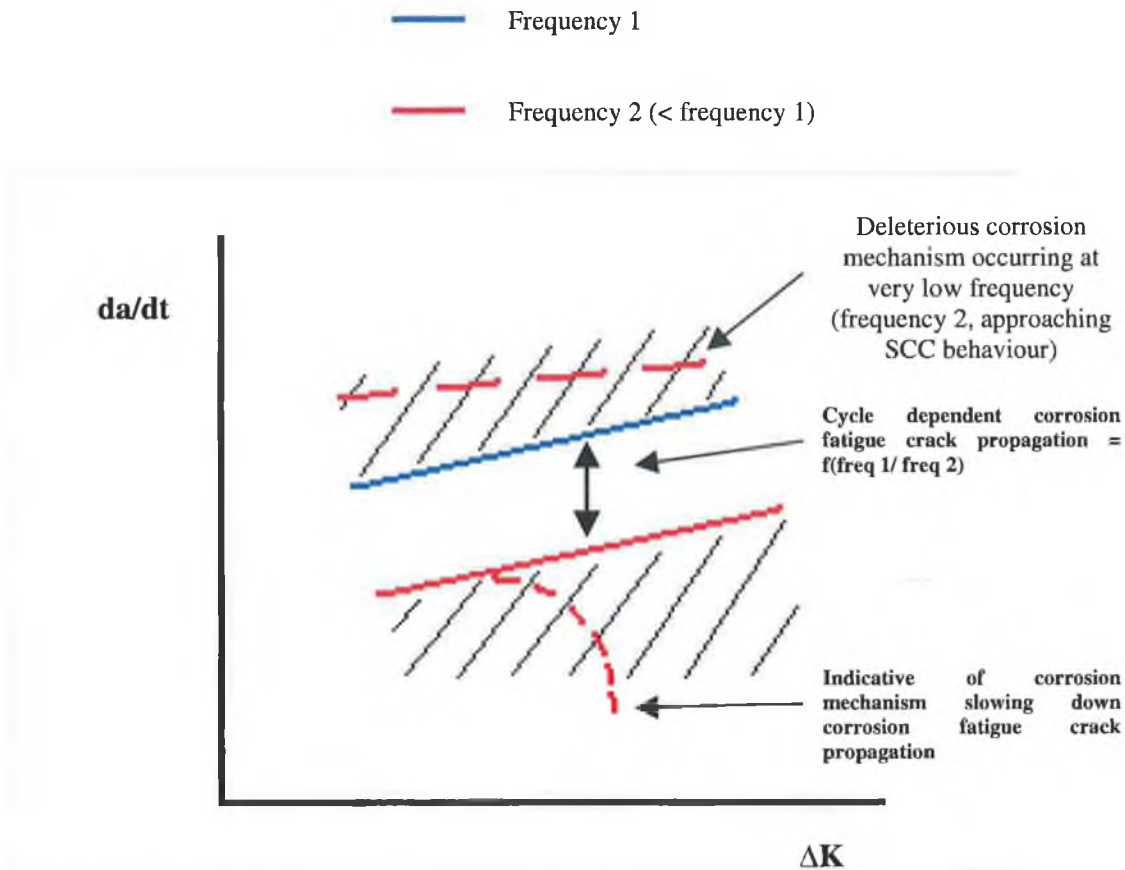


**Figure 4.54 Schematic of the effect of loading frequency on corrosion fatigue crack propagation on a time basis.**

Data from stress corrosion cracking (SCC) tests on high strength (0.4-0.8% carbon) steel [144] is shown in figure 4.55. Yield strengths of the steels tested are in the range 1400-1950MPa. This data corresponds to the first scenario (red line long dash, figure 4.54, i.e. the corrosion mechanism is capable of increasing the crack propagation rate independent of an applied fluctuating load. Only a constant load is required for crack propagation.

With regard to the current data, figure 4.55 shows that consistency in crack extension per unit time for two different loading frequencies has been lost. At 0.02Hz, crack extension takes a significantly longer time than at 0.1Hz. At  $\Delta K=20\text{MPa}\sqrt{\text{m}}$ , the ratio of  $da/dt$  at 0.1Hz to  $da/dt$  at 0.02Hz is 5.6. Therefore, crack propagation is 5.6 times faster at 0.1Hz than at 0.02Hz. This is typical of scenario two type behaviour where the ratio of loading frequencies ( $0.1/0.02 = 5$ ) corresponds with the increase in crack propagation rate (5.6).

Scenario three type behaviour is prevalent at  $\Delta K > 20\text{MPa}\sqrt{\text{m}}$ . The crack propagation rate is reduced significantly to below crack growth rates in laboratory air.

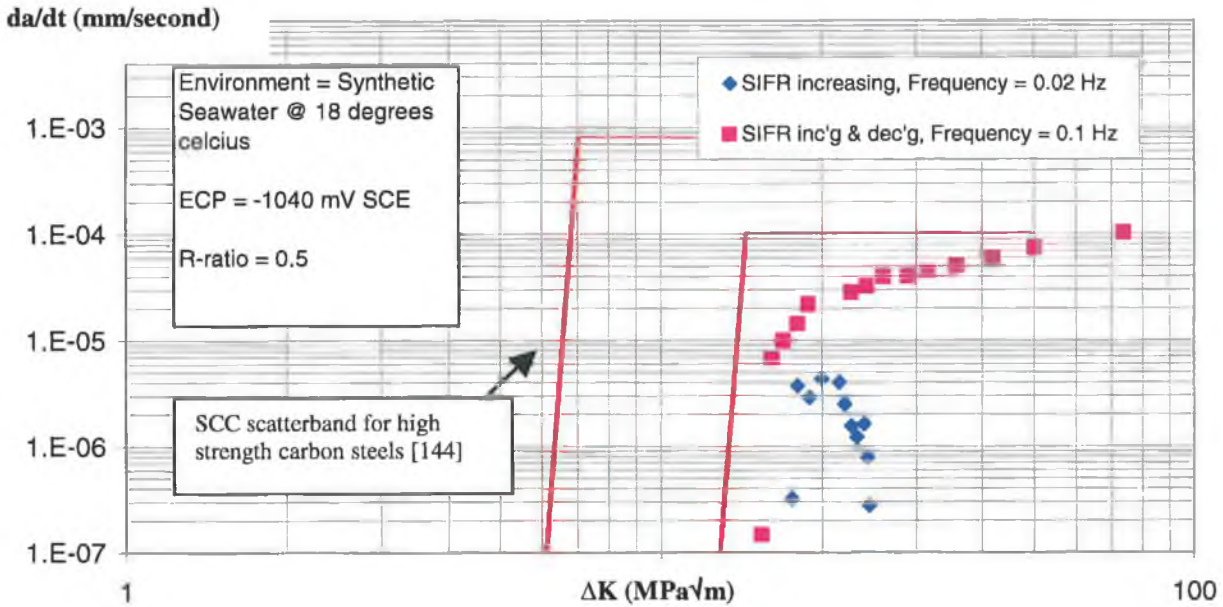


**Figure 4.55 Crack propagation data for base metal cathodically overprotected expressed on a time basis.**

It is thought that crack closure caused by calcareous deposit formation resulted in the reduction in crack growth rates at 0.02Hz ( $\Delta K > 20\text{MPa}\sqrt{\text{m}}$ ). Significant calcareous deposit had sufficient time to form on the fracture surfaces during the loading part of each load cycle, which at 0.02Hz lasted 25 seconds.



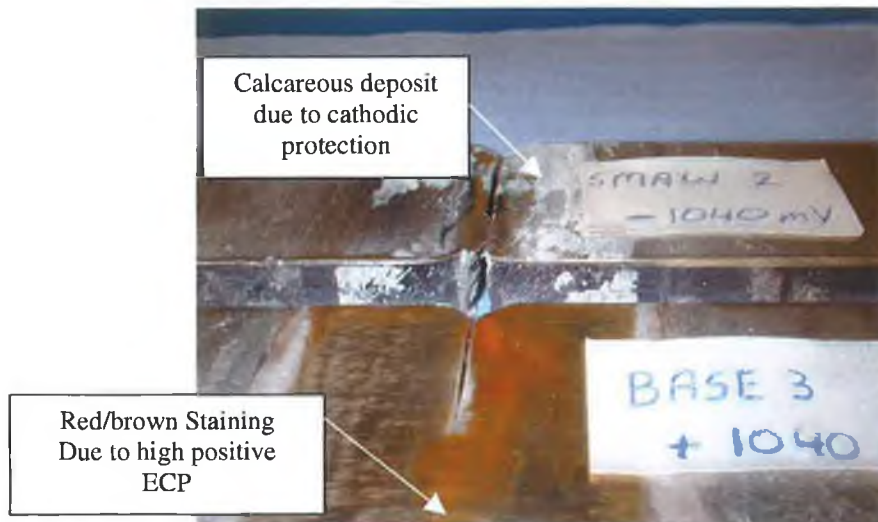


**Figure 4.56 Calcareous deposit formation and rust staining on SENB4 samples subsequent to testing.**

The calcareous deposit increased in thickness during each load cycle causing progressive crack closure. As such,  $\Delta K$  effective was reduced and consequently crack propagation rates dropped rapidly to below rates obtained in laboratory air. Therefore, both mechanical and chemical damage were minimised. It appears that there was insufficient time for significant calcareous deposit formation to occur at 0.1Hz. As such,  $\Delta K$  effective was maximised. Overall, significant calcareous formation is possible during a half load cycle at 0.02Hz (25 seconds) at  $20\text{MPa}\sqrt{\text{m}}$  but not possible at 0.1Hz (5 seconds) at  $20\text{MPa}\sqrt{\text{m}}$  in synthetic seawater at  $20^{\circ}\text{C}$ .

### ***Mechanistic information***

With regard to the hydrogen damaging mechanism, the common consensus is that hydrogen embrittles a percentage of the ferrite present along the crack front. Marrow postulated that, the degree of embrittlement reflected the rate of hydrogen entry to the crack tip [145].

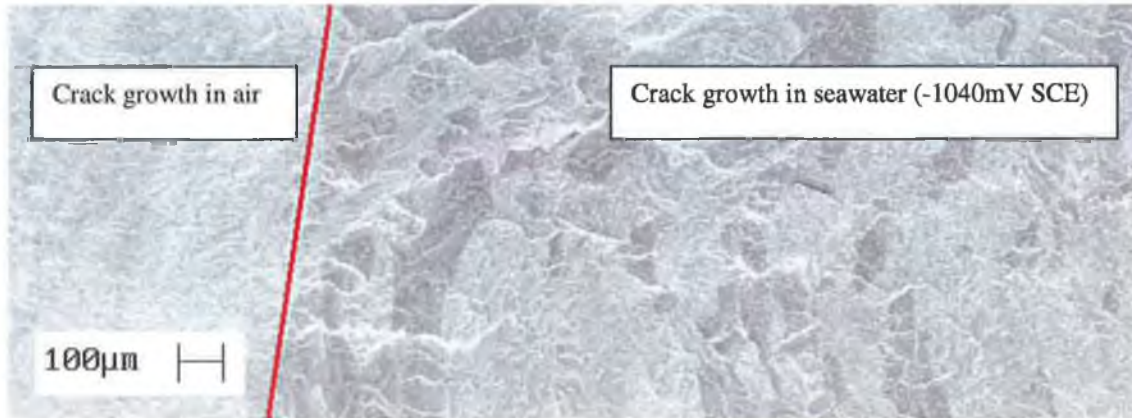


**Figure 4.57** GTA weld metal fractograph showing precrack grown in laboratory air and brittle facets, which occurred in synthetic seawater (-1040mV SCE). Crack propagation direction, left to right.



**Figure 4.58** Base metal fractograph showing distribution of brittle cleavage facets, which occurred in synthetic seawater (-1040mV SCE).

Evident from the fractographs above is the effect of the structure of the weld metal on the distribution of cleavage. Columnar type grains are embrittled preferentially in the weld metal. This shows that the primary ferritic structure of the weld metal initially formed on cooling, dominates even after the formation of austenite in the columnar grains. Perhaps austenite reformation was suppressed in some columnar grains due to an absence of austenite promoting alloying elements such as nitrogen. Columnar

grains with low austenite contents would be more susceptible to embrittlement as austenite is known to act as a hydrogen sink.

However, Bulloch [146] established that the degree of environment assisted crack growth, under ambient conditions is uniquely related to the extent of static failure mode and not the type (intergranular, cleavage etc). Therefore, the distribution of embrittlement is insignificant. The percentage cleaved is the critical variable. Bulloch proposed an environment enhancement ratio, which relates the extent of cleavage to the increase in crack growth rate caused by an embrittling environment [146]:

$$\frac{(da/dN)^*}{da/dN} = \frac{1}{(1 - mC)^5} \quad 4.4$$

where

$da/dN^*$  is the crack propagation rate in aggressive environment

$da/dN$  is the crack propagation rate in laboratory air

$C$  is the fraction of crack front exhibiting environmental assisted cracking

$M = 0.65$  for average line or  $M = 1$  for upper bound.

As can be seen from figure 4.59, the current data agrees reasonably well with Bulloch's model. The data is biased towards the upper bound, and this may be a result of charging the samples. Bulloch verified his model using granular bainite and pearlitic steels; as such the model appears to be insensitive to microstructure.

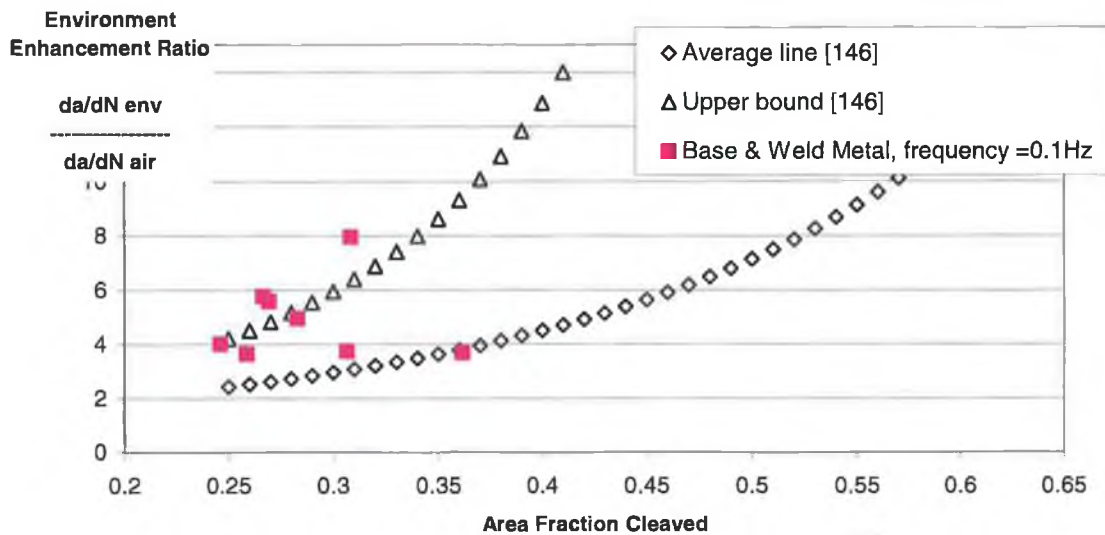


Figure 4.59 Environment enhancement ratio v area fraction cleaved.

The area fraction cleaved ranged from 24 to 36% for the base and two weld metals. There was no significant dependence on  $\Delta K$ . As such, the average cleavage was 30%.

Implicit in Bullochs model, is the assumption that the crack growth rate is controlled by the remaining ductile ligaments. Support for this point is evident in the current work, where good agreement exists between the ductile striations measured on the fracture surfaces of the base and GTA weld metal samples and the macrocrack growth rates (figure 4.60).

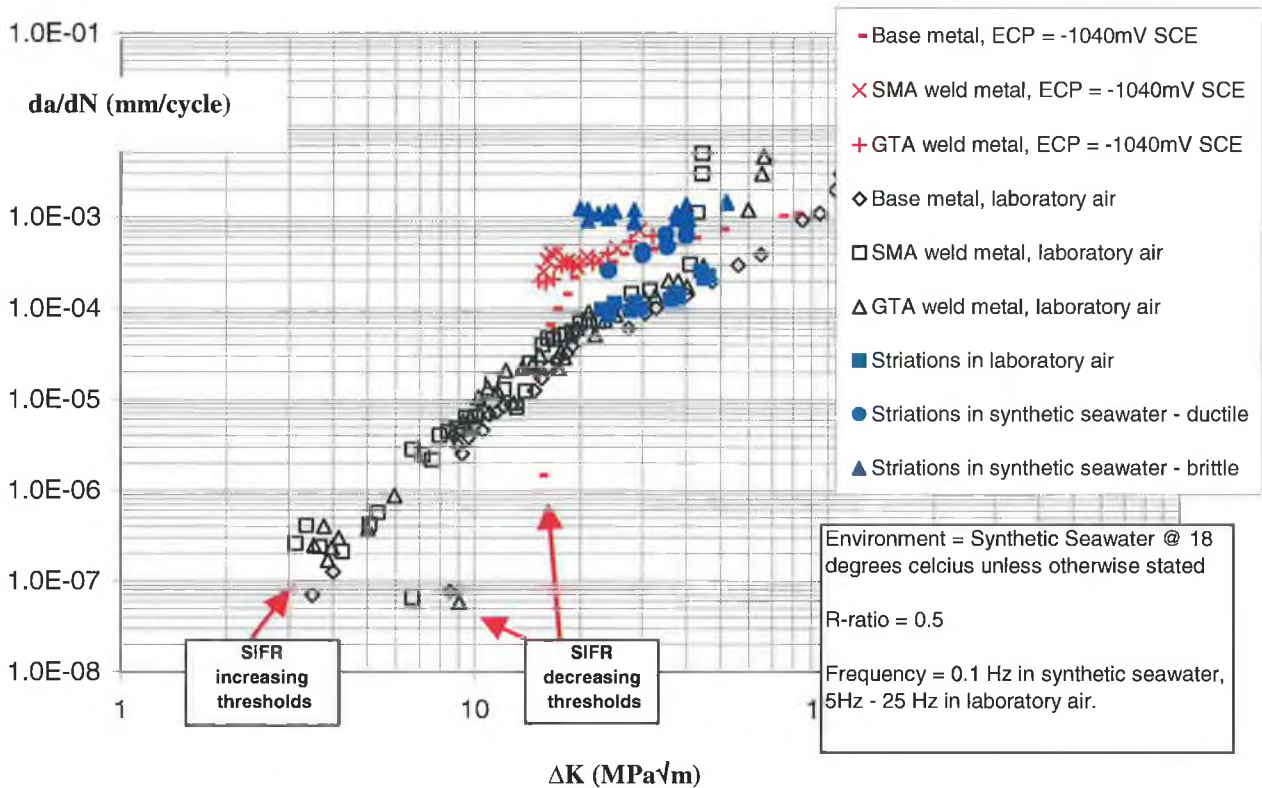


Figure 4.60 Ductile and brittle striations relative to macrocrack growth rates.

Therefore, crack growth rates are increased due to embrittled ferrite fracturing prematurely on the positive portion of a load cycle. This serves to increase the effective  $\Delta K$  acting on the remaining ligaments, leading to much faster crack growth rates than those obtained in benign environments such as laboratory air.

It was noted earlier that the average percentage of ferrite cleaved in the base and weld metals was 30%. Therefore, practically all of the ferrite must have cleaved in the weld metals as ferrite contents average just over 30% ferrite (figure 4.20). Consequently, austenite ligaments controlled crack propagation in the weld metals. Because of the large reversibility of slip in austenite, crack nucleation is delayed, and initiation resistance is good [141]. Perhaps this is the reason why the slope of the curves in synthetic seawater (-1040mV SCE) are shallower (1.1) than in laboratory air (3). Due to the good slip reversibility of austenite, the dependence on  $\Delta K$  is reduced compared to that in laboratory air.

However, with regard to the base metal, a considerable percentage of ferrite (20%) was not embrittled, and it still exhibits the same slope as the weld metals. The fact that the crack propagation rates of the base and weld metals are comparable shows that the effect of phase content on crack propagation rates was negligible. The percentage cleaved had the dominant effect.

Even though the crack propagation rate in the current work is controlled by ductile deformation and hence ductile striation spacing, it is important to consider the brittle striations present, as these could take on added significance if embrittlement was more severe, i.e. occupied a greater percentage of the fracture surface.

Marrow carried out tests on Zeron 100 in brine (3.5% NaCl,  $R = 0.5$ ,  $f = 0.1\text{Hz}$ ) with cathodic overcharging and in high purity water ( $R=0.5$ ,  $f = 5\text{Hz}$ ) over a  $\Delta K$  range of 20 MPa $\sqrt{\text{m}}$  to failure [26]. Crack growth rates in both cases were similar to the current results in synthetic seawater under cathodic protection. The average cleavage fraction in high purity water in the  $\Delta K$  range 20 to 28MPa $\sqrt{\text{m}}$  was approximately 30%, which is the same as the average percentage found in the current research (figure 4.59). Brittle striation spacing averaged at 1 micron at  $\Delta K = 30\text{MPa}\sqrt{\text{m}}$  and  $\Delta K$  dependence was low at 0.4 [26].

A similar phenomenon was found in the current research where the brittle striation spacing measured on the base and GTA weld samples ranged between 1 and 1.5 microns over a  $\Delta K$  range of 28 – 52MPa $\sqrt{\text{m}}$  (figures 4.60 and 4.68). This implies that the macroscopic crack growth rate was 3.3 times less than the brittle striation spacing at  $\Delta K = 20\text{MPa}\sqrt{\text{m}}$ . As such, 3.3 ductile striations were formed to every one brittle striation at  $\Delta K = 20\text{MPa}\sqrt{\text{m}}$ . This reduced to 1.5 ductile striations at approximately  $\Delta K = 40\text{MPa}\sqrt{\text{m}}$ . Therefore, a conditioning period took place during/before the formation of a brittle striation. Brittle striation measurements were also carried out on the base metal sample tested at 0.02Hz in synthetic seawater at -1040 mV SCE. Striation spacing at  $\Delta K = 20\text{MPa}\sqrt{\text{m}}$  agreed well with striation spacings measured on samples tested at 0.1Hz. In addition,  $\Delta K$  dependence was low at 0.4.

Makhlouf working, on an X6 duplex stainless steel, found that by heating synthetic seawater (+70°C so that aggressivity was increased), crack growth rates at 0.1Hz increased dramatically at free ECP [108]. Brittle striation width corresponded with macroscopic growth rates. Therefore, brittle striation formation controlled the macroscopic crack growth rate. In addition, brittle striation spacing was highly  $\Delta K$  dependent, i.e. 3.84. This is also thought to be the case for the test on the superduplex stainless steel UR52N+ [98] shown in figure 4.53. Cleavage percentages were not stated for Makhlouf's test but it is thought that percentage cleaved approached 50%.

Therefore, it is clear that if sufficient hydrogen is continuously produced at the crack tip, it is possible to obtain data, which is highly  $\Delta K$  dependent and crack growth rates are maximised. In other words, brittle striation formation can control the crack propagation rate. This is a worse case scenario, and is not represented by the current data.

It is thought that the quantity of hydrogen produced at the crack tip is the decisive influencing factor. This is controlled by the charging method. In Makhlouf's case, high solution aggressivity caused a high current density to concentrate and flow on the fresh metal exposed at the crack tip. As such, hydrogen evolution was maximised and increased in proportion to the fresh metal exposed. In the current research, a limit (constant ECP) was present on hydrogen evolution. The current density dropped with increase in fresh metal exposed, due to the sample potential being controlled. Therefore, the extent of embrittlement/striation spacing remained practically constant.

## **4.4 Modelling**

This section concerning modelling is composed of two parts. First, the crack propagation data from the current research is manipulated into a format where the number of load cycles to failure at a given stress range can be determined. Data in this form is extremely useful as design data and can be easily compared to existing design data for structural steel butt welds. Secondly, a new mechanistic model for subcritical brittle crack growth in superduplex stainless steel base and weld metals is proposed. The new model is based on fractographic evidence and aims to further understanding of environmental assisted cracking phenomena. Through increased understanding of failure mechanisms, improvements in alloy and weld metal synthesis may be possible.

### ***4.4.1 Fatigue life modelling***

In the case of welded structures, the most widely used method for performing fatigue checks at the design stage is to refer to a 'stress range' versus 'number of cycles to failure' curve commonly termed an S-N curve. S-N curves depict the number of cycles to failure of a particular material/weldment subjected to a specific stress range. Therefore, the design engineer can ensure the weldment of interest will not fail at least until a minimum number of fatigue load cycles have been completed while operating at the maximum allowable stress range.

Fatigue design rules have been developed extensively over the last twenty years. Initial standards were directed at the fatigue design of steel bridges (BS 5400). Design rules are now available for pressure vessels (BS PD 5500), aluminium (BS 8118) and general fatigue design (BS 7608). In addition to the British Standards, European standards such as Eurocode 3 (steel structures) and Eurocode 9 (aluminium structures) are available. However, all of these standards are based on the same approach, providing similar design data [147]. They are strongly influenced by the assumption that the fatigue lives of welded joints are strongly influenced by crack propagation [147].



For the purposes of fatigue design, each part of a welded joint which could act as a site for fatigue cracking is placed into one of nine classes, designated B, C, D, E, F, F<sub>2</sub>, G and W (figure 4.61). The critical site for cracking determines the classification of a welded joint.

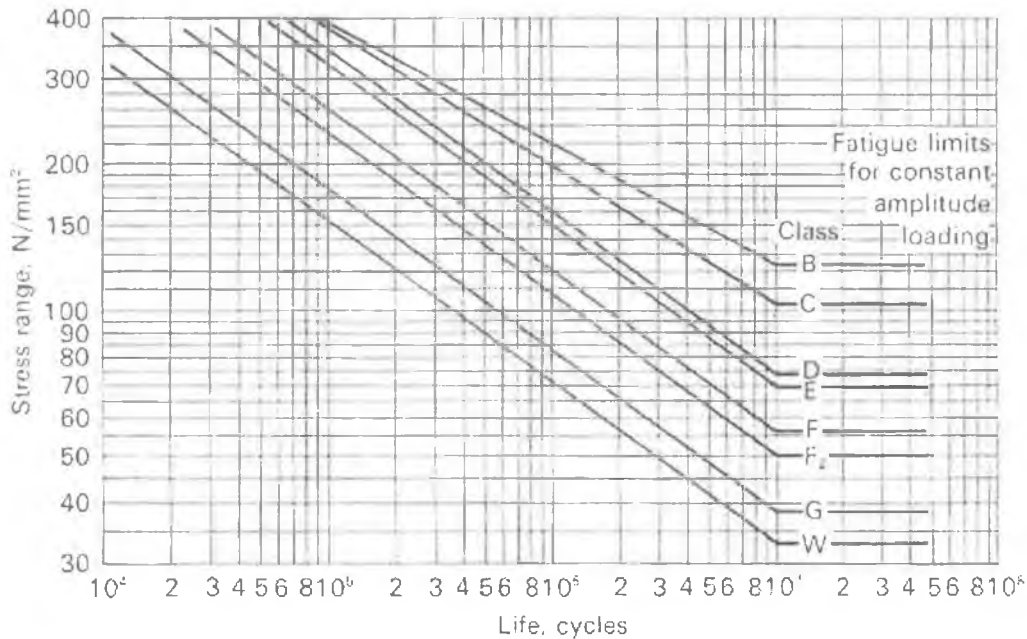


**Figure 4.61 Standard S-N design curves (50% probability of failure) for steel weldments [19].**

It is important to note that weldment fatigue design lines as in figure 4.61 are independent of R-ratio. Stress range is the dominant factor affecting fatigue life. The mean stress is assumed to be distorted by the presence of residual stresses in the weldments.

The weldments in the current research are full penetration butt welds. The weld is transverse to the direction of the maximum principal stress for both the SENB4 and CCT samples. Welding was carried out manually on a shop floor in the flat position for both the SMA and GTA welds. These details dictate that both the SMA and GTA weldments should be considered as class D weldments.

For as-welded steel joints, class D implies that a mean endurance limit of 74 MPa exists at 10<sup>7</sup> cycles. There is a 50% probability of failure anywhere along the mean line. The mean minus two standard deviations is 53MPa. Here the probability of failure is 2.3%.

The S-N curves ‘cut off’ at two points. The first cut off point is the endurance limit, which for all classes in air is assumed to occur at  $10^7$  cycles. This limit is shown in figure 4.61. A cut off at high stresses is also implied by general design rules. This is usually taken as the yield stress of the steel concerned. However, the S-N curves are often extrapolated beyond yield. Such loading can occur in reality. In the current research, it was noted that the direct bending stress acting normal to the propagating crack at fracture for the SMA sample was 869MPa. The GTA and base metal samples managed even higher direct stresses. These stresses are in excess of the design UTS (750 MPa) of the alloy in question. The key point is that the overall behaviour of the samples remained elastic allowing these excessive stresses to exist locally.

The Paris-Erdogan power law was used to estimate the crack propagation life of the base and weld metals.

$$\frac{da}{dN} = C(\Delta K)^m \quad 4.5$$

where

da/dN = rate of crack growth (mm/cycle)

C & m = coefficients.

$\Delta K$  = stress intensity factor range

The coefficients of the Paris law (C & m), which have been the subject of the current research are tabulated below for the base and weld metals in air and seawater under cathodic overprotection.

	Laboratory air		Seawater (-1040mV SCE)	
	C	m	C	m
Base metal	4E-9	3	2E-5	0.9
GTA weld metal	6E-9	3	5E-6	1.3
SMA weld metal	5E-9	3.1	1E-5	1.1

**Table 4.21 Experimental data from current research.**

The crack growth life was estimated by integrating the Paris model over the limit from the initial crack length  $a_i$  to the final crack length  $a_f$ . The total propagation life was calculated from:

$$N = \frac{1}{C} \int_{a_i}^{a_f} \frac{da}{(\Delta K)^m} \quad 4.6$$

At this stage,  $C$ ,  $m$ ,  $a_0$ ,  $a_f$  are available. Initial crack size depends on the flaw size present in the weld metal. Final crack size was defined as the crack length at  $\Delta K_C$  of the particular sample. In addition,  $\Delta K$  as a function of crack length is known:

$$\Delta K = \frac{Y(a)\Delta P}{B\sqrt{W}} \quad 4.7$$

However, it proved awkward to integrate equation 4.6 with respect to crack length ( $a$ ) since the  $K$  calibration function for an SENB4 sample is of the following form:

$$Y(a) = \frac{3 \sqrt{\left(2 \tan \frac{\pi a}{2W}\right) \left(0.293 + 0.199 \left[1 - \sin \frac{\pi a}{2W}\right]^4\right)}}{\cos \frac{\pi a}{2W}} \quad 4.8$$

Therefore, it was decided to establish a simple relationship between  $\Delta K$  and crack length ( $a$ ). A reasonable correlation between  $\Delta K$  and crack length was obtained using an exponential function (figure 4.62).

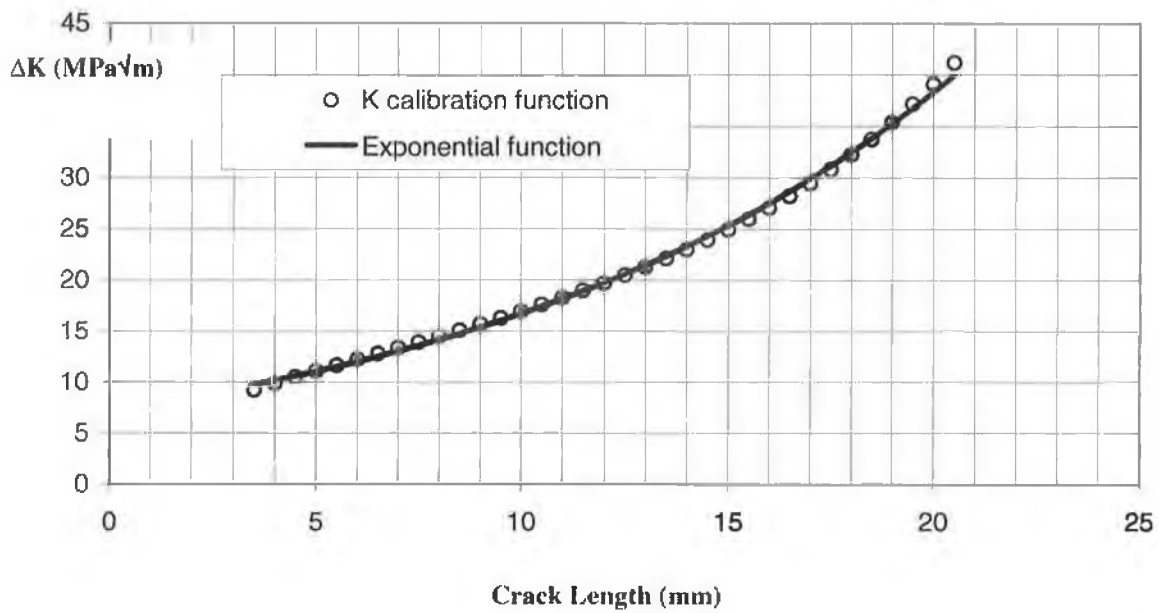


**Figure 4.62 Correlation between  $\Delta K$  and crack length for  $\Delta P = 11\text{kN}$  using an exponential function.**

The exponential function is stated below along with the coefficients  $D$  and  $n$  for six load ranges.

$$\Delta K = De^{na} \quad 4.9$$

where:

$a$  = crack length

$D$  and  $n$  are coefficients

Load range $\Delta P$	Stress range $\Delta \sigma$	Base metal		Weldment	
(kN)	(MPa)	D	n	D	n
5	73	--	--	2.19	0.105
9	131	--	--	4.34	0.097
11	160	--	--	5.50	0.094
15	218	--	--	7.89	0.089
18	261	11.62	0.086	9.70	0.088
25	363	16.64	0.083	13.90	0.084

**Table 4.22 Coefficients for exponential function.**

Since  $\Delta K$  was modified to take the angular misalignment of the weldments into account, two sets of coefficients are listed, one set for the base metal and one set for the weldments. Only two sets of coefficients (for  $\Delta P = 18$  and  $25\text{kN}$ ) are given for the base metal. The difference between the data and the trendline exceeded 5% at  $\Delta K_C$  ( $94 \text{ MPa}\sqrt{\text{m}}$ ) for the lower load ranges. Similarly, the trendline for the  $5\text{kN}$  load range was not considered for the GTA weldment. However, all trendlines were considered for the SMA weldment, as the error was less than 5% up to  $\Delta K_C$  ( $41 \text{ MPa}\sqrt{\text{m}}$ ) for all load ranges.

An initial crack length of  $3.5\text{mm}$  was chosen in the calculation because the correlation between  $\Delta K$  and crack length was poor ( $>5\%$  error) below  $3.5 \text{ mm}$ . In order to be able to compare the data from the model with data from actual smooth samples, a method of taking the initial  $3.5\text{mm}$  crack length into account was required. This was achieved by calculating the nominal stress range (Y-axis figure 4.63) applied to the sample using a cross sectional area calculated from the width minus the initial crack length ( $3.5\text{mm}$ ) x sample thickness. Therefore the data from the model approximates the crack propagation life of a smooth sample with an extremely sharp initial flaw (length  $< 0.1\text{mm}$ ) and not a sample with initial flaw size =  $3.5\text{mm}$ . Using this method, the crack propagation lives predicted by the model fell into the class  $D \pm 2$  standard deviation scatter band for initial flaw lengths from  $3.5\text{mm}$  up to  $15\text{mm}$ .

The stress ranges were calculated using simple beam theory considering the SENB4 samples accessed in the current work.

Substituting the exponential function in for  $\Delta K$  gives:

$$N = \frac{1}{CD^m} \int_{a^i}^{a^f} e^{-nam} da \quad 4.10$$

Integrating with respect to  $a$  gives the fatigue life or more precisely the crack propagation life,  $N$ . The crack propagation life  $N$  can be determined for a particular stress range by substituting the appropriate  $D$  and  $N$  values from table 4.22.

$$N = \frac{1}{CD^m} \left[ \frac{1}{-nm} e^{-nam} + c \right]_{a^i}^{a^f} \quad 4.11$$

Where  $c$  is a constant.

In addition, average values for the base and weld metals relating to the onset of crack growth and to the onset of environmental assisted cracking are tabulated below. This data is incorporated into the S-N curves.

	$\Delta K$ (MPa $\sqrt{m}$ )	$\Delta\sigma$ (MPa)	$\sigma_{max}$ (MPa)
Onset of environmental assisted cracking	11	191	382
Onset of crack growth in laboratory air	3.1	60	120

**Table 4.23 Additional experimental data calculated using simple beam theory considering SENB4 samples employed in the current work.**

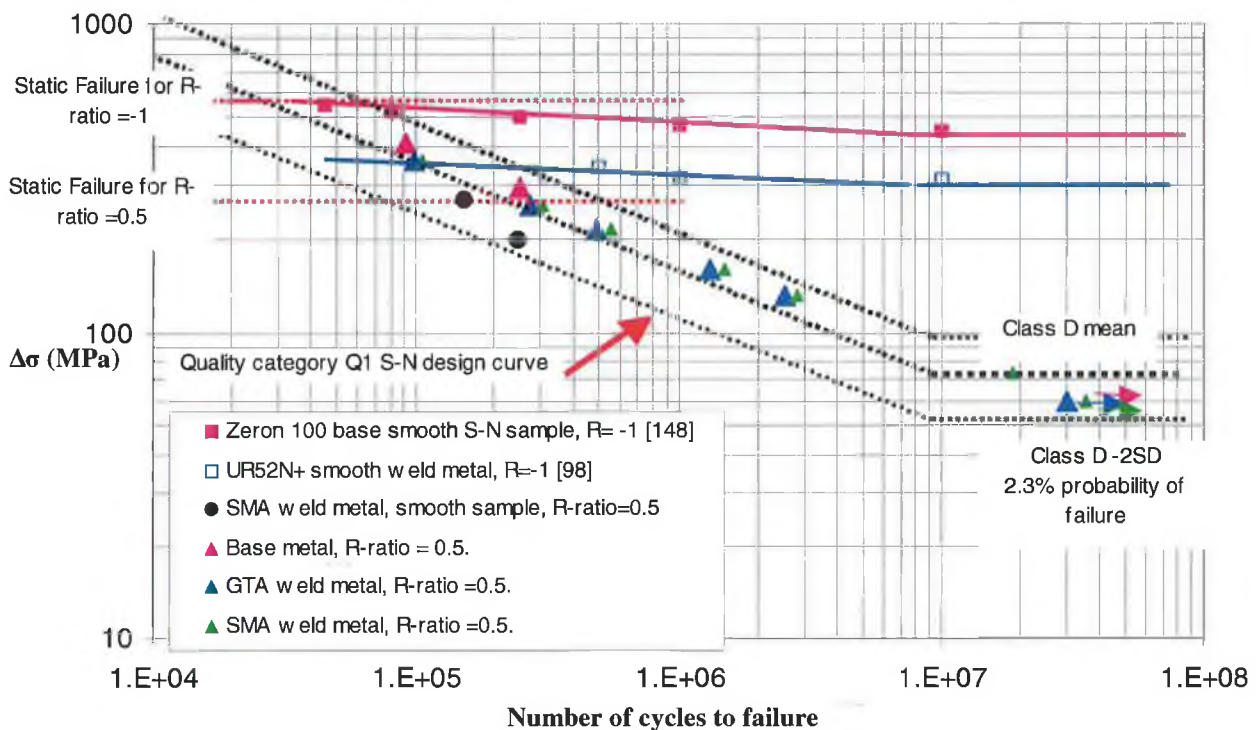


**Figure 4.63 Crack propagation life of weld metals in laboratory air and class D design line.**

Two S-N type tests were carried out on smooth SMA samples to investigate if the model was accurate. The samples were similar to the samples used in the tensile tests (figure 3.3). Relatively high stress ranges were applied to ensure that the number of cycles before crack initiation was minimal. An R-ratio of 0.5 was used. The number of cycles to failure is plotted in figure 4.63. The results fall inside the class D scatter band.

It has been found that there is reasonably good correlation between fatigue crack growth data for various welded metals on the basis of  $\Delta K/E$  where E is Young's modulus [19]. This is partly a consequence of the dominance of fatigue crack growth as opposed to crack initiation [19]. It has been speculated that due to the similar E values of austenitic and duplex stainless steels to structural C and C-Mn steels that design data for such welded structural steels is applicable to welded stainless steels [147]. The S-N curve in air presented above supports this proposal. Evident from figure 4.63 is that the current fatigue life data correlates well with the class D design line for C, C-Mn structural steel weldments. One noticeable difference is that the

endurance limit for the current data is delayed to approximately  $3 \times 10^7$  cycles whereas the design line endurance limit starts at  $1 \times 10^7$  cycles.

In addition, from the flaw assessments carried in sections 4.2.2, it was concluded that the butt weldments in the current research were top quality category Q1 butt welds with regard to the presence and severity of flaws present in the weldments. Evident from figure 4.63 is that this is the case for both types of weld metal as the S-N curve for quality category Q1 coincides with the mean minus two standard deviation line of the class D design curve.

An important point with regard to the current data presented on the S-N curve is that the loading conditions are all known. As mentioned previously, weldment fatigue design lines presented in international standards are represented by a single curve irrespective of the R-ratio used/mean stress applied. Stress range is seen as the dominant factor affecting fatigue life. The mean stress applied is not reported as it is assumed to be distorted by the presence of residual stresses in the weldment. In the current research, the effect of any residual stress fields, which may have been present, was ascertained to be minimal. Therefore, the R-ratio (0.5) applied to the weldments is the effective mean stress experienced during the tests and is not distorted to a major degree by residual stress effects.

The combined effect of seawater and cathodic overprotection can be seen in figure 4.64.



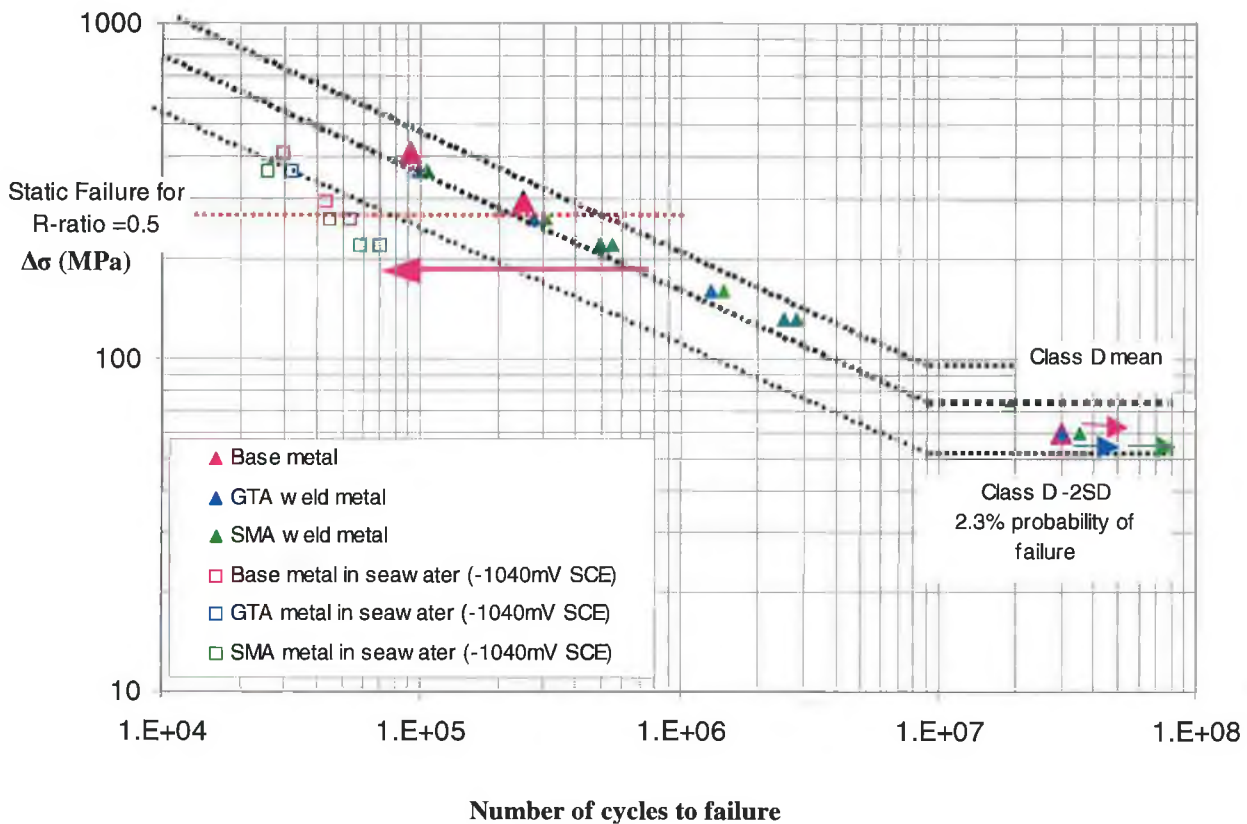


**Figure 4.64 Crack propagation life of weld metals in synthetic seawater cathodically overprotected. R-ratio=0.5.**

It is clear from the figure 4.64 that the weld metals are no longer class D, once seawater and cathodic overprotection are introduced. At a stress range of approximately 190MPa the fatigue life of the base metal and weld metals is reduced by 630,000 load cycles or by over 10 weeks taking a loading frequency of 0.1Hz, which is the average frequency of waves. This significant reduction in fatigue life has critical consequences when defining NDT inspection intervals.

Overall, it is clear that in air at least, the Zeron 100 superduplex stainless steel weld metals considered, can be represented by standard structural steel weldment design lines. However, a significant reduction in fatigue life occurs above a critical stress level when tested at a sufficiently low loading frequency in seawater with cathodic overprotection.

#### ***4.4.2 Mechanistic model of hydrogen assisted fatigue crack propagation***

Up to now, the mechanism of hydrogen assisted cracking has been discussed in terms of subcritical cleavage of ferrite which implies crack propagation depends on the failure of the remaining ductile ligaments mainly composed of austenite. In addition, it was seen that the enhancement of crack growth rates in seawater could be related to the extent of cleavage, independent of the distribution of cleavage sites. It is now necessary to examine the possible embrittling mechanisms, which cause cleavage to occur. This analysis is aided by the use of fractographs of cleavage facets.

First, it is pertinent to discuss some models proposed concerning hydrogen embrittlement and hydrogen assisted crack propagation. Subsequently a new model for hydrogen assisted fatigue crack propagation based on the current data and fractographic evidence is proposed.

A hydrogen embrittlement model was proposed for duplex stainless steels where initially both phases expand as they absorb hydrogen [81]. The ferrite (low solubility) soon becomes saturated at a hydrogen level, which depends on the fugacity of the hydrogen. The fugacity may be looked upon as a vapour pressure modified to correctly represent the escaping tendency of the molecules from one phase (in this case water  $H_2O$ ) into another (e.g. hydrogen gas  $H_2$ ) [149]. In the current research, the fugacity of the hydrogen is mainly a function of the hydrogen charging method employed. The austenite (high solubility) continues to expand as more hydrogen is dissolved acting as a hydrogen sink. Strains generated during the absorption give rise to plastic flow. Twinning in the ferrite may be a result of the generation of local plastic strains in the surface layer due to hydrogen charging.

Support for this theory was found when the surface microstructure of ferritic chromium stainless steel subjected to hydrogen charging was investigated [150]. Hydrogen charging brought about the formation of needle shaped twins. Inside the needles, microcracks formed. Dislocation density and microhardness increased due to the presence of hydrogen.

Further, the deformations around nano-indentations into a charged BCC Ti alloy have been shown to support a mechanism of reduced cross slip in the presence of hydrogen [151]. Reduced cross slip explains the increase in hardness and decrease in ductility associated with hydrogen concentration. A reduction in the ability to cross slip enhances motion on a given slip plane. Further, Marrow noted that ferrite had a high tendency to twin with maximum twinning occurring about yield point in tensile tests carried out on aged Zeron 100 [26]. Ageing simulates hydrogen absorption, in that ferrite hardness increases while ductility decreases.

A resemblance to this theory was found where instead of hydrogen, laboratory air influenced slip. The effect of air on fatigue life was described in terms of enhanced strain localisation, and thus, easier microcrack initiation and early growth, the latter being an alternative method of stress relaxation and further deformation [152]. Under vacuum, such cracking phenomena were delayed as a consequence of less localised strain, possibly associated with more reversible deformation at slip bands.

Marrow postulated a mechanistic bulk embrittlement model to explain the mechanism responsible for increased crack growth rates due to the presence of hydrogen [26]. This model is the closest with regard to the phenomena observed in the current research.

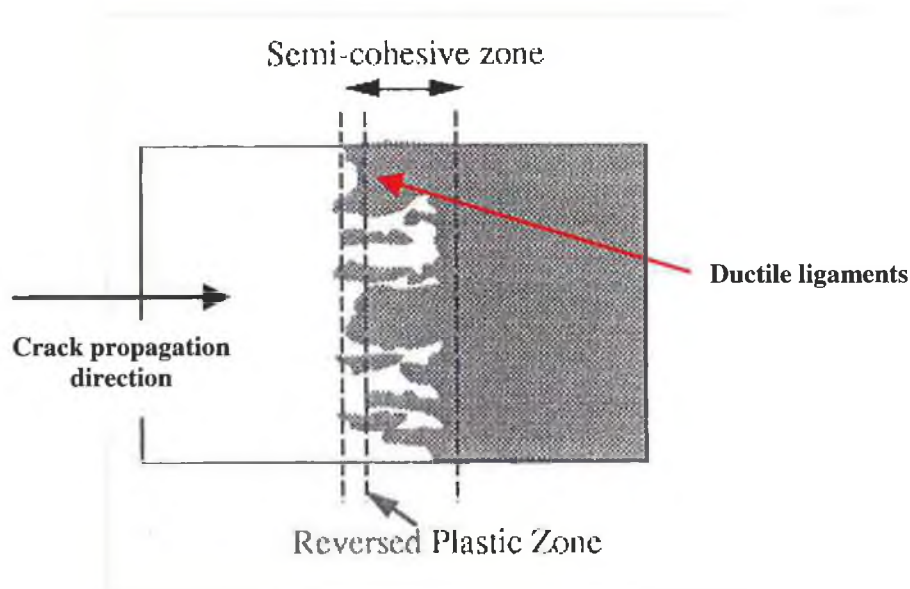


Figure 4.65 Bulk embrittlement model featuring semi-cohesive zone [26].

The key points of Marrows model are that:

- Twins are formed in a region of intense plastic strain (reversed plastic zone) without the aid of hydrogen. Twin concentration is therefore a function of  $\Delta K$ .
- Twins act as hydrogen traps and subsequently cleavage initiation sites.
- Hydrogen reduces the stress required to link microcracks.
- Cleavage facets propagate out of the reversed plastic zone on the attainment of a critical stress over a critical distribution of initiation sites (twins).
- Crack growth rate is controlled by the rate of rupture (by ductile striated cracking and shearing) of remaining ductile ligaments.

In the next section, a model is proposed for hydrogen assisted brittle crack propagation in the ferrite of Zeron 100 base and weld metal in an aqueous solution under cathodic overprotection. The new model deviates from Marrows model on a number of points including the formation of twins and their role in the actual mechanism of brittle crack growth. In addition, the role of hydrogen is different and cleavage doesn't propagate outside of the reversed plastic zone. The new model is based on fractographic observations from the current research and recent findings reported in the literature [150-152].

***New model for hydrogen assisted fatigue crack propagation.***

As reported and discussed in the results section, crack propagation in synthetic seawater (-1040mV SCE) is controlled by the failure of ductile ligaments. The new model presented here explains the mechanism of subcritical brittle crack propagation occurring in a proportion of the ferrite at the crack tip during each load cycle. This subcritical failure causes the overall crack propagation rates to be dependent on the failure of the remaining ductile ligaments.

The assumptions made are as follows:

- The model applies to steady state hydrogen assisted brittle crack growth.

- Hydrogen with high fugacity is available at the crack tip due to cathodic overprotection.
- Loading frequency is low enough (~0.1Hz) to allow sufficient time for hydrogen transportation, which occurs by diffusion and dislocation motion.

During ductile striation formation of the remaining ligaments, the concentration of hydrogen in the ferrite ahead of the brittle crack tip rises above a critical level (figure 4.66). With reference to a study on hydrogen cracking in duplex weld metal, the critical concentration of hydrogen in ferrite required to cause embrittlement is somewhere approaching 0.1 milliliter per gram of ferrite [153].

The critical concentration of atomic hydrogen occurs over a critical depth ( $L_{crit}$ ). Cathodic over protection allows twin formation a distance of up to about 2 microns ahead of the brittle crack tip at high  $\Delta K$ . Even so,  $L_{crit}$  is much less than the cyclic plastic zone size which is approximately 100 microns at  $\Delta K = 20 \text{MPa}\sqrt{\text{m}}$ . From measurements of brittle striations in the current research,  $L_{crit}$  is thought to be at least 1 micron at  $\Delta K = 20 \text{MPa}\sqrt{\text{m}}$  and increases marginally as a function of  $\Delta K^{0.4}$  (determined in the current research).

The ferrite encompassed by  $L_{crit}$  is embrittled by the presence of hydrogen, which is thought to reduce the stacking fault energy of ferrite. Therefore, cross slip is impeded and slip planarity promoted. Consequently, twinning is the preferred deformation mechanism.

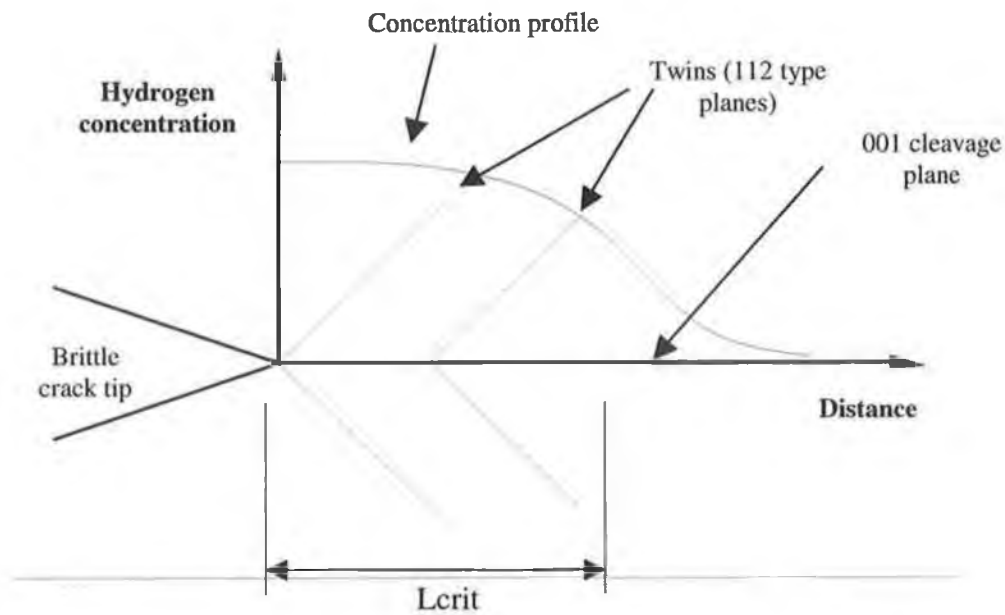


**Figure 4.66 Schematic of hydrogen concentration profile ahead of brittle crack tip. Ductile crack tip is up to three load cycles behind brittle crack tip.**

High hydrogen concentration together with the propensity for twin formation in ferrite under load leads to the formation of a twin boundary at approximately  $L_{crit}/2$  ( $\approx 1$ micron). Due to the fluctuating nature of fatigue loading and the 3D stress system prevalent over  $L_{crit}$ , twin boundaries can be formed on any of the family of 112 type planes.

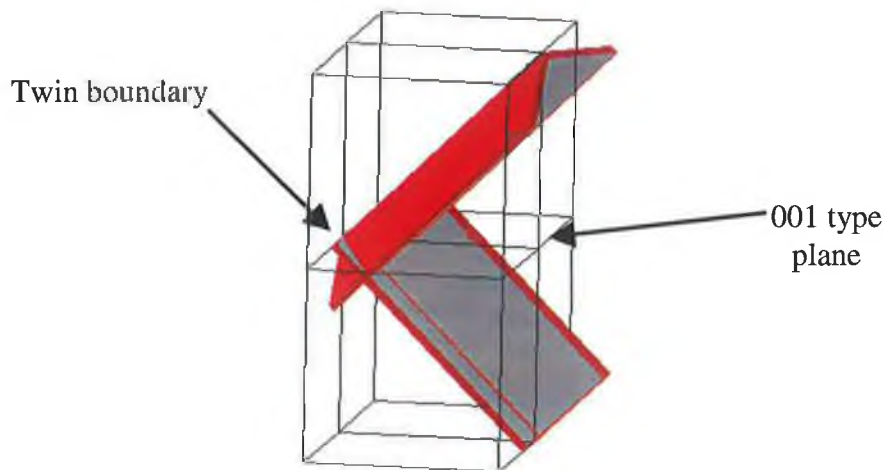


**Figure 4.67 Twins formed along 112 type planes ahead of brittle crack tip. Cleavage occurs on the 001 plane. Bursts of brittle crack growth initiate and arrest at twin boundary.**

It has been observed for FCC type structures at least, that even when slip activity within grains has been suppressed, slip bands are activated at twin interfaces due to local stress concentration [cited in 86]. In addition, it has been observed that cracks initiate only at every other twin due to the nature of internal stresses at twin boundaries [cited in 86]. Once the ductile crack tip (remaining ligaments) reaches the brittle crack tip, a high stress is induced along the crack front. Due to the microcrack/stress concentration at the twin at the crack tip, a burst of brittle crack growth occurs in the embrittled ferrite on the 001 plane. The brittle crack arrests at the twin formed at  $L_{crit}/2$ . This process is subsequently repeated.

It is widely agreed that cleavage occurs on the 001 plane in embrittled ferrite, however, {112} type planes are thought to play an important role. It is thought that twins formed on {112} type planes serve two critical purposes in hydrogen assisted crack propagation:

- Initiation locations for brittle crack growth.
- Arrestors for brittle crack growth. Propagating brittle cracks arrest at the subsequent twin boundary.

In addition, it is thought that a reduction in cathodic protection would lower the fugacity of hydrogen at the brittle crack tip consequently reducing the concentration of hydrogen ahead of the brittle crack tip and the distance at which a twin can form. Since, brittle crack growth is thought to arrest at twin boundaries, reducing hydrogen fugacity reduces the length of a brittle cleavage burst.

The actual fractography backing up this model is now considered. Cleavage tongues and steps are characteristic of twin-induced cleavage and are present in ferrite on the samples fatigued in synthetic seawater. Ferrite cleaves on the 001 plane, while; tongues (112 type planes) protrude onto this plane. These features are evident in figures 4.68 and 4.69.

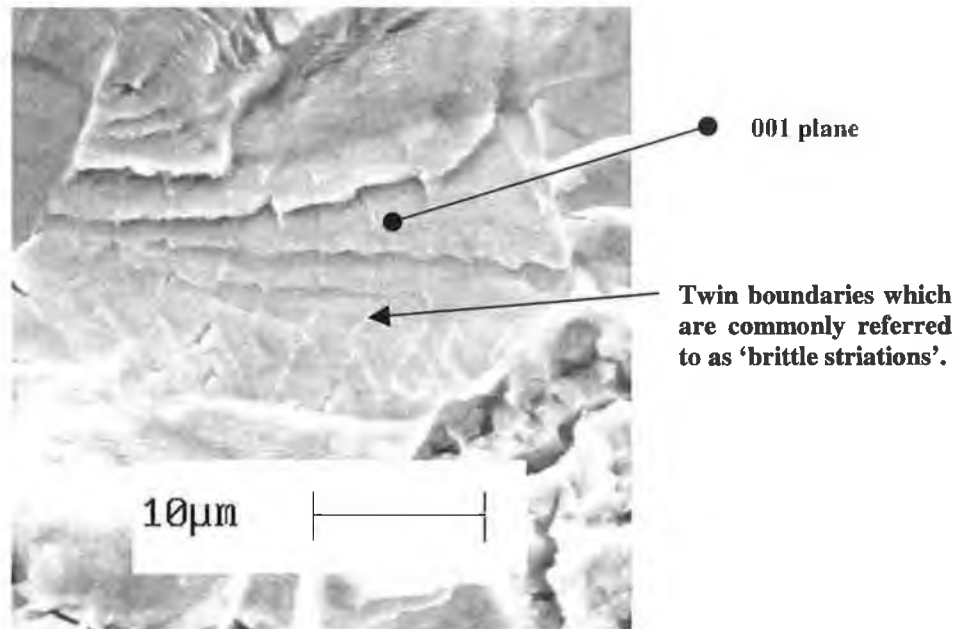


**Figure 4.68 Brittle striations 2-3 micron in width on base metal fracture surface at high  $\Delta K$ .**



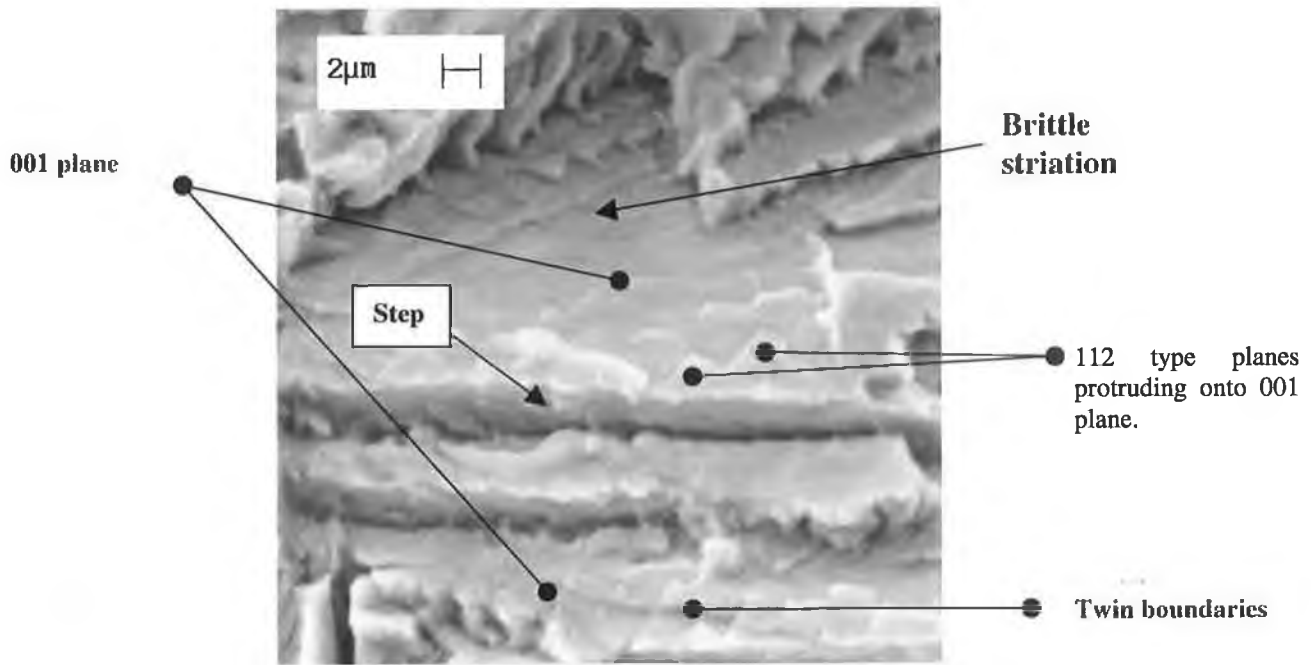


**Figure 4.69 Twin boundaries and {001} & {112} type planes evident on fracture surface of GTA weld metal.**

It is generally agreed that tongues and steps are formed by fracture along twin boundaries, which are interfaces with the lowest energy. This is particularly evident on the fracture surface of the GTA weld (figure 4.70), where a high density of twin boundaries is evident.

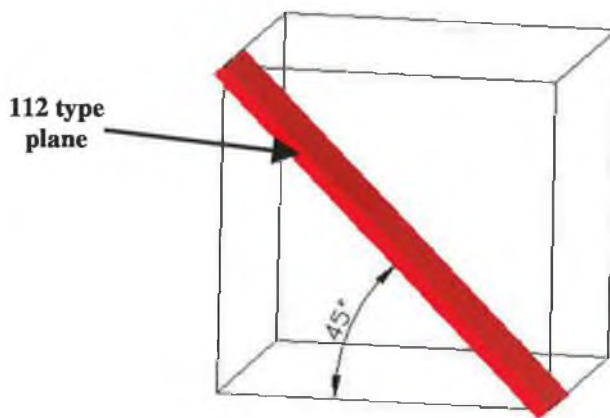
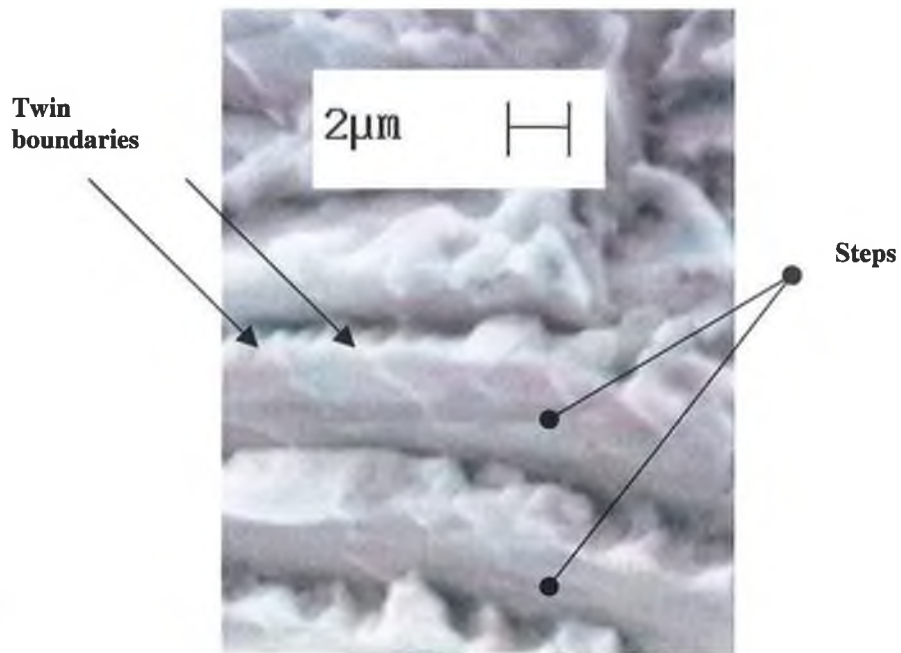


**Figure 4.70 Twin boundaries on 112 type planes prevalent on fracture surface of GTA weld metal.**

Figure 4.71 shows a twin boundary occurring along a 001 type plane (green line) with 112 type planes (red lines) meeting at the 001 type twin boundary. It is thought that the twin boundaries are formed during fatigue loading. Evident is that the angle between the 112 type planes approaches  $90^\circ$ .

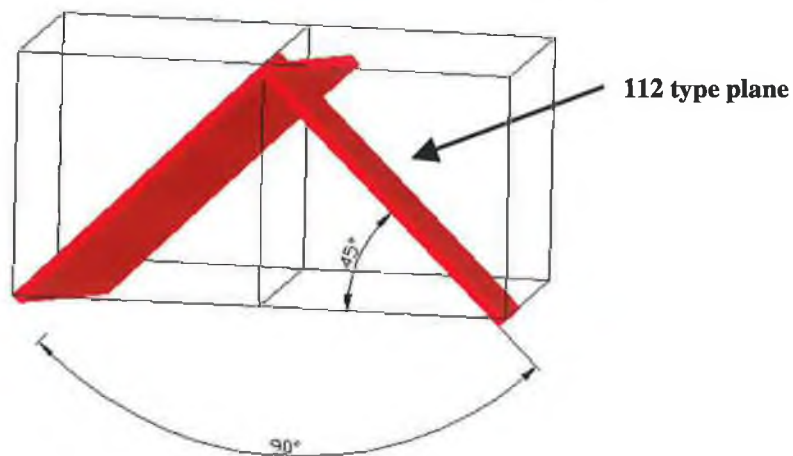
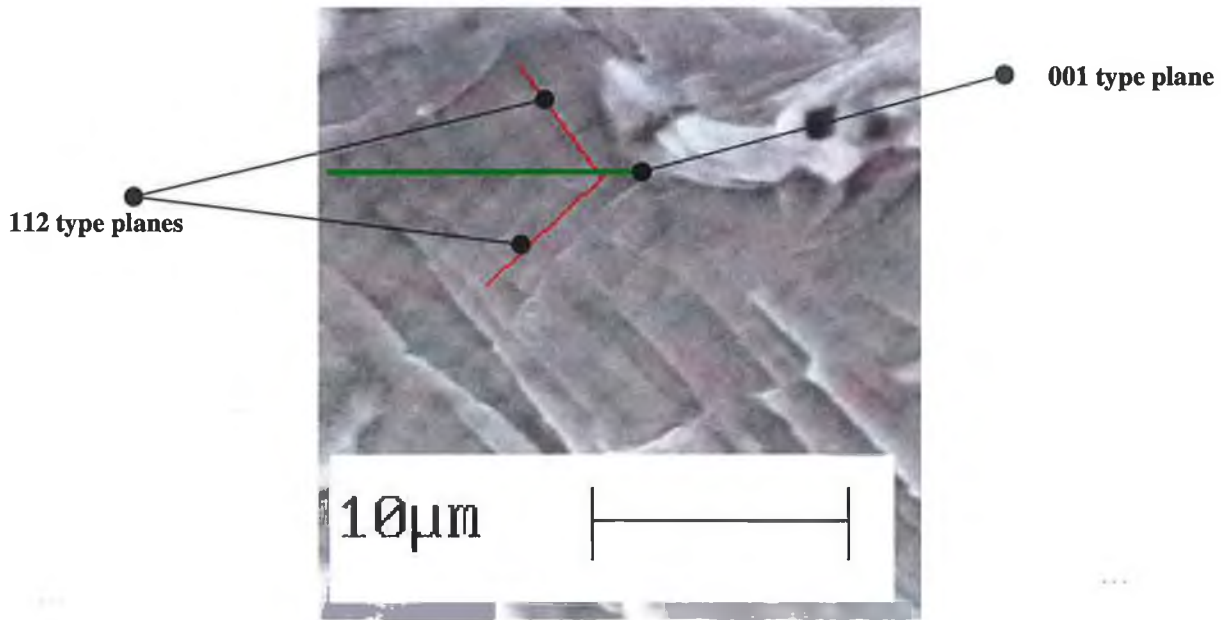


**Figure 4.71 112 and 001 type planes formed during fatigue loading in the presence of a critical concentration of hydrogen.**

In summary, this section shows firstly that cathodic overprotection of Zeron 100 weld metals in seawater induces a significant reduction in fatigue life. This occurs above a critical stress range which is 190MPa for R-ratio = 0.5. In a worst case scenario the reduction in fatigue life can be up to 10 weeks, which has critical consequences for defining NDT inspection intervals.

Secondly, the key point of the mechanistic model proposed is that brittle crack growth initiates and arrests at twin boundaries. A twin forms at a critical distance ahead of the brittle crack tip and arrests brittle crack propagation. The hydrogen concentration ahead of the brittle crack tip determines the location for the formation of the twin boundary and as such the extent of brittle crack growth.

## 5. CONCLUSIONS AND FUTURE WORK

### 5.1 Conclusions

Zeron 100 (SMA/GTA) weld metals with adequate basic mechanical and corrosion properties (as defined in current off shore industry standards) can be produced by a welder (inexperienced in welding superduplex stainless steels) working to the producers welding guidelines.

The crack propagation life of Zeron 100 weld metals at an R-ratio of 0.5 (effect of residual stresses thought to be negligible) were shown to be similar to standard design curves for class D, carbon and carbon-manganese structural steel butt welds. This was achieved through a numerical model. Thresholds for the onset of crack growth in Zeron 100 base and weld metals are similar and correspond well with the endurance limit specified on the standard design line. The macrocrack is thought to follow a path defined by the grain boundaries of columnar weld metal grains at low stress levels.

Cathodic overprotection (-1040mV SCE) in synthetic seawater leads to an increase in crack propagation rates on average by a factor of 4.3 over rates in air. Cathodic over protection is much more deleterious than high positive potentials above a critical stress intensity factor range ( $11\text{MPa}\sqrt{\text{m}}$ ) for Zeron 100 base and weld metals.

The fatigue crack propagation life of Zeron 100 weld metals operating in seawater cathodically overprotected can be reduced by up to 10 weeks for loading at a frequency of 0.1Hz, which is the typical frequency of wave motion. This has serious consequences for the establishment of NDT inspection intervals.

With regard to fatigue crack propagation in air and in synthetic seawater under cathodic overprotection, the GTA root/SMA fill weld metal performs equally well as the GTA root/GTA fill weld metal. Since the SMA welding process is generally quicker and cheaper than the GTA method, a potential economic saving is evident.

A new model for hydrogen assisted subcritical brittle crack propagation in ferrite is proposed. The key points are that brittle cracks both initiate and arrest at twin boundaries, which are formed in the surface layer of the ferrite (<3microns). Twins

are formed due to two factors. First, the presence of a critical level of hydrogen thought to be approaching 0.1ml/g of ferrite and secondly due to the presence of a fluctuating load. High hydrogen fugacity at the brittle crack tip due to cathodic overprotection causes a high hydrogen concentration in the surface layer of the ferrite.

## 5.2 Future Work

In order to verify the S-N curves, which were derived from  $da/dN-\Delta K$  type data, it is suggested that S-N type tests are carried out on weldments. Crack should be introduced into the weldment samples perhaps by means of a notch and cyclic compression loading before an S-N type test commences. The resulting number of load cycles to failure would be conservative. In addition, such tests could quite easily be carried out in seawater under cathodic overprotection at a low frequency.

The threshold  $\Delta K$  for the onset of crack growth in Zeron 100 base and weld metals has been determined in air. However, short crack growth tests need to be carried out on smooth samples to establish if the threshold data obtained in the current research with the aid of the cyclic compression technique is conservative threshold data.

In addition, it has been established that the onset of hydrogen assisted crack growth requires a critical stress level. Therefore, it would be pertinent to assess the effect of high positive ECPs on crack propagation around the threshold  $\Delta K$  for the onset of crack growth. It is thought that dissolution mechanisms have their greatest effect at low  $\Delta K$  where hydrogen mechanisms are negligible.

Another important area is the effect of temperature on crack growth rates in Zeron 100 base and weld metals. From the current research, it was seen that the pitting ECP was significantly reduced and the rate of repassivation diminished at 80°C in synthetic seawater. Both the effects of dissolution on crack propagation at low  $\Delta K$  and hydrogen effects at relatively high  $\Delta K$  need to be investigated in synthetic seawater at 80°C. Such testing requires a fully enclosed environmental chamber with automated crack length monitoring equipment.

Finally, crack propagation tests are required to correlate the level of hydrogen charging and the width of brittle striations formed. This requires an extensive fractographic investigation. If a correlation were obtained where brittle striation width increased with charging level, this would give support to the suggested model for brittle crack growth and arrest. Perhaps cast superduplex alloy with relatively large grain sizes may aid the visualisation of twins/brittle striations.

## REFERENCES

- [1] White Paper: Energy for the future - renewable sources of energy, Directorate General energy and transport, European Commission, (1997).
- [2] Green Paper on Energy, Dept. of Public Enterprise, (1999).
- [3] Life cycle assessment of a wind farm and related externalities, *Renewable Energy*, 20, (2000), 279-288.
- [4] Wavedragon, a large offshore wave energy converting device, [[www.wavedragon.net](http://www.wavedragon.net)], accessed May (2003).
- [5] British Wind Energy Association Website, Wind Turbine Technology/ Offshore Wind Energy, [<http://www.bwea.com>], accessed Feb. (2001).
- [6] Patel H, Offshore engineering, in Smith EH ed., *Mechanical Engineers reference book*, Butterworth-Heinemann, 12<sup>th</sup> ED., (1994).
- [7] Gooch DJ, Materials issues in renewable energy power generation, *International Material Reviews*, Vol. 45, 1 (2000), 1-13.
- [8] Wahab MA, Sakano M, Experimental study of corrosion fatigue behaviour of welded steel structures, *Journal of Materials Processing Technology*, 118, (2001) 117-122.
- [9] Schijve J, Fatigue of structures and materials in the 20<sup>th</sup> century and the state of the art, *International Journal of Fatigue*, 25, (2003) 679-702.
- [10] Charles J, Why and where duplex stainless steels, *Proc Duplex Stainless Steels 5<sup>th</sup> world conference*, Maastricht, Netherlands, (1997), 29-42.
- [11] Charles J, Super duplex stainless steels: structure and properties, *Proc Duplex Stainless Steels*, Beaune, France, (1991), 3-48.



- [12] Gunn RN, Duplex stainless steels, Microstructure, properties and applications, Abington publishing, (1997).
- [13] Johansson KA, Duplex stainless steels in offshore applications-experiences from projects and operations, Proc Duplex Stainless Steels, Glasgow, Scotland, (1994), paper KVII.
- [14] Charles J, Verneau M, Audouard JP, Demars S, Some duplex applications-test results and practical experience, Proc Stainless Steel World, The Hague, Netherlands, (1999), 473-485.
- [15] Woollin P, Senior Section Manager, Metallurgy and Corrosion, Metallurgy, Corrosion, Arcs and Surfacing Technology Group, The welding institute (TWI Ltd), Cambridge, UK. [Private Communication Jan (2001)].
- [16] Francis R, Corrosion Services Manager, Weir Materials, Manchester, UK. [Private Communication March (2001)].
- [17] Komai K, Failure analysis and prevention in SCC and corrosion fatigue cases, International Journal of Fatigue, Vol. 20., 2, (1998), 145-154.
- [18] Griffith AA, The phenomenon of rupture and flow in solids, Phil. Trans of the Royal London Society, London A221, (1921), 163-197.
- [19] Maddox SJ, Fatigue strength of welded structures, Abington Publishing, 2<sup>nd</sup> ED., (1991).
- [20] Bulloch JH, Understanding and eliminating crack extension behaviour in feed water deaerator systems – a critical review, International Journal of Pressure Vessels and Piping, 53, (1993), 1-21.

- [21] Bulloch, JH, Electrochemical potential variations in a small 40 MW feedwater storage vessel – the influence of weldment surface condition, *International Journal of Pressure Vessels and Piping*, 71, (1997), 1-5.
- [22] Bulloch JH, Rochford E, In service electrochemical potential data in a deaerator feedwater storage vessel; the influence of a noble metal coating, *International Journal of Pressure Vessels and Piping*, 77, (2000), 485-499.
- [23] Bulloch JH, Rochford E, Analysis of electrochemical potential data trends in the weldments of a working deaerator storage vessel, *International Journal of Pressure Vessels and Piping*, 79, (2002), 263-272.
- [24] Bulloch JH, Deaerator feedwater storage vessel weldment cracking: some fractographic and crack extension details, *International Journal of Pressure Vessels and Piping*, 68, (1996), 81-97.
- [25] Mayaki CM, Aspects of fatigue crack propagation behaviour of duplex stainless steels, Ph.D thesis, Nottingham, (1989).
- [26] Marrow TJ, Fatigue mechanisms in an embrittled duplex stainless steel, Ph.D thesis, Cambridge, (1991).
- [27] Gough PC, Farrar JCM, Fracture toughness of duplex and superduplex stainless steel welds, *Proc. Duplex Stainless Steels 5<sup>th</sup> World Conference*, Maastricht, Netherlands, (1997), 483-490.
- [28] Wiesner CS, Toughness requirements for duplex and superduplex stainless steels, *Proc. Duplex Stainless Steels 5<sup>th</sup> World Conference*, Maastricht, Netherlands, (1997), 979-990.
- [29] Dhooge A, Deleu E, Weldability and fracture behaviour of duplex and superduplex stainless steels. *Proc. Duplex Stainless Steels*, Glasgow, Scotland, (1994), paper 77.

- [30] Deleu E, Dhooge A, Fracture toughness of welded thick walled stainless steels, Proc. Duplex Stainless Steels 5<sup>th</sup> World Conference, Masstricht, Netherlands, (1997), 387-394.
- [31] Dupoirion F, Bonnefois B, Verneau M, Charles J, Superduplex stainless steels for offshore applications: high performance welded joints, Proc. Duplex Stainless Steels, Glasgow, Scotland, (1994), paper 129.
- [32] Charles J, Bonnefois B, Superduplex stainless steels: properties & weldability, Proc. Duplex Stainless Steels, The Hague, Netherlands, (1986), 1108-1121.
- [33] Gunn RN, Comparison of the corrosion and mechanical properties of weldments in wrought 25%Cr and superduplex stainless steels, Proc. Duplex Stainless Steels, Glasgow, Scotland, (1994), paper32.
- [34] Index to theses, [<http://www.theses.com>], accessed October 2003.
- [35] Sharpe R, Materials properties and selection, in Smith EH ed., Mechanical Engineers reference book, Butterworth-Heinemann, 12<sup>th</sup> ED., (1994).
- [36] Olsson COA, Landolt D, Passive films on stainless steels-chemistry structure and growth, *Electrochimica Acta*, 48, (2003), 1093-1104.
- [37] Roberge PR, Handbook of Corrosion Engineering, McGraw Hill, New York, (1999).
- [38] Cunha Belo MD, Rondot B, Compere C et al, Chemical composition and semiconducting behaviour of stainless steel passive films in contact with artificial seawater, *Corrosion Science*, Vol. 40, 2/3, (1998), 481-494.
- [39] Andersen O, Johansson K, Lian B, The use of stainless steels in the offshore industry, Proc. Duplex Stainless Steels, The Hague, Netherlands, (1986), 618 – 624.

- [40] Davis, JR, Properties and Selection: Stainless Steels, Tool Materials and Special Purpose Metals, in ASM Metals Handbook, Lampman SR ed., 10<sup>th</sup> ED, Vol. 2, (1990).
- [41] Redmond JD, Stainless Steels, Materials of Engineering, in Avallone EA, Baumeister III T eds., Marks standard hand book for Mechanical Engineers, 10<sup>th</sup> ED, McGraw Hill, New York, (1996).
- [42] Koch GH, Stress corrosion cracking and hydrogen embrittlement, in ASM Fatigue and Fracture Handbook, Lampman SR ed., Vol.19, (1996).
- [43] Hutchinson WB, Schlippenbach UV, Jonsson J, Textures and anisotropy in duplex stainless steel SS 2377, Proc. Duplex Stainless Steels, The Hague, Netherlands, (1986), 326-330.
- [44] Gooch TG, Corrosion resistance of welds in duplex stainless steels, Proc. Duplex Stainless Steels, Beaune, France, (1991), 325-346.
- [45] Stevenson AW, Gough PG, Farrar JCM, The weldability of superduplex alloys – welding consumable and procedure development for zeron 100, Proc. Duplex Stainless Steels, The Hague, Netherlands, (1986), 290-306.
- [46] Atamert S, King JE, Elemental partitioning and microstructural development in duplex stainless steel weld metal, Acta Metalurgical et Materialia, Vol. 39, 3, (1991), 273-285.
- [47] Nassau LV, Meelker H, Hilkes J, Proc. Duplex Stainless Steels, Beaune, France, (1991), 303-323.
- [48] Lippold JC, Varol I, Baeslack WA, Microstructural evolution in duplex stainless steel weldments, Proc Duplex stainless Steels, Beaune, France, (1991), 383-391.

- [49] Rouault P, Bonnet C, Make the duplex and superduplex welding easier through metallurgical and practical simple recommendations!, Proc Duplex Stainless Steels – 5<sup>th</sup> world conference, Masstricht, Netherlands, (1997), 297-304.
- [50] Gunn RN, Reduction in fracture toughness due to intermetallic precipitates in duplex stainless steels, Proc Duplex America, Houston, USA, (2000), 299-314.
- [51] Lundqvist B, Norberg P, Olsson K, Influence of different welding conditions on mechanical properties and corrosion resistance of SAF 2205, Proc Duplex Stainless Steels, The Hague, Netherlands, (1986), 16-29.
- [52] Karlsson L, Andersson SL, Rigdal S, Welding superduplex stainless steels with Ni-base consumables, Proc Duplex Stainless Steels-5<sup>th</sup> world conference, Masstricht, Netherlands, (1997), 433-443.
- [53] Doyen R, Niset M, Welding of duplex and superduplex stainless steels, Proc Duplex Stainless Steels, Beaune, France, (1991), 1043-1051.
- [54] Baxter CFG, Irwin J, Francis R, The weld zone hardness and serviceability of Zeron 100 Super Duplex Stainless Steel, Proc International Offshore and Polar Engineering Conference, Singapore, (1993), 401-407.
- [55] Hertzman S, Roberts W, Lindenmo M, Microstructure and properties of nitrogen alloyed duplex stainless steels after welding treatments, Proc Duplex stainless steels, The Hague, Netherlands, (1986), 257-267.
- [56] Wahlburg G, Dunlop GL, Nitrogen strengthening of duplex stainless steels, Proc. Stainless Steels, the Hague, Netherlands, (1986), 291-295.
- [57] Liljas M, Qvarfort R, Influence of nitrogen on weldments in UNS S31803, Proc. Duplex Stainless Steels, The Hague, Netherlands, (1986), 244-256.

- [58] Fager SA, Design of consumables for the welding of superduplex stainless steels, Proc. Duplex Stainless Steels, Beaune, France, (1991), 403-411.
- [59] BS 131-6:1998, Notched bar tests, method for precision determination of charpy V notch impact energies for metals, (1998).
- [60] BS 7448-1:1991 Fracture mechanics toughness tests – part 1: method for determination of  $K_{IC}$ , critical CTOD and critical J values of metallic materials, (1991).
- [61] Dawes MG, Metal Construction and British Welding Journal, Vol. 3, 2, (1971), 61-65.
- [62] Byrne G, Francis R, Warburton G, Variation in mechanical properties and corrosion resistance of different alloys within the generic designation UNS S32760, Proc. Duplex America, Houston, USA, (2000), 113-125.
- [63] Bernhardsson S, The corrosion resistance of duplex stainless steels, Proc. Duplex Stainless Steels, Beaune, France, (1991), 185-209.
- [64] Dupouiron F, Verneau M, Audouard JP, Charles J, Industrial experience of duplex and superduplex stainless steels in the chemical, mineral and petrochemical industries, Proc. Duplex Stainless Steels, Glasgow, Scotland, (1994), paper 92.
- [65] Kivisakk U, SAF 2507 in seawater, 10 years of experience, Proc. Stainless Steel World, The Hague, Netherlands, (1999), 519-528.
- [66] Corrosion Survey Database (COR·SUR), NACE International, (2002). [Accessed on line through Knovel database 'www.knovel.com', October 2003].

- [67] ASTM G48-03 Standard Test Methods for Pitting and Crevice Corrosion Resistance of Stainless Steels and Related Alloys by Use of Ferric Chloride Solution, (2003).
- [68] Kain R, Crevice corrosion resistance of duplex stainless steels in chloride containing waters, Proc. Duplex stainless steels, 5<sup>th</sup> world conference, Maastricht, Netherlands, (1997), 627-638.
- [69] Trethway KR, Chamberlain J, Corrosion – for students of science and engineering. Longman Scientific and Technical, New York, (1988).
- [70] Scully JR, Electrochemical, in ASM Handbook, Corrosion tests and standards, application and interpretation, Baboian R ed., (1995).
- [71] Francis R, Galvanic corrosion - a practical guide for engineers, National Association of Corrosion Engineers (NACE) International, (2001).
- [72] Haynes AG, Some influences of composition on the corrosion resistance of duplex and higher alloyed austenitic steels and alloys, Proc. Duplex Stainless Steels, The Hague, Netherlands, (1986), 415-435.
- [73] Perren RA, Suter TA, Uggowitzer PJ, Weber L, Magdowski R, Bohni H, Speidel MO, Corrosion resistance of superduplex stainless steels in chloride ion containing environments: investigation by means of a new microelectrochemical method I. Precipitation free states, Corrosion Science 43, (2001), 707-726.
- [74] Weber L, Uggowitzer PJ, Partitioning of chromium and molybdenum in super duplex stainless steels with respect to nitrogen and nickel content, Materials Science & Engineering A242, (1998), 222-229.
- [75] ASTM, G61-86, Standard test method for conducting cyclic potentiodynamic polarisation measurements for localised corrosion susceptibility of iron, nickel or cobalt based alloys, (1986), re-approved 1993.

- [76] ASTM, G78-95, Standard guide for crevice corrosion testing of iron base and nickel base stainless alloys in seawater and other chloride containing aqueous environments, (1995).
- [77] Verneau M, Audourard JP, Charles J, Properties and examples of practical applications of superduplex stainless steels, Proc. Duplex Stainless Steels – 5<sup>th</sup> World Conference, Maastricht, Netherlands, (1997), 845-855.
- [78] Francis R, Byrne G, Warburton GR, Effects of cathodic protection on Duplex Stainless steels in seawater, Corrosion, NACE, Vol. 53, 3, (1997), 234-240.
- [79] Wessman SM, Pettersson RFA, Hydrogen cracking of cathodically polarised duplex stainless steels and weld metals, Proc. Duplex Stainless Steels, Venice, Italy, (2000), 279-287.
- [80] Olive JM, Cweik J, Desjardins D, Quantification of the hydrogen produced during corrosion fatigue crack propagation, Corrosion Science, 41, (1999), 1067-1078.
- [81] Cohen LJR, Charles JA, Smith GC, Influence of cathodic hydrogen on microstructure of duplex stainless steels, Proc. Stainless Steels, York, UK, (1987), 363-374.
- [82] Iacoviello F, Habashi M, Cavallini M, Hydrogen embrittlement in the duplex stainless steel Z2CND2205 hydrogen-charged at 200<sup>0</sup>C. Materials Science and Engineering, A224, (1997), 116-124.
- [83] Turnbull A, Lembach-Beylegaard E, Hutchings RB, Hydrogen transport in duplex stainless steels, Proc. Duplex Stainless Steels, Glasgow, Scotland, (1994), paper 80.
- [84] Walker RA, Gooch TG, Hydrogen cracking of welds in duplex stainless steel, Proc. Duplex Stainless Steels, Beaune, France, (1991), 1053–1063.



- [85] Fang PJ, Kirkwood D, Power LJ, Baxter CFG, The resistance of superduplex stainless steel to hydrogen cracking, Proc. Duplex Stainless Steels, Glasgow, Scotland, (1994), paper 51.
- [86] Suresh S, Fatigue of Materials, Cambridge University Press, 2<sup>nd</sup> ED., (1998).
- [87] Jarvis AR, Bulloch JH, The effect of nickel content on the environmental assisted cracking (EAC) behaviour of low alloy steels in sour environments-a review, International Journal of Pressure Vessel & Piping, 49, (1992), 271-307.
- [88] Woolin P, Murphy W, Hydrogen embrittlement stress corrosion cracking of superduplex stainless steel, Proc. Corrosion, NACE, Houston, USA, (2001), paper 01018.
- [89] Olsson P, Bauer AD, Eriksson H, Hydrogen embrittlement of duplex grades UNS S32750 and UNS S31803 in connection with cathodic protection in chloride solutions, Proc. Duplex Stainless Steels-5<sup>th</sup> world conference, Masstricht, Netherlands, (1997), 607-618.
- [90] Kivisakk UH, Holmquist M, Influence of cathodic protection on hydrogen embrittlement on annealed and cold worked duplex stainless steels, Proc. Corrosion, NACE, Houston, USA, (2001), paper 01019.
- [91] Francis R, Environmental cracking and embrittlement of duplex stainless steel, Proc Duplex stainless steels, Glasgow, Scotland, (1994), paper KIV.
- [92] Crooker TW, Bogar FD, Cares WR, Effects of flowing natural seawater and electrochemical potential on fatigue crack growth in several high strength marine alloys, Corrosion fatigue technology, ASTM STP 642, (1978), 189-201.

- [93] Jaske CE, Broek D, Slater JE, Anderson WE, Corrosion fatigue of structural steels in seawater and for offshore applications, Corrosion fatigue technology, ASTM STP 642, (1978), 19-47.
- [94] ASTM E 647-95a, Standard Test Method for Measurement of fatigue Crack Growth Rates. This standard also contains an annex concerning “special requirements for testing in aqueous environments”, (1995).
- [95] BS ISO 11782-2:1998, Corrosion of metals and alloys – Corrosion fatigue testing – part 2, Crack propagation using pre-cracked specimens (1998).
- [96] BS 6835-1: 1998, Method for the determination of the rate of fatigue crack growth in metallic materials-part 1, (1998)
- [97] Johansson RE, Groth HL, Corrosion fatigue and fatigue data for duplex stainless steels, Proc. Duplex Stainless Steels, Beaune, France, (1991), 283-294.
- [98] Coudreuse L, Charles J, Fatigue and corrosion fatigue behaviour of duplex stainless steels, Proc. Duplex Stainless Steels, Venice, Italy, (2000), 629-638.
- [99] Schmitt-Thomas KG, Wunderlich R, Simon R, Investigation of corrosion fatigue and crack initiation with the new developed duplex steel X3CrMnNiMoN 2564 in comparison with the ferritic-austenitic steel X2CrNiMoN 22, Proc. Duplex Stainless Steels, Beaune, France, (1991), 915-920.
- [100] Ebara R, Kai T, Inoue K, Corrosion fatigue behaviour of 13Cr stainless steel in sodium chloride aqueous solution and steam environment, Corrosion fatigue technology, ASTM STP 642, (1978), 155-168.
- [101] Amzallag C, Rabbe P, Truchon M, Failure of stainless steels by corrosion fatigue, Proc. Advances in Research on the Strength and Fracture of Materials, Vol. 2B, Waterloo, Canada, (1978), 873-878.

- [102] Linder J, Corrosion fatigue of duplex and austenitic stainless steels in 3.5% NaCl at 80°C and room temperature, Proc. Duplex stainless steels, Glasgow, Scotland, (1994), paper 47.
- [103] Marrow TJ, King JE, Microstructural and environmental effects on fatigue crack propagation in duplex stainless steels, Fatigue & Fracture of Engineering Materials and Structures, Vol. 17, 7, (1994), 761-771.
- [104] Marrow TJ, King JE, Fatigue crack propagation mechanisms in a thermally aged duplex stainless steel, Materials Science and Engineering, A 183, (1994), 91-101.
- [105] Nakajima M, Tokaji K, Okamoto Y, Effects of microstructure and corrosive environment on fatigue crack growth behaviour in a duplex stainless steel, Journal of the Society of Material Science, Japan, Vol. 48, 12, (1999), 1379-1385.
- [106] Misawa T, Effects of cathodic protection potential on corrosion fatigue crack growth for a duplex stainless steel in synthetic sea water, Corrosion Engineering, 38, (1989), 315-318.
- [107] Komai K, Minoshima K, Kim G, Irifune K, Corrosion fatigue crack growth characteristics of duplex stainless steel weldment in synthetic seawater, Journal of the Society of Material Science, Japan, Vol. 39, 439, (1990), 343-349.
- [108] Makhoulf K, Sidhom H, Trigui I, Braham C, Corrosion fatigue crack propagation of a duplex stainless steel X6 Cr Ni Mo Cu 25-6 in air and in artificial seawater, International Journal of Fatigue, Vol. 25, 2, (2003), 167-179.

- [109] Ramsamooj DV, Shugar TA, Modelling of corrosion fatigue in metals in an aggressive environment, *International Journal of Fatigue*, Vol. 23, supplement 1, (2001), S301-S309.
- [110] Karlsson L, Rigdal S, Lake F, Effects of intermetallic phases in duplex stainless steel weldments, a critical review, *Proc. Duplex America*, Houston, USA, (2000), 257-272.
- [111] Zeron 100 welding guidelines, Weir Materials & Foundries (WMF), Manchester, UK, available at [www.weirmaterials.co.uk](http://www.weirmaterials.co.uk), [Last Accessed Sept 03]. See appendix C.
- [112] Zeron 100 technical information, Weir Materials & Foundries (WMF), Manchester, UK, available at [www.weirmaterials.co.uk](http://www.weirmaterials.co.uk), [Last Accessed Sept 03].
- [113] ASTM E 384-89, Standard test method for Microhardness of materials, (1989).
- [114] BS 7910, Guide on methods for assessing the acceptability of flaws in metallic structures, (1999).
- [115] BS EN 571-1, Non-destructive testing. Penetrant testing. General principles, (1997).
- [116] ASTM E1558-93, Standard guide for electrolytic polishing of metallographic specimens, (1993).
- [117] Johansen RB, Leinum BH, Karlsen S, Trandem HA, Valdo G, Tjernaes AO, Helgesen T, Duplex stainless steels-measurement of intermetallic phase content and the connection to impact toughness and corrosion resistance, *Proc. Duplex Stainless Steels*, Venice, Italy, (2000), 405-414

- [118] ASTM E 562-95, Determining volume fraction by systematic manual point count, (1995).
- [119] Dowling NE, Mechanical Behavior of Materials, Engineering Methods for Deformation, Fracture and Fatigue, Prentice-Hall INC, (1993).
- [120] Turnbull A, National Physical Laboratory (UK) Co-Author of BS ISO 11782-2:1998, [Private Communication June (2001)].
- [121] Galatalo R, Lanciotti A, Fatigue crack propagation in residual stress fields of welded plates, International Journal of Fatigue, Vol. 19, 1, (1997), 43-49.
- [122] Kitsunai Y, Tanaka M, Yoshihisa E, Influence of residual stresses and loading frequencies on corrosion fatigue crack growth behaviour of weldments, Metallurgical and Materials Transactions A, Vol. 29A, (1998), 1289-1298.
- [123] ASTM E813 89E01, Annex A1 special requirements for testing bend samples, Test method for JIC, A measure of fracture toughness, (1989).
- [124] ASTM G31-72 (Reapproved 1995), Laboratory immersion corrosion testing of materials, (1995).
- [125] Fehl BD, Truman KZ, An evaluation of fracture mechanics quarter point displacement techniques used for computing stress intensity factors, Engineering Structures, 21, (1999), 406-415.
- [126] Forth SC, Newman JC, Forman RG, On generating fatigue crack growth thresholds, International Journal of Fatigue, 25, (2003), 9-15.
- [127] Nystrom M, Karlsson B, Plastic deformation of duplex stainless steels with different amounts of ferrite, Proc. Duplex Stainless Steels, Glasgow, Scotland, (1994), paper 104.

- [128] Kivineva EI, Eriksson JI, Astrom H, Weldment toughness of duplex stainless heavy steel castings at  $-40^{\circ}\text{C}$ , Proc. Duplex Stainless Steels-5<sup>th</sup> World Conference, Maastricht, Netherlands, (1997),.
- [129] Jutla T, Fatigue and fracture control of weldments, in ASM Fatigue and Fracture Handbook, Lampman SR ed., Vol.19, (1996).
- [130] Brooks CR, Choudhury A, Failure analysis of engineering materials, McGraw-Hill, (2002).
- [131] Friel JJ, X-ray and image analysis in electron microscopy, Princeton gamma tech, Princeton, New Jersey, (1998).
- [132] Tavara SA, Chapetti MD, Otegui JL, Manfredi C, Influence of nickel on the susceptibility to corrosion fatigue of duplex stainless steel welds, International Journal of Fatigue, 23, (2001), 619-626.
- [133] Dufrane JJ, Heat affected zone simulation of superduplex stainless steel UNS S32760 – Zeron 100, Proc Duplex Stainless Steels, Beaune, France, (1991), 967-975.
- [134] Francis R, The repassivation of high alloy stainless steels, Proc. Duplex Stainless Steels, Glasgow, Scotland, 1994, paper 22.
- [135] Sadananda K, Vasudevan AK, Fatigue crack growth mechanisms in steels, International Journal of Fatigue, Volume 25, (2003), 899-914.
- [136] Hope AD, Atamert S, King JE, Fatigue crack growth in heat affected zone microstructures in duplex stainless steel, Proc. Fatigue 90, Hawaii, USA, (1990), 155-160.
- [137] Nystrom M, Karlsson B, Fatigue of duplex stainless steel influence of discontinuous spinodally decomposed ferrite, Materials Science and Engineering A215, (1996), 26-38.

- [138] Beretta S, Boniardi M, Microstructure and fatigue properties of a welded duplex stainless steel, *Fatigue & fracture of Engineering Materials & Structures*, Vol. 19, 6, (1996), 647-654.
- [139] Stolarz J, Foct J, Microstructural barriers to fatigue crack propagation in duplex stainless steels-the influence of ageing and nitrogen additions, *Proc. Duplex Stainless Steels*, Venice, Italy, (2000), 639-650.
- [140] Akdut N, Is the fatigue life of duplex stainless steels a function of the second phase, the morphology and /or the nitrogen content ?, *Proc. Duplex America*, Houston, USA, (2000), 79-87.
- [141] Perdriset F, Magnin T, Cassange T, Hoch P, Dupouiron F, Environmental effects on low cycle fatigue behaviour of Z3 CND 2205 duplex stainless steel, *Proc. Duplex Stainless Steels*, Glasgow, Scotland, (1994), paper 13.
- [142] Wei RP, Gao M, Xu PY, Peak Bare-Surface Current Densities Overestimated in Straining and Scratching Electrode Experiments, *Journal of Electrochemical Society*, Vol. 136, 6, (1989), L1835. [Cited in ref. 102].
- [143] Femenia M, Luukkonen P, Pan J, Leygraf C, In situ electrochemical STM study of dissolution behaviour of duplex stainless steels in aggressive solutions. *Proc. Duplex Stainless Steels*, Venice, Italy, (2000), 261-270.
- [144] Bulloch JH, Stress corrosion cracking of low alloy steels in natural seawater environment – the influence of carbon level, *Theoretical and Applied Fracture Mechanics*, 16, (1991), 1-17.
- [145] Marrow TJ, King JE, Charles JA, Hydrogen effects on fatigue in a duplex stainless steel, *Proc. Fatigue 90*, Hawaii, USA, (1990).
- [146] Bulloch JH, Fatigue fracture surface features prevalent in steels at ambient temperatures, *Theoretical & Applied Fracture Mechanics*, 20 (1994), 133-140.

- [147] Maddox SJ, Welded joints-fatigue design developments, Fatigue-real life solutions seminar held at the Institution of Mechanical Engineers head quarters, Birdcage walk, London, February, (2003).
- [148] Francis R, Byrne G, Corrosion fatigue resistance of Zeron 100 super duplex stainless steel, Weir Materials and Foundries Technical Report, (1994).
- [149] Ahmed T, Reservoir Engineering Handbook, 2<sup>nd</sup> Ed, Gulf Professional Publishing, (2001).
- [150] Szummer A, Jezierska E, Lublinska K, Hydrogen effects in ferritic stainless steels, Journal of Alloys and Compounds, (1999), 356-360.
- [151] Morasch KR, Bahr DF, The effects of hydrogen on deformation and cross slip in a BCC titanium alloy, Scripta Materialia, 45, (2001), 839-845.
- [152] Llanes L, Mateo A, Villechaise P, Mendez J, Anglada M, Effect of testing atmosphere (air/in vacuo) on low cycle fatigue characteristics of a duplex stainless steel, International Journal of Fatigue, 21, (1999), S119-S125.
- [153] Gooch TG Leonard AJ, Gunn RN, Hydrogen cracking of ferritic-austenitic stainless steel weld metal, Proc. Duplex America, Houston, USA, (2000), 345-357.
- [154] Herro HM, Port RD, The Nalco guide to cooling water system failure analysis, Nalco chemical company, McGraw Hill, New York, (1993).
- [155] Andresen PL, Corrosion fatigue testing, in ASM Corrosion tests and standards Hand book, application and interpretation, Baboian R ed., (1995).
- [156] Shreir LL, Localised Corrosion, in Corrosion, Shrier LL ed., Vol. 1, Newnes-Butterworths, (1976).



- [157] Oldfield JW, Sutton WH, Crevice Corrosion of stainless steels- part I. A mathematical model, *British Corrosion Journal*, Vol. 13, 1, (1978), 13-22. [Cited in ref. 69/220].
- [158] Mears RB, Evans UR, Corrosion at Contact with Glass, *Transactions of the Faraday Society*, Vol. 30, (1934), 417-423. [Cited in ref. 69/220].
- [159] Oldfield JW, Sutton WH, Crevice Corrosion of Stainless Steels, part II. Experimental Studies, *British Corrosion Journal*, Vol. 13, 3, (1978), 104-111. [Cited in ref. 69/220].
- [160] Crolet JL, Defranoux JM, Calculation of incubation times in crevice corrosion of stainless steels, *Corrosion Science*, Vol. 13, 7, (1973), 575-585. [Cited in ref. 69/220].
- [161] Fontana MG, Greene ND, *Corrosion Engineering*, McGraw-Hill, (1978), 41-44. [Cited in ref. 69/220].
- [162] Peterson MH, Lennox TJ, Groover RE, *Materials Protection*, (1970), 23. [Cited in ref. 69/220].
- [163] Korovin YM, Ulanovskii IB, *Corrosion, SBIIA*, Vol. 22, 16, (1966). [Cited in ref. 69/220].
- [164] Wilde BE, On pitting and protection potentials: their use and possible misuses for predicting localised corrosion resistance of stainless alloys in halide media, *Localised Corrosion, NACE*, (1974), 342-352. [Cited in ref. 69/220].
- [165] Sedriks AJ, *Corrosion*, Vol. 42, 7, (1986), 376. [Cited in ref. 42/221].
- [166] Smith R, Fatigue a continuing problem despite its long history, *IMECHE fatigue real life solutions seminar*, IMECHE HQ, London, February, (2003).

- [167] Dover WD, Rudlin JR, Topp DA, Fatigue crack measurement in offshore structures, in Marsh KJ, Smith RA, Ritchie RO eds., Fatigue crack measurement techniques and applications, EMAS Ltd., (1991).
- [168] Collins J, Daniewicz S, Failure considerations, in Mechanical Engineers HB, Kutz M ed., 2<sup>nd</sup> ED, Wiley, New York, (1998).
- [169] Taylor D, Modelling of fatigue crack growth at the microstructural level, *Computational Materials Science* 25, (2002) 228-236.
- [170] Taylor D, Lee TC, A crack growth model for the simulation of fatigue in bone, *International Journal of Fatigue*, Vol. 25, 5, (2003), 387-395.
- [171] Lee TC, O'Brien FJ, Taylor D, The nature of fatigue damage in bone, *International Journal of Fatigue*, Vol. 22, 10, (2000), 847-853.

## APPENDIX A

This appendix provides background information on fundamental corrosion mechanisms. Much of the content is widely acknowledged and numerous handbooks and chapters of handbooks were consulted [37, 70, 154, 42, 155]. A selection of text books [69, 71, 156] were also consulted in the writing of this appendix and all applicable information is rewritten in light of the current project. The primary sources are also stated.

### Introduction to corrosion and electrochemistry

Almost all engineering alloys are highly reactive in most environments, consistent with the observation that, with rare exceptions, metals are found in nature in an oxidised state. Thus, the use of most engineering alloys relies on the presence of a kinetic surface barrier (passive film) to reduce oxidation to manageable proportions.

Metallic corrosion is usually an electrochemical process in aqueous solutions at ambient temperatures [69]. Electrochemical processes occur when a galvanic cell is formed. A galvanic cell requires an anode and cathode in electrical contact, as well as an ionic conduction path through an electrolyte. Figure A.1 shows a galvanic cell, where the metal on the left is rendered anodic due to the higher electrochemical potential (ECP) of the dissimilar metal on the right.

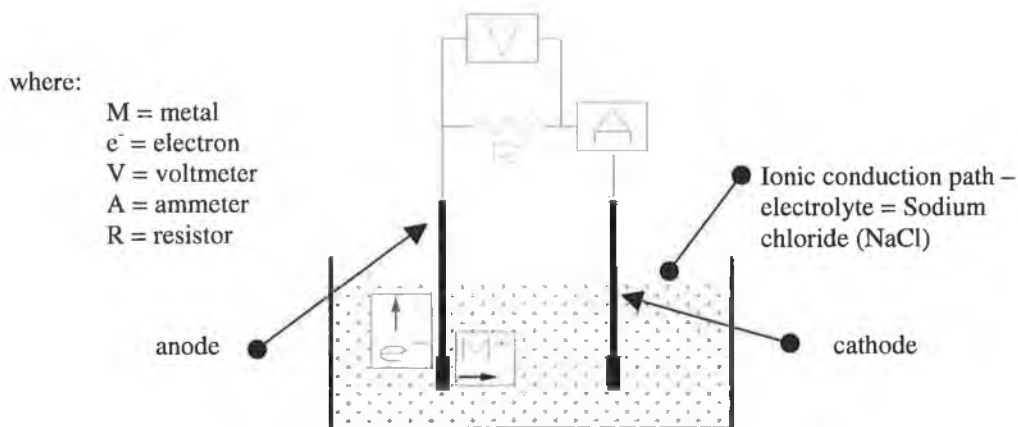
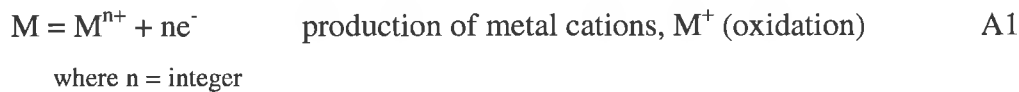
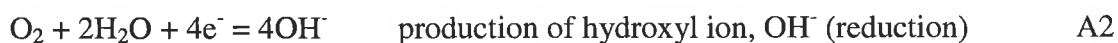


Figure A1 Simple electrochemical cell/corrosion system.

The phenomenon experienced by the metal on the left is termed “anodic dissolution”- as the metal is effectively oxidised/dissolved into solution. This can be considered as an oxidation half-cell reaction where electrons are given up to the metal of higher electrochemical potential on the right.



The other half of the corrosion cell concerns the metal on the right (cathode). The metal on the right attracts electrons from the anode. Specie dissolved in the electrolyte such as oxygen are simultaneously reduced (gain electrons).



The reduction oxidation (redox) reaction is a particular reaction type just as acid base reactions are a particular reaction type. The reaction specified above is oxygen supported and the reaction rate is maximised when oxygen is in plentiful supply at the cathode.

The oxidation of the metal and the reduction of oxygen occur simultaneously at the metal/electrolyte interface. The reactions are under charge transfer control, which means the electrochemical process is controlled by the charge transfer across the metal/electrolyte interface. In this way, the rate of the redox reaction can be quantified by measuring the flow of electrons (monitoring the current) between the anodic and cathodic areas [69]. The sample surface area is often taken into account through calculation of current density. For example, when passivity is disturbed (e.g. by local strains in the underlying material), the reaction rate (current density) of the exposed metal is generally very high ( $>1A/cm^2$ ) as the passive film is reformed [cited in 155].

The purpose of a potentiostat (an electronic instrument) is to control the ECP of an alloy in order to simulate potentials that the alloy may reach in reality due to electrolyte conditions. For experimental purposes the alloy under investigation is termed the working electrode while the other electrode in the cell is termed the

auxiliary electrode which is unaffected by the corrosion reaction. Electrodes are conducting media, which provide an interface between the electron current in wired electrical circuits and the ionic current of aqueous solutions. The potentiostat controls the ECP of the working electrode. Therefore, the working electrode can either be set as the anode as in figure A2 or the cathode. Therefore, the corrosion rate/current density of the working electrode can be determined over a full range of ECPs.

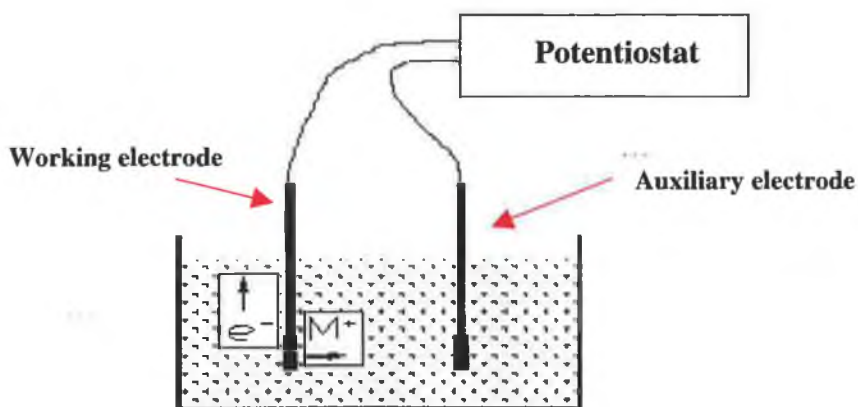


**Figure A2 Potentiostat controlled electrochemical cell.**

In order, to be certain of the ECP of the working electrode, it is necessary to set the ECP of the working electrode with reference to a stable potential. A reference electrode is used for this purpose. The potentiostat uses the reference electrode to set the ECP of the working electrode.

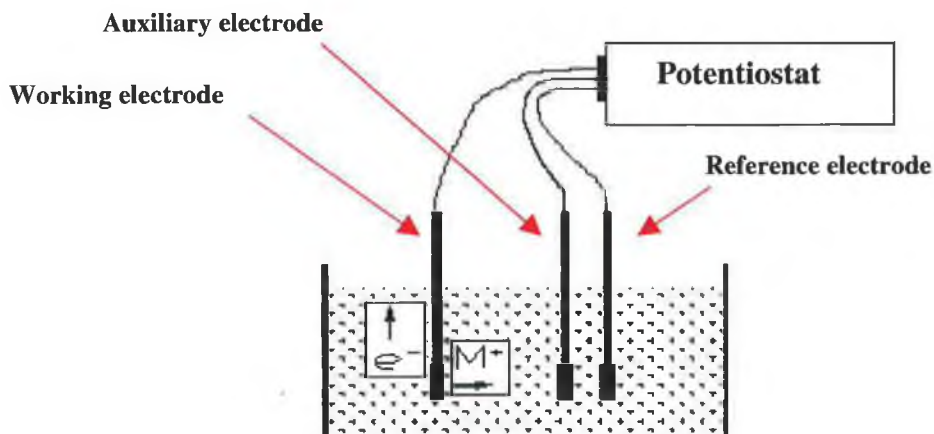


**Figure A3 ECP of working electrode referenced to reference electrode.**

From a practical viewpoint, it is clear that general corrosion mitigation can be achieved by having a sacrificial anode coupled to an engineering component in seawater. The 'sacrificial anode' method for corrosion prevention concerns the consumption of a sacrificial anode instead of the engineering component. The sacrificial anode must have a free ECP lower than that of the engineering component. Aluminium and zinc are commonly used for this purpose in the offshore and shipping industries. Alternatively, as just seen, a potentiostat can be used to render the engineering component cathodic and thus protected. This method is termed the 'impressed current' method. These types of corrosion prevention mechanisms are known as cathodic protection.

In the absence of an applied ECP (free ECP), an alloy immersed in seawater could be described as being in a pseudo-equilibrium condition. In practice, equilibrium conditions i.e. when no applied ECP is present are impossible to achieve; the alloy surface acts as an assembly of many tiny anodes and cathodes [69]. Under these circumstances, the net measurable current density,  $i_{app}$ , is zero. However, a finite rate of current defined by  $i_{corr}$  occurs at local anodic sites on the metal surface as indicated.

The information obtained in a polarization scan is current density as a function of the potential (ECP) applied. An example of such data for a stainless steel in seawater is shown in the schematic below.

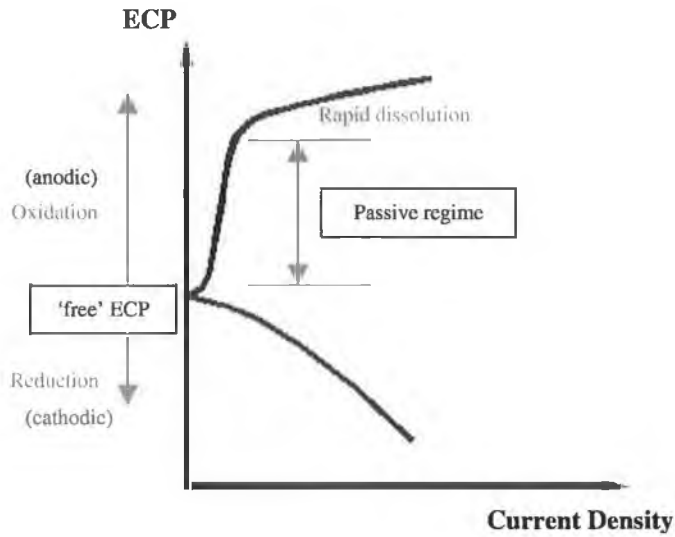


**Figure A4 Polarisation scan for a stainless steel.**

This data is extremely useful for alloys such as stainless steels. Even if stainless steels are cathodically protected in seawater, local regions can assume different ECPs than the bulk material. Local variations in ECP can arise due to a number of reasons including metallurgy and geometry. Two of the most important localised corrosion mechanisms which can arise are introduced in the next section. ECP also depends on the local condition of the seawater (oxygen content, chlorine level) [71]. This phenomenon is shown in figure A5.

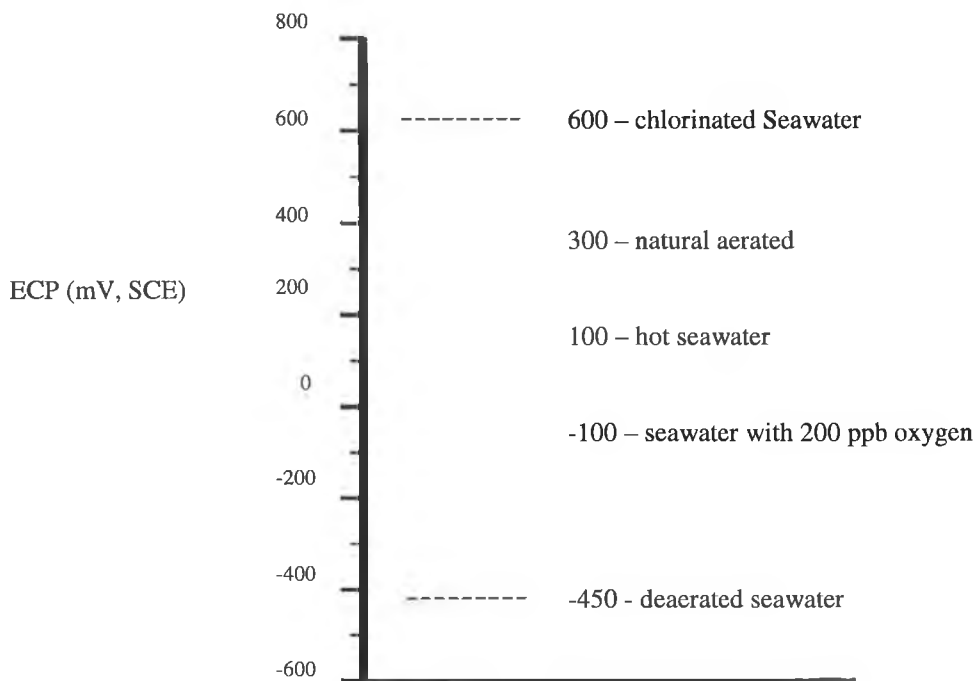


**Figure A5 Potentials of high alloy stainless steels in seawater under a variety of conditions [71].**

### ***Crevice Corrosion***

Since an alloy could be corroding locally while the bulk of the material is cathodically protected it is important to discuss local corrosion mechanisms.

Crevice corrosion occurs when discreet areas on an alloy are physically isolated or occluded such as in figure A6. Crevices can be formed at flanged joints, beneath weld spatter and as a rule, the tighter the gap the more likely that crevice corrosion will occur for a given bulk environment. It is thought that typical crevice widths range from 25 to 100 $\mu$ m [156]. Consequently a crack may be considered as an efficient crevice. Repercussions of crevices include increases in local ECP and reduction of local pH leading to ideal conditions for dissolution.

In the Oldfield and Sutton (O&S) model for crevice corrosion [157], the crevice corrosion process is described in four stages: (1) deoxygenation, (2) increase of the salt acid concentrations (development of a critical crevice solution), (3) depassivation, and (4) crack propagation.



On a boldly exposed passive surface, the oxidation of metal ions through the passive layer combined with the reduction of dissolved oxygen at the same rate results in a uniform current density over the alloy surface and thus a uniform passive layer. The generation of positive metal ions ( $M^+$ ) is counterbalanced electrostatically by the creation of negative hydroxyl ions ( $OH^-$ ) as seen in equations A1 and A2.

Crevice corrosion begins when discrete areas on a passive surface are physically isolated or occluded such as in a crack (figure A6). Convection between the solution entrapped within an occluded area on a passive surface and the bulk environment is slow, so the dissolved oxygen in a crevice solution is rapidly depleted. This lack of oxygen impedes the cathodic process and the associated generation of negative hydroxyl ions is diminished within the confined space. A local galvanic cell is established due to the difference in the oxygen concentrations of the solution within the crevice (anode) and the surrounding surface (cathode). The depletion of oxygen in the crevice solution shifts the local ECP in the active direction. Although “differential aeration” [158] is sufficient to induce crevice corrosion of certain metals and alloys, it only provides the initial driving force for further excessive dissolution.

As oxidation continues within the crevice, iron and chromium cations ( $Fe^{2++}$  and  $Cr^{3+}$ ) that have passed through the local passive film are concentrated in the stagnant solution within the crevice. In order for the maintenance of charge neutrality, mobile anions such as  $Cl^-$  are attracted to the crevice. The crevice solution becomes concentrated in metallic chlorides. Dissolved metal chloride-salts hydrolyse (react with water) and form hydrochloric acid (HCl), which results in “progressive acidification” [157, 159] of the crevice.

Excessive dissolution occurs when the pH of the crevice solution is sufficiently low and the concentration of chlorides is high enough to break down the passive film. The reaction proceeds rapidly due to the unfavourable area ratio of the small anodic crevice to the large cathodic bulk material surface. The electrochemical reaction results in the formation of “pits” on the walls of the crevice. What is visually identified as corrosion often consists of many minute coalesced pits. The incubation period required to develop a critical crevice solution with a particular crevice

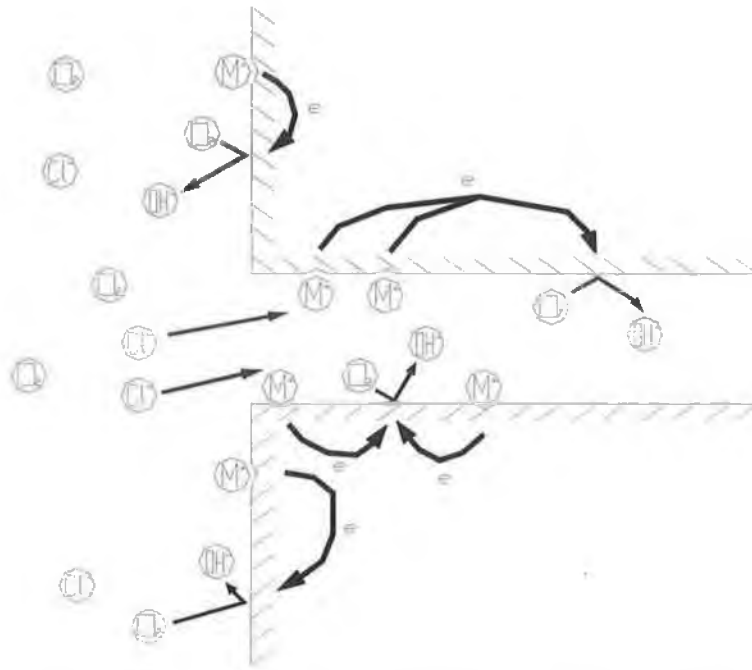
geometry determines the effective crevice corrosion resistance of a stainless steel alloy. The development of a critical crevice solution is governed by alloy composition, crevice geometry, and bulk solution chemistry [160].

In summary, the Oldfield & Sutton model suggests that firstly oxygen is consumed in the crevice. Consequently, local ECP rises and local dissolution is possible. Dissolution leads to the concentration of iron and chromium cations which attract anions such as  $\text{Cl}^-$  into the crevice. The metallic chlorides hydrolyse to form hydrochloric acid (HCl), the local pH falls and dissolution accelerates.

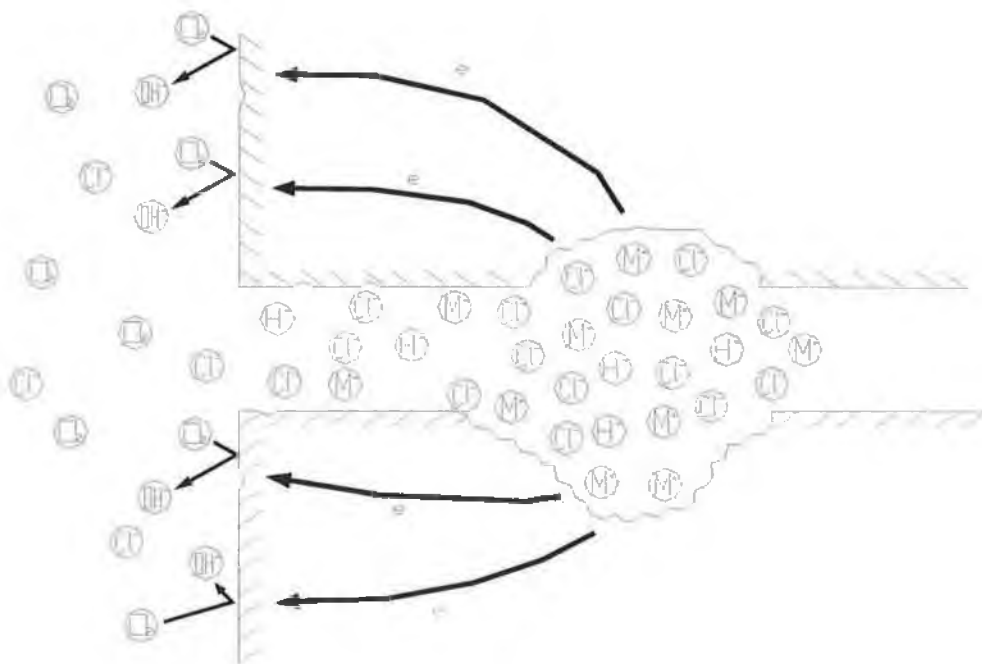
Fontana and Greene [161], propose that complex ions are formed between chloride and metal ions and water molecules in the occluded region. These undergo hydrolysis, giving corrosion product, and more importantly, hydrogen ions, which reduce the local pH. This can be described by the simplified equation:



The presence of the chloride ion is well known to be conducive to the development of low pHs because of its extremely low tendency to associate with hydrogen ions in water. (Hydrochloric acid completely dissociates in water  $\text{HCL} \rightarrow \text{H}^+ + \text{Cl}^-$ ). The increase of hydrogen ion concentration accelerates the metal dissolution process. So also does the concomitant increase of anion (chloride) concentration within the crevice. An important feature of active crevice corrosion cells is that they are autocatalytic, that is once started they are self sustaining.



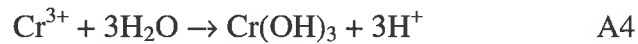
(a). Initial conditions: general corrosion occurs over the whole of the metal surface.



(b). Crevice corrosion conditions: metal dissolution occurs only inside the crevice where acidity is high, concentration of chloride ion increases, and reaction becomes self-sustaining.

**Figure A6 Fontana-Greene mechanism of crevice corrosion [161].**

Evidence has been produced [162], that it is not the corrosion of the iron in stainless steels which is the most damaging process to the alloy, but the hydrolysis of chromium which causes a significant fall in pH, again, summarised in the simplest form by:



Ion concentration more so than oxygen concentration is thought to have the most significant effect upon the level of attack, because of its effect upon local pH [163].

### ***Pitting Corrosion***

Unlike crevice corrosion, which requires a tight gap to occur, pitting corrosion can occur on a plane surface. Pitting corrosion occurs when discrete areas of a material undergo rapid attack while the vast majority of the surface remains virtually unaffected. Areas, which are selectively, attacked include:

- A surface scratch or other mechanically induced breaks in an otherwise protective film;
- An emerging dislocation or slip step caused by applied or residual tensile stresses;
- A compositional heterogeneity such as an inclusion, segregate or precipitate.

Similar to crevice corrosion, pitting depends strongly on the presence of an aggressive specie (e.g.,  $\text{Cl}^-$  ion in aerated aqueous solution) and a sufficiently high oxidising ECP. It has been proposed that the propagation mechanisms of crevice and pitting corrosion are similar [164]. However, pitting is distinguishable from crevice corrosion in the initiation phase. Whereas crevice corrosion is initiated by differential concentration of oxygen or ions in the electrolyte, pitting corrosion is initiated (on plane surfaces) by metallurgical factors alone.

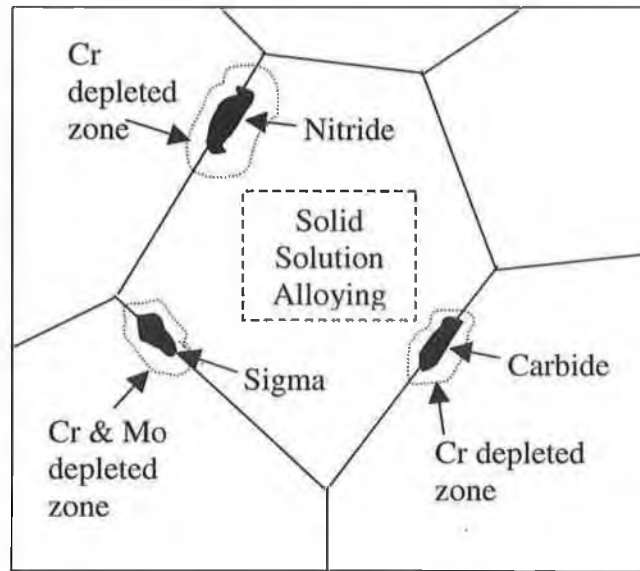


**Figure A7 Schematic diagram of metallurgical variables which may initiate pitting in stainless steels [165].**

Initiation of pitting comprises local breakdown of the surface passive layer. Pitting resistance is influenced by factors such as grain size, inclusion distribution and the presence of intermetallic phases [165] (figure A7).

The classic description of pit formation beneath a drop of water on an iron surface is credited to Evans [164]. The initiation of a pit is preceded by general corrosion over the whole of the wetted surface.

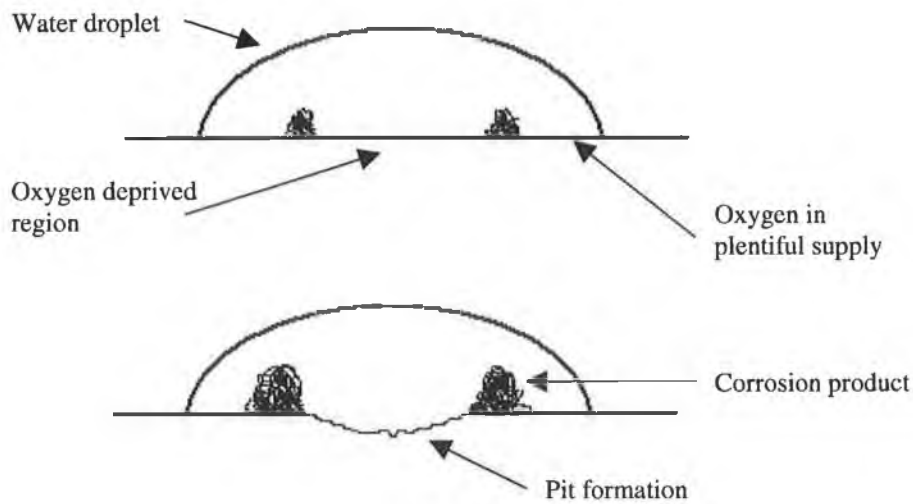
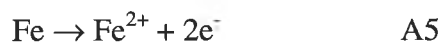


**Figure A8 Schematic of pit formation as proposed by Evans [164].**

The consumption of oxygen by the normal cathode reaction causes an oxygen concentration gradient within the drop of water. The wetted area adjacent to the circumference of the water drop receives more oxygen by diffusion than the area at the centre of the drop, which is at a greater distance from the oxygen supply. This concentration gradient renders the central region anodic and a galvanic cell is set up.



The hydroxyl ions (OH<sup>-</sup>) generated at the cathode diffuse inwards and react with the iron ions diffusing outwards, causing the deposition of insoluble corrosion product in a circular distribution. The corrosion product further retards the diffusion of oxygen, accelerates the anodic process in the centre of the drop, and causes the reaction to be autocatalytic.

The corrosion product “grows” over the pit and its immediate surroundings forming a scab or tubercule isolating the environment within the pit from the bulk electrolyte. It is thought that the autocatalytic process is assisted by an increase of the chloride ion concentration within the pit.

### ***Intergranular Corrosion***

Intergranular corrosion occurs when a material is sensitised, a phenomenon often associated with stainless steels [37]. Sensitisation produces a chromium-depleted envelope around each grain, which is less corrosion resistant than the bulk material. As a result intergranular corrosion occurs by dissolution mechanisms.

### ***Stress Corrosion Cracking***

Stress corrosion cracking has been defined as failure by cracking under the combined action of stress and corrosion [37]. The stress and corrosion components interact synergistically to produce cracks, which initiate on the surface exposed to the corrosive media and propagate in response to the stress state. Different alloys are susceptible to SCC in different aggressive media. However SCC only occurs above a specific threshold stress.

## **APPENDIX B**

The following is a review of the fundamental concepts underlying the analysis of fatigue crack propagation through a fracture mechanics approach. The sources for these concepts were principally textbooks concerning fracture and fatigue analysis by means of fracture mechanics methods.

### **Introduction to fracture mechanics**

Fatigue concerns the initiation and propagation of cracks. It is acknowledged that a number of short cracks (short cracks are defined as cracks which have length similar to the characteristic grain size of the alloy) can initiate from regions of high stress concentration or 'hotspots' under fluctuating load. Many short cracks may propagate from the hotspot region. Some of these short cracks may arrest at for example, microstructural barriers. However, one or a number of the short cracks may coalesce and nucleate into a dominant long crack, which may then propagate to a critical length causing catastrophic failure.

Short cracks due to their low driving force are strongly affected by microstructural features [166]. They are mostly analysed by continuum mechanics approaches e.g. safe life approach. Dominant or long cracks are much less sensitive to microstructure due to a typically high driving force [166]. Long cracks are mostly analysed by fracture mechanics approaches.



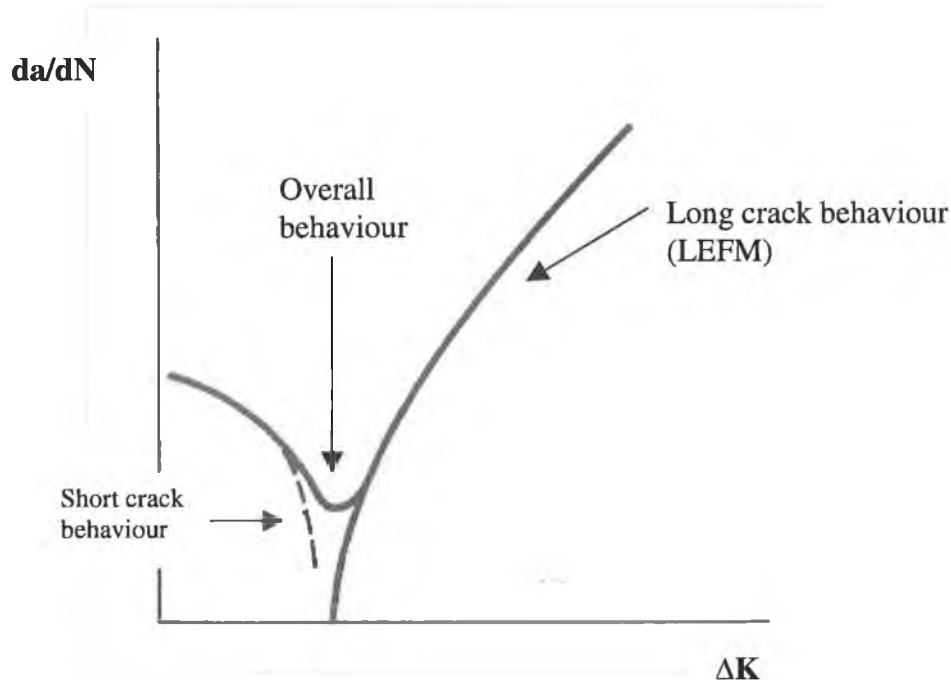


**Figure B1 Schematic of short and long crack growth behaviour.**

Therefore, two approaches exist when designing against fatigue failure, safe life and fail-safe approaches [86]. The first approach implies that an engineering component will function properly for a predetermined life. Therefore, short cracks will either not initiate or not propagate enough to cause failure over a predetermined lifetime. In order to achieve this aim, stress/strain based fatigue tests are carried out on smooth samples, e.g. S-N curves. Sample failure is the point when a dominant crack causes fracture. The number of cycles to failure at a particular stress range ( $\Delta\sigma$ ) is logged. For welded samples the tests are independent of mean stress applied (R-ratio) due to inherent residual stresses in the weld metal [19]. Of particular importance is the stress range at which  $1 \times 10^7$  load cycles are obtained. This stress range is usually described as the fatigue limit of a material. Up to 90% of the total fatigue life of the sample is required to initiate a dominant crack at the fatigue strength. Therefore, these tests are essentially crack initiation tests.

However, initiation resistance in components joined by welding is typically very low due to the presence of inherent cracks or flaws from the joining process [19]. Flaws are present before the structure is even commissioned. In this way, the crack propagation resistance of the component is most important. Therefore, the fail-safe or

defect tolerant approach is more appropriate for relatively large-scale welded structures such as pressure vessels and offshore structures.

With regard to the damage tolerant approach, the nucleation of a dominant fatigue crack and the initial crack size used for design depends on the resolution of the non-destructive crack detection (NDT) method employed [86]. This is typically a fraction of a millimetre. Using material constants found from laboratory crack propagation tests; the time taken for an initial crack of known length (determined by NDT) to grow to a critical length can be estimated. Inspection and repair intervals can be easily specified.

The need for frequent inspection intervals shows that fatigue mechanisms are not well understood or easily predicted. Indeed, they are less well understood in aggressive environments due to synergistic corrosion effects. In addition, NDT evaluation is expensive and often subjective [167]. Overall, the need for a mechanistic basis for corrosion fatigue is apparent if failures are to be minimised.

The reason that the micro mechanisms of corrosion fatigue are not well understood is perhaps largely due to the size scale over which permanent damage occurs at the tip of a fatigue crack. This scale is comparable to the characteristic microstructural dimension of the material - even for cracks visible to the naked eye. In addition, cracks with a low driving force can be markedly affected by microstructure regardless of their dimension [166]. As a result, subtle changes in microstructure and environment can lead to drastic alterations in the extent of cyclic damage and fatigue life – thus complicating matters.

### ***Fracture Mechanics Approach***

Fracture mechanics is concerned with the analysis of objects containing cracks and how they behave under load. The simplest useful model for stress at the tip of a crack is based on two assumptions:

- The material exhibits linear elastic behavior
- The system can be analysed in two-dimensions.

The analysis procedure is often referred to as linear elastic fracture mechanics (LEFM). As long as the plastic zone size prevalent at the tip of a crack remains small (small scale yielding) compared to the dimensions of the crack, the linear elastic model gives good engineering results [168].

AA Griffith formulated criteria for the unstable extension of a crack in a brittle solid in terms of a balance between changes in mechanical and surface energies in what is accepted to be some of the earliest work on fracture mechanics in the 1920's [86]. In the 1950's, Orowan extended Griffith's brittle fracture concept to metals by supplementing surface energy with plastic energy dissipation. However, the critical conditions for the growth of cracks can be formulated in more precise terms than energy balances by means of linear elastic stress analysis.

It was Irwin (1957) that succeeded in quantifying the near crack tip fields of a linear elastic crack in terms of a stress intensity factor,  $K$ . Essentially, an annular zone exists ahead of the crack tip, known as the region of  $K$ -dominance, within which the stress intensity factor provides a unique measure of the intensity of stress, strain or deformation. In ductile solids such as metals, the material at the crack tip yields when the near tip stresses exceed the flow strength and the linear elastic solutions lose their validity within this plastic/process zone. Continuum solutions are considered not to hold within the near tip region of intense deformation. Thus, the inner radius of the region of  $K$ -dominance is dictated by the size scale of the microscopic failure process.

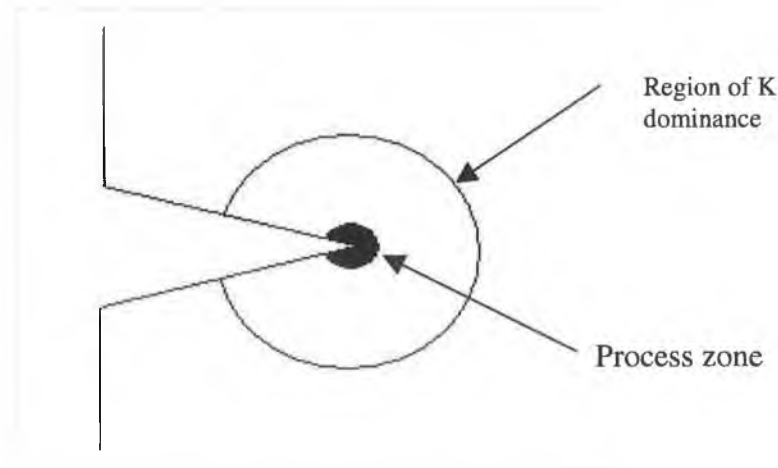


**Figure B2 Schematic of crack tip showing process zone and region of K dominance.**

The usefulness of the K-field to characterise the propagation of crack advance is predicted on conformity to the 'small scale yielding' condition [86]. This requires that the process zone is confined well inside the region of K-dominance. Therefore, linear elastic fracture mechanics (LEFM) prescribes valid ranges for specimen thickness, width and crack length in relation to the plastic zone size developed around the crack tip.

Each of the three basic modes of fracture (figure B3) can be analysed using K. Mode I is the tensile opening mode in which the crack faces separate in a direction normal to the plane of the crack. Mode II is the in-plane sliding mode in which the crack faces are mutually sheared in a direction normal to the crack front. Mode III is the tearing or anti-plane shear mode in which the crack faces are sheared parallel to the crack front. The tensile opening mode is generally considered the most common and the most severe loading mode and as such is of greatest concern in the current work.

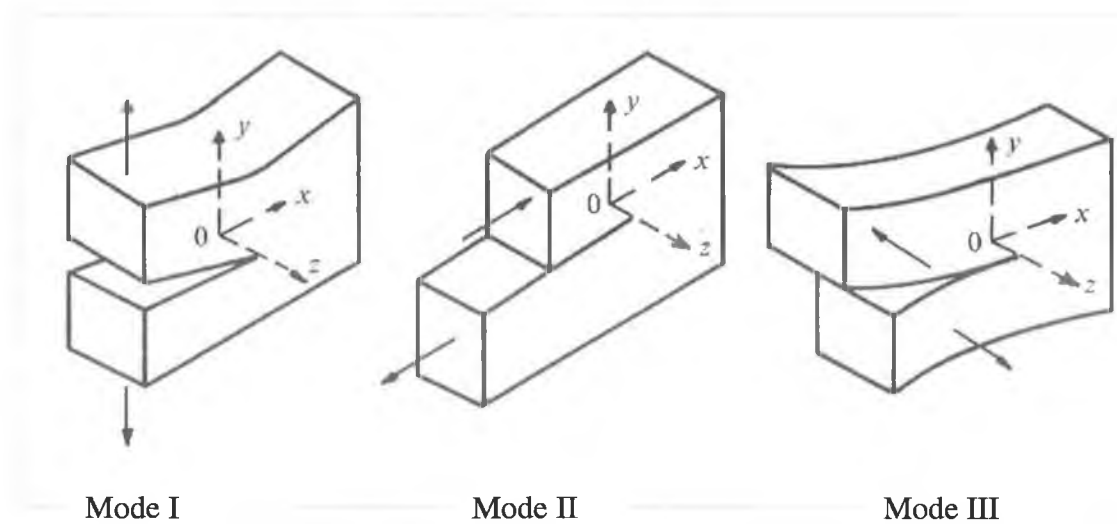


**Figure B3 Schematic of three basic modes of fracture.**

The diagram below shows the coordinate system and stresses in the near tip region of a crack in a large plate [86].

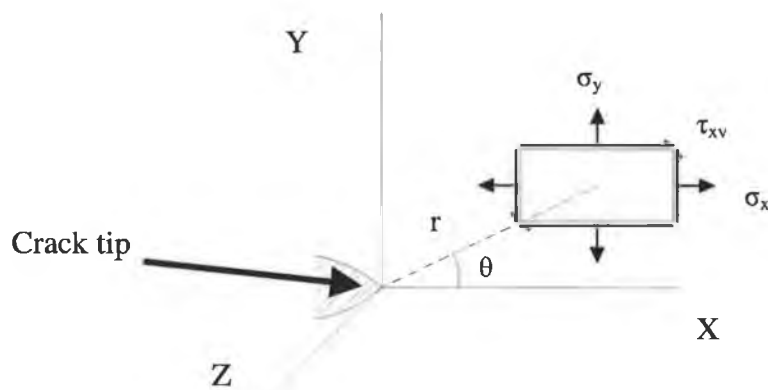


**Figure B4 Distribution of stresses in vicinity of a crack tip,  $r$  and  $\theta$  are polar coordinates [86].**

For plane stress/strain the leading terms for mode I stress fields in Cartesian coordinates are as follows [86]:

$$\sigma_x = \frac{K_I}{\sqrt{2\pi r}} \cos \frac{\theta}{2} \left[ 1 - \sin \frac{\theta}{2} \sin \frac{3\theta}{2} \right] \dots B1$$

$$\sigma_y = \frac{K_I}{\sqrt{2\pi r}} \cos \frac{\theta}{2} \left[ 1 + \sin \frac{\theta}{2} \sin \frac{3\theta}{2} \right] \dots B2$$

$$\tau_{xy} = \frac{K_I}{\sqrt{2\pi r}} \cos \frac{\theta}{2} \left[ \sin \frac{\theta}{2} \cos \frac{3\theta}{2} \right] \dots B3$$

Where

- K = stress intensity factor
- r = distance from crack tip
- $\theta$  = angle from crack plane
- $r \ll a$
- a = crack length

For remote loadings, the general expression for the stress intensity factor is of the form:

$$K = Y \sigma \sqrt{\pi a} \quad B4$$

Where:

- $\sigma$  is the tensile stress perpendicular to the crack,
- Y is a compliance function, a dimensionless parameter which depends on the sample geometry and crack length,
- a is the crack length.

Evident is the fact that K is a function of loading, geometry and crack length. By using K, general relationships can be developed which are applicable to cracks and components with a variety of geometries.

Each material has a critical value of K, i.e.  $K_C$  that represents the onset of unstable crack growth. Since mode I loading is considered the most deleterious mode, it is usual for material handbooks to state only the mode I  $K_C$ . For a given material,

depending on the state of stress at the crack tip, the critical stress intensity  $K_C$  decreases to a lower limiting value as the state of strain approaches the condition of plane strain [168]. The plane strain condition occurs when displacements in the z direction are zero on loading and is dependent on material thickness [168].

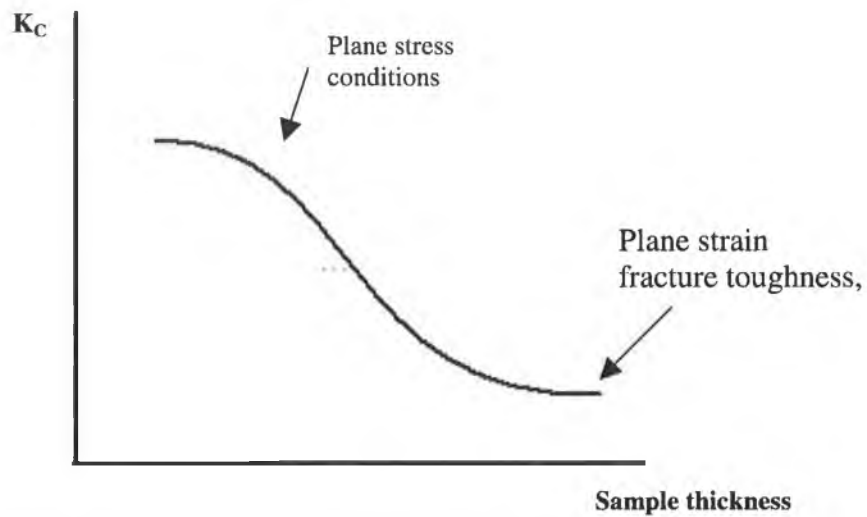


**Figure B5 Schematic of variation of  $K_C$  with sample thickness.**

This lower limiting value of  $K_C$  defines a basic material property  $K_{IC}$ , the plane strain fracture toughness of a material. Standard test methods such as BS 7448-1:1991 [60] have been established for the determination of  $K_{IC}$  values. With reference to the standard, for plane strain conditions the minimum material thickness  $B$  must be

$$\geq 2.5 \left( \frac{K_{IC}}{\sigma_y} \right)^2 \quad \text{B5}$$

where:

$\sigma_y$  = yield stress of material.

The linkage of what actually happens in service to an experiment performed in the laboratory designed to generate appropriate data, has been termed *similitude* [166]. In order for the data generated in a laboratory test to accurately represent real life behaviour, the similitude must be very high.

### ***Fatigue Crack Propagation***

Fracture mechanics is a useful method for characterising the resistance of a particular microstructure/environment couple to crack propagation under cyclic loading. Through controlled fracture mechanics tests and fracture surface examination, it is possible to gain an insight into the microscopic mechanisms of failure.

The basis of the application of fracture mechanics to fatigue is the relationship between the rate of crack propagation  $da/dN$  and the stress intensity factor range ( $\Delta K = K_{\max} - K_{\min}$ ). Fatigue crack growth rates have a strong dependence on the stress intensity factor range ( $\Delta K$ ), which is the difference between the maximum and minimum stress intensity factors experienced by the crack [86], and for many practical cases the *Paris* law is applicable (equation B6).

$$da/dN = C\Delta K^m \quad \text{B6}$$

Where:

- C and m are material constants, which are found experimentally by measuring the rate of growth of a crack under known loading conditions in a simple test specimen.

The Paris law is probably the most popular and useful relationship concerning fatigue crack growth. Smaller values of  $\Delta K$  result in a much slower asymptotic growth rate than the Paris equation predicts, eventually leading to a threshold value. Conversely increasing  $\Delta K$  (or rather  $K_{\max}$ ) towards the plane strain fracture toughness,  $K_{IC}$ , yields an accelerated crack growth rate. Despite these deviations from the Paris equation at high and low growth rates, it describes the majority of crack growth adequately.



With regard to the Paris law, fatigue crack growth rate,  $da/dN$ , is typically plotted against the stress intensity range,  $\Delta K$ , on a log-log scale and the sigmoidal characteristics typically found are illustrated in figure B6.

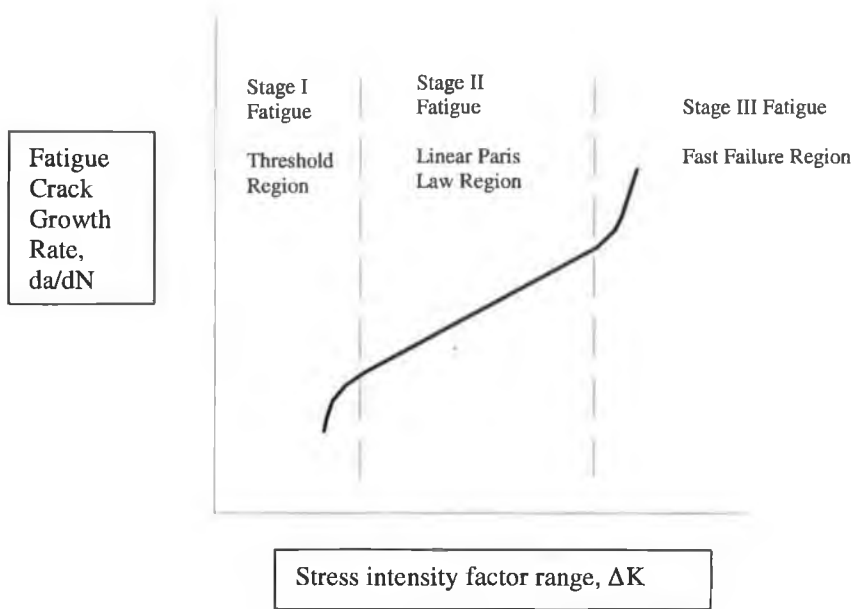


**Figure B6 Schematic of the various fatigue regions and sigmoidal nature of fatigue crack extension in steels.**

An extensive review [9] of published literature concerning *fatigue problems* in the 20<sup>th</sup> century concluded that the variety of practical problems is large. Consequently, one fatigue problem may be concerned with stage I threshold crack behaviour, whereas another problem may concern stage II steady state crack propagation. For instance, fatigue of bone in athletes due to heavy training schedules is entirely different from fatigue of a welded offshore structure in the open sea.

### *Short Cracks*

Short cracks are of concern where long service lives are required without the need or possibility of frequent inspection as in the case of human bone. Much work is currently being carried out on bone where typically short cracks exist of approximately 100  $\mu\text{m}$  in length [169-171]. Stage I is the region of concern for short cracks – more specifically below the critical threshold stress intensity range  $\Delta K_{th}$  after

which long cracks are dominant. Threshold is largely influenced by microstructural parameters, such as grain size [166]. Therefore, it is desirable to gain understanding of the interaction of these short cracks with microstructural features. Short cracks typically initiate where the microstructure is weak e.g. large grains. The crack will subsequently grow away from this weak region and sample the rest of the microstructure, which inevitably will be stronger [166]. It is widely acknowledged that environment and mean stress have a large influence in stage I and may aid crack closure and subsequent reduction in crack tip driving force. Eventually when the crack becomes large compared to microstructural features, it will experience the material as a homogenous continuum [166]. As a result, multiple short cracks may initiate and grow rapidly slowing as they extend. Some cracks may stop growing while others after passing through a minimum growth rate will coalesce and speed up becoming a dominant long crack.

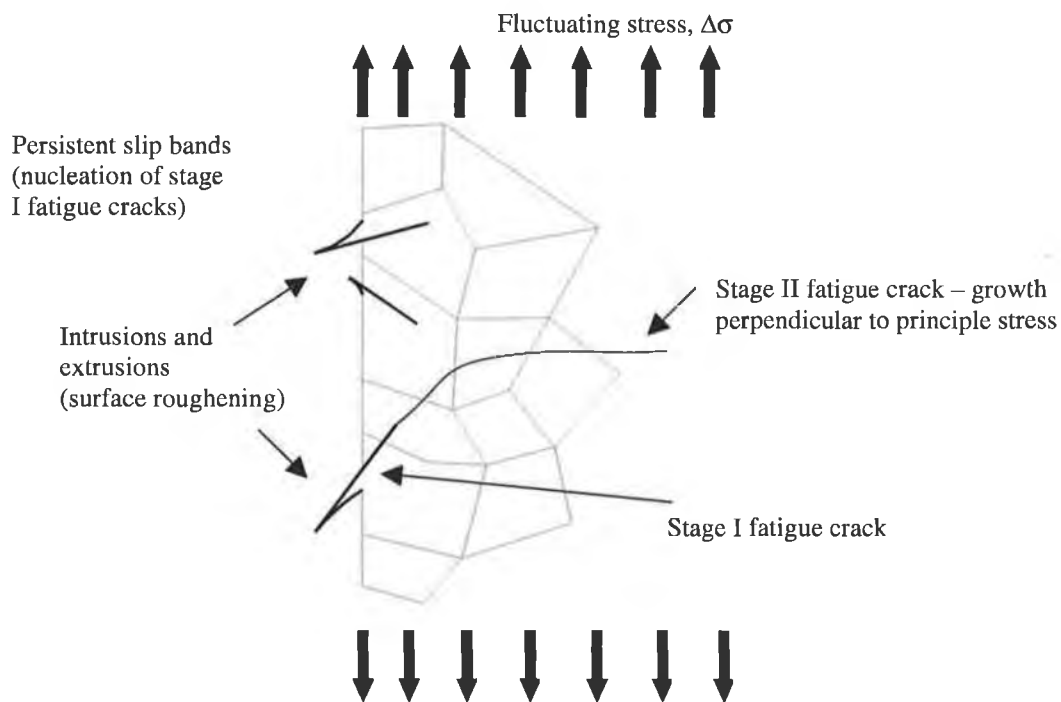


**Figure B7 Metallic fatigue; crack initiation, stage I and II crack propagation.**

### *Long Cracks*

Long cracks are the main source of concern for relatively large components where designers must 'live with cracks' such as in offshore structures [19]. It is clear that the growth rates of cracks in their early stages 'short crack growth' is not of immediate

concern in such applications as a high percentage of the crack initiation stage is typically complete before the structure enters service due to the presence of flaws in weld metal. Therefore, the current project deals with long crack propagation and the effect of environment on the crack propagation mechanism.

A fraction of long crack growth is stage I type fatigue crack growth. Here the crack and the zone of plastic deformation surrounding the crack are confined within a few grain diameters. Crack growth occurs by single shear in the direction of the primary slip system [86, 166].

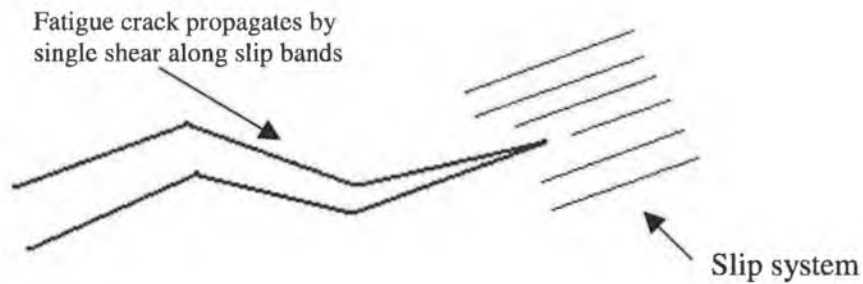


**Figure B8 Schematic of stage I type crack growth.**

At higher stress intensity range values, the plastic zone at the crack tip encompasses many grains. The attendant crack growth process involves simultaneous or alternating flow along two slip systems [86]. This duplex slip mechanism, termed stage II by Forsyth (cited in [86]) results in a planar (mode I) crack path normal to the far field tensile axis.

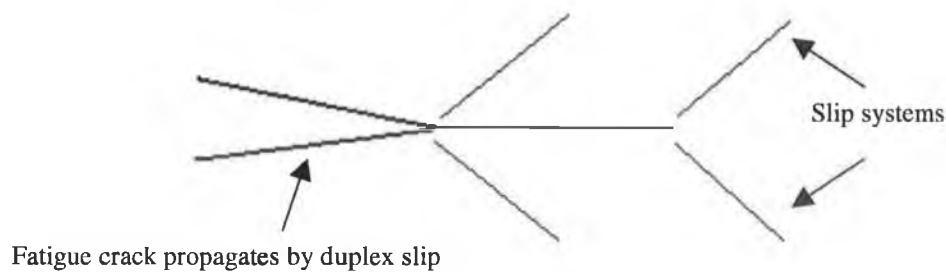


**Figure B9 Schematic of stage II type crack growth.**

The complex stage II region is the subject of much research. Crack growth rates in this region depend exponentially on the stress intensity factor range [86]. The experimentally determined values of  $m$  and  $C$  vary, but for structural steel the most common value found for  $m$  is 3 [114]. A corresponding value of  $C$  representing conservative estimates of the rate of crack propagation (excluding environmental effects) is  $4 \times 10^{-13}$  [114]. In contrast, to stage I growth, the crack growth rate is only weakly dependent on microstructure [166, 86]. Mean stress or R-ratio ( $K_{\min}/K_{\max}$ ) can have a significant influence [86].

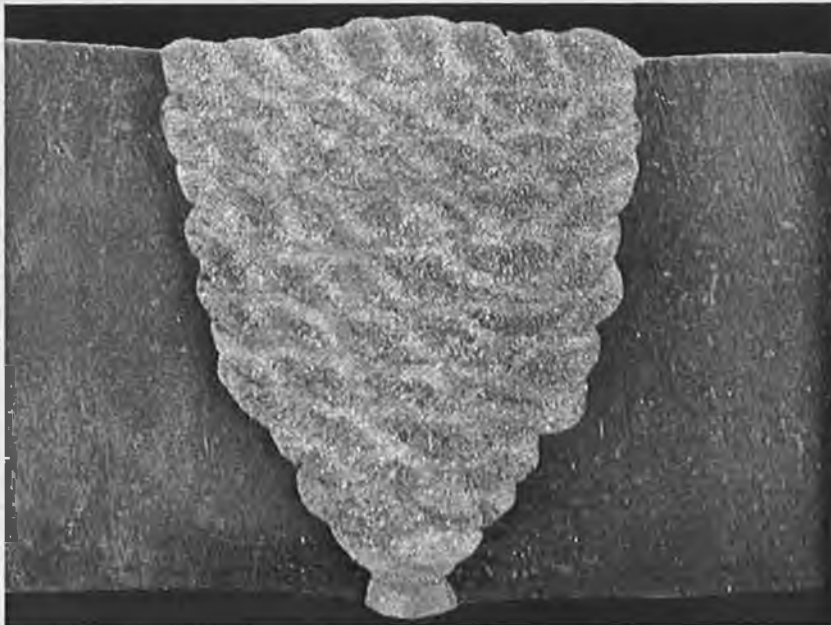
The main fatigue crack extension mode in this region usually exhibits crack arrest marks, known as fatigue striations, which essentially are a visual record of the fatigue crack front during crack growth through a material. Unlike stage III growth, material thickness has little influence on steady state crack propagation [119].

At high stress intensities, the plastic zone size becomes sufficiently large for  $K_{\max}$  dependant static fracture modes to occur such as microvoid nucleation and growth, and bursts of cleavage cracking - intergranular and fibrous modes are sometimes evident [86]. Stage III crack growth is characterised by this behaviour. These static modes become increasingly dominant with increasing stress intensity until unstable crack propagation ensues. The onset of stage III is strongly dependant on R-Ratio [86]. Microstructure, mean stress and thickness have greatest influence in this region [86]. Environment is widely known to have little influence.

**APPENDIX C**

**ZERON 100 WELDING GUIDELINES**

WEIR MATERIALS & FOUNDRIES  
*Guidelines for Welding*  
*ZERON 100*  
*SUPER DUPLEX*  
*STAINLESS STEEL*



**ZERON**  
100

ZERON 100 SUPER DUPLEX STAINLESS STEEL

## CONTENTS

	PAGE
<i>Preparation for welding Zeron 100</i>	3
<i>Welding Consumables</i>	4
<i>Typical Joint Configurations</i>	4
<i>Welding</i>	6
<i>Welding Procedure</i>	8
<i>Post Weld Cleaning</i>	14
<i>Health and Safety</i>	16
<i>Summary</i>	16
<i>Contacts</i>	16

Zeron 100\* invented and developed by Weir Materials & Foundries was the first of the super duplex stainless steel alloys. The unique chemical composition has been shown to be correctly balanced to offer the best combination of corrosion resistance and strength. The steel is tightly controlled from melting through manufacture to ensure a better performance than other steels from the same generic grade. Zeron 100 is available in all product forms, many ex stock, with a proven track record through manufacture fabrication and successful service.

When welding Zeron 100 super duplex stainless steel, there are several factors that must be considered. This pamphlet highlights the main factors that must be taken into account. It relates particularly to welds to be used in the "as-welded" condition, made using all the common welding processes. The same principles will apply if post weld heat treatment is being applied.

\*Zeron is a registered trade mark of Weir Materials & Foundries.

## **PREPARATION FOR WELDING ZERON 100**

It is strongly recommended that a Welding Procedure Specification (WPS) and corresponding Welding Procedure Qualification Record (WPQR) are available prior to commencement of production welding. The WPS should be qualified to a higher level than the statutory requirements of the base codes such as ASME etc. and should include an ASTM G48 Method A corrosion test, a microstructural evaluation and ferrite determination in addition to the mechanical and non-destructive tests required. Welder qualification (WQR) should also carry these extra requirements to show that the metallurgical quality of the weld area is satisfactory as well as the structural integrity for the codes.

There should be considerable emphasis by the Welding Engineer on maintaining the qualified parameters throughout production welding.

### **Handling and Storage of Parent Material**

All duplex stainless materials should be handled and stored under conditions which prevent contamination from other ferrous and non ferrous alloys.

Use stainless steel, wood, plastic or other non-metallic materials as protective covers with storage racking, fork lift truck arms, overhead crane slings etc. Welding should be carried out in a contaminant free work area as recommended for other stainless steel fabrications. Only qualified duplex stainless steel should be used for temporary attachments at the corrosion side. A minimum number of temporary attachments should be employed.

### **Handling and Storage of Welding Consumables**

Welding consumables for Zeron 100 should be handled and stored accordance with the manufacturer's recommendations. In general, the consumables should be stored in an "electrode store" held at approximately 10°C above ambient temperature and with a relative humidity below 60%.

Opened packs of electrodes and flux should be baked in accordance with the manufacturer's recommendations.

### **Identification of Materials to be Welded**

Check against the welding procedure, specifications and drawings that the materials and welding consumables issued are correct and identified. Where it is necessary to mark materials using pens or paint markers, these must be free of chlorides, sulphides, halides and Zinc.



### Welding Procedure Specification

Check that an appropriate WPS and WPQR are available, outlining the welding procedure to be followed. The procedure should be qualified in accordance with the recommendations of the latest issue of MDS 12804/21, or other similar specifications.

### Tooling

Use only stainless steel grade cutting tools, grinding discs, grinding wheels, wire brushes and polishing wheels. Avoid the use of power wire brushes at the corrosion side so as not to smear the weld zone which has been shown to lead to reduced corrosion resistance.

### Joint Preparation

Welding bevels should preferably be prepared by cold methods. Where plasma cutting is used the process should be under water and at least 1 mm of material be ground off to remove the heat affected zone. When machining preparations, outline machining details are available from WMF upon request. Recommended joint configurations for single sided welds are detailed in the next section. The recommended root gaps, root faces and joint angle are based on the need to:-

- maximise production
- minimise parent metal dilution in the root
- control the heat input

For this reason, control of the root gap is considered an important factor.

Compound bevels must be balanced to ensure access whilst minimising joint volume.

## **WELDING CONSUMABLES**

Two grades of welding consumables are available.

Zeron 100 "M" grade has a composition matching that of the parent material and should generally be used for joints to be solution annealed. Zeron 100 "X" grade is overalloyed with nickel and is intended for use in joints that are to be put into service in the "as-welded" condition.

Autogenous welding of square close butt preparations can only be used under specific circumstances and its use needs to be considered on a case by case basis. Advice on specific situations can be supplied on request.

## **TYPICAL JOINT CONFIGURATIONS**

### Manual Welding

The joints detailed in Fig.1 are for single sided manual welding with the GTAW or GMAW-STT\* process in the root. Other joints, for example two sided, are similar to those applied in general stainless steel practice.

*\*STT - Surface Tension Transfer - Registered trademark of the Lincoln Electric Company.*

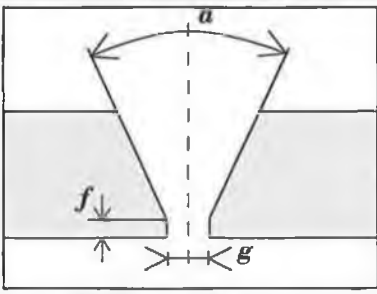
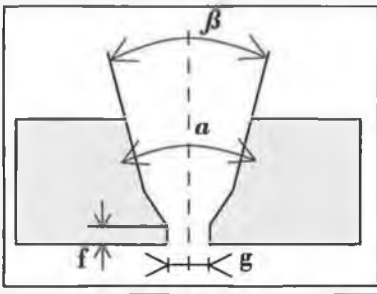
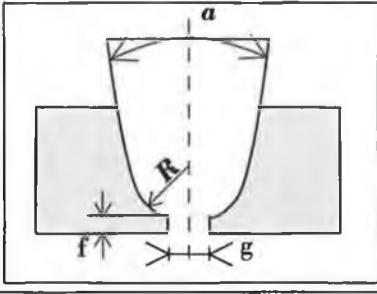
JOINT GEOMETRY	WALL THICKNESS t (mm)	Included angle (°)		Root gap g (mm)	Root face f(mm)
		$\alpha$	$\beta$		
	2-3	70-90	-	2-3	0.5-1.5
	>4	70-80	-	2-3	0.5-1.5
	>20	70-80	15-20	2-3	0.5-1.5
	>20	15-30	4-6	2-3	0.5-1.5

Fig. 1 Typical manual welding joint configurations.

Automated Welding

For automated GTAW welding a closed butt (zero root gap) may be used. The joint is designed to maximise the filler addition to the root bead and to achieve adequate root bead thickness. Care must be taken to ensure that there is sufficient filler metal addition. A typical joint is shown in Fig.2.

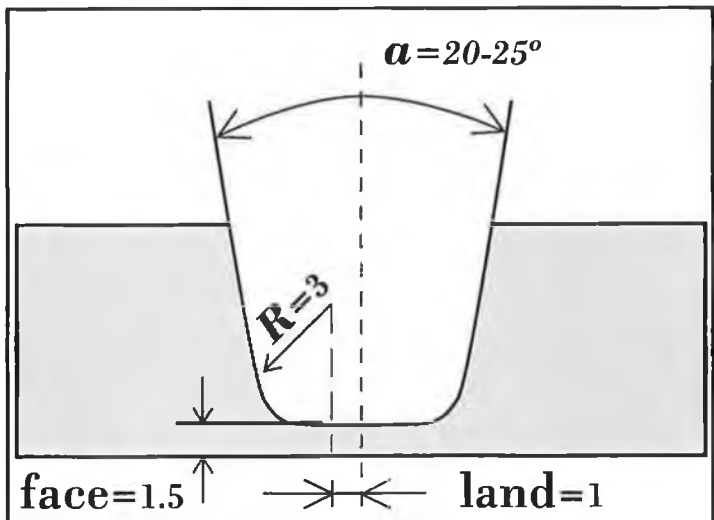


Fig. 2 Typical automated weld joint configuration.

## Welding Equipment

There are no specific welding equipment requirements associated with Zeron 100 over and above good stainless steel welding practice.

As with sophisticated stainless steel welding, slope in/out facilities together with pre and post gas purge are important requirements for GTAW welding plant. Equipment with pulsed arc facilities is considered beneficial for GTAW and GMAW welding of Zeron 100 due to optimal control of arc energy.

Newer processes where high deposition rates are achieved with lower arc energy are particularly suited for welding Zeron 100 super duplex stainless steel. Processes such as GMAW-STT, GTAW-DSP\* and the use of consumable socket rings are typical of recent developments. Further details are available on request.

## Joint Cleanliness

Joint faces and pipe/vessel surfaces 50 mm either side of joint seam should be cleaned and degreased using acetone and lint free cloth. Abrasive cleaning is rarely necessary. Should mechanical cleaning be necessary, light grinding or grit (alumina) blasting may be used.

## WELDING

### Joint Fit Up

Line up clamps can be used to assist joint fit up. The clamp may be either internal or external. Excessive mismatch of abutting joint edges ("Hi-Lo") should be avoided in order to ensure a satisfactory final root underbead profile and weld quality.

Counterboring of tubular components can be carried out to achieve the required fit up alignment. Care must be taken to avoid reducing the wall thickness excessively and to taper in the counterbore in accordance with the specification.

Joint fit up, and plate pre-setting, must be related to the normal distortion control techniques including balanced welding and back step welding.

\* DSP - Dual Sync Pulse Welding - registered trade mark of Dimetrics Inc.

## Tack Welding

Several options are available:

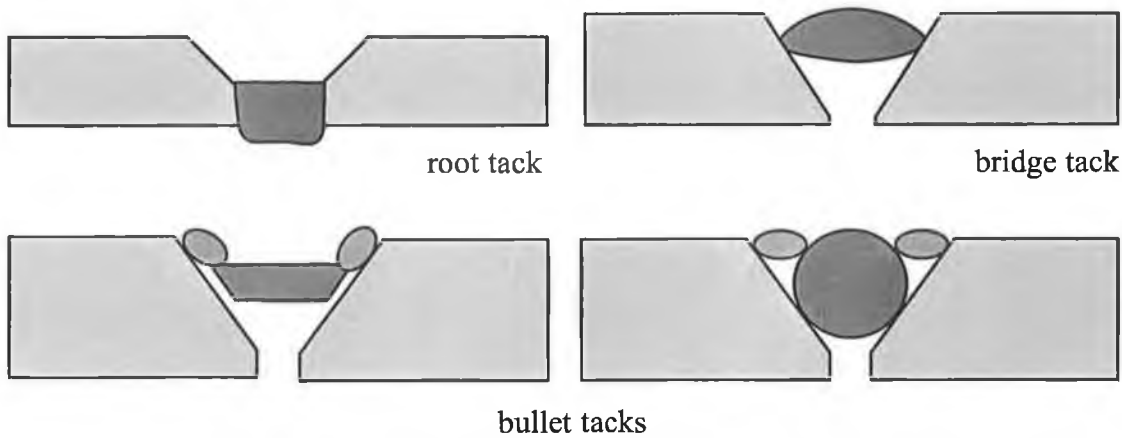


Fig. 3 Tack welding

Bridge tacks or spacer “bullet” blocks are recommended to maintain the root gap and joint alignment. Plate joints must be pre-set as normal to counteract distortion. All spacer blocks are to be stainless steel and they should be tacked at a controlled heat input in accordance with the WPS.

Where tack welds are intended to form an integral part of the weld root bead, the root tack welds should be deposited in accordance with the approved WPS and the ends should be taper ground to ensure fusion with subsequent weld runs. Back purging should be employed when GTAW is used to deposit integral tacks.

The tack welds should be balanced around the joint in order to maintain the root gap and joint alignment.

## Back Purging

When welding Zeron 100, it is recommended that commercial purity argon is used to displace the air behind the joint. The oxygen content of the resulting argon/air mixture must be monitored and controlled to ensure that sufficient nitrogen is retained in the backing gas “mixture” in order to inhibit loss of nitrogen from the weld pool. In practice the oxygen level of this mixture should be controlled at approx 0.5% oxygen monitored at the start of the welding sequence. In this way, a positive partial pressure of nitrogen is maintained behind the joint thus preventing nitrogen loss from the root bead, whilst the oxidation produced remains acceptable. Passes subsequent to the root pass can be made with minimum oxygen contents.

The backing gas composition should be monitored at the joint line using a portable oxygen monitor immediately prior to starting or re-starting welding in order that consistency can be maintained. Adhesive tape low in sulphur and chloride is used around the open joint seam, and the tape should be removed progressively during the welding sequence.

Care should be taken to regulate the flow rate of the back purge gas to prevent gas turbulence and possible air entrainment through the open weld seam. The flow rate of the backing gas is typically 10-15 L/min although it is necessary to reduce flow rate at the tie-in location to avoid risk of expulsion of molten metal and root underhead concavity.

Gases containing hydrogen, eg, Formier gas, should not be used.

## **WELDING PROCEDURE**

### **Preheat**

Preheat is normally not required. It should only be applied where material is not dry or is below 5°C prior to welding. Also in highly restrained heavy constructions or in particularly thick fabrications, preheating up to 100°C has been shown to be beneficial, further details available upon request. Oxyfuel or carburising flames should not impinge directly onto the material. Hot spots should not occur.

### **Arc Energy**

Arc energy is the common parameter controlled during the welding process. However, when welding duplex/super duplex it is the cooling rate which controls the microstructure and so the arc energy should be controlled in conjunction with the joint thickness.

It is more effective in the control of optimum arc energy to maintain faster welding travel speeds and associated higher welding currents rather than lower welding current and slower travel speeds.

To ensure a consistent arc energy, weaving of the weld bead should be kept to a minimum with a maximum of 3 x filler wire diameter.

### **Interpass**

Interpass temperature, together with welding arc energy, is important in optimising the cooling rate of a joint. Excessively high interpass temperature or arc energy may impair the corrosion resistance and impact toughness of the joint. The interpass temperature and welding arc energy must always be balanced in order to optimise the properties of the joint. If, for example, the arc energy cannot be maintained in the appropriate range, it would be necessary to reduce the interpass temperature.

The maximum interpass temperature should be as detailed in appropriate WPS and certainly less than 150°C.

The interpass temperature is measured immediately prior to any welding directly at the points where a weld run is to commence and where it is proposed to terminate. A contact thermocouple should be used. The weld zone must be below the interpass temperature before restarting welding. The interpass temperature must be measured at each break in welding and not just when starting a new pass.

**Root Pass**

The GTAW process is normally specified to enhance control of root bead quality. Whilst fabricator choice and the practices used in a particular shop are very important, it is generally found that:

- 1.6 mm or 2.0 mm diameter filler wire is often used for material up to 4 mm thick.
- 2.4 mm or 3.2 mm diameter filler wire is generally used for other material thicknesses.
- Keyhole rooting practice is considered to be a preferred technique to obtain the optimum properties within the arc energy restraints in the root pass.

Welder preference can be considered but it should be recognised that it is beneficial to deposit larger bead thicknesses within the arc energy restrictions.

Welding arc energy must be controlled to avoid adversely slow weld cooling rates developing during welding cycles. Practical guidelines based on industrial experience are given in the table below:

*Table 1 Typical root arc energy and layer thicknesses*

Wall thickness (mm)	Arc energy (kJ/mm)*	Typical Pass Thickness (mm)
2.88	0.4-0.6	2
7.11	0.8-1.2	3-3.5
17.5	1.5-1.8	3-3.5

\*Arc Energy = 
$$\frac{\text{Amps} \times \text{Volts} \times 60}{\text{Travel Speed (mm/min)} \times 1000} \text{ kJ/mm}$$
  
 OR  
 \*Arc Energy = 
$$\frac{\text{Amps} \times \text{Volts} \times \text{Arc time(s)}}{\text{Run Out Length (mm)} \times 1000} \text{ kJ/mm}$$

It should be considered that one important variable that is not commonly controlled during manual GTAW welding is filler metal addition. The typical root pass thickness indicated in the table above is based on:

- a) Welding into the controlled root gaps specified in figure 1.
- b) Addition of maximum and consistent levels of filler metal into the weld pool to promote optimum cooling rates.

An excessively thick root pass is generally associated with too high an arc energy, whereas too thin a root pass is likely to result in burn through by the second pass. Root beads that are either too thick or too thin do, of course, result in practical welding problems and are likely to result in poor penetration bead profile. The root pass thicknesses shown are typical for the thickness being welded at the appropriate arc energy.

It may be considered advisable to deposit weld beads as a series of balanced segments, for example such as shown in figure 4, at this offers the advantage of:

- Controlling joint gap closure
- Reducing overall joint distortion
- Maximising production whilst maintaining interpass temperature requirements.

The stop and start regions of all weld beads should be taper ground to facilitate smooth tie in. In GTAW welding industrial grade argon (99.995%) is recommended as shielding gas at typical flow rates of 8-12 L/min.

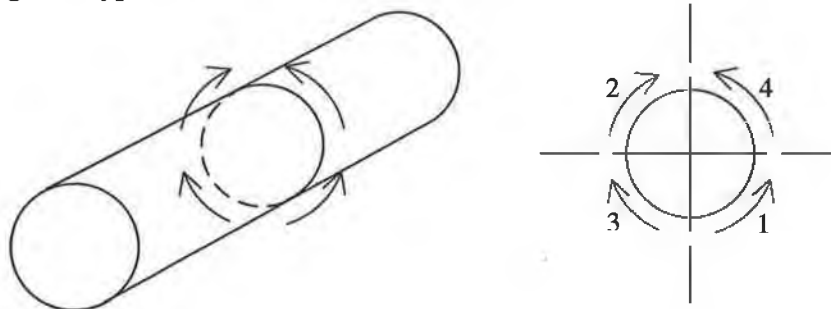


*Fig. 4 Balanced Joint sequences*

Nozzles incorporating a gas lens ensure good gas coverage and effective weld protection with the avoidance of gas turbulence where extended tungsten electrode stick out is being applied.

Slope down techniques at the termination of a weld to control phase balance should be used.

#### Second Layer 'Cold Pass'

The root weld bead upper surface should, if necessary, be dressed smooth and stainless steel wire brushed. However, grinding is rarely required.

As a general guide the second "cold" pass is deposited at a lower arc energy than that of the root pass. GTAW welding is normally used. Interpass temperature control as detailed previously must be maintained. It may be necessary to manipulate the weld pool in order to ensure that the pool is "washed in". This can be achieved by "flicking" the weld pool up onto the side wall. Weaving must be minimised. Single bead or split layer welding techniques can be used within arc energy and joint configuration requirements.

A single bead “cold pass” is preferred. Figure 5 below illustrates the effect of different root pass and 2nd “cold” pass arc energy combinations.

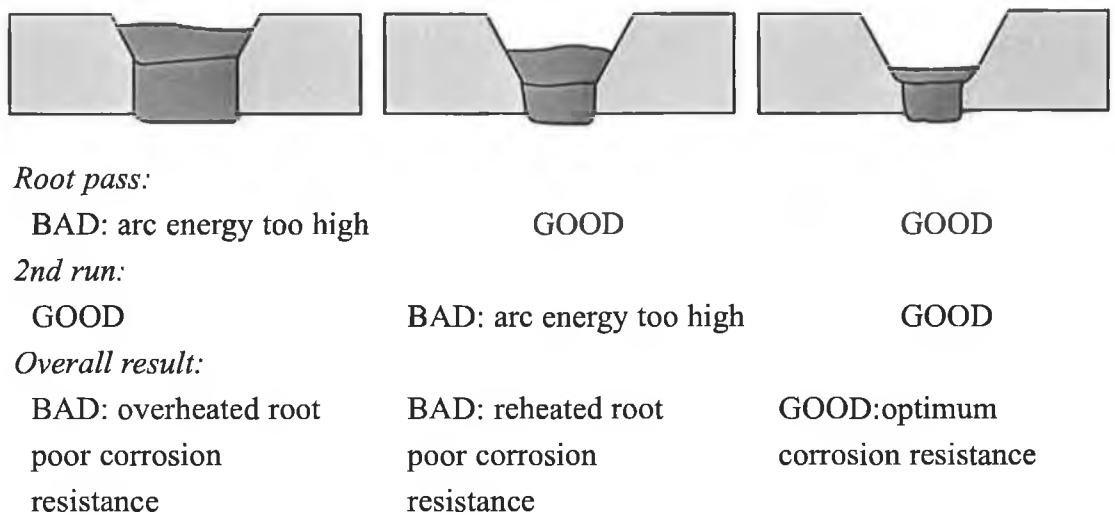


Fig. 5 Variations in welding GTAW root and second pass; COLD PASS technique

### Joint Filling Passes

Argon back purging of single sided welds should be maintained throughout the welding of pipe and plate with weld deposit thicknesses up to 12 mm, to avoid progressive root underbead oxidation through reheating. The back purging of double sided welds can be stopped earlier. Balanced weld sequences should be maintained for the initial 5 mm of joint thickness. Control of interpass temperature and arc energy should be maintained throughout the welding of the whole joint.

### Joint Filling Using SMAW Process

Zeron 100 requires correct electrode handling procedures, in particular, protection against moisture pick-up. Electrodes should be used directly from unopened containers, vacuum pack containers or from a 150°C minimum temperature storage oven.

Electrodes should be issued and stored on the job in heated quivers in quantities suitable for 4 to 5 hours production or consumed within 8 to 10 hours of removal from vacuum packaging. In all cases the Manufacturers recommendations for the particular type of flux coating should be followed.

Welding techniques are based on electrode manipulation avoiding distinct weaving and associated high heat input. Arc strikes should be avoided.



Electrodes should be operated within the amperage range recommended by the manufacturers. These are typically:

*Table 2 Range of recommended SMAW electrode current settings*

Electrode diameter (mm)	Current range DC + (A)
2.5	50-65
3.2	70-90
4.0	100-140

#### Joint Filling Using GMAW Process

Both 1.0 mm and 1.2 mm diameter wires are available for welding. Multipass weld layers employing minimum weave and controlled arc energy are advocated for joint filling. Argon/helium (CO<sub>2</sub>) gas mixtures have been successfully used for welding.

Typical parameters are given below:

*Table 3 GMAW parameters*

Position	Wire diameter (mm)	Current (A)	Arc voltage (V)	Travel speed (mm/min)	Arc energy (kJ/mm)	Gas flow (L/min)
1G	1.2	220-240	30-32	250-400	1.0-1.5	20
6G/6G	1.0	80-95	30-32	200-300	0.6-0.8	20

Welding practice should aim to combine the productivity benefits of the process with maintenance of arc energy control. A typical WPS is available on request.

#### Joint Filling with Submerged Arc (SAW) Process

Submerged Arc Welding (SAW) combining fast deposition of high quality weld metal with mechanised process productivity, is a very viable alternative for joint filling with:

- Material thickness in excess of 15-20 mm
- Pipe or vessel diameters in excess of 150 mm
- Circumferential or longitudinal seams can be welded in the downhand (ASME: IG) position.

The welding procedure with Zeron 100 is similar to that with standard austenitic stainless steels (316L etc) although in order to maintain requisite arc energy/weld cooling rate control, use of smaller diameter wires (eg 2.4 mm) and modest welding parameters is recommended. The comparatively fast travel speed and low arc energy conditions facilitate the benefits of continuous (eg full circumferential) welding and a reduced level of interruptions associated with interpass temperature control.

Control of weld bead shape is very important. The depth to width ratio must be less than 1, which requires careful selection of arc voltage, to avoid risk of centreline

solidification cracking. Avoid too heavy beads per layer. The process is normally introduced to fill out joints following deposition of 8-10 mm of TIG(GTAW) and MMA (SMAW) root weld layers. An interpass temperature of 150°C maximum throughout the joint is recommended.

The flux used must be maintained in a reliable dry condition i.e., either directly from new, unopened bags/drums or storage ovens operating at 250°C. Unfused flux recovered from the weld should be sieved and rebaked before further use.

With the agglomerated fluxes involved, repeated recycling will lead to excessive build-up of fines and a shift in flux grain size balance, ultimately causing a deterioration in operating characteristics. To counter this effect, recycled flux should be diluted with new unused flux in a 1:1 ratio.

The recommended 25-30 mm deep flux pile is intended to prevent arc flaring through the flux cover, leading to loss of arc/weld pool stability, possible entrainment of air into the arc cavity, potential risk of weld surface ‘gas flats’ and; at worst, internal porosity. Above 30 mm, flux pile depth will tend to inhibit release of gases generated during welding.

With regard to electrode extensions, ‘stick-out’ of less than 20 mm, resistive heating effects and metal droplet detachment may become unstable, resulting in weld bead wander (“slalom effect”). Typical welding parameters are:

*Table 4 SAW welding parameters*

Wire diameter (mm)	Welding current DC+ (A)	Arc voltage (V)	Travel speed (mm/min)	Arc energy (kJ/mm)	Electrode extension (mm)	Flux height (mm)
2.4	280-350	28-30	450-500*	0.9-1.2	20-25	25-30

*\*Travel speeds up to 750 mm/min may be required with smaller diameter, e.g. 6" (150mm), pipe butt welds.*

### Repair welding

Zeron 100 has excellent welding properties and consequently gives a low repair rate even when extensive NDE is applied on completed welds. If repairs are required then it has been found that it is easier and preferable to cut out and completely re-weld all small diameter thin wall welds (Typically <4" dia and <3 mm wall thickness) rather than repair. When repairs are required on larger diameter, thicker welds then these should be carried out in accordance with a qualified weld repair procedure. It is essential on repair welds that the procedures are designed to prevent excessive heating of the previous weld zone especially where a thin ligament remains after any cut out.



## *POST WELD CLEANING*

Care should be taken to ensure that all flux or light spatter is removed from the weld zone. Careful light grinding may be used in conjunction with wire brushing.

### Pickling

Pickling of the local weld area has been found to significantly improve corrosion resistance of the weld zone. Specific pickling pastes are available for super duplex stainless steels and give excellent improvements in properties when used in line with the manufacturer's recommendations.



## *NOTES*



*Z E R O N 1 0 0 S U P E R D U P L E*

**NOTES**

*EX STAINLESS STEEL*

ST

15

## HEALTH AND SAFETY

Health and Safety requirements associated with welding Zeron 100 in relation to:

- Electrical Equipment
- Pressurised Gases
- Personnel Protection
- Fire
- Fume
- Arc Radiation

must be observed. If in doubt, your company Safety Officer should be consulted. Specific product safety data sheets are available on request from the distributors for each of the products when required.

## SUMMARY

Golden Rules

Many thousands of Zeron 100 joints have been successfully welded utilising and implementing this good welding practice. The main points to be remembered are:-

- i) Use good stainless steel fabrication practice.
- ii) Use a consistent joint fit up as detailed in the qualified WPS.
- iii) Control the backing gas composition and flow rate.
- iv) Choose the correct arc energy relative to the joint thickness.
- v) Control the arc energy during production welding of the qualified WPS.
- vi) Ensure consistent and maximum filler wire additions are made.
- vii) Monitor and control the interpass temperatures and ensure that the maximum temperature quoted in qualified WPS is not exceeded.
- viii) Utilize stringer bead techniques with minimal weaving (maximum 3 x wire diameter).

## CONTACTS

*Further information or advice can be obtained from:*

**MANCHESTER HEAD OFFICE:** Technical Department, Weir Materials & Foundries, Park Works, Newton Heath, Manchester, M40 2BA.

Telephone +44 (0)1 61 954 4678 Fax +44 (0)1 61 954 4739 email: [wmlinfo@wml.weir.co.uk](mailto:wmlinfo@wml.weir.co.uk)  
[www.weirmaterials.com](http://www.weirmaterials.com)

**ABERDEEN OFFICE:** Howe Moss Terrace, Kirkhill Ind. Estate, Dyce, Aberdeen, AB2 0GR

Telephone: +44 (0)1224 775 644 Fax: +44 (0)1224 775 646

**OSLO OFFICE:** Strandveien 5E, 1324 Lysaker, Norway

Telephone: +47 67 59 21 50 Fax: +47 67 59 21 69 email: [bjarne.olsen@weir.no](mailto:bjarne.olsen@weir.no)

**PERTH OFFICE:** 44-56 Fisher Street, Belmont, Western Australia, 60104.

Telephone: +61 894 799 670 Fax: +61 894 799 671 email: [keithj@weir.com.au](mailto:keithj@weir.com.au)

---

THIS DOCUMENT HAS BEEN PREPARED FOR ZERON 100 WELDERS AND ENGINEERS USING THE LATEST INFORMATION. JOINTLY BY WMF, METRODE AND LINCOLN SMITWELD. RESPONSIBILITY FOR IMPLEMENTING THESE GUIDELINES TO MEET SPECIFIC REQUIREMENTS REMAINS WITH THE FABRICATOR.

---